TUDelft

Delft University of Technology

The climate impact of hypersonic transport

Pletzer, Johannes

Important note
To cite this publication, please use the final published version (if applicable).
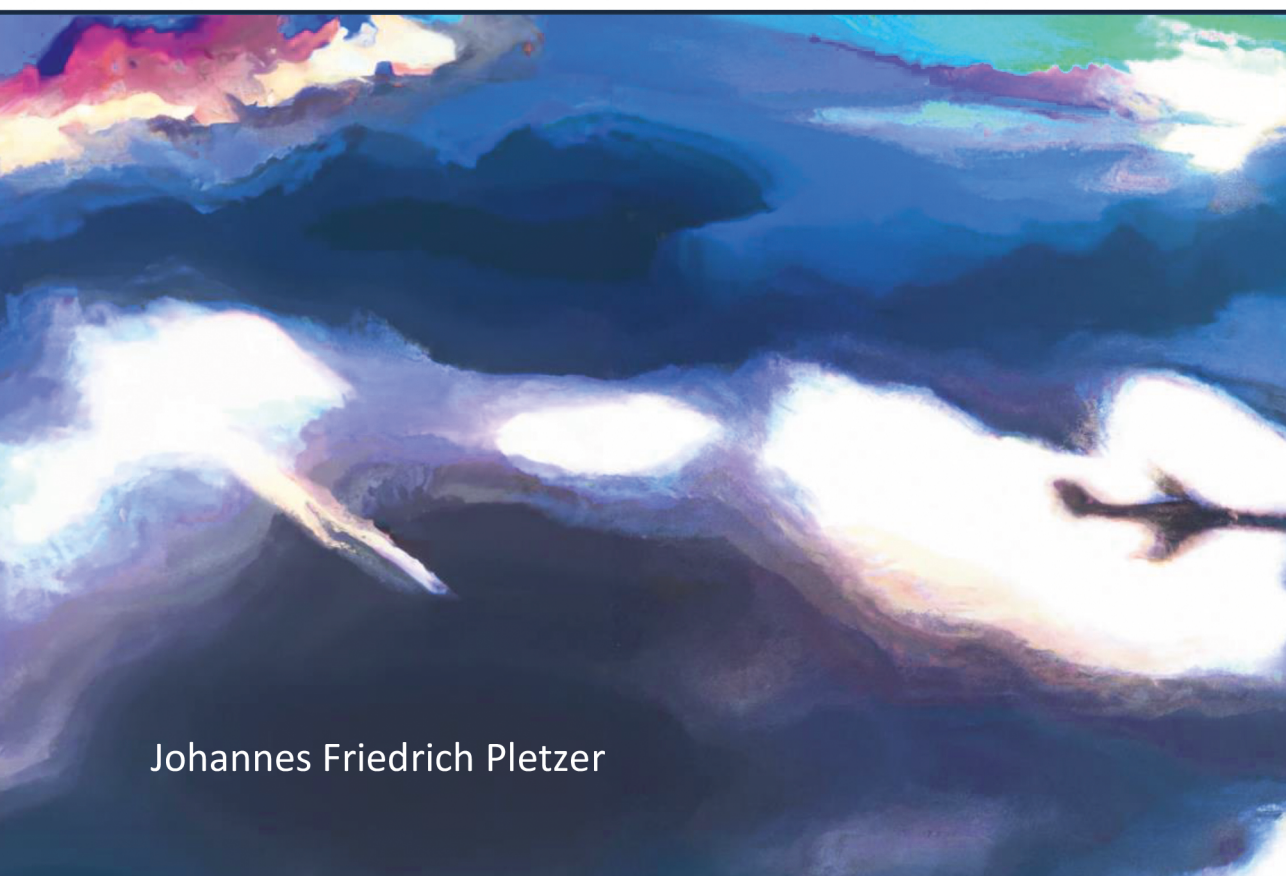Please check the document version above.

THE CLIMATE IMPACT OF HYPERSONIC TRANSPORT

Johannes Friedrich Pletzer
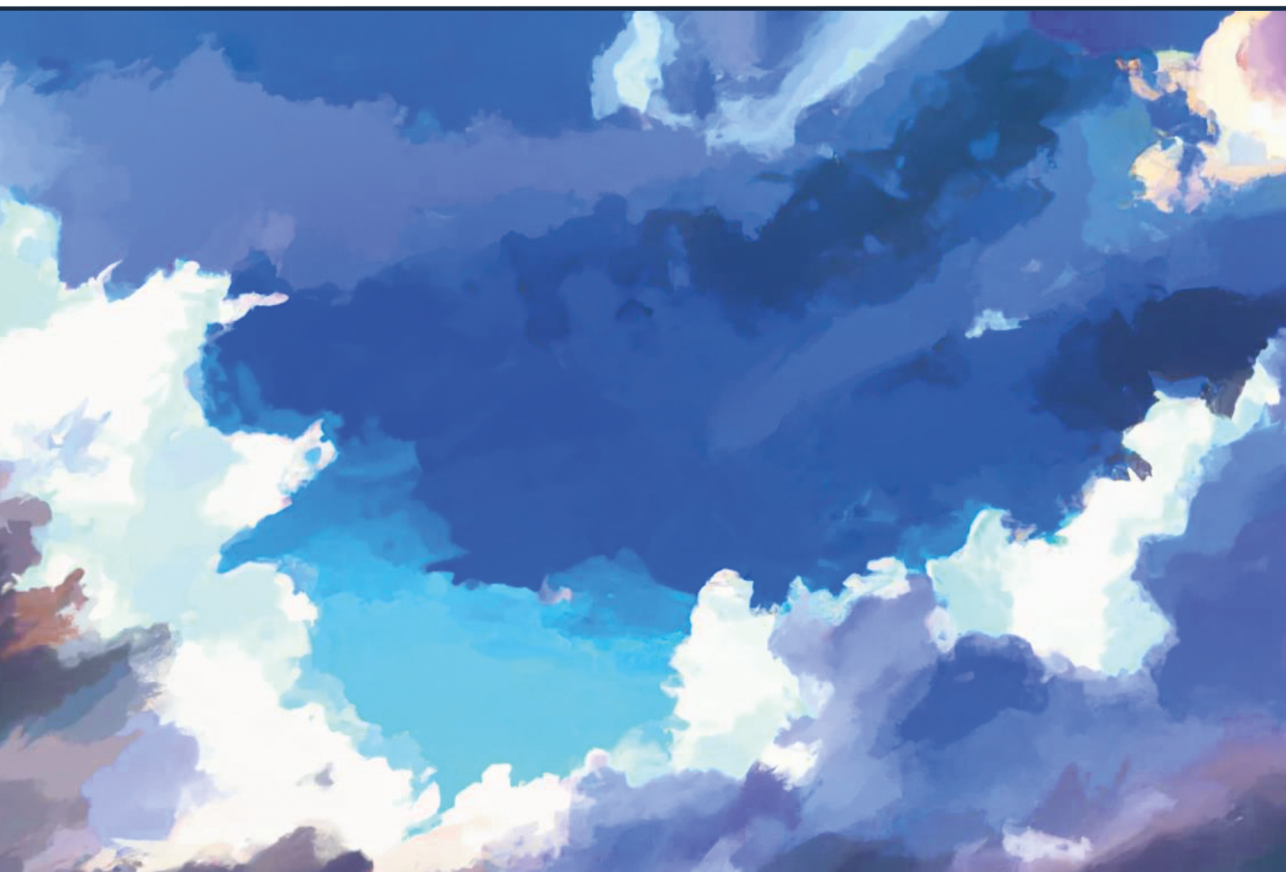
THE CLIMATE IMPACT OF HYPERSONIC TRANSPORT

THE CLIMATE IMPACT OF HYPERSONIC TRANSPORT

Dissertation

for the purpose of obtaining the degree of doctor
at Delft University of Technology
by the authority of the Rector Magnificus, Prof.dr.ir. T.H.J.J. van der Hagen,
chair of the Board for Doctorates
to be defended publicly on
Thursday 22 February 2024 at 10:00 o'clock

by

Johannes Friedrich PLETZER

Master of Science in Physics, Ludwig-Maximilians-Universität, Germany
born in Ebersberg, Germany

This dissertation has been approved by the promotors.

Composition of the doctoral committee:

Rector Magnificus,	chairperson
Prof.dr. V. Grewe,	Delft University of Technology, *promotor*
Dr. I.C. Dedoussi,	Delft University of Technology, *copromotor*

Independent members:

Prof.dr.ir. H.W.J. Russchenberg	Delft University of Technology
Prof.dr. L.L.A. Vermeersen	Delft University of Technology
Prof.dr. A. Schmidt	Ludwig-Maximilians-Universität, Germany
Prof.dr. M. Dameris	Ludwig-Maximilians-Universität, Germany
Dr. D. Hauglustaine	Centre National de la Recherche Scientifique, France

An electronic copy of this dissertation is available at
`https://repository.tudelft.nl/`.

Wege entstehen dadurch, dass wir sie gehen.
Paths are created by us walking them.

Antonio Machado

CONTENTS

SUMMARY

At speeds roughly between five and ten thousand km/h, hypersonic aircraft offer the promise of an extremely fast means of transport. Growing concerns about climate warming, however, direct attention to sustainability. This thesis focuses on atmospheric composition and radiation changes by considering a range of individual hypersonic aircraft designs on trajectory and route network level.

State-of-the-art Earth system models are used for simulations, and results calculated with the EMAC model are subsequently compared with simulations performed elsewhere with the LMDZ-INCA model. The comparison to a third model, i.e. WACCM, with a very similar – but independent – model setup allows even further clarification. For model validation satellite measurements (ozone, water vapor) and aircraft measurements (ozone, water vapor, temperature) are taken into account.

After the introduction in the first chapter, the second chapter is a general description of the Earth system including anthropogenic perturbations, in particular perturbations from subsonic, supersonic and hypersonic aircraft emissions followed by a detailed explanation of methods and the EMAC model setup in the third chapter. A new research finding in the context of middle atmospheric chemistry is the increased methane and nitric acid oxidation following hypersonic emissions. This effect results in a (photo-)chemical net production of water vapor and eventually increases water vapor perturbations further, which is described in detail in chapter 4. In chapter 5 an analysis of atmospheric dynamics and transport of emitted trace gases in the middle atmosphere underlines the importance of the Brewer-Dobson circulation and shows the impact of polar stratospheric clouds on water vapor perturbations during polar winter. The evaluation of multiple hypersonic aircraft designed for different cruise altitudes shows that their climate impact increases with cruise altitude and can be approximately 10-20 times as much as a conventional aircraft (chapter 6). Emissions at different hypersonic cruise altitude and latitude regions show that the climate impact can vary more with latitude of emission than with altitude of emission (chapter 7). With rf_of_hypersonic_trajectories() a software was developed to estimate the climate impact of aircraft design and flight trajectory/network options in seconds based on robust results from Earth system modelling. Using the software it is shown that a cruise altitude optimization loop can reduce the overall climate impact of a state-of-the-art aircraft design (chapter 8).

There are two methodological highlights to mention in the context of the EMAC model. The first is a new MESSy submodel H2OEMIS, which was created as part of this thesis. H2OEMIS is an interface to include water vapor emissions in EMAC model simulations, which was not possible before. This submodel will generally be of interest for future evaluations of e.g. any vehicles emitting water vapor and the impact of volcanic eruptions with EMAC. The second methodological highlight is the application of a novel

speed-up technique during simulation runs, which reduces the simulated years by two-thirds.

To conclude the summary, the four following points are important to take away. This thesis brought

- A new research finding on middle atmospheric chemistry: The identification of a chemical feedback that enhances the water vapor perturbation lifetime albeit an increasing chemical water vapor destruction

- A robust estimate of the climate impact of hypersonic aircraft for both specific aircraft designs and general atmospheric and radiative sensitivities showing a large altitude and latitude dependence

- An easily accessible tool for researchers and companies to estimate the climate impact of new hypersonic aircraft designs with low cost and low time

- An estimate how the development of hypersonic aircraft would contribute to a road map to a climate optimal aircraft industry compared to conventional aircraft

SAMENVATTING

Met snelheden ruwweg van vijf tot tienduizend kilometer per uur biedt hypersonische luchtvaart de belofte van een extreem snel verkeersmiddel. Klimaatverandering noodzaakt echter tot aandacht voor duurzaamheid. Dit proefschrift plaatst de focus op gevolgen voor atmosferische samenstelling en straling. Met modellen van de aarde-als-systeem is een spectrum van vliegtuigontwerpen in relatie tot vluchttrajecten en trajectnetwerken overwogen. Voor berekeningen is het EMAC model ingezet. Voorts zijn resultaten vergeleken met simulates die elders met het LMDZ-INCA model zijn uitgevoerd. Door uitbreiding van de vergelijking met het WACCM model, eveneens elders onafhankelijk toegepast, maar met een vergaand overeenkomstige instelling, verduidelijken de uitkomsten verder. Ter validatie zijn er tevens metingen per satelliet (ozon en waterdamp) en per vliegtuig (ozon, waterdamp en temperatuur) bij betrokken.

Na het inleidende eerste hoofdstuk schetst hoofdstuk twee een model van de aarde-als-systeem dat toegespitst is op antropogene verstoringen veroorzaakt door uitstoot van sub-, super- en hypersonische vliegtuigen. Hoofdstuk drie volgt met methodologische uitleg inclusief de gekozen instelling van het EMAC model. In het vierde hoofdstuk staat, als bevinding van het onderzoek naar chemische samenstelling van de midden-atmosfeer, de verhoogde oxidatie verklaard van methaan en salpeterzuur als gevolg van hypersonische uitstoot. Op hun beurt leiden die veranderingen netto tot (foto)chemische productie van waterdamp met nog weer verdere verstoringen tot gevolg. Dan komt hoofdstuk vijf met een analyse van de midden-atmosferische transportdynamiek van uitgestoten sporengassen. Kenmerkend is de Brewer-Dobson circulatie met invloed van polair-stratosferische wolken tijdens de poolwinter. Hoofdstuk zes evalueert variëteit van ontwerpen van hypersonisch vliegtuig voor verschillende kruishoogtes. De uitwerking op klimaat neemt toe met die hoogte en bereikt een omvang van tien tot twintig keer meer dan huidige luchtvaart veroorzaakt. Nadere analyse in hoofdstuk zeven toont dat klimatologische gevolgen van hypersonische luchtvaart sterker afhangen van respectievelijk variëren met breedtegraad waarop gevlogen wordt afhangen dan van de hoogte van kruisvlucht. Hoofdstuk acht behandelt het ontwikkelde computerprogramma
rf_of_hypersonic_trajectories(). Daarmee kunnen, uitgaande van erkende modellering van de aarde-als-systeem, met seconde-nauwkeurigheid schattingen worden opgesteld van de invloed op het klimaat van diverse opties van zowel ontwerp van hypersonisch vliegtuig als vluchttraject/–netwerk. Daaruit blijkt dat geavanceerd ontwerp en een daarvoor optimale kruishoogte de klimaatinvloed kunnen verminderen.

Methodologisch van belang is dat EMAC model twee uitbreidingen verkrijgt. In de eerste plaats is H2OEMIS ontwikkeld als nieuw MESSy submodel ervan. Daarmee is een voorziening beschikbaar om uitstoot van waterdamp mee te laten tellen. Dat was voorheen met EMAC niet mogelijk. Genoemd submodel is meteen ook veel ruimer bruikbaar, zoals voor evaluatie met EMAC van willekeurige voertuigen die aangedreven door

waterstof waterdamp uitstoten en van vulkaanuitbarstingen. De tweede bijdrage onder methodologische noemer betreft versnelling van verwerking; de duur van een simulatie laat zich met twee-derde verkorten.

Op een rijtje zijn de voornaamste resultaten van het onderzoek:

- Inzicht in de chemische samenstelling van de midden-atmosfeer is uitgebreid met identificatie van een chemische terugkoppeling. De duur van de verstoring van waterdamp houdt langer aan en gaat met afname van waterdamp gepaard.

- De klimaatinvloed van hypersonische luchtvaart valt met aanzienlijke zekerheid te schatten voor enerzijds concrete vliegtuigontwerpen, anderzijds algemene atmosferische en stralingsomstandigheden. De invloed blijkt sterk te variëren afhankelijk van zowel kruishoogte als breedtegraad waarop hypersonisch wordt gevlogen.

- Er is een eenvoudig stuk gereedschap ontwikkeld. Onderzoekers en bedrijven kunnen er meteen in de ontwerpfase vlot en zonder hoge kosten de verwachte klimaatinvloed van hypersonische vliegtuigen respectievelijk luchtvaart mee nagaan.

- De mogelijkheid om hypersonische luchtvaart onder de noemer van klimaatinvloed te vergelijken met conventionele luchtvaart biedt de luchtvaartindustrie strategische aanknopingspunten.

1

INTRODUCTION

1.1. MOTIVATION

T HE climate impact of aircraft emissions has been studied for decades and becomes more and more important. Estimated aviation growth rates will increase aviation's contribution to climate warming and by that challenge the support of the Paris Climate Agreement [1–4]. A recent study estimates the contribution of aircraft activity to human-made climate warming to 3.5 (3.4, 4.0) % [5]. Furthermore, while carbon dioxide (CO_2) effects contribute one-third to the effective radiative forcing, non-CO_2 effects contribute two-thirds. This estimate is based on conventional aircraft fleets that are powered with kerosene and fly at altitudes from 10-12 km. With these aircraft, it takes travellers approximately one day to fly to the other end of the world.

Development of the Aircraft Industry Two development goals for future aircraft fleets are on the one hand to reduce climate impact and on the other hand to reduce travel time. Numerous estimates of the climate impact and the growth potential of the current aircraft industry have been published [6–9], including projections with different technological development scenarios combining both [3]. Road-maps for a more climate-friendly liquid hydrogen based aviation industry have been developed in agreement with existing research and estimate the potential reduction in climate impact to be 50-75 % [10]. But this mainly addresses the concept of subsonic aircraft flying at 10-12 km altitude. Technically there are three categories of aircraft: subsonic aircraft that fly slower than the speed of sound, supersonic aircraft, whose speed exceeds the speed of sound, whereas the speed of hypersonic aircraft is at least five times the speed of sound. Higher altitudes are especially interesting for the supersonic and hypersonic high-speed aircraft concepts that promise customers to save a considerable amount of travel time, especially on middle- and long-range flights. For the same distance, the travel time of supersonic aircraft is advertised as approximately half that of subsonic aircraft[1]. Of course the different supersonic aircraft designs each have their specific speed and may deviate from

---

[1]https://boomsupersonic.com/company

1

this number. In comparison, hypersonic aircraft, which are in development and not as technologically advanced as supersonic aircraft, would by design fly at higher altitudes and higher speed compared to supersonic aircraft. Hence, they reduce travel time by a factor four to eight or even more instead of two. Currently, civil hypersonic aircraft and hypersonic transporters are being developed by e.g. the Destinus company, the Sierra Space Corporation or the Hermeus company. Clearly, on the one hand, the aircraft industry strives to satisfy customer's needs with potential innovations like supersonic and hypersonic aircraft. On the other hand, the aircraft industry currently is in a transformation process to build a climate compatible aircraft infrastructure.

Aircraft and the Ozone Layer   The largest ozone concentrations are found at polar regions between 16-24 km and between 24-28 km at equatorial regions (Fig. 2.10). These are the altitudes where supersonic and hypersonic aircraft designs should reach cruise altitude. The first notes that nitrogen oxides from supersonic aircraft might significantly affect the ozone layer were published in the 1970s [11–13]. Nitrogen oxides are produced at high temperatures during combustion and originate from ambient air (N_2 and O_2). Today it is known that not only nitrogen oxide emissions affect ozone, but water vapor emissions as well [14]. A depletion of the ozone layer affects live on earth by contributing to climate warming and an increase in UV radiation, which can cause health problems like skin cancer.

High-Speed Aircraft and their Impact on Climate   Multiple publications on the quantitative climate impact of supersonic aircraft fleets exist. A review of a selection of research programs including a direct comparison of radiative forcings was given in 2010 by Grewe et al. [15], who estimated the ratio of radiative forcing from supersonic to subsonic aircraft to be 3 (S4TA fleet, eight passengers), 6 (Airbus fleet, 250 passengers) and 14 (Boeing fleet, 309 passengers). The latter two numbers were adapted by the author from Grewe et al. [16] and IPCC [17], respectively. While these numbers initially appear to differ greatly, the authors present a correlation of flight altitude (range from 15-20 km) and radiative forcing of non-CO_2 effects and additionally state that climate warming of supersonic aircraft approximately scales with fuel consumption. Hence, cruise altitude, i.e. speed and in turn fuel consumption, clearly is a crucial factor for the climate impact of aircraft. Generally, the contribution from H_2O emissions is the main climate driver for supersonic aircraft and becomes more and more important with altitude because of the dry atmosphere in comparison to the troposphere and the longer residence time, i.e. perturbation lifetime, above the tropopause [14, 17].

Accumulation of Climate Relevant Species   The contributors to climate impact of aircraft are many and a direct comparison is often difficult. One measure to compare is the (perturbation) lifetime of emissions. For example, cirrus clouds are created by aircraft flying in cold air and cause a large ratio of the non-CO_2 aircraft climate warming by containing longwave radiation in the atmosphere. However, the lifetime of cirrus clouds is somewhere between some minutes to a day [18–20]. Hence, there is no accumulative effect and the warming stops quickly after aircraft are put out-of-service or other measures reducing cirrus clouds take effect. The lifetime of ozone perturbations

is some months and the lifetime of water vapor perturbations increases from hours to years with altitude [21]. The perturbation lifetime of methane (which is not equal to the (photo-)chemical lifetime) is slightly above a decade [22, 23]. The carbon dioxide perturbation originating from fossil fuel is subject to a large variety of sinks with different lifetimes. In general, the range is approximated with 2-20 centuries, where most of the carbon dioxide is taken up by ocean and biosphere sinks and 20-35 % remain in the atmosphere for longer time. Hence, released carbon dioxide will affect climate for tens of thousands to hundreds of thousands of years [24, 25]. Clearly, for carbon dioxide the cause (emission) and effect (warming) are difficult to estimate and this long tail of carbon dioxide lifetime is most probably one of the largest motivations to find alternative fuels for aircraft or new aircraft designs with a at least lower associated climate warming.

Climate Compatibility and Mitigation Options It easily takes decades to develop new aircraft before they can be launched on the market and the lifetime of aircraft can also be counted in decades. Hence, the climate compatibility of new aircraft has a long-lasting effect and is therefore of utmost importance. The technological reality that aircraft operated with fuel will ultimately emit climate drivers seems inevitable, since purely battery-powered aircraft do not seem like a viable option for middle to long-range flights due to the batteries weight. Taking 100 % sustainable alternative fuels provides the option of net-zero CO_2 emission flights, although availability and the degree of sustainability is likely to be a limitation for the coming decades and non-CO_2 effects would remain active. Hydrogen-powered aircraft are a promising alternative mostly for shorter range or lower altitude flights [26]. Therefore, the importance of improving in-flight climate efficiency of fueled aircraft cannot be emphasized enough. The potential of climate optimised routing [19, 27–30] and climate optimised design [31, 32] of conventional aircraft had been shown before. Since the development of high-flying, i.e. supersonic and hypersonic, aircraft is currently ongoing, the use of mitigation options during commercial use for the lowest possible climate warming will be crucial and should be fully exploited.

1.2. SCIENTIFIC QUESTIONS

The development and growth of the aircraft industry continues to date. However, the transformation to a climate friendly aircraft industry is very challenging and far from over, especially for high-flying aircraft. Hence, estimates of the climate impact of new aircraft designs are crucial and become increasingly important to their commercial viability. For futuristic high-flying aircraft, i.e. hypersonic aircraft, many open scientific questions remain to be answered and this thesis addresses the most important ones.

The following list of open scientific questions will be addressed within the framework of this dissertation.

1. By how much do emissions of hydrogen powered hypersonic aircraft affect atmospheric composition?

2. Which and to what extent do dynamical and chemical processes control the perturbation lifetime of atmospheric composition changes?

1

3. How does cruise altitude control the atmospheric composition changes?

4. How large is the radiative forcing caused by these atmospheric composition changes?

5. How does the change in radiative forcing affect climate?

6. How does the climate impact of hypersonic aircraft compare to subsonic and supersonic aircraft?

7. What is the climate optimal cruise altitude of one of the currently most advanced hypersonic aircraft?

1.3. STRATEGY AND METHODOLOGY

Two steps are crucial to estimate the climate impact of aircraft. First, calculate the atmospheric composition changes caused by hypersonic aircraft emissions. Second, estimate the climate impact, e.g. radiative forcing, associated with these atmospheric composition changes. For this approach the standard tools are numerical models of the Earth system. In this thesis two Earth system models, EMAC and LMDZ-INCA, are used to obtain comparable and robust results, whereof EMAC is used for all simulations and LMDZ-INCA is used only for the first set of simulations. The first set of simulations estimates the impact of *combined* aircraft emissions of a hypersonic route network. The second set of simulations aims to assess atmospheric and radiative sensitivities of *individual* emissions at typical hypersonic cruise altitudes and latitudes. That means the impact of each emitted trace gases on atmosphere and climate is quantified separately. The performance of the EMAC and LMDZ-INCA models in modelling atmospheric composition is evaluated with aircraft measurements of the upper–troposphere lower–stratosphere and a test to assess radiative sensitivity to stratospheric perturbation. Additionally, EMAC results are validated with satellite data.

2

BACKGROUND

This chapter presents the scientific background and the context of the climate impact of hypersonic transport. Section 2.1 presents the Earth system and relevant processes with a focus on the atmosphere. Section 2.2 gives an overview on how the Earth system and the atmosphere are simulated by numerical models as digital representations. Section 2.3 addresses aircraft emissions and their distribution in the Earth system and section 2.4 focuses on the related impact on climate.

2.1. THE EARTH SYSTEM

T HE Earth system is a term that has been in existence for only a few decades. However, first theories that Earth system science is based on exist since the 1920's [35]. In 2001, at a major conference in Amsterdam a declaration on Earth system science was presented to the public. The following citation from it describes the most important features of the Earth system.

'The Earth system behaves as a single, self-regulating system comprised of physical, chemical, biological and human components. The interactions and feedbacks between the component parts are complex and exhibit multi-scale temporal and spatial variability. [..]'[1]

Clearly, Earth system science is very challenging, since its goal is to describe the very complex Earth system with fitting concepts like the geosphere, biosphere or the anthroposphere (Fig. 2.3). When looking at satellite images, like shown in Fig. 2.1, the challenges become clear, simply due to the Earth's scale, its surface variation and the existence of human population.

Figure 2.1: Processed satellite image of the Earth, atmosphere and stars. Designed by freepik.

The biological, physical, and chemical conditions that make up the Earth system vary greatly by location, such as the Earth's core, oceans, land, or atmosphere. The boundary of the Earth system is simply the top of the atmosphere [36]. The timescales of processes

---

[1]www.igbp.net/about/history/

vary from extremely small time steps, e.g. solar irradiation causing atomic or molecular transformations in the atmosphere or on the surface, to extremely large time steps like it is seen with plate tectonics. Processes that aren't interconnected do barely exist. However, humanity has been accumulating knowledge since it's existence and is able to describe important subsystems, often referred to as 'spheres' of the Earth system quantitatively and qualitatively.

2.1.1. THE EARTH SYSTEM AND ITS MAIN SUBSYSTEMS

Nowadays, the Earth system is divided into geosphere, atmosphere, biosphere and hydrosphere [37]. The geosphere refers to rocks and minerals from Earth's molten core to the uppermost crust, i.e. the surface. The latter is also called lithosphere. The atmosphere is the gas layer from the solid surface to where the gas particles kinetic energy becomes larger than the geosphere gravity and they eventually leave the Earth system.
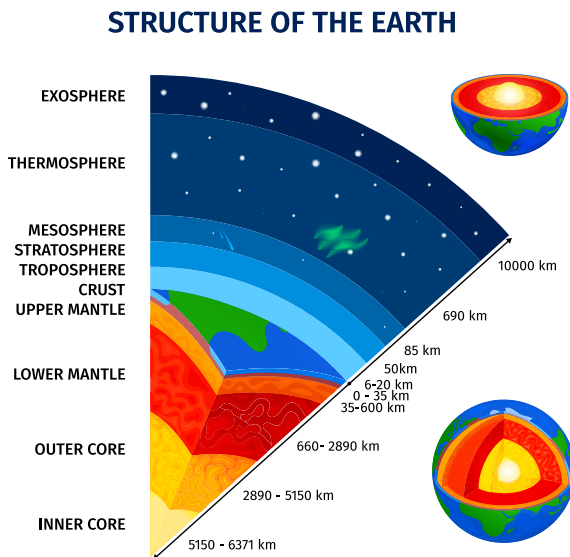
Figure 2.2: The layers from the Earth's core to the top of the atmosphere. The distance is not drawn to scale. Designed by freepik

The biosphere refers to all living beings and their connection to the other spheres. The hydrosphere contains all water in liquid (oceans, seas, lakes, rivers), gaseous (water vapor) and solid form (sea ice, glaciers). A newer addition is the 'anthroposphere', referring to the environment that is altered significantly by human activities [38]. A conceptual model combining these spheres, with a focus on bio- and geosphere, is shown in Fig. 2.3 highlighting their interconnection. The overlap of the different spheres is clearly visible. The hydrosphere, for example, is not mentioned and its components are attributed to geo- and biosphere. This is similar to the book by Gettelman and Rood

[39], where the hydrosphere is not explicitly mentioned and the authors refer directly to the hydrologic cycle, cryosphere and oceans. Since hypersonic aircraft emit water vapor, the hydrosphere is highly relevant. In Fig. 2.3 the sun, volcanoes and fossil fuels are not treated as a part of the Earth system, but as external factors, which contribute to the energy budget by incident sunlight, blocking incident sunlight or increasing greenhouse gas concentrations, respectively. The connection between anthroposphere and geosphere are namely emissions and in return climate impacts, which very much reflects the method of this thesis to estimate the impact of aircraft emissions on the atmosphere and the resulting impact on climate.

2.1.2. The Atmosphere and Atmosphere Dynamics

The most important subsystem for the context of this work is the atmosphere. The atmosphere consists of different gases and surrounds the solid earth, attracted by gravity. The largest parts of dry air are nitrogen (N_2), oxygen (O_2) and argon with approximately 78 % and 21 % and 0.93 %, respectively. Other gases with low concentrations are referred to as 'trace gases', e.g. carbon dioxide (CO_2), methane (CH_4), hydrogen (H_2) and ozone (O_3). Concentrations are so low that they are often presented in form of 'mixing ratios' (e.g. *parts per million*), i.e. parts of a certain gas compared to parts of dry air in a specific volume, either as a weight (ppmw) or volume ratio (ppmv). Water vapor in the atmosphere is very variable and therefore not treated as a trace gas in most cases, even though the total mass of water vapor in the atmosphere is small compared to the whole atmosphere. Both, trace gases and water vapor, are very important for the atmosphere and surface temperature, since they absorb some of the incoming radiation and contain some of the outgoing radiation. The additional energy remains in the Earth system, which in turn affects weather and climate [41].

Radiation Energy Budget   These global energy flows are shown in Fig. 2.4, where shortwave radiation from the sun, i.e. high energy radiation, penetrates the atmosphere and reaches the Earth surface. On the way parts of the radiation are absorbed by the atmosphere, while some parts are reflected by clouds, aerosols, gases and the surface. Like any other surface, the Earth's surface, which absorbed the shortwave radiation, emits longwave radiation depending on its temperature and composition. A large part of longwave radiation is contained in the lower atmosphere due to various trace gases and water vapor. These are collectively described as 'greenhouse' gases (GHG), since they heat the atmosphere in a similar fashion to a greenhouse for growing plants. The most important ones are H_2O, CO_2, CH_4, O_3 and nitrous oxide (N_2O). Water vapor contributes half of the total atmospheric back radiation, clouds 25 %, CO_2 19 % and there are small contributions by O_3, N_2O, CH_4, aerosols and chlorofluorocarbons (CFCs) [42]. Aircraft cause perturbations of trace gas concentrations and thus influence the radiation energy budget. This is discussed in more detail in the context of emitted trace gases and climate impact starting on p. 28.

Atmospheric Layers   Gravity attracts most of the atmosphere to the surface. Therefore, the atmosphere consists of different vertical regions with decreasing density and in combination with incident sunlight these vertical regions are in unique chemical and
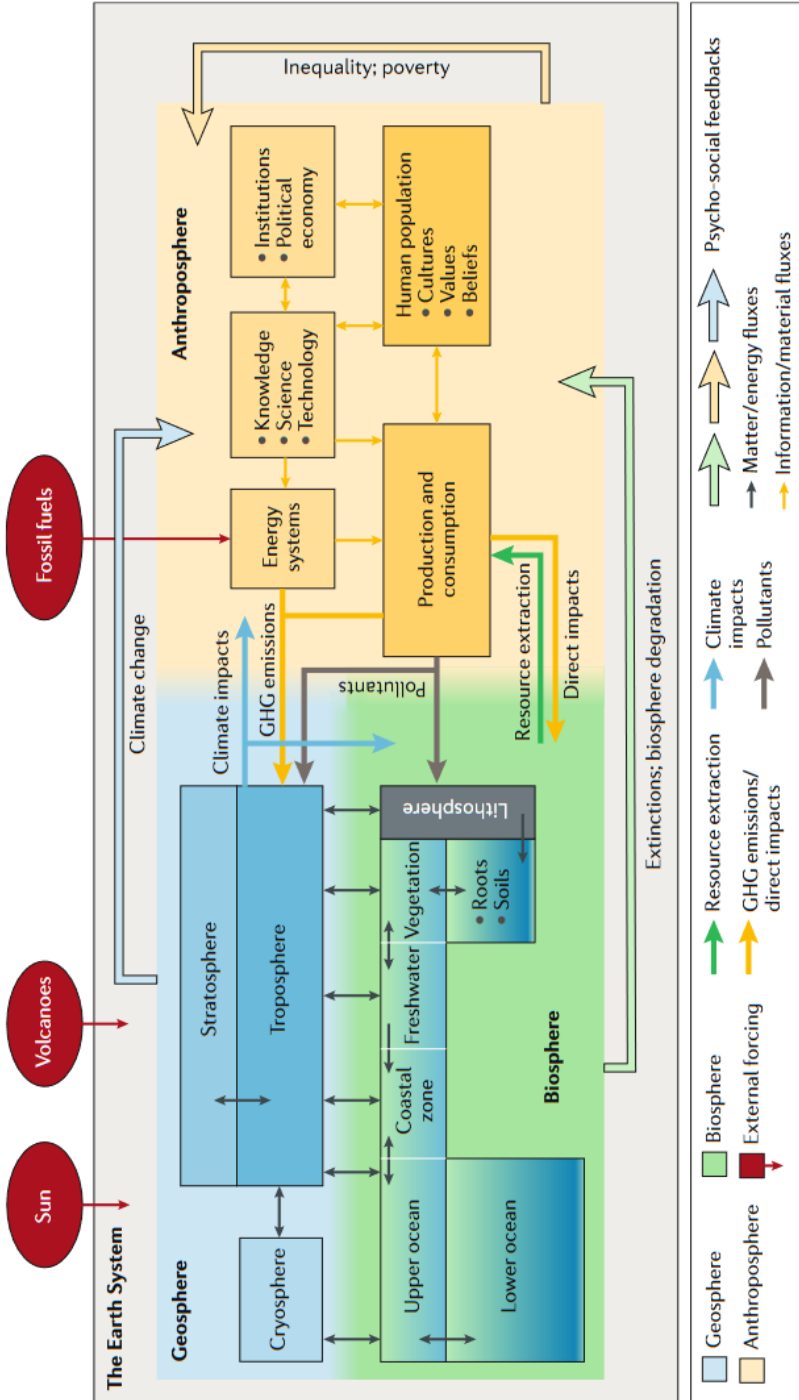
Figure 2.3: Updated conceptual model of the Earth system published by Steffen et al. [40] and inspired by the Bretherton diagram. Image reproduced with permission of the rights holder, *Springer Nature* through RightsLink.

2
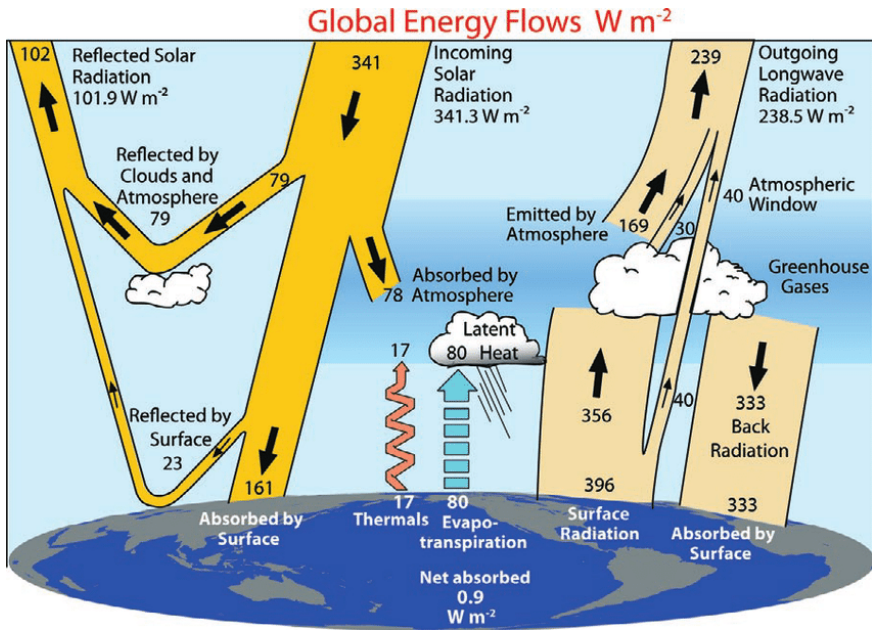
Figure 2.4: The global annual mean Earth's energy budget for the March 2000 to May 2004 period (Wm^{-2}). The broad arrows indicate the schematic flow of energy in proportion to their importance. The figure and caption were published by Trenberth, Fasullo, and Kiehl [41]. The image was reproduced with permission of the rights holder, the *American Meteorological Society*.

physical states (Fig. 2.2). They are called the troposphere, stratosphere, mesosphere, thermosphere and exosphere. The troposphere is named after dynamical mixing caused by rotation. The stratosphere is named after the thermally layered, i.e. stratified, layers. The mesosphere is referred to as the 'middle' atmosphere and the coldest layers of the atmosphere are part of it. The other spheres are for the most part above the Kármán line at approx 100 km, which divides aero- and astronautic activities, and are therefore not as crucial for the scope of this work. By design conventional aircraft fly mostly in the troposphere and the lowermost stratosphere, supersonic aircraft fly in the lower stratosphere and hypersonic aircraft fly in the middle stratosphere.

Hydrologic Cycle   A very important process of the Earth system, and especially for the atmosphere, is the hydrologic cycle. It describes the cycle of water from the ocean and land surfaces to the atmosphere and back. The hydrologic cycle is responsible for the main energy flow through the atmosphere [43]. As mentioned, it's role in the radiative budget as a greenhouse gas is dominant over many other processes. Additionally, water transfers latent heat by evaporation and condensation and drives large scale dynamic movements in the atmosphere. Following evaporation and condensation, precipitation of aqueous or frozen water defines the lifetime of atmospheric water in the troposphere. The commonly used term is residence time of water vapor and is quantified with 4-5 days [44, 45]. The timescale that water vapor emitted by aircraft remains in the atmosphere

depends heavily on altitude of emission and can range from hours to years [21, Fig. 6a].
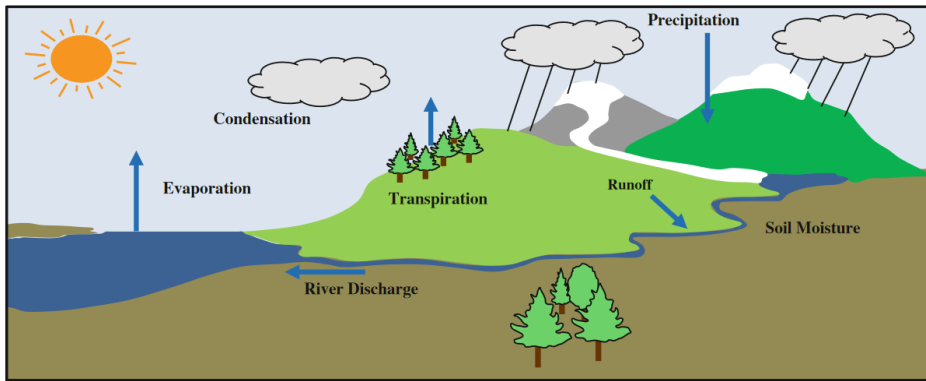
Figure 2.5: The hydrologic cycle. Water evaporates from the ocean and is carried in the atmosphere as vapor. It condenses into clouds, and precipitates to the surface, where it can become soil moisture, glaciers, or runoff as surface water into lakes and back to the ocean. Plants move soil water back to the atmosphere through transpiration. The figure and caption were published by Gettelman and Rood [39] and is licensed under CC BY-NC 2.5.

TROPOSPHERE DYNAMICS

Most of the air mass in the atmosphere is located close to the Earth's surface and decreases with altitude due to gravity. Most atmospheric water is therefore found in the troposphere and occurs in three states; gaseous as water vapor, liquid as water droplets in clouds or ice as frozen water droplets. Another mechanism, the freeze-drying of air at the tropical cold point tropopause, contributes strongly to contain water vapor in the troposphere and is one of the main mechanisms causing a dry stratosphere [46, 47]. The movement of tropospheric air masses, i.e. atmospheric dynamics or wind, is cyclic. On the one hand there is horizontal, i.e. longitudinal and latitudinal, movement and on the other hand vertical movement, which together form a closed or non-closed cyclic movement.

Horizontal Motion of Air   Longitudinal motion of air originates from the Earth's rotation and the related 'Coriolis' effect. Depending on wind direction the movement of air is deflected to the right on the Northern Hemisphere and to the left on the Southern Hemisphere. The initial movement of air, to which the Coriolis force applies, originates from differences in pressure gradients, i.e. low and high pressure fields. These pressure fields come from uneven solar heating. The latitudinal winds and the Coriolis force create a horizontal pattern of western and eastern winds (Fig. 2.6, left).

Vertical Motion of Air   Latitudinal and vertical motion are closely connected and collectively combined as three cells, which are the Hadley, Ferrel and Polar cells (Fig. 2.6, right). The main tropospheric upward motion can be found at the Equator in the so

2

called intertropical convergence zone (ITCZ), where vertical winds dominate. This up-ward motion is part of the Hadley cell, where warm and moist air rises from the surface to the tropopause and, while it cools radiatively, is transported pole-wards. The then cold air sinks back to the surface at the subtropics and returns to equatorial regions, where the cycle begins anew. The polar cell is very similar to the Hadley cell, since it is also driven by convection. Warm air rises at around 60° latitude and moves pole-ward at the tropopause, where it eventually sinks and closes the cycle. Between the polar and Hadley cell is another cell, the Ferrel cell. It is not driven by convection, but rather ex-isting due to the strong motion of the polar and Hadley cell. The presentation as shown in Fig. 2.6 has been widely accepted for a long time. New views on the air movement in Ferrel cells were published, highlighting a smaller closed loop at lower mid-latitudes in addition to a non-closed loop, i.e. pole-ward transfer for all vertical levels, at higher mid-latitudes [48, 49]. On the interface of these cells are additional fast air currents flow-ing west to east called jet streams. The polar jet stream is located between the polar and Ferrel cell at 9-12 km. The subtropical jet stream exists between the Hadley and Ferrel cell at 10-16 km.
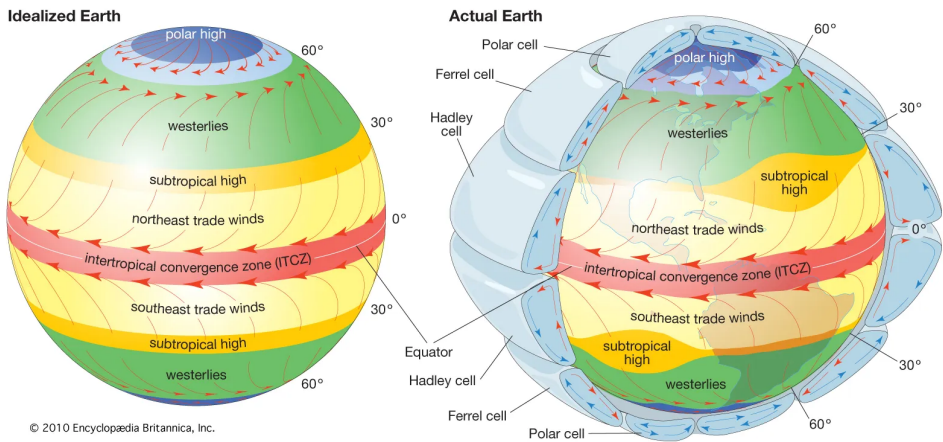
Figure 2.6: General patterns of atmospheric circulation over an idealized Earth with a uniform surface (left) and the actual Earth (right). Both horizontal and vertical patterns of atmospheric circulation are depicted in the diagram of the actual Earth. The figure and caption are used according to the Terms of Use from Encyclopædia Britannica.

MIDDLE ATMOSPHERE DYNAMICS

The middle atmosphere covers altitudes from approximately 10-90 km and the strato-sphere and mesosphere are part of it [50]. The stratosphere extends from the tropopause – whose height depends on latitude – to the stratopause at about 50 km (Fig. 2.7). Tem-peratures have a low-point at the tropopause and and a high-point at the stratopause. The atmospheres lowest temperature is at the mesopause. The transition is continuously increasing or decreasing, for the stratosphere and mesosphere, respectively. Clearly, the middle atmosphere has a wide scale of temperature depending on altitude. Vertical mix-

ing and convection is weak compared to the troposphere and it is common to describe it as vertically 'stratified' with cold layers at lower and warm layers at higher altitudes.
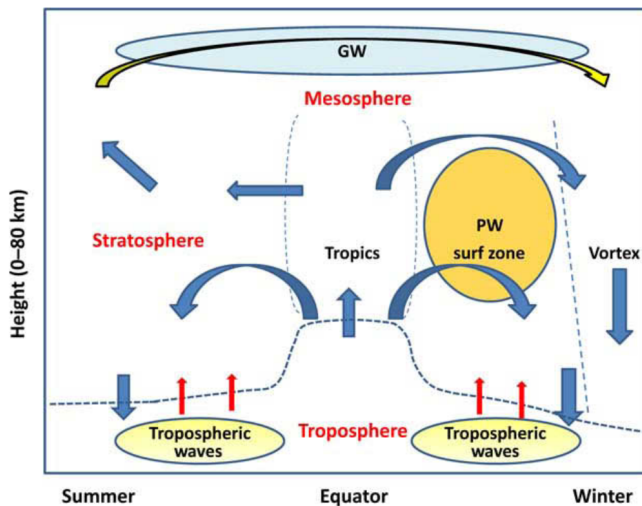
Figure 2.7: Schematic of transport circulation in the middle atmosphere. Transport by the Brewer–Dobson circulation (BDC) is shown by blue arrows. In the lower stratosphere, the BDC transports air from the tropics into both Hemispheres, then downward through the tropopause. In the middle and upper stratosphere, the BDC has a strong pole-ward, downward circulation in the winter Hemisphere where there is planetary wave (PW) breaking. In the summer Hemisphere the upper stratospheric circulation is pole-ward and upward. The pole-to-pole transport in the mesosphere is shown by the yellow arrow. Gravity waves (GWs) are the major source of wave energy in the mesosphere. The year-round source of tropospheric wave energy propagating into the stratosphere is depicted by red arrows. Regions with restricted two-way transport ('mixing barriers') are indicated by vertical dotted lines. The dashed thick blue line above the troposphere is the tropopause. The figure and caption were reprinted from North, Pyle, and Zhang [51] with permission from *Elsevier* through RightsLink.

Main Air Flow in the Middle Atmosphere   The main meridional (south-north or north-south) and vertical (upwards and downwards) air flow in the middle atmosphere is called the Brewer-Dobson circulation (BDC, [52]). Air enters through the tropical tropopause, where it passes the cold point and is therefore very dry. While ascending to higher altitudes, the air moves pole-ward and gradually starts to sink back to the tropopause. There it reenters the troposphere at the extratropical tropopause. The BDC is, compared to tropospheric dynamics, a slow process. A correlated measure is the age of air. It refers to the transport time an air parcel needs from a source (tropical tropopause) to a specific stratospheric location and the age of air shows a wide spectrum from months to 6-8 years [53, 54]. Therefore, a full cycle, i.e. entering and leaving the middle atmosphere from and to the troposphere, can take several years. Currently, many open questions about the BDC remain. However, the main drivers are, firstly, diabatic heating at the tropics and diabatic cooling at mid- to polar-latitudes (in winter) and, secondly, waves, which deposit their momentum [51, 55, 56]. Clearly, many processes contribute to dynamics and they differ in magnitude, frequency and region of appearance. The following

2

paragraphs introduce the most important processes.

Gravity Waves   Gravity waves originate most likely from topography and convection and contribute strongly to atmospheric dynamics. They have a wide scale of spatial (few to thousands of kilometers) and temporal (minutes to tens of hours) propagation and drive large-scale circulation of the middle atmosphere [57]. For example these waves introduce an additional mesospheric air flow from the summer to winter pole (Fig. 2.7). The stratified middle atmosphere very much facilitates wave propagation due to the decreasing density with altitude and in turn larger wave amplitudes. Dissipation and momentum deposition of these waves were identified quite early as important processes in the middle atmosphere [58], disrupting radiative equilibrium of thermal layers and countering zonal mean winds [57]. Furthermore, gravity waves contribute to oscillations like the quasi-biannual oscillation or the semi-annual oscillation by weakening or strengthening the phase depending on altitude [57, 59, 60].

Planetary Wave Breaking   While vertical mixing is weak at stratospheric altitudes, strong horizontal mixing happens especially in the surf zone at mid-latitudes and is caused by planetary (also called Rossby) wave breaking (Fig. 2.7). Additionally, the mid-latitudinal wave breaking causes a net pole-ward and down-ward transport of air towards polar regions, effectively causing the 'extratropical pump', where air at the tropics follows with a rising motion. The horizontal mixing and transport is quite important for the transport of trace gases emitted in the stratosphere.

Polar Vortex   Besides the main air flow, another large-scale air movement in both Hemispheres is associated with the polar vortex, which is driven by the stratospheric polar jet. It originates from a stratospheric temperature gradient between tropics, heated by ultraviolet absorption of ozone, and polar regions, cooled by infrared emission, and the Coriolis force. This creates fast west to east winds (westerly), which appear every polar winter. The resulting vorticity extends up to the mesosphere, with fastest speeds at the stratopause. There, the speeds decrease, since the temperature gradient is reversed. With an active polar jet, stratospheric air at mid-latitudes is nearly completely isolated from the very cold air at the polar stratosphere [61]. The cold conditions within the stratospheric polar vortex facilitate the condensation of polar stratospheric clouds (PSCs) in the lower stratosphere, which are a precursor for heavy ozone depletion. Note that PSC coverage is generally larger in the Antarctic than the Arctic [62, Fig. 17]. The chemical schematic of PSCs is covered in section 2.1.3. Both, the direct transport via the vortex and the indirect effect of PSCs control water vapor perturbations from high altitude aircraft, which is analysed in detail in chapter 5 (p. 73).

Stratospheric Sudden Warming   Another dynamic process is stratospheric sudden warming (SSW), where air on the Northern Hemisphere warms rapidly in a few days [63]. The resulting large scale quasi-horizontal mixing affects weather and trace constituents, especially ozone, and break the polar vortex. How this affects air transport from stratosphere to troposphere and, subsequently is currently an open question.

Quasi-Biannual Oscillation   In contrast to the annual appearance of the polar vortex, the quasi-biannual oscillation (QBO) has a longer frequency of approximately two to three years. It affects interannual variability of wind and temperature, mostly in the lower and middle tropical stratosphere. West- and eastward winds alternate and descend, with largest wind-speeds at 30 to 10 hPa [59, 64]. The QBO is important for the variability of trace constituents like ozone and additionally affects other oscillations like the semi-annual oscillation (SAO).

Semi-Annual Oscillation   Semi-annual oscillations appear both near the stratopause and mesopause and are strong out-of-phase zonal winds. These winds change temperature and vertical movement of air, which in turn affects long-lived trace constituents like nitrous oxide and methane. Layers of these constituents in the course of the semi-annual cycle, i.e. SAO, are clearly visible in equatorial measurements.

Change in Main Air Flow with Time   The Brewer-Dobson circulation could become stronger in the future [65] and, subsequently, the mean age of air might decrease [66, 67], due to climate change. This in turn would most probably reduce the perturbation lifetime of emitted species from high altitude aircraft in the stratosphere. Further information on the change in main air flow in the context of perturbation lifetime is discussed on p. 6.3.1.

TRANSPORT BETWEEN TROPOSPHERE AND STRATOSPHERE IN THE EXTRA-TROPICS

The interface of the troposphere and middle atmosphere is generally the tropopause. However, to address the air transport between the well mixed troposphere and the more stratified middle atmosphere, it is important to include the surrounding region. This extended interface of the troposphere and middle atmosphere is called the upper–troposphere lower–stratosphere (UTLS). As depicted in Fig. 2.8, tropospheric air enters the stratosphere in the tropics. Contributors to tropical up-welling, aside from the extratropical pump, are still in discussion [55, 56, 68, 69]. The mainly down-ward transport in the extra-tropics and polar regions is of particular importance for the removal of emitted species from aircraft. The tropopause can be seen as a barrier and there are several processes that can weaken or overcome its stability. Tropospheric wave dynamics can reach into the lower stratosphere and facilitate troposphere-stratosphere exchange. These are for example warm deep convection (clouds), conveyor belts, tropopause folds and cutoff lows [70–72]. From the stratosphere, the Brewer-Dobson circulation continuously transports air into the extratropical UTLS region and is strongest in winter to spring. Quasi-local (depending on season) dynamics are e.g. the polar vortex and subtropical jet. The subtropical jet acts as a barrier for horizontal transport at the core, but at outer regions shows wave breaking and instability as a precursor for mixing and exchange of stratospheric-tropospheric trance constituents [73]. Quasi-isentropic exchange very much depends on season [74, Fig. 12] and – for water vapor – is larger in the Northern Hemisphere and can be on the same order of magnitude as cross-isentropic exchange in the tropical pipe [75]. Additionally, there are regions with reduced vertical exchange. So called tropopause inversion layers (TIL), which originate partly from radiative feedback connected to the water vapor and ozone distributions in the UTLS (green shading,

Fig. 2.8). These do not appear at regions where the polar vortex or subtropical jet are active.
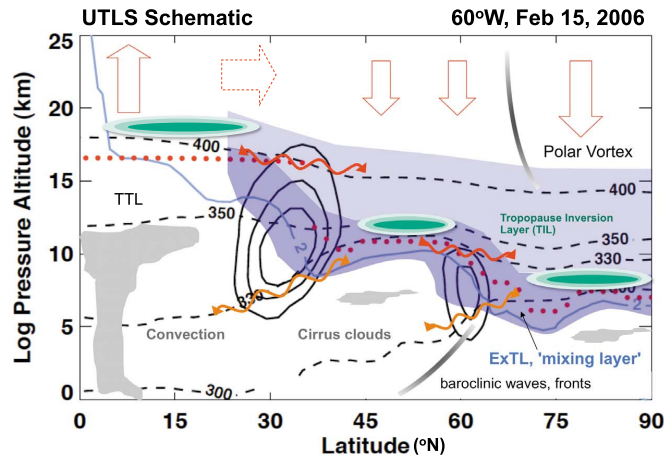
Figure 2.8: Schematic snapshot of the extratropical UTLS using data from a Northern Hemisphere section along 60° W longitude on 15 February 2006. Wind contours (solid black lines 10 ms^{-1} interval), potential temperature surfaces (dashed black lines), thermal tropopause (red dots), and potential vorticity surface (2 PVU: light blue solid line). Illustrated schematically are the Ex-UTLS (dark and light blue shading), ExTL (dark blue shading), clouds and fronts (gray shading), static stability contours in the TIL (green shading), quasi-isentropic exchange (red wavy arrows), cross-isentropic exchange (orange wavy arrows), and the Brewer-Dobson circulation (deep, red solid outline; shallow, dotted solid outline). The figure and caption were published by Gettelman et al. [73] and is free for non-commercial use according to Wiley's terms and conditions.

The described dynamic processes are highly important in the context of aircraft emissions. Middle atmospheric dynamics in the context of hypersonic aircraft emissions are discussed in detail in chapter 5.

2.1.3. ATMOSPHERE CHEMISTRY AND (PHOTO-)CHEMISTRY

This chapter contains parts of tropospheric (photo-)chemistry that are important to understand the climate impact of (hypersonic) aircraft. The main focus is on processes that take place in the middle atmosphere and additionally can affect troposphere (photo-)chemistry through transport of chemical constituents to lower altitudes. There, removal processes, chemical transformation processes and radiation effects related to these chemical constituents are important. For completeness, important processes and constituents, which are not covered or only briefly, are aerosols and most particles, hydrocarbons excluding methane (aliphatic, aromatic, biogenic), tropospheric cloud chemistry, mercury, peroxyacetyl nitrate, sulfur chemistry (organic) and volatile organic compounds (for further reading refer to North, Pyle, and Zhang [76] or Brasseur et al. [77]). The focus is on water vapor, molecular hydrogen, the hydroxyl and hydroperoxyl radicals, methane, nitrogen oxides, ozone and the general oxidizing capacity.

Reaction Rate An important relation in understanding atmospheric chemistry pathways is the reaction rate as a function of concentration (equation 2.1). [A] and [B] are

concentrations, κ is the reaction rate coefficient, also named reaction rate constant, and α and β are the order of reaction [78].

$$Rate = -\frac{d[A]}{dt} = -\frac{d[B]}{dt} = \kappa [A]^{\alpha} [B]^{\beta} \qquad (2.1)$$

TROPOSPHERE CHEMISTRY AND (PHOTO-)CHEMISTRY

The general composition of air has been presented before in section 2.1.2 and its main constituents are chemically stable molecules. Minor constituents, i.e. trace gases or small particles, are in most cases the main reactants in the troposphere, since radiation with enough energy to convert chemically stable molecules is already filtered at higher altitudes. Surface emissions of minor constituents and the resulting transport through the troposphere build a complex net of (photo-)chemical pathways including removal processes. In addition, air transport from middle atmospheric altitudes contribute other atmospheric constituents participating in tropospheric (photo-)chemical pathways. A schematic of the main processes has been published in a book by Brasseur et al. [77, Fig. 1.8]. There, the main surface emissions from natural or anthropogenic sources are water vapor, methane, carbon monoxide and carbon dioxide. Nowadays, hydrogen sources are in discussion due to the prospect of a developing global hydrogen economy. Ozone and nitrogen oxides originate partly from higher altitudes. Additionally, lightning discharges increase nitrogen oxide concentrations. Further constituents that are eventually created through (photo-)chemistry, are the hydroxyl and hydroperoxyl radicals, and in turn nitric acid, and others like organic radicals. Removal processes in the troposphere are dry or wet deposition, i.e. deposition at the surface or within cloud droplets.

Tropospheric (photo-)chemical pathways are important in the context of hypersonic aircraft, since emitted trace gases or other perturbed constituents are transported to lower altitudes and affect trace gas concentrations along these pathways there. This includes besides hydroxyl radicals most importantly methane, ozone and nitrogen oxides.

Troposphere Hydroxyl Radical The hydroxyl radical OH oxidizes many gases, including most greenhouse gases. The main source, initiated by an ozone reaction, is the oxidation of water vapor during daytime (reaction R1).

$$O(^1D) + H_2O \longrightarrow 2\,OH \qquad (R1)$$

Additional sources include (photo-)chemical reactions of acetone, nitrous acid and formaldehyde, peroxyacyl nitrates decomposition initiated by nitrogen trioxide and ozonolysis of alkenes. OH concentrations are larger at low latitudes.

An overview of global emission rates of trace gases and the consecutive removal by reaction with OH was published by Ehhalt [79, Table 3]. OH removes up to 90 % of carbon monoxide, methane and others and 50 % of nitrogen dioxides. Chlorofluorocarbons remain unaffected.

Other Troposphere Radicals and Lifetimes Apart from OH, the oxidation capacity of the troposphere is supported by the nitrate radical (NO_3) and ozone. Many lifetimes of

2

tropospheric trace gases are controlled by these radicals and have a wide range from hours to centuries. The whole-atmosphere lifetime of methane is approximately 8 years, of carbon monoxide 1.5 months, of hydrogen 2 years, of nitrogen oxides 0.3-5 days and of nitrous oxide 120 years, based on a list published in North, Pyle, and Zhang [76, Table 2]. Note that these values depend very much on the specific years of evaluation, since atmospheric composition, especially OH concentrations, changes with time. For example an estimate for the whole-atmosphere methane lifetime for the year 2010 is 9.1 ± 0.9 years [80, 81]. Therefore, these lifetimes are to be understood as a reference for an order of magnitude.

Troposphere Nitrogen Oxide   Net ozone change due to nitrogen oxides ($NO_x = NO + NO_2$) is non-linear. Ozone production is mostly dominant, apart for low levels of NO_x mixing ratios, where ozone depletion takes over [76]. Additionally, NO_x concentrations show a nonlinear relation to OH concentrations at tropospheric altitudes, where low values of the former result in OH increase and high values result in reduced OH. In the troposphere the relation of NO_x increase causing OH increase is dominant [79]. Reaction R2 describes how NO participates in HO_2 to OH recycling. Reaction R3 is a major NO_x loss mechanism where the NO_2 increases OH loss.

$$NO_2 + h\nu \longrightarrow NO + O(^3P) \tag{R2}$$

$$OH + NO_2 + M \longrightarrow HNO_3 + M \tag{R3}$$
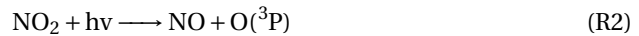
Troposphere Ozone   Ozone concentrations control the abundance of radicals OH and NO_3. Reaction R4 creates single oxygen, which in turn facilitates the creation of OH radicals in reaction R1.

$$O_3 + h\nu\,(\lambda \leq 330\,\mathrm{nm}) \longrightarrow O_2 + O(^1D) \tag{R4}$$
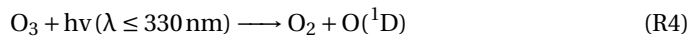
On its own, ozone is a greenhouse gas and its impact, i.e. warming or cooling, depends heavily on altitude. An increase is associated with warming from the surface to approximately 30 km, where an increase is associated with cooling instead [82, 83]. A radiative sensitivity including a latitude distribution was published by Riese et al. [84], where cooling does not appear for the modelled domain.

Troposphere Methane   Methane sources are both, natural and anthropogenic. Reaction R5 is the main sink in the troposphere and removes 90 % of methane [85]. In literature annual values of total oxidized methane range from 330-900 $\mathrm{TgCH_4\,yr^{-1}}$ [86–88].

$$CH_4 + OH \longrightarrow H_2O + CH_3 \tag{R5}$$

To summarize tropospheric chemistry, Fig. 2.9 shows the main chemical mechanism that control ozone abundance. The main cycles are HO_x and NO_x partitioning and the scheme includes NO_y reservoirs, with PAN and HNO_3, and carbon based mechanisms.
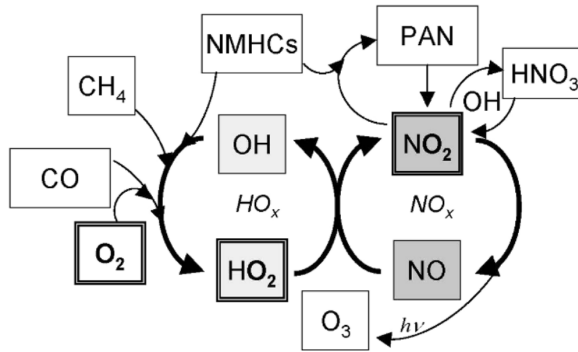
Figure 2.9: Scheme of the main tropospheric chemical mechanism controlling ozone. NMHC are non-methane hydrocarbons, PAN is peroxi-acetyl-nitrate, which serves as a reservoir for nitrogen oxides. Caption and figure were published by Grewe [89].

Troposphere Hydrogen   Surface hydrogen emissions are to a large part (70-80 %) taken up by soils via diffusion or bacteria. The rest (20-30 %) is oxidized by hydroxyl to a large part in the troposphere and to a lesser extent in the middle atmosphere. Please refer to Table 3.3 for a comparison of produced water vapor from hydrogen oxidation in model simulations. A global hydrogen economy would emit hydrogen into the atmosphere from e.g. leakage and contribute to warming from indirect effects [90, Fig. 1]. A question is how these surface emissions compare to direct emissions in the atmosphere from e.g. hypersonic aircraft. This is answered in the discussion of chapter 7 (p. 122).

MIDDLE ATMOSPHERE CHEMISTRY AND (PHOTO-)CHEMISTRY

Some species emitted at the surface aren't (photo-)chemically converted or removed at tropospheric altitudes and eventually reach the stratosphere. These gases, which are nitrous oxide, chlorofluorocarbons, halons, methane, water vapor and bromomethane, are eventually dissociated by high-energy shortwave radiation and are the source for a variety of radicals like hydroxyl, hydroperoxyl, nitrogen oxides, chloride- and bromide-compounds. Parts of these radicals are 'stored' in reservoirs, i.e. more stable compounds, like hypochlorous acid (ClOH), dinitrogen pentoxide (N_2O_5), chlorine nitrate ($ClONO_2$) and bromine nitrate ($BrNO_3$). Additional reservoirs, which are reduced through rain-out or deposition, are hydrogen peroxide, nitric acid, hydrogen chloride and hydrogen fluoride. At stratospheric altitudes these residual trace gases and radicals encounter comparably high concentrations of the greenhouse gas ozone, which is naturally produced by the combination of ambient oxygen and high-energy shortwave radiation. The radicals cause catalytic depletion of ozone, which eventually forms an equilibrium with the natural ozone production [77, Fig. 1.9]. Another greenhouse gas in the middle atmosphere besides ozone is water vapor. Chemical reactions including methane are a large source of water vapor at middle atmospheric altitudes.

Trace gases emitted from aircraft in the stratosphere affect ozone catalytic cycles,

methane lifetime from oxidation and other processes. Due to the lower air density continuous emission of trace gases has the potential to change background concentrations significantly.

Satellite Measurements of Ozone and Water Vapor in the Middle Atmosphere   Measurements of both, ozone and water vapor, have become increasingly accurate over time and extensive evaluation of available measurements were published from the SPARC (Stratospohere-troposphere Processes And their Role in Climate) Data Initiative [91, 92]. An available measurement record of ozone water vapor and ozone is the 'Stratospheric Water and OzOne Satellite Homogenized data set' (SWOOSH) published by Davis et al. [93]. SWOOSH contains water vapor and ozone mixing ratios for the time period 1984 to 2022 and data are available for nearly all the stratosphere and parts of the mesosphere. See Fig. 2.10 and 2.12.

Reactions Controlling Ozone Abundance   The most important reactions for stratospheric ozone abundance were made public by Sidney Chapman in 1930.

$$O_2 + h\nu \xrightarrow{J_1} O + O \tag{R6}$$

$$O + O_2 + M \xrightarrow{k_2} O_3 + M \tag{R7}$$

$$O_3 + h\nu \xrightarrow{J_3} O + O_2 \tag{R8}$$

$$O + O_3 \xrightarrow{k_4} O_2 + O_2 \tag{R9}$$

M refers to a third body, which participates in the reaction to conserve energy and momentum of the termolecular reaction [94]. In contrast to ozone production, catalytic cycles reduce the ozone abundance by overcoming the high activation energy of reaction R9. These cycles involve the radicals as part of the group of catalytic species X and XO. The following two reactions effectively catalyze reaction ozone.

$$X + O_3 \longrightarrow XO + O_2 \tag{R10}$$

$$XO + O \longrightarrow X + O_2 \tag{R11}$$

Further information on the participating radicals – halogen, nitrogen and hydrogen – is available in the following three paragraphs.

Figure 2.10: Multi-annual mean of ozone volume mixing ratios and concentrations measured by Aura Microwave Limb Sounder (MLS) for the years 2013-2016. The data were provided by Davis et al. [93]. Transformation of mixing ratios to concentrations was done by using standard atmosphere. The annual average sums up to 142 Dobson units for reference, which is a common measure equal to the total amount of a trace gas per unit area.

Halogens   Halogens like fluorine, chlorine, bromine and iodine have anthropogenic and natural sources. Halogen source gases are less reactive at tropospheric altitudes and eventually are converted with shortwave radiation in the stratosphere to create halogen radicals. Both, homogeneous (gas phase) (photo-)chemistry and heterogeneous (liquid and solid phase) chemistry of halogens, were responsible for heavy ozone depletion over the past decades. The former is active where radiation is strongest (tropics), while the latter becomes similar effective in ozone destruction in regions with low shortwave radiation (polar regions) and at temperatures below 210 K, which is associated with the appearance of polar stratospheric clouds. Main areas of ozone depletion are the middle stratosphere during the whole year and the polar vertices during spring [94].

Reactive Nitrogen   Nitrogen oxides are strongly participating in ozone depleting catalytic cycles described in reaction R10 and 11. Out of all nitrogen oxide compounds these are the most reactive and consist of NO and NO_2. The whole group of reactive nitrogen is described as NO_y and contains the additional nitrogen species nitrogen trioxide (NO_3), dinitrogen pentoxide (N_2O_5), nitric acid (HNO_3), peroxynitric acid (HO_2NO_2), chlorine nitrate ($ClONO_2$) and bromine nitrate ($BrONO_2$). The main source of NO_y is nitrous oxide (N_2O), which originates from natural surface processes and reacts to 2 NO with the following reaction.

$$N_2O + O(^1D) \longrightarrow 2\,NO \qquad \qquad \text{(R12)}$$

Another, secondary, source is the transport from the upper mesosphere and thermosphere to lower altitudes. Overall, the net production of NO_y is at the tropics from roughly 25-42 km with a maximum at 35 km. Sinks are the (photo-)chemical conversion to N_2 via the sequence of reactions R13 [95] and through transport to the troposphere, followed by rain-out of dissolved HNO_3.

2

$$2\,(N + NO) \longrightarrow N_2 + ON + NO \longrightarrow 2\,(N_2 + O) \tag{R13}$$
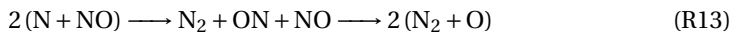
NO is highly reactive and oxidized to NO_2 by ozone. NO_2 reacts quickly to NO within roughly one minute during daytime [95, Fig. 7]. Other components of NO_y, like HNO_3, $ClONO_2$ or $BrONO_2$, have longer lifetimes and reduce ozone loss of catalytic ozone cycles. Among NO_y, concentrations of HNO_3 are larger in high-latitude winter. In combination with water vapor, liquid sulfuric acid, which is an aerosol, and low temperatures HNO_3 forms nitric acid trihydrate (NAT) particles. These facilitate the change of unreactive chlorine to reactive chlorine, which in turn depletes ozone drastically. Normally, this effect would be stopped by rising temperatures in spring, since polar stratospheric cloud particles revert to gas phase at higher temperatures. However, denitrification, i.e. freeze-out of nitric acid trihydrate, which sediment to lower altitudes, reduces NO_y. Therefore, reformation of the more stable reservoirs species is hindered and the chlorine is active longer. In contrast to $ClONO_2$ abundance, which decreases very quickly in early winter and slowly builds back up in spring, HCl abundance – another chlorine reservoir – decreases slowly in winter and deactivates chlorine radicals faster by reforming rapidly in spring [62, Fig. 37]. The two reactions to inactivate chlorine are the following.

$$Cl + CH_4 \longrightarrow HCl + CH_3 \tag{R14}$$

$$ClO + NO_2 + M \longrightarrow ClONO_2 + M \tag{R15}$$
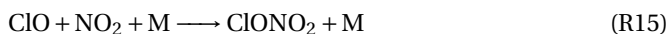
Hydrogen Radicals   Atomic hydrogen (H), hydroxyl (OH) and hydroperoxyl (HO_2) are hydrogen radicals and collectively described as HO_x. Hydrogen radicals participate in ozone chemistry and further ozone depletion in many reactions, either directly or in combination with halogen and nitrogen compounds. Generally, mixing ratios of these radicals increase with altitude due to the increasing high-energy radiation and they are mostly sourced from water vapor, methane and hydrogen. Figure 2.11 shows the reaction pathways, acting as sinks and sources of HO_x.

The three main sources of HO_x are converted by a sequence of gas phase reactions. These result in the following three net reactions, which are initiated by $O(^1D)$.

$$O_3 + H_2O \longrightarrow 2\,OH + O_2 \tag{R16}$$

$$CH_4 + 3\,O_2 \longrightarrow H + OH + 2\,HO_2 + CO \tag{R17}$$

$$O_3 + H_2 \longrightarrow H + OH + O_2 \tag{R18}$$
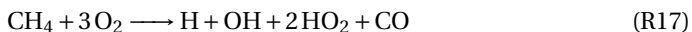
For the first net reaction R16 two other – heterogeneous – pathways exist and rely on, first, dinitrogen pentoxide (N_2O_5), and, second, chlorine nitrate ($ClONO_2$) to produce
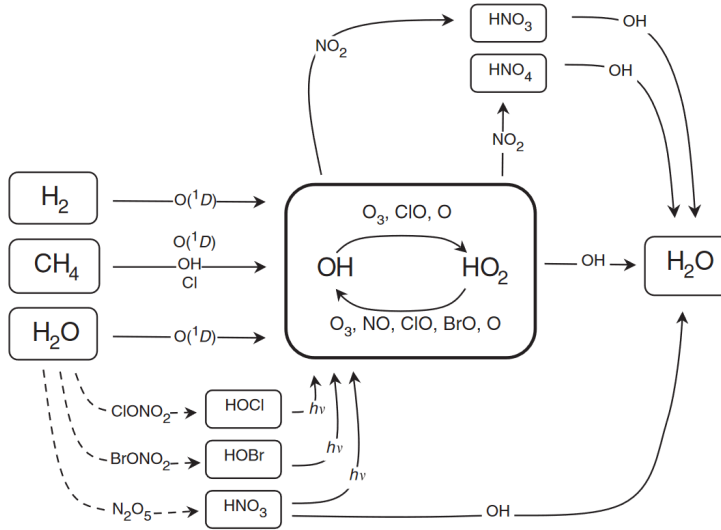
Figure 2.11: Primary sources and sinks of HO_x are shown. Gas phase reactions are denoted with solid lines and heterogeneous reactions with dashed lines. The figure and caption were reprinted from North, Pyle, and Zhang [94] with permission from *Elsevier* through RightsLink.

HNO_3 and eventually OH. For both pathways aerosols are important as nuclei to initiate the liquid or solid phase.

Generally, HO_x removal creates water vapor. Some removal processes are strongest in the lower stratosphere and they include HNO_3 and HNO_4 as gas phase reactions and N_2O_5 and aerosols as liquid or solid phase reactions. The respective net reactions are 19 and 20. At higher altitudes the abundance of HO_x facilitates the net reaction R19 as a self reaction.

$$OH + HO_2 \longrightarrow H_2O + O_2 \qquad \text{(R19)}$$

$$2\,OH \longrightarrow H_2O + O \qquad \text{(R20)}$$

Ozone Mixing Ratios and Concentrations The zonal ozone abundance is often presented as a mixing ratio where the maxima appears at the tropics around 10 hPa. However, this presentation might cause a misunderstanding on where most of ozone molecules persist. Unit transformation to concentration shows clearly that three regions show the highest accumulation of ozone molecules. North polar latitudes just above 100 hPa, the tropics at around 20 hPa and south polar latitudes at 50 hPa (Fig. 2.10).

Aerosols The atmosphere contains a variety of liquid or solid particles, called aerosols, which size ranges from nanometers to micrometers. They are either directly emitted
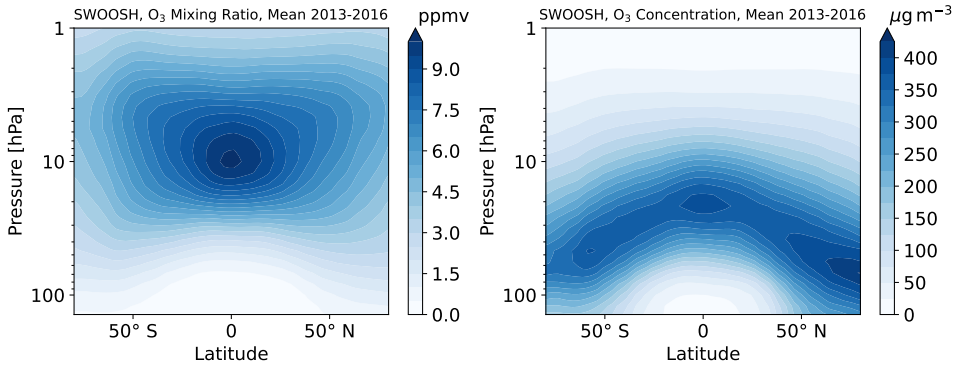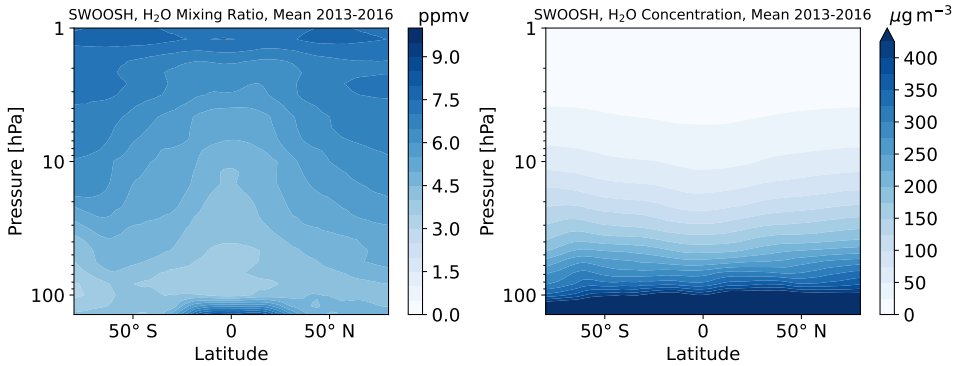
Figure 2.12: Multi-annual mean of water vapor volume mixing ratios measured by Aura Microwave Limb Sounder (MLS) for the years 2013-2016. The data were provided by Davis et al. [93]. Transformation of mixing ratios to concentrations was done by using standard atmosphere.

from the surface and aircraft or can form through certain processes in the atmosphere. Generally, aerosols are important for nucleation and cloud processes and the Earth's radiative budget. Stratospheric aerosols affect the formation of polar stratospheric clouds [96]. Aerosol lifetime ranges from a few days to a few weeks and they can be found nearly everywhere in the atmosphere [76].

MIDDLE ATMOSPHERIC WATER VAPOR

Water Vapor and Cold Temperatures The stratospheric water vapor near the tropopause is important for surface temperatures, i.e. climate, since it acts as a greenhouse gas. The cold point in the tropical tropopause was addressed briefly in troposphere and middle atmosphere dynamics (p. 11). It causes dehydration of warm and rising humid air that cools at the cold point and forms ice, which then falls out. The exact details of the specific environment are still in discussion and therefore continue to be a uncertainty factor in projections of stratospheric water vapor. Another dehydration process happens in the stratospheric vertices at polar regions in winter, where temperatures are cold enough. Water vapor at lower stratospheric altitudes cools the atmosphere radiatively and contributes to the appearance of polar stratospheric clouds. In the presence of certain radicals, these add to the ozone depletion at polar regions, especially in the Southern Hemisphere [94]. In this context both nitrogen oxide and water vapor emissions of aircraft flying in the middle atmosphere are highly relevant. Details are discussed in chapter 5 and 7.

Water Vapor and (Photo-)Chemistry Water vapor is part of the hydrogen budget, which itself is a source of various radicals and of high importance to middle atmospheric (photo-)chemistry. The (photo-)chemical lifetime of water vapor (and hydrogen) decreases from many decades to some months between the tropopause and stratopause (Fig. 2.13). From there on the former continues to decrease to a few days, whereas the latter increases to approximately a century. Both, methane (CH_4) and molecular

hydrogen (H_2), contribute to the total budget of water vapor as shown in chapter 3 and 5 (Table 3.3 and 5.1, respectively).
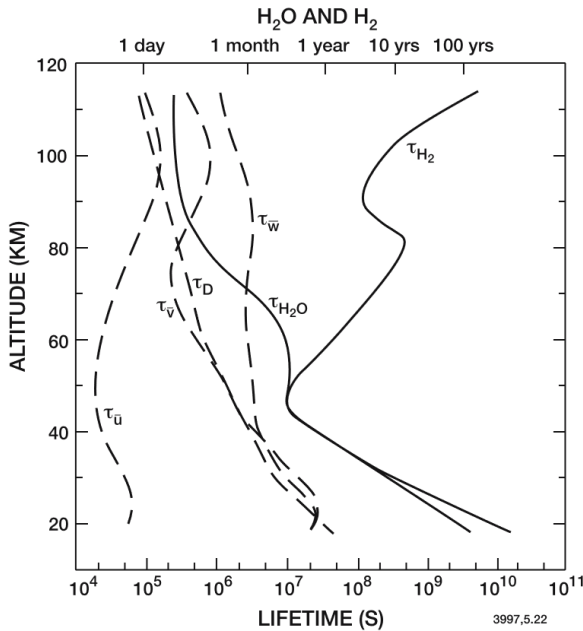
Figure 2.13: (Photo-)chemical lifetimes of water vapor and molecular hydrogen, and the time constants for atmospheric transport processes in the middle atmosphere. Note that values on the x-axis are shown in seconds (below) and recalculated to day, month, etc. (upper). Image and caption reproduced from Brasseur and Solomon [97] with permission of the rights holder, *Springer Nature* through RightsLink.

Water Vapor from Methane Oxidation   The oxidation of methane, as a sequence of the methyl radical (CH_3) and formaldehyde (CH_2O), eventually increases hydrogen and water vapor mixing ratio with altitude (Fig. 2.12). Note that compared to tropospheric concentrations, low amounts of water vapor reach the stratosphere and concentrations continuously decrease with altitude. The ratio $R = \frac{\Delta H_2O}{\Delta CH_4}$ describes the increase of water vapor in relation to the decrease in methane. It is altitude dependent, with lower values (R = -1.6) from the tropopause to the lower stratosphere and higher values (R = -2.0) at higher altitudes. Methane oxidation is more rapid at higher altitudes and therefore R = -2.0 is of higher significance for water vapor abundance [94].

Water Vapor Lifetime and Hypersonic Aircraft   Hypersonic aircraft are designed to reach cruise altitudes where the (photo-)chemical water vapor lifetime already starts to significantly decrease. From this aircraft developers expected synergy effects to reduce the climate impact of high-speed aircraft designs [98]. A combination with net-zero CO_2 fuels and a reduced non-CO_2 effect sounded very promising. However, results of this

work show that this prospect does not hold at altitudes up to 40 km. The underlying (photo-)chemical process is described in detail in chapter 4.

2.2. MODELLING THE EARTH SYSTEM

Numerical models that simulate the Earth system or components of it have been continuously developed and went from single grid box models like the relation of carbon dioxide abundance on surface temperature by Arrhenius [99] to high resolution models like EMAC (p. 26). Nowadays, the highest resolution simulations are difficult to distinguish from satellite images of the Earth with the bare eye [100]. This may be one of the reasons why the term 'digital twin' is becoming increasingly popular today, because in a sense the Earth has been given a numerical twin that is – depending on the viewpoint – indistinguishable to measurements.

2.2.1. EARTH SYSTEM MODELS

Earth system models (ESMs) include numerical presentations of Earth system components (Fig. 2.3), which can be combined to form a digital twin. Today many ESMs exist and their performance is continuously evaluated in respect to, e.g. satellite or aircraft measurements, to historical measurements and to the performance between the models.

Coupled Model Intercomparison Project   One project where most of the existing ESMs are part of is the Coupled Model Intercomparison Project (CMIP), where the multi-model comparison reduces the uncertainty of climate projections. The project published multiple extensive comparisons and the most recent ones are phase 5 and phase 6 [101, 102].

Grid-Structure and Global Circulation   ESMs consists of a 3D global and vertical grid structure, where in each box chemical and physical processes are calculated and radiation and surface fluxes are applied. The interconnection and exchange between boxes are solved by equation of motions [103, Fig. 5.7].

Resolution and Computation Time   The resolution in ESMs is variable, ranging from several hundred kilometers to a kilometer or potentially less for future exa-scale computers. However, increasing resolution is accompanied by an increase in computation time and required data storage and thus power consumption and cost.

Earth System Components and Coupling   Digital representations of Earth system components, for example ocean, land and atmosphere have to be connected in a full-scale ESM. The coupling combines physical, chemical and biological processes. For further reading visit Gettelman and Rood [104, chapter 8].

EARTH SYSTEM MODELS

In the context of this thesis simulation results from three different Earth system models are compared. Simulations with EMAC were run by Johannes Pletzer, simulations with

LMDZ-INCA were run by Didier Hauglustaine and simulation results from WACCM orig-inate from an independent publication [105]. The main model here is EMAC, which was used for all simulations. LMDZ-INCA was added for validation of results with a very sim-ilar model setup using the same input data to estimate the climate impact of two aircraft designs. Results from WACCM simulations were used to compare to EMAC and LMDZ-INCA results, such as (photo-)chemical water vapor lifetime, ozone sensitivities and wa-ter vapor production from methane oxidation and is based on an independent model setup and different input data. All three models regularly participate in the Coupled Model Intercomparison Project and they are briefly introduced in the following three paragraphs.

EMAC   EMAC (ECHAM/MESSy Atmospheric Chemistry) consists of ECHAM (European Centre HAMburg general circulation model, [106]) and MESSy (Modular Earth Submodel System) [107–109]. It provides among others an atmospheric chemistry model setup used for numerous applications like calculating atmospheric composition changes as a result of emissions or the radiative impact of atmospheric composition changes [107–109]. Detailed information on the model is presented in section 3.1.

LMDZ-INCA   LMDZ (Laboratoire de Météorologie Dynamique, [110]) is a general cir-culation model (GCM) that – in combination with INCA (INteraction with Chemistry and Aerosols, [111]) and ORCHIDEE dynamical vegetation model (ORganizing Carbon and Hydrology In Dynamic Ecosystems, [112]) – forms a global chemistry-aerosol-climate model.

CESM-WACCM   The Community Earth System Model (CESM) and the Whole Atmo-sphere Community Climate Model (WACCM) combine to an atmosphere chemistry-climate model that in contrast to EMAC and LMDZ-INCA includes thermosphere and ionosphere in addition to troposphere and stratosphere.

FINITE RESOURCES AND THE COLD-START PROBLEM
Resolution and power consumption of model simulations are heavily correlated. Another factor controlling power consumption is the length, i.e. simulated years, of model runs. The 'cold-start' problem from Hasselmann et al. [113] refers to coupled atmosphere-ocean simulations that are started close to the present and not early at the beginning of anthropogenic greenhouse gas emission. This approach without correct initialisation of the model generated a significant error in the forcing results. The message here is that to reduce power consumption of model runs by reducing the spin-up time has to be handled carefully. A new method to reduce spin-up time for EMAC simulation runs while keeping the results consistent with the original approach is presented in chapter 3. In total the simulation time is reduced to approximately two-thirds with the new method.

2.2.2. INTRODUCING EMISSIONS TO THE EARTH SYSTEM MODEL
To accurately represent the Earth system, Earth system models include a variety of emis-sions. They are natural or anthropogenic, in gaseous, liquid, or solid form. Examples are

carbon dioxide emissions from fossil fuel combustion or aerosols from volcanic eruptions. Future projections of anthropogenic emissions are estimated in representative concentration pathways (RCPs) or shared socioeconomic pathways (SSPs). Scenarios for high greenhouse gas emission are RCP6 and SSP3-7.0
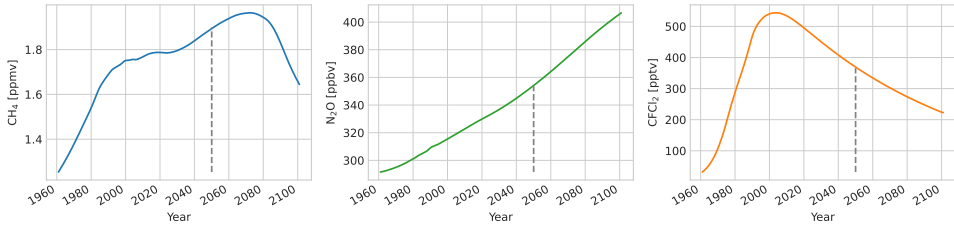
Figure 2.14: Timeline for RCP6 scenario volume mixing ratios of methane (a), nitrous oxide (b) and CFCl$_2$ from chlorofluorocarbons (c). Ticker gray lines mark the year 2050, where a potential fleet of hypersonic aircraft might enter commercial operation.

These include greenhouse gases like CO_2, N_2O and CH_4, chlorofluorocarbons like $CFCl_3$, CF_2Cl, CH_3CCl_3 and CCl_4, hydro-chlorofluorocarbons like CH_3Cl and CH_3Br, halons like CF_2ClBr and CF_3Br. Additionally, emissions from ships, aircraft, land transport and biomass burning are generally included in model simulations.

2.3. EMISSIONS OF AIRCRAFT

In contrast to most other emissions, aircraft exhaust is not solely emitted from the surface but disturbs the atmosphere along the aircraft's flight path. There they often encounter different atmospheric conditions than emitted trace gases at the surface. Generally, emissions depend on fuel type, is mixed and burned with ambient air and a variety of aircraft fuels are theoretically available. The most important one has been and still is kerosene. Others are cryogenic fuels, i.e. cooled from the gaseous to the liquid phase, like liquefied natural gas or liquid hydrogen, or drop-in fuels [114, 115] and sustainable aviation fuels [116, SAF]. The latter two have the advantage of leaving a smaller carbon footprint compared to fossil fuels, however, they have either not been researched well enough or are not (yet) economically viable. Further note that these fuels still cause non-CO_2 effects from e.g. emitted water vapor. On a side-note, carbon dioxide emissions from e.g. kerosene are generally well mixed in the atmosphere due to their long perturbation lifetime which is hundreds to hundred thousands of years [24, 25]. Two conclusions can be drawn from this. First, the aircraft industry is looking intensively for carbon-neutral fuels to reduce the aircraft industries carbon footprint and avoid the long warming of carbon emissions. Here, hypersonic aircraft fueled with liquid hydrogen certainly are an interesting prospect. Especially, if the contribution to surface temperature warming from water vapor should decrease with cruise altitude. Second, the impact of carbon emissions depends less on altitude or latitude of emission compared to water vapor or nitrogen oxide emissions, since eventually the emitted carbon dioxide molecules will be well mixed.

The following three subsections address emissions of conventional aircraft, super-

sonic aircraft and hypersonic aircraft in more detail.

2.3.1. EMISSIONS OF CONVENTIONAL AIRCRAFT

Kerosene, which consists mostly of hydrocarbons and to some parts of sulfur, is almost exclusively used in conventional aircraft today. The high temperatures and the mixing of fuel with ambient air during combustion eventually leaves, to the largest part, carbon dioxide and water vapor and, to smaller parts, nitrogen oxides, sulfur oxides, unburnt hydrocarbons and black carbon, i.e. soot, in the atmosphere. Conventional aircraft emit trace gases during take-off, the cruise-phase and landing. Highest speeds are achieved during the cruise-phase and most of the trace gases are emitted at altitudes from 9-13 km in the upper troposphere–lower stratosphere, especially at northern latitudes. Longitudinal transport of emitted trace gases is faster than the vertical transport and aircraft emissions are therefore affecting atmospheric composition on a significantly larger scale than common flight corridors might suggest [117].

Figure 2.15: A conventional aircraft, more specifically the Airbus A320-ATRA (Advanced Technology Research Aircraft), which is part of the German Aerospace Center's aircraft fleet. Copyright ©2023 DLR. All Rights Reserved.

2.3.2. EMISSIONS OF SUPERSONIC AIRCRAFT

In principle, emissions by supersonic aircraft are not different to emissions by conventional aircraft. However, what differs significantly is the amount of emission and the altitude of emission. Supersonic aircraft offer shorter flight times compared to conventional aircraft and therefore travel faster. However, this is accompanied by the increase in fuel consumption. For comparison, the 1999 IPCC report on global aviation states that fuel consumption per passenger kilometer is more than twice as high for supersonic aircraft as for subsonic aircraft [17]. It is important to note that the amount of emitted trace

2

gases correlates directly with the fuel consumption (Table 2.1).

Table 2.1: Stoichiometric relation of ideal combustion for three different fuel types and the resulting exhaust of trace gases CO_2 and H_2O. Values for kerosene are taken from the collection of Lee et al. [5, Table 1] and the others are ratios of molecular mass. The table focuses on CO_2 and H_2O. Other exhaust products are therefore not listed.

Fuel [1 kg] / Emission [kg]	CO_2	H_2O
Kerosene	3.16	1.231
Liquid Hydrogen	0	9
Liquefied Natural Gas	2.74	2.25

The other difference is altitude of emission since supersonic aircraft fly at higher altitudes compared to conventional aircraft. Most supersonic aircraft are designed to fly at around 15-21 km in the lower stratosphere. The combusted fuel is therefore emitted rather in the stratosphere than the troposphere or their interface region, i.e. the upper troposphere–lower stratosphere. Two supersonic aircraft build for civil transport were the *Concorde*, which reached cruise altitude at 18 km, and the *Tupolew Tu-144*, which reached cruise altitude at 19 km. Apart from these, multiple supersonic aircraft were designed, but never entered service. Small-scale supersonic transport aircraft (*S4TA*) fly at around 15-16 km [118], a potential fleet of large second-generation supersonic transport (HSCT) developed in NASA's high speed research program (HSRP) would fly at 17-20 km [119] and on Wikipedia exists a list with many others [120]. Almost all of these aircraft were designed for conventional fuel, i.e. kerosene, or alternatively SAF rather than fuels like liquefied natural gas or liquid hydrogen.

2.3.3. EMISSIONS OF HYPERSONIC AIRCRAFT

In contrast to supersonic aircraft, a flying hypersonic civil aircraft has not yet been built. Again, the potential fuels are kerosene, liquefied natural gas or liquid hydrogen. The latter has the advantages of a higher payload and greater range of the aircraft due to the physical properties of liquid hydrogen [121]. Additionally, the exhaust of liquid hydrogen combustion consists mainly of water vapor, nitrogen oxides and to a certain percentage of unburnt hydrogen. Therefore, hydrogen fuel exhaust is carbon-free, as long as the initial fuel is produced with renewable energies from solar power or other renewable sources, and is a potential alternative to conventional fuel. In contrast, the exhaust of fuels based on carbon, like kerosene or liquefied natural gas, is not carbon-free (Table 2.1). Note that with the use of additional processes it is possible to produce these carbon-neutral. In a sense that for the production carbon is extracted from the global carbon cycle and simply returns to the cycle after combustion without adding extra. The cost for fuel including these additional processes is high to this date compared to the use of conventional kerosene. To summarize, carbon-based fuels are seen as an option, but most current research about hypersonic aircraft focuses on liquid hydrogen propulsion due to cost, potential synergies with other industries, including subsonic aircraft industry, and various technical advantages [122–124].

Properties of Liquid Hydrogen   The basic physical properties of liquid hydrogen differ very much compared to kerosene. Mass per unit of energy is 2.8 times higher for kerosene. Hence, hydrogen offers more energy for the same mass or in other words weighs less for the same energy. However, liquid hydrogen requires approximately four times the volume for the same energy compared to kerosene, which results in larger storage tanks and asks for sophisticated aircraft designs [121, 125]. Besides the larger tank volume, another challenge here are the low temperatures needed to store liquid hydrogen and liquid hydrogen as a fuel is rather seen as a long-term solution and not as a short- or mid-term solution [126, 127].

Hydrogen Economy and Climate   It is current reality that production, distribution and storage infrastructure of fuel like liquefied natural gas has leaks, which are a constant source of emissions. Similar systems would be required for the operation of hypersonic aircraft. Hydrogen molecules are even smaller than other gases and it most probably will be very challenging to maintain systems that do not leak. Hence, if these land hydrogen emissions perturb the atmosphere they will contribute to warming [128]. Emitted hydrogen from the surface is oxidised in the atmosphere, which results in longer methane lifetimes and increased tropospheric ozone and stratospheric water vapor concentrations [90].

High-Speed Propulsion Systems   Conventional jet propulsion is limited to Mach 3, whereas with ramjet propulsion – based on airbreathing engines forcefully compressing air by design – Mach 5 is possible. Even higher speeds can be achieved with scramjet propulsion (supersonic combustion ramjet) that compresses the incoming air without slowing it down as much. The higher mass based energy density of hydrogen compared to e.g. kerosene makes it a fuel without any currently known alternatives for speeds above Mach 8 [129]. Three examples of aircraft using the ramjet or scramjet technology are presented in the next chapter (p. 49).

Hypersonic Combustion and Emissions   The emission magnitude of nitrogen oxides and unburnt hydrogen depends very much on the combustion. The design of the combustion chamber controls air flow, local temperatures and flame stability – to name a few – and and in turn emissions. Nitrogen oxide emissions can be lessened by increasing mixing intensity in the combustion chamber [121]. Hydrogen is a leftover of unburnt fuel and a high efficiency during combustion is crucial for an optimised fuel use and a reduced emission of unburnt fuel. Nitrogen oxide emission in modern engines is optimised with experiments and numerical models to ensure the least amount of ozone depletion [130, 131]. Since the technology is still under development, emission of unburnt hydrogen and nitrogen oxides can vary strongly depending on aircraft design, i.e. propulsion system, cruise altitude, etc., while water vapor emissions have an optimisation limit and depend to a lesser extent on aircraft design as shown in Table 3.4 (p.51).

2.4. The Climate Impact of Aviation

Emissions of aircraft change the atmospheric composition of radiatively important gases. The resulting change in Earth's radiative budget and surface temperature due to a whole fleet of aircraft cannot be measured directly and has been quantified with numerical models to date. The term *radiative forcing* is used extensively in this dissertation and in literature various definitions exist, depending on the context. Therefore, if used in the text of this dissertation, radiative forcing refers to the IPCC definition described in Schmidt et al. [42].

> *'[...] "radiative forcing" in the sense used by the Intergovernmental Panel on Climate Change (IPCC) assessment reports is a metric that is designed to allow comparisons of different external forcings (such as changes in greenhouse gases, solar irradiance or aerosols), such that the climate response [...] only depends on the net radiative forcing rather than the physics of the specific forcing agent. Neither total water vapor nor clouds have a radiative forcing in this IPCC sense.'*

To my understanding total water vapor partly affects radiative fluxes, by e.g. containing longwave radiation in the troposphere. Hence, changes in total water vapor would in turn cause a change of radiative fluxes. The definition according to IPCC simplifies *change of radiative fluxes* to *radiative forcing*. The IPCC definition very much suits the approach in this thesis, where *changes of atmospheric composition* – or for convenience *perturbations* – are used to calculate the *change in radiative fluxes* and – again for convenience – describe it as *radiative forcing*.
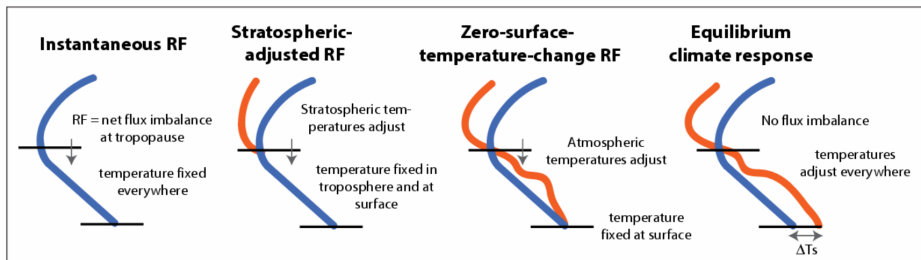
Figure 2.16: Schematic comparing RF calculation methodologies. RF, defined as the net flux imbalance at the tropopause, is shown by an arrow. The horizontal lines represent the surface (lower line) and tropopause (upper line). The unperturbed temperature profile is shown as the blue line and the perturbed temperature profile as the red line. From left to right: Instantaneous RF: atmospheric temperatures are fixed everywhere; Stratospheric-adjusted RF: allows stratospheric temperatures to adjust; Zero-surface-temperature-change RF: allows atmospheric temperatures to adjust everywhere with surface temperatures fixed; and Equilibrium climate response: allows the atmospheric and surface temperatures to adjust to reach equilibrium (no tropopause flux imbalance), giving a surface-temperature change (δT_S). The figure and caption were reprinted without changes from Forster et al. [132].

Radiative Forcing Calculation Methodologies Various methodologies of radiative forcing exist and an overview was published in the IPCC report from 2014 (Fig. 2.16).

In model calculations of the instantaneous radiative forcing, temperature is fixed at all altitudes and adjustments are not allowed. In contrast, the stratospheric-adjusted radiative forcing allows stratospheric temperatures to adjust above the tropopause to reach a new radiative equilibrium. The advantage is that stratospheric-adjusted radiative forcing is closer to surface temperature change than instantaneous radiative forcing [5]. For well mixed perturbations like CO_2 the instantaneous radiative forcing is mostly used, whereas for ozone perturbations, which often include a large variation horizontally and vertically, the stratospheric-adjusted radiative forcing or the effective radiative forcing (see below) is a better choice [5, 83, 133].

Effective Radiative Forcing   A nowadays widely used term is effective radiative forcing (ERF). It not only accommodates the instantaneous radiative forcing, but also adjustments from the atmosphere and surface [134]. In particular, the effective radiative forcing includes non-cloud (air temperature, surface temperature, specific humidity or surface albedo) and cloud adjustments, which decrease or increase the initial instantaneous radiative forcing. Clearly, it incorporates the stratospheric-adjusted radiative forcing.

To calculate the stratospheric-adjusted radiative forcing caused by greenhouse gas perturbations, a few months spin-up are required for temperatures to adjust [135]. In comparison other adjustments that are part of the effective radiative forcing require longer timescales and its calculation is therefore more complex and costly.

In general, the climate impact of conventional aircraft has been quantified extensively and alternative strategies to reduce climate warming from aviation have been developed for years [10]. In contrast, the climate impact of supersonic aircraft is well known, but to a lesser extent than conventional aircraft. The climate impact of hypersonic aircraft has barely been evaluated and only a few publications exist. The following subsections address each individual climate impact.

2.4.1. THE CLIMATE IMPACT OF CONVENTIONAL AIRCRAFT
Depending on latitude conventional aircraft fly in the upper troposphere or lower stratosphere, which are two very different regimes. In turn, many factors contribute to the climate impact of conventional aircraft, which overall has a net surface warming. Lee et al. [5] published the most recent overview about the (effective) radiative forcing by global aviation (Fig. 2.17) and they estimate the contribution of aviation to be 3.5 (3.4, 4.0) % of the total anthropogenic effective radiative forcing.

The factors contributing to the forcing are grouped as CO_2 and non-CO_2 or in more detail as contrail cirrus, carbon dioxide and nitrogen oxide emissions, stratospheric water vapor emissions and aerosol interactions with various subgroups. Water vapor emissions in the stratosphere have a small warming contribution compared to other factors. In comparison, nitrogen oxide emissions, the related ozone change and the methane and stratospheric water vapor decrease, contribute overall with a larger net warming.

2.4.2. THE CLIMATE IMPACT OF SUPERSONIC AIRCRAFT
The historically most well known contributors to the climate impact of supersonic aircraft are water vapor and ozone. Other less known contributors are aerosols, carbon

2
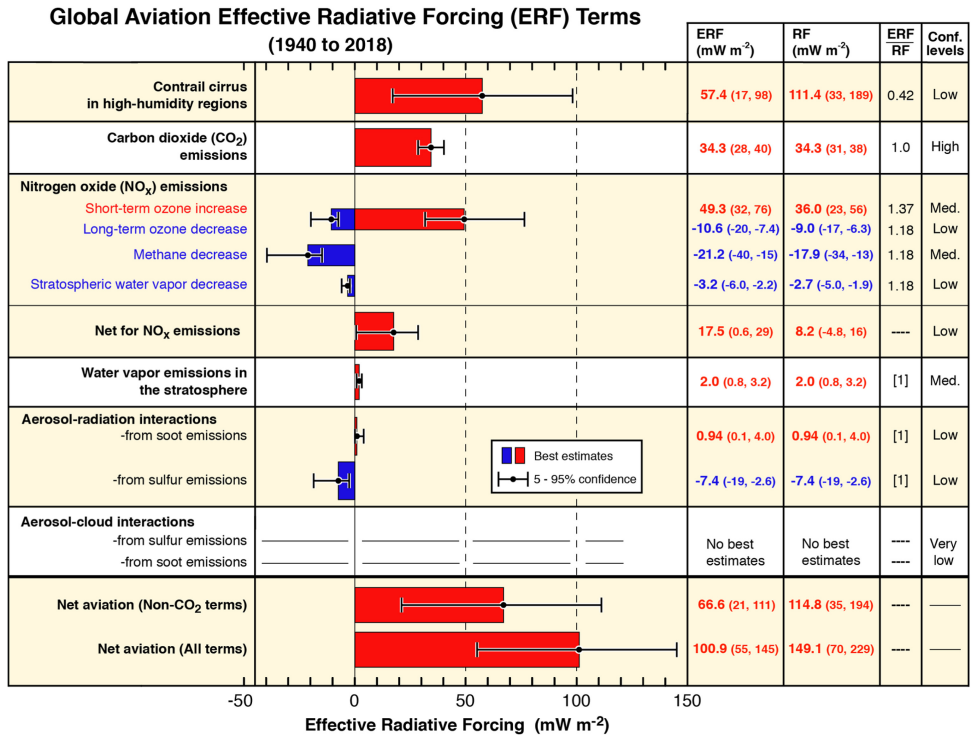
Figure 2.17: Best-estimates for climate forcing terms from global aviation from 1940 to 2018. The bars and whiskers show ERF, best estimates and the 5–95 % confidence intervals, respectively. Red bars indicate warming terms and blue bars indicate cooling terms. Numerical ERF and RF values are given in the columns with 5–95 % confidence intervals along with ERF/RF ratios and confidence levels. The figure and caption were reprinted from Lee et al. [5] with permission from *Elsevier* through RightsLink.

dioxide and cirrus-effects. Uncertainties remain for all contributors, especially aerosols [14]. The impact on climate by water vapor emission increases with altitude as has been shown for altitudes from 13-23 km with the whole-atmosphere chemistry and climate model WACCM [136, Fig. 11]. There, the impact on climate by ozone perturbation is non-linear and causes either warming for emission at 13-19 km or cooling for emission at 19-23 km. Aerosols, either black carbon, i.e. soot, or sulfate aerosols, affect the radiative budget directly by absorption or scattering and indirectly by changing the atmospheric composition through heterogeneous chemical pathways. The climate impact of carbon dioxide emission is well known in comparison, however, uncertainties originate from the long atmospheric lifetime involving the difficulty to assess the cumulative effect over centuries to hundreds of thousands of years [14, 25]. The contrail cirrus depends heavily on ambient conditions. Fuel type and aircraft design are important parameters for the climate impact of supersonic aircraft. New aircraft designs relying on other fuel types like liquid hydrogen or liquefied natural gas might be alternatives for conventional aircraft at certain altitudes [32]. However, the impact of different supersonic aircraft designs fueled with liquefied natural gas or hydrogen has not been assessed to this date with

atmospheric-chemistry general circulation models, but only climate functions, which can be used as a first estimate [15, 137]. The IPCC report from 1999 [17] made it public knowledge that at supersonic cruise altitudes water vapor contributes significantly more than CO_2. Furthermore, compared to kerosene combustion, both, liquefied natural gas and liquid hydrogen, will emit more water vapor per unit energy, which overshadows other advantages that e.g. liquid hydrogen propulsion has [137]. To compare: Supersonic aircraft have a radiative impact many times higher than conventional aircraft if compared with the same transport volume. Comparisons are based on carbon dioxide, water vapor and ozone perturbations for supersonic aircraft and include other effects like e.g. contrails for subsonic aircraft. The exact number depend on aircraft design, i.e. fuel consumption, cruise altitude and flight route, and the currently known range is 3-14 [17, 118].

2.4.3. THE CLIMATE IMPACT OF HYPERSONIC AIRCRAFT

In recent years – excluding publications originating from this thesis – two publications on the impact of hypersonic aircraft appeared. Both focus on the impact on ozone, while just one includes an estimate on the climate impact of hypersonic transport based on water vapor perturbations.

INGENITO (2018)

The first one, Ingenito [138], estimates the climate impact by a fleet of hypersonic aircraft based on water vapor perturbation only. In her study a fleet of 200 hypersonic aircraft (type LAPCAT II MR2.4) fly from Brussels to Sydney 365 days a year and emit 376 Tg of water vapor, which results in a water vapor perturbation that increases surface temperature by 100 mK. The estimate is based on a correlation of an increase in global atmospheric water vapor and near-surface temperature change from a third publication and the whole calculation can be described as a 1D box model. The results on near-surface temperature change are compared to results from this thesis for two hypersonic aircraft designs on p. 96.

KINNISON ET AL. (2020)

Kinnison et al. [105] estimate the perturbation by a fleet of hypersonic aircraft flying at 30 and 40 km with the whole-atmosphere chemistry climate model WACCM. They present zonal mean perturbations of important chemical compounds like water vapor, ozone, nitrogen oxides, hydroxyl radicals and others and mass perturbations of ozone, but not water vapor. Similar to model setups presented in this thesis the atmospheric composition is based on projected emissions for 2050 and the method is to calculate atmospheric sensitivities with specified dynamics. Comparisons of results from this thesis to results of Kinnison et al are part of chapter 4, 6 and 7, which address (photo-)chemical lifetime of water vapor and ozone sensitivities in particular.

WORLD METEOROLOGICAL ORGANIZATION (2022)

Results of these two publications were included in the 'Scientific Assessment of Ozone Depletion' report of 2022 by the World Meteorological Organization (WMO) [139]. The report contrasts results from Kinnison et al, which show that ozone is reduced substantially, with results from Ingenito, which estimate the impact on ozone to be minor.

3

METHODS AND MODEL SETUP

This chapter addresses the methods and Earth system models used to assess the climate impact of hypersonic aircraft. Section 3.1 introduces the numerical model EMAC and LMDZ-INCA, with a focus on EMAC, which is the only model used for all simulations and section 3.2 presents the simulation setup for both, an atmospheric-chemistry general circulation model setup and a radiation model setup. This includes the new MESSy submodel H2OEMIS, which I developed to add water vapor emissions to the model's specific humidity, which was not possible before. section 3.3 validates the performance of the model setups to assess the climate impact of hypersonic aircraft. This includes a model setup evaluation with satellite and aircraft data and a radiative forcing standard calculation. Section 3.4 reports on the hypersonic aircraft emission scenarios and idealized box emission scenarios used for the evaluation of two hypersonic aircraft designs and general atmospheric and radiative sensitivities at hypersonic cruise altitudes, respectively. The methods further include a new spin-up method to reach atmosphere equilibrium faster and to eventually reduce the total power consumption of model simulations to two-thirds, while maintaining the validity of results.

Parts of this chapter were published in *Atmospheric Chemistry and Physics*, Pletzer et al. [33] and Pletzer and Grewe [34] or will be part of a forthcoming publication in *Geoscientific Model Development*, Christoudias et al. [140].

3.1. THE EARTH SYSTEM MODEL EMAC (AND LMDZ-INCA)

EMAC (ECHAM/MESSy Atmospheric Chemistry) consists of ECHAM (European Centre HAMburg general circulation model, [106]) and MESSy (Modular Earth Submodel System) [107–109].

Similarly, LMDZ-INCA consists of a general circulation model LMDZ (Laboratoire de Météorologie Dynamique, [110]) and an extension for chemistry and aerosols INCA (INteraction with Chemistry and Aerosols, [111, 141]). For detailed information on the LMDZ-INCA model setup please refer to the publication Pletzer et al. [33].

3

3.1.1. THE GENERAL CIRCULATION MODEL ECHAM5

The atmospheric general circulation model ECHAM5 was developed by the Max Planck Institute for Meteorology. A set of governing equations from fluid dynamics calculate dynamical processes in the atmosphere and returns parameters like winds and temperature. The model includes an interface to other spheres of the Earth system like the ocean or land and options like nudging.

Grid Resolution and Model Domain   EMAC model simulations presented in this thesis are based on version 5.3.02 of ECHAM. The associated grid is T42L90MA. T42 describes the triangular truncation at wave number 42, which corresponds to a quadratic Gaussian grid of approximately 2.8° by 2.8° in latitude and longitude. This resembles a grid of approximately 250 km by 250 km on the Earth surface. L90MA denotes the 90 vertical hybrid pressure levels in the model, which extends from the surface to the middle atmosphere at approximately 80 km (0.01 hPa).

Comparison of EMAC and LMDZ-INCA Setups   Table 3.1 shows key properties of model setups. The model domain of both models reaches up to approximately 80 km. The nudging limits of atmospheric dynamics to ERA-Interim data are higher with 1 hPa and the time of the applied Newtonian relaxation is shorter for LMDZ-INCA. The grid resolution is smaller horizontally and larger vertically for EMAC.

Table 3.1: Table stating the key properties of model setups for EMAC and LMDZ-INCA as applied for the estimate of the climate impact of two hypersonic aircraft designs.

Model	EMAC	LMDZ-INCA
General circulation model	ECHAM	LMDZ
Vertical limits [km]	0-80	0-80
Vertical limits [hPa]	Surface-0.01	Surface-0.04
Nudging limits [hPa]	Surface-10.0	Surface-1.0
Nudging data	ERA-Interim	ERA-Interim
Nudging relax. time	6-48 hrs	2.5 hrs
Grid cells (lon,lat,lev)	128·64·90	144·143·39

3.1.2. THE MODULAR EARTH SUBMODEL SYSTEM MESSy

The framework in which ECHAM5 is embedded is called MESSy. It combines global circulation models like ECHAM5 with digital representations of many other physical and chemical Earth system components. In total, MESSy has more than 120 submodels, including diagnostic submodels. Figure 3.1 shows different model setups of EMAC that are commonly used in a variety of applications.
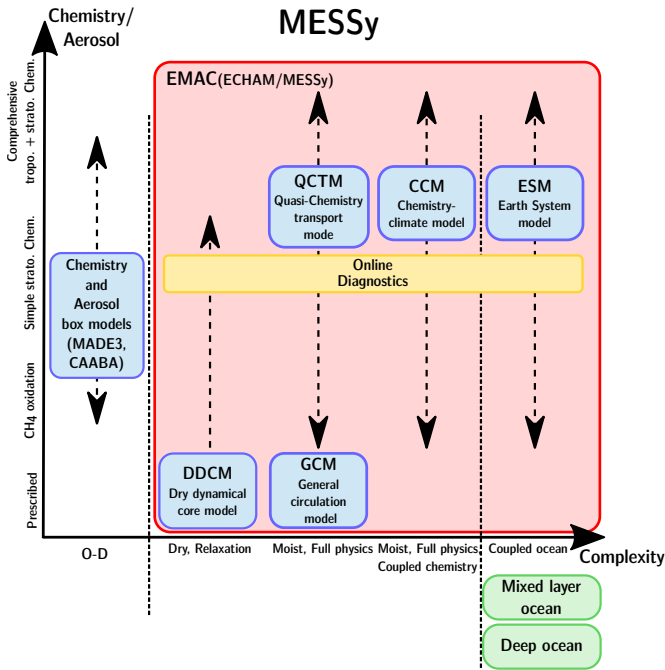
Figure 3.1: Overview of different setups of the Modular Earth Submodel System (MESSy) with different complexity and chemistry settings.

Reference Simulations   Results of a variety of reference simulations with MESSy including ECHAM5 were published by Jöckel et al. [108]. These include model setups – progenitors to the here used model setups – with nudging excluding wave zero of the temperature field. The most similar setup is RC1SD-base-10. For this setup, tropospheric CH_4 lifetime ranges from 7.9-8.2 and lightning NO_x production is estimated to be 4.5 TgN per year on average for the years 1980-2015. This specific setup excels among the others in simulating the stratospheric age of air, especially in the mid-latitudes, and the tropical upward mass flux. Compared to reanalysis data and satellite observations, the Brewer-Dobson circulation is reasonably well replicated [108].

3.2. MODEL AND SIMULATION SETUP

In this thesis, simulations are based on two different EMAC model setups. First, an atmospheric chemistry general circulation model setup to calculate atmospheric composition changes. Second, a radiation model setup to quantify – based on the atmospheric composition changes – the stratospheric adjusted radiative forcing.

3.2.1. ATMOSPHERIC CHEMISTRY GENERAL CIRCULATION MODEL SETUP

The atmospheric chemistry general circulation model setup is on the upper end of complexity and active chemistry (Fig. 3.1), which means it includes most physical and chemical processes (including coupling between both) that are available. However, compared to a full-scale Earth system model, it is not fully coupled to a ocean model, since, first, this requires a far more complex spin-up procedure and, second, the coupled model does not only come with better performance, but could decrease performance in some relevant areas like e.g. stratospheric dynamics or O_3 [108]. Overall, most available submodels, for chemical and physical parametrisations and diagnostic purposes, are active. In the model setup calculating atmospheric composition changes caused by hypersonic aircraft emissions ten years are used as a spin-up phase, because then annual equilibrium of perturbations is reached, and another five years are simulated for statistical evaluation. Table 3.2 shows markers for three levels of probability for results to not be statistically significant. Statistical significance is tested with the students t-test. If hatched areas are shown in plots the title of the plot contains one of these markers for the reader to know, which significance level the hatched areas refer to.

Table 3.2: Markers for probability levels of significance test.

Probability	p≤0.05	p≤0.01	p≤0.001
Marker	*	**	***

ACTIVATED SUBMODELS

Submodels can be coarsely divided into physics, chemistry and other, e.g. diagnostic, submodels.

Activated Physics Submodels AEROPT (AERosol OPTical properties), CLOUD, CLOUD-OPT (CLOUD OPTical properties), CONVECT (CONVECTion), CVTRANS (Convective Tracer tRANSport), E5VDIFF (ECHAM5 Vertical DIFFusion), GWAVE (Gravity WAVE), OROGW (OROgraphic Gravity Wave), QBO (Quasi Biannual Oscillation) and RAD (RADiation).

AEROPT calculates aerosol optical properties and CLOUDOPT cloud optical properties. CLOUD accounts for cloud cover, cloud micro-physics and precipitation and is based on the original ECHAM5 subroutines, as is CONVECT, which calculates convection processes. CVTRANS is directly linked and calculates the transport of tracers due to convection. E5VDIFF addresses vertical diffusion and land-atmosphere exchanges excluding tracers. GWAVE and OROGW account for (non-)orographic gravity waves.

QBO includes winds of observed quasi-biannual-oscillations. RAD and RAD_FUBRAD contain the extended ECHAM5 radiation scheme and allow multiple radiation calls like stratospheric adjusted radiative forcing.

Activated Chemistry Submodels   AIRSEA, CH4, DDEP (Dry DEPosition) H2OEMIS (H2O EMISsion), JVAL (J VALues), LNOX (Lightning Nitrogen OXides), MECCA (Module Efficiently Calculating the Chemistry of the Atmosphere), MSBM (Multiphase Stratospheric Box Model), OFFEMIS (OFFline EMISsion), ONEMIS (ONline EMISsion), SCAV (SCAVenging), SEDI (SEDImentation), SURFACE and TNUDGE (Tracer NUDG(E)ing) and TREXP (Tracer Release EXPeriments).

AIRSEA addresses air and ocean surface interaction [142]. CH4 [143] issues CH_4 oxidation (while MECCA feedbacks to specific humidity). In the setup the feedback to specific humidity is activated in MECCA and deactiva ted in the submodel CH4. DDEP accounts for the dry deposition of aerosol tracers and gas phase tracers and SEDI for the sedimentation of aerosols and their components. H2OEMIS adds H_2O emissions to specific humidity via TENDENCY. JVAL calculates the photolysis rate coefficients. LNOX includes NO_x production by lightning, where the 'Grewe' coupling parameterisation was applied [16, 144], which is based on convective mass-flux. The resulting total lightning NO_x for the baseline simulation is 5.0 TgN yr^{-1}. MECCA accounts for all internal tracers related to production and destruction of chemical components. MSBM calculates the polar stratospheric cloud-chemistry and is based on the PSC submodel code [109]. The representation of polar stratospheric clouds includes three sub-types of polar stratospheric clouds, i.e. solid nitric acid trihydrate (NAT) particles (type 1a), super-cooled ternary solutions (HNO$_3\cdot$ H$_2$SO$_4\cdot$ H$_2$O, type 1b) and solid ice particles (type 2) [145]. H_2SO_4 is part as background concentrations in the EMAC model simulations. The latter start to form below the frost point. Multiple parameters regarding polar stratospheric clouds are written as output within EMAC. Examples are mixing ratios of relevant trace gases (HNO$_3$, HCl, HBr, HOCl, HOBr) in liquid, solid or gas phase, number densities of ice and nitric acid trihydrate particles and loss and production of nitric acid trihydrate through sedimentation. Further included are physical parameters velocity and radius and surface of particles. OFFEMIS and ONEMIS add prescribed and online-calculated emissions [146]. SCAV includes aqueous phase reactions in clouds and precipitation and the corresponding induced removal of trace gases and aerosols by wet deposition [147]. SURFACE originates from several ECHAM5 subroutines and calculates temperatures of different surfaces. TNUDGE is responsible for tracer nudging.

Other Activated Submodels   CONTRAIL, DRADON (Decay RADioactive ONline), O3ORIG (O3 ORIGin), ORBIT, PTRAC (Passive TRACer), SATSIMS (Satellites Simulator), SCALC (Simple CALCulations), TBUDGET (Tracer BUDGET), TENDENCY, S4D (Sampling in 4 Dimensions), SCOUT (Stationary Column OUTput), SORBIT (Satellite ORBIT), TROPOP (TROPOsPhere) and VISO (Vertically layered ISO-surfaces and maps).

PTRAC helps with the verification of emitted trace gases and allows to compare emitted trace gases that did not experience chemical conversion to emitted trace gases ac-

tively participating in chemical pathways. TENDENCY accounts for and verify the specific humidity budget and TROPOP contributes the global WMO tropopause height during post-analysis. ORBIT calculates parameters related to the Earth's orbit like the solar zenith angle and others.

Nudging/Specified Dynamics   Nudging is a technique used to specify dynamics in the model where for example meteorological data are assimilated in the model by using Newtonian relaxation [148]. The atmospheric chemistry general circulation model simulations include nudging of ERA-Interim reanalysis data. Dynamics are specified, i.e. nudged, by Newtonian relaxation that is applied to the general circulation model variables divergence (48 h), vorticity (6 h) and the logarithm of the surface pressure (24 h) up to a pressure level of 10 hPa. The relaxation time is given in brackets.

Applied Emission Scenario   For lower boundary conditions, chemical species, direct and traffic emissions the projections of the RCP6 scenario were applied for the year 2050. For reference, the development of mixing ratios over time of CH_4, nitrous oxide and chlorofluorocarbon are shown in Fig. 2.14. Aircraft emission from the RCP scenario were excluded and hypersonic aircraft emissions are used instead. Note that emission data are interpolated to the model grid.

Methane Oxidation   The total annual CH_4 that is oxidized in the EMAC reference scenario is 586 $TgCH_4\,yr^{-1}$, which produces 658 $TgH_2O\,yr^{-1}$. Orders of magnitude are shown in Table 3.3. This value very much agrees with the order of magnitude in literature and is within the estimate range (p. 18). Above 100 hPa 12 TgH_2O are produced each year. Note that CH_4 mixing ratios (RCP6) are expected to increase until beyond 2050, however CH_4 lifetime in EMAC simulations (based on RCP6) [108] and other models [149] is expected to level off sooner than CH_4 mixing ratios. This should come from increased H_2O in the atmosphere due to increased tropospheric temperatures [150, 151], which should result in larger hydroxyl concentrations and in turn increased CH_4 oxidation. The WACCM model simulation results from Kinnison et al. [105], which are also based on 2050 boundary conditions, show approximately 620 $TgH_2O\,yr^{-1}$ from CH_4 oxidation, whereof 30 $TgH_2O\,yr^{-1}$ are produced above 100 hPa [152]. For the whole-model-domain this agrees very well with EMAC results (difference 6 %). Above 100 hPa the differences are larger by a factor of 2.5.

Table 3.3: Orders of magnitude of multi-annual mean water vapor production from three oxidation reactions, i.e. methane (CH_4), formaldehyde (CH_2O) and hydrogen (H_2) oxidation in the troposphere and the middle atmosphere.

Reactions	H_2O [Tropopsphere]	H_2O [Middle atmosphere]
$CH_4 + OH \longrightarrow H_2O + ...$	660 $Tg\,a^{-1}$	17 $Tg\,a^{-1}$
$CH_2O + OH \longrightarrow H_2O + ...$	260 $Tg\,a^{-1}$	9 $Tg\,a^{-1}$
$H_2 + OH \longrightarrow H_2O + ...$	200 $Tg\,a^{-1}$	9 $Tg\,a^{-1}$

Additional Diagnosis of Chemical Destruction and Production of H_2O with MECCA
Above 20 km the largest contribution to H_2O comes from transport through the tropical tropopause layer via the deep branch of the Brewer-Dobson circulation and oxidation of CH_4, which was recently reconfirmed with EMAC model studies [153, 154] and satellite studies [155]. The net of chemical production and destruction of H_2O is important for the partitioning of HO_x, i.e. H_2O, in the middle atmosphere. In EMAC the chemical mechanism is applied among others via the MESSy submodel MECCA (Module Efficiently Calculating the Chemistry of the Atmosphere) developed by Sander et al. [156, 157]. This specific submodel is able to include tracers that keep track of production as well as destruction of chemical reactants. Five tracers for chemical destruction of H_2O and 45 tracers for chemical production of H_2O were included for a deeper understanding of underlying processes. Further information on the H_2O-specific reaction rates and all other reaction rates are given in the supplement of Pletzer et al. [33] and beyond that in the supplement of Jöckel et al. [108]. Chapter 4 contains a detailed analysis of H_2O production and H_2O destruction in the context of hypersonic aircraft emissions in the middle atmosphere.

3.2.2. SUBMODEL H2OEMIS
Water vapor and the associated hydrological cycle play an important role in atmospheric radiation and dynamics and thereby the general circulation. As it is a precursor of the atmospheric hydroxyl radical (OH), it also largely controls atmospheric chemistry. For earlier versions of the MESSy model, the chemistry calculations operated with a H_2O-tracer that had to be kept synchronous with the prognostic specific humidity of the underlying general circulation model. In recent versions, the chemistry feedback on the hydrological cycle now directly alters the specific humidity. Due to this internal structure it was not possible to simply include H_2O-fluxes to alter the prognostic specific humidity directly. The new submodel H2OEMIS allows to emit H_2O-fluxes in the atmosphere by adding their tendency to specific humidity. The submodel was integrated in the submodel core layer (smcl) and the subroutines placed in the submodel interface layer (smil), where the tendency is added on *physc* (column vector) level [33, 140].

Subroutine Calculations   The subroutines of H2OEMIS include *h2oemis_initialize*, *h2oemis_init_coupling* and *h2oemis_physc*. The latter does the calculations with the current vector of the grid-point fields and contains the equations 3.1, 3.2 and 3.3. Briefly summarized, gridded H_2O emission flux data are imported into the model via the IMPORT submodel [158], then H2OEMIS converts the resulting H_2O mixing ratios into a tendency of the specific humidity and adds this tendency to the prognostic variable qm1, i.e. specific humidity in MESSy. This scheme is shown in Figure 3.2. The key equations for the conversion of H_2O mixing ratios H_2O_{mr} to specific humidity q and vice versa, including the tendencies $H_2O_{mr}^{ten}$ and q^{ten}, are 3.1-3.3.

$$H_2O_{mr} = \frac{q}{1-q} \cdot \frac{M_{air}}{M_{H_2O}} \tag{3.1}$$

M_{air} and M_{H_2O} are the molar mass of dry air and H_2O, respectively.
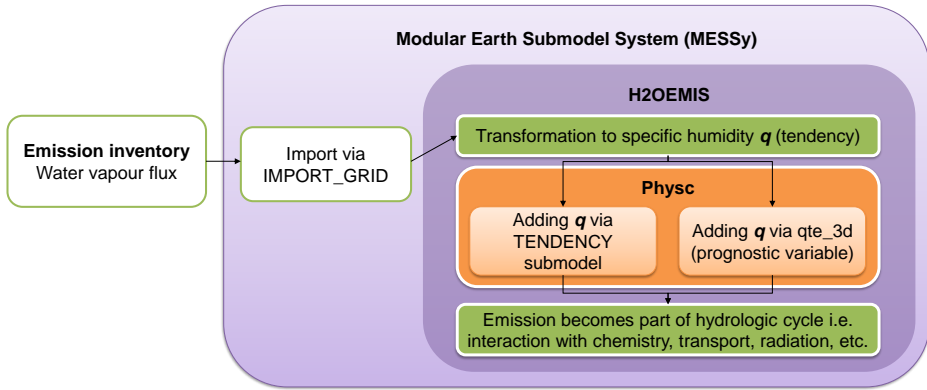
Figure 3.2: Scheme of MESSy and the new submodel H2OEMIS version 1.0 including data flow and calculation steps.

$$H_2O_{mr}^{ten} = \frac{q^{ten}}{(1-q)^2} \cdot \frac{M_{air}}{M_{H_2O}} \tag{3.2}$$

$$q^{ten} = \frac{H_2O_{mr}^{ten}}{(\frac{M_{air}}{M_{H_2O}} + H_2O_{mr})^2} \cdot \frac{M_{air}}{M_{H_2O}} \tag{3.3}$$

Equation 3.1 gives the relation of H_2O mixing ratios to specific humidity. Equation 3.2 gives the H_2O tendency, with the input of specific humidity and the tendency of specific humidity. Equation 3.2 in combination with equation 3.1 results in equation 3.3, which is used to convert H_2O mixing ratios to specific humidity tendency in the H2OEMIS submodel.

3.2.3. RADIATION GENERAL CIRCULATION MODEL SETUP

The model setup to calculate the stratospheric adjusted radiative forcing is less complex and mostly radiation and physics related submodels are activated. The calculations are based on the standard ECHAM5 shortwave radiation scheme. A fixed troposphere height (WMO, 1957) is imported from an external file, which originates from the atmospheric chemistry general circulation model simulations.

Activated Submodels   AEROPT, CLOUD, CLOUDOPT, CONVECT, E5VDIFF, GWAVE, ORBIT, OROGW, RAD, SURFACE, VISO.

Aerosol optical properties (AEROPT), clouds and cloud optical properties (CLOUD, CLOUDOPT) and radiation (RAD) are used for radiation calculations. Convection

(CONVECT), diffusion (E5VDIFF) and wave processes (GWAVE, OROGW) are crucial parametrisations for dynamical processes. Surface temperatures are included with SURFACE and ORBIT (Earth orbit around the sun) calculates parameters that are important for incident sunlight like the solar zenith angle. FUBRAD is deactivated. The background radiation calls for CO_2, N_2O, $CFCl_3$ and CF_2Cl_2 are based on the relative concentration pathway 6 (RCP6) for the year 2050 and are 479 ppmv, 355 ppbv, 366 pptv and 126 pptv, respectively (gray vertical line, Fig. 2.14). Other parameters like aerosol optical thickness or cloud cover and other parameters are calculated in the related submodels and fed to the radiation submodel.

The model is set to calculate the stratospheric-adjusted radiative forcing (p. 32), instead of the instantaneous radiative forcing. Three months are used as a spin-up phase to reach the new radiative equilibrium and to let temperatures adjust. Another twelve months of simulations are used to calculate the average over one year.

3.3. MODEL EVALUATION

3.3.1. MODEL EVALUATION WITH SWOOSH SATELLITE DATA

SWOOSH (Stratospheric Water and OzOne Satellite Homogenized data set) contains H_2O and O_3 mixing ratios for the time period 1984 to 2022 and data are available for nearly all the stratosphere and parts of the mesosphere. The next two paragraphs compare multi-annual mean for the years 2013-2016 of measurements to model setups stratospheric O_3 and H_2O. The applied boundary conditions, i.e. RCP6.0, for the year 2050, make a direct comparison to measurements challenging, since they set on the one hand CH_4 sources, and in turn stratospheric H_2O mixing ratios, and on the other hand nitrous oxide, chlorine and bromine source gases, and in turn O_3 mixing ratios. Differences to measurements are to be expected due to the 2050 boundary conditions in the model results for O_3 and H_2O, respectively. Another EMAC simulation with measured concentrations of trace gases for the years 2013-2016 helps to evaluate the model performance.

Figure 3.3: Multi-annual mean (2013-2016) of O_3 volume mixing ratios for the EMAC setup used in this thesis (left), SWOOSH satellite data (middle) and the difference (observation-model) in percent (right).

The SWOOSH data consist of O_3 and H_2O measured with the satellite Aura Microwave Limb Sounder (*aura*; latin for breeze; MLS) and show no gaps for the years 2013-2016. To compare, Aura MLS measurements of H_2O are quite close to the multi instrumental mean (MIM), published by the SPARC Data Initiative (Fig. 16, [91], p. 11),

with a continuous and moderate overestimation at all pressure levels and for both the tropics and extra-tropics. Aura MLS measurements of O_3 agree very well with the MIM at 100-5 hPa and show a small underestimation at 5-1 hPa for both, tropics and mid-latitudes (Fig. 12, [92], p. 12).

SWOOSH Metadata The comparison is based on version 2.6 of the SWOOSH data with a horizontal resolution of 2.5° and 31 vertical levels. The vertical limits are 316-0.002 hPa for H_2O and 261-0.02 hPa for O_3. The vertical resolution of SWOOSH data is 2.5-3.5 km for both O_3 and H_2O. For the comparison, EMAC data were interpolated to vertical and horizontal levels of SWOOSH data.
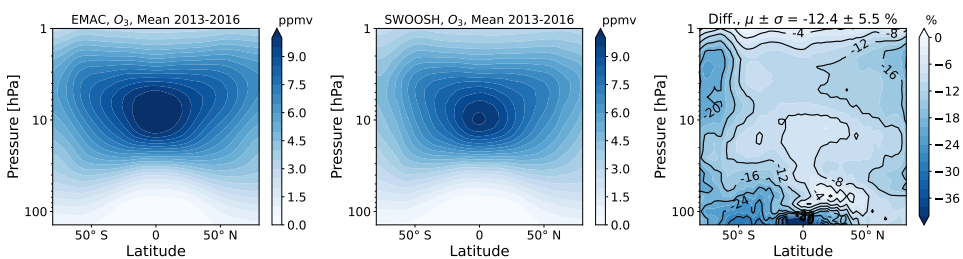

Figure 3.4: Multi-annual mean (2013-2016) of H_2O volume mixing ratios for the EMAC setup applied used in this thesis (left), SWOOSH satellite data (middle) and the difference (observation-model) in percent (right).

Ozone Evaluation with Satellite Data The multi-annual mean of O_3 shows very good agreement between model and observations (Fig. 3.3). Clearly, the features look the same and the difference in average magnitude with -12 ± 6 % between observation and model is rather small. Additionally, O_3 mixing ratio are expected to increase over time compared to the 2010s, since emission of chlorine and bromine source gases stagnate significantly. Hence, the difference, when comparing measurements of the 2010s and model results with boundary conditions for the 2050s, is to be expected. This is verified with O_3 model results for the RC1SD-base-10 scenario, where trace gases affecting O_3 concentrations are not a projection to 2050, but correspond to measurements of atmospheric composition of the simulated years (Fig. A.2). There, the average magnitude is -5 ± 6 % and SWOOSH observations are within the standard deviation of model simulations. Therefore, the conclusion is that EMAC shows a very good agreement of stratospheric O_3 mixing ratios compared to observations for both our model results and the RC1SD-base-10 scenario and recreates expected ozone trends of the coming decades.

Water Vapor Evaluation with Satellite Data The feature of increasing H_2O mixing ratio with altitude is well represented for both, model results and observations (Fig. 3.4). Clearly, the observation features are more detailed and not as homogeneous as model results, but the general agreement is very good. The relative differences show that the magnitude of H_2O mixing ratio in EMAC is 33 ± 8 % smaller than observations on average. The largest differences appear particularly at southern latitudes. For RC1SD-base-10 the deviations are larger and the results of the model setup used in this thesis show an

approximately 12 % better agreement with SWOOSH on average (Fig. A.1). However, the increase in average CH_4 mixing ratio of the RCP scenario between the 2010s and 2050s is about 6 %, which increases stratospheric H_2O and could explain the larger difference of observations to RC1SD-base-10 simulations partly. Differences between model and observations should in reality be less since H_2O of Aura MLS is slightly overestimated at these altitudes, compared to the MIM of the SPARC Data Initiative [91]. In summary, EMAC underestimates the H_2O mixing ratio at stratospheric altitudes for both the here used model setup results, which are a projection to 2050, and the RC1SD-base-10 results, which are based on trace gas measurements from 2013-2016.
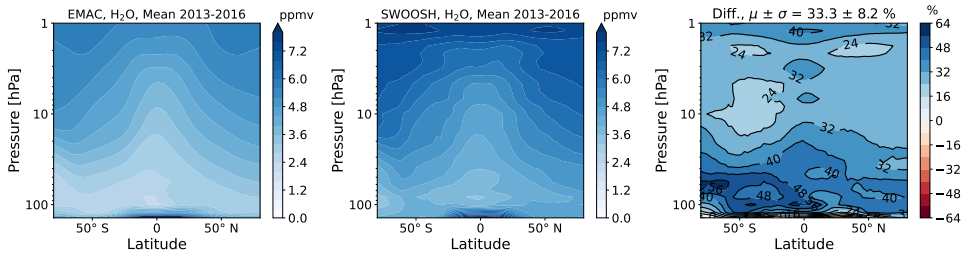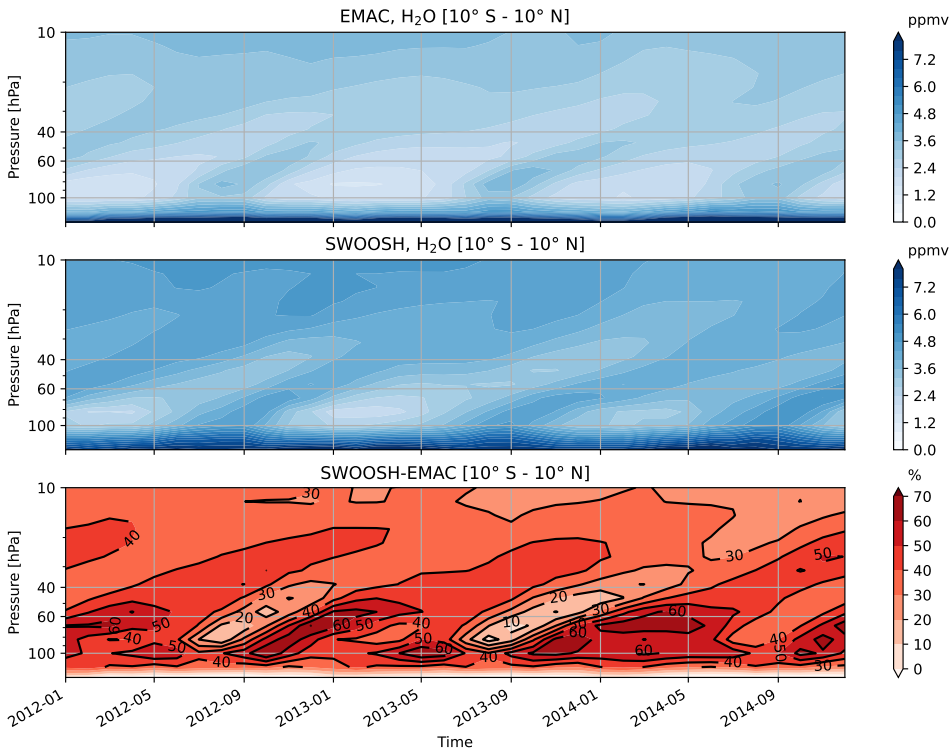

Figure 3.5: Multi-annual mean (2013-2016) of H_2O volume mixing ratios for the EMAC setup of this thesis (upper) and SWOOSH satellite data (middle) and the difference (observation-model) in percent (lower).

Water Vapor Tape Recorder Evaluation with Satellite Data   Figure 3.5 shows a comparison of the tape recorder of satellite data and EMAC results. The intervals of ascending H_2O overlap well and might be slightly earlier for EMAC results. Eichinger et al. [153] reported a phase shift of maxima of 2-3 months between EMAC and MIPAS (Michelson Interferometer for Passive Atmospheric Sounding) satellite data, which we cannot confirm with a newer EMAC version and AURA MLS satellite data. The main difference is the magnitude of model results and measurements. It agrees best during the ascent phase

beginning approximately in July and can be distinguished from the large background at
100 hPa. Largest differences do appear during the ascent phases, which extends from
approximately September to June at 100 hPa. Since the absolute values are low in this
time span compared to the rest of a year the impact of the larger differences are lower
than they appear.

Interannual Changes of Water Vapor   EMAC simulations over a time span of 20 years
(1991-2014) with specified dynamics from results of another publication show strato-
spheric H_2O mixing ratios of satellite measurements at 83 hPa with a correlation coeffi-
cient of 0.68-0.73 [159, Fig. 1].

Cold-Point Temperature at Tropopause   The EMAC model simulates cold-point tem-
perature and simulations with specified dynamics (ERA-Interim) capture the interan-
nual variability well, compared to radiosonde measurements. However, the magnitude
is not always on point, which results in a correlation coefficient of r=0.61 [159, Fig. 2].

3.3.2. Model Evaluation with IAGOS Aircraft Measurements
Uncertainties remain in the upper–troposphere lower–stratosphere (UTLS) region,
especially in a changing climate, which are for example addressed in the German
national project *TPCHANGE* (The Tropopause Region in a Changing Atmosphere,
2021-2025 [160]). In the context of aircraft, trace gases emitted at stratospheric altitudes
are transport through the UTLS to the troposphere. To validate the model performance
in this important region, the temperature, O_3 and H_2O representation in EMAC was
evaluated with aircraft measurements from the UTLS [33]. To summarize briefly, the key
message for EMAC is, firstly, a systematic cold bias of -3.8 to -2.5 K in the extra-tropics,
responsible for an upward shift of the tropopause and as a consequence an under-
and overestimation of O_3 and H_2O mixing ratios, respectively. Secondly, the Taylor
correlation coefficient, estimating correlation between observations and model results
in the UTLS, is r~90 for H_2O and r~0.95 for O_3 and temperature. The upward shift of the
tropopause might cause a larger (seasonal) variability of H_2O in perturbation results due
to the increase in background H_2O. which is taken into account by an additional error
estimate including tropospheric perturbations in section 6.2. Please refer to Pletzer
et al. [33] for the detailed evaluation including multiple figures.

3.3.3. Validation of Radiative Forcing Calculations
For the largest contribution to radiative forcing at high altitudes – coming from H_2O
perturbation – a comparison to other radiation calculations was performed. The per-
formance test was done like by Myhre et al. [161]. Briefly described, they calculate the
radiative forcing caused by an increase of H_2O mixing ratio from 3.0 to 3.7 ppmv above
the tropopause. The LMDZ-INCA result is 0.18 Wm^{-2}, which is below the mean of Myhre
et al. [161] (mean 0.25 Wm^{-2}, range 0.16 – 0.38 Wm^{-2}), while the EMAC result is larger
than the mean with 0.28 Wm^{-2}. Hence, EMAC results are larger by 55 % compared to
LMDZ-INCA based on radiative forcing calculations. Both models are in the range of dif-
ferent models presented by Myhre et al. [161], with LMDZ-INCA at the lower and EMAC
in the mid-upper range.

3.4. EMISSION SCENARIOS

As anthropogenic emissions in the Earth system model, the emission scenarios are used as an input to the atmospheric chemistry general circulation model setup to calculate atmospheric composition changes between reference and emission scenario simulations. The emissions are included in the chemical conversion processes and the dynamic air transport. Two types of emission scenarios were included, idealized and aircraft emission scenarios. All emission scenarios are based on hydrogen propulsion and the exhaust is therefore H_2O, nitrogen oxides and unburned hydrogen.

3.4.1. AIRCRAFT EMISSION SCENARIOS

Aircraft emission scenarios are different to idealized emission scenarios. First, they include a horizontal distribution pattern of flight paths between city pairs (Fig. 3.6). The pattern is based on estimates of potential transport volumes. Second, the vertical distribution of emissions include the exhaust of the whole flight path, i.e. from take-off, cruise phase and landing. Note that the sum of annually emitted trace gases remains the same for both idealized and aircraft emission scenarios.
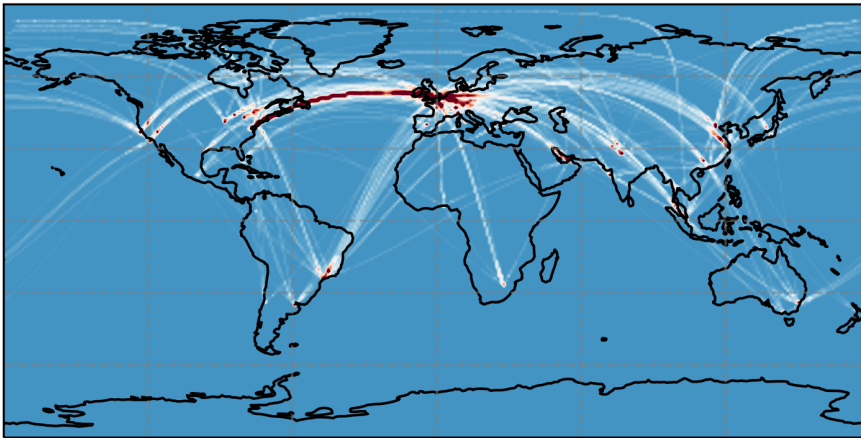
Figure 3.6: Global exhaust location of a fleet of aircraft between city pairs. Blue represents background, while white and red show the exhaust location, where red represents more exhaust.

HIKARI HIKARI ('light' in Japanese) was an international project of Europe and Japan for high-speed transport resulting in a potential timeline for further development of high-speed transportation up to commercial operation. Blanvillain and Gallic [162] published the roadmap study, which combines economic viability, environmental constraints as well as technological requirements.

HIKARI Emission Inventory   The HIKARI emission inventory has three scenarios. A subsonic reference (Airbus A350) and two hypersonic and subsonic mixed fleets based on A350, ZEHST and LAPCAT. For the mixed fleets, market penetration is a measure of how many of the global flight routes are suited for the specific hypersonic aircraft compared to subsonic aircraft and how much of the market could be covered by hypersonic aircraft. Hence, the market for the aircraft LAPCAT, which is able to travel extremely large distances (approximately 18,000 km), is smaller due to the limited selection of appropriate city pairs like for example Brussels-Sydney. In comparison, ZEHST is a potential faster alternative for 25 % of the subsonic aviation market with a smaller range (approximately 9,000 km).

Zero Emission High Speed Transport   ZEHST is short for Zero Emission High-Speed Transport and is a high-speed aircraft project, which includes a strategy to reduce environmental impact with a zero CO_2 emission policy. The aircraft is based on a ramjet engine for cruise phase and travelling speed is at Mach 4-5. This aircraft is developed for 60 passengers and has an intermediate transport range of approximately 9 000 km (e.g. Paris-Tokyo, [163]). The vertical exhaust patterns show an increased emission at altitudes from 8-10 km, not visible for subsonic emission features, which comes from a speed-up of the ZEHST aircraft to reach higher altitudes (Fig. 3.7)
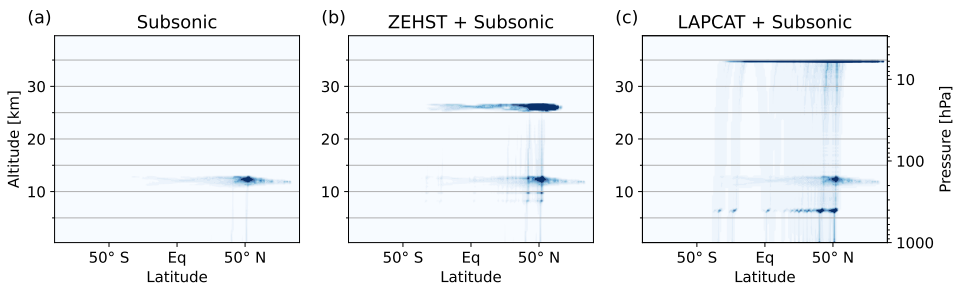
Figure 3.7: Zonal sum of trace gas emission location. (a) Subsonic reference scenario, (b) ZEHST scenario with a hypersonic market penetration of 26.0 % and (c) LAPCAT scenario with a hypersonic market penetration of 9.8 %. For magnitude of annual water vapor emission rates at each altitude refer to Fig. A.3.

Long Term Advanced Propulsion Concepts And Technologies   LAPCAT is short for Long-Term Advanced Propulsion Concepts and Technologies. It is a joint effort of many European institutes, resulting among others in an aircraft model meant to travel at Mach 8 with scramjet technology, carry up to 300 passengers and for long-range flights of approximately 18 000 km (e.g. Brussels-Sydney, [98, 164]). The LAPCAT PREPHA-type is based on the technology level developed in the French high speed propulsion program PREPHA [165, 166, Programme de REcherche et de technologie sur la Propulsion Hypersonique Avancée]. The vertical exhaust patterns show an increased emission at altitudes from 6-7 km from a speed-up of the LAPCAT aircraft similar to the ZEHST aircraft (Fig. 3.7).

STRATOFLY MR3   STRATOFLY is an European innovation project developing strato-spheric flying opportunities for high-speed propulsion concepts. The novelty is the op-timisation of the aircraft design across many disciplines like combustion, emission, climate, noise and human health to name a few. The resulting aircraft design, called the STRATOFLY MR3, is based on the LAPCAT II MR2.4 and should be the current (European) reference, where hypersonic aircraft are at in terms of technology readiness level.

Table 3.4: Annual emission of trace gas species H_2O, NO_x and H_2 in the HIKARI emission inventory and in addition annual emissions of the further developed STRATOFLY MR3 aircraft (cruise at 33 km), which do not include subsonic emissions. The upper three rows contain amounts of trace gases emitted in the whole atmosphere, while the lower three rows contain amounts of trace gases emitted at stratospheric altitudes only (above 100 hPa). Note that for ZEHST and LAPCAT only a part of the subsonic aviation is replaced by hypersonic transport and subsonic exhaust features remain.

Scenario	Domain	H_2O [Tg]	NO_x [TgNO$_2$]	H_2 [Tg]
Subsonic	whole	5.022	0.072	0.0
ZEHST	whole	21.581	0.113	0.163
LAPCAT	whole	31.366	0.115	0.307
STRATOFLY	whole	38.957	0.347	0.192
Subsonic	above 18 km	0.0	0.0	0.0
ZEHST	above 18 km	13.741	0.020	0.153
LAPCAT	above 18 km	21.237	0.031	0.236
STRATOFLY	above 18 km	20.824	0.332	0.021

Combustion Efficiency   In the context of HIKARI emission scenarios, combustion efficiency for hydrogen of 50 % were reported from other projects. The latter was eventually used for the emission inventory to account for a real combustion that is close to 100 %, but never ideal.

3.4.2. Idealized Emission Scenarios
Idealized emission scenarios are box emissions at specific latitude and altitude regions as shown in Fig. 3.8. They are based on of three types of emission – H_2O, NO_x and H_2 – that were emitted at eight different prescribed locations. In total, the method then includes 24 idealized simulations and one reference simulation.

Location   The emission scenarios vary in latitude and altitude. Altitudes are 30 km and 38 km. Note that the height of the box, where the aircraft exhaust is emitted, is approximately 1 km. Therefore, it is rather an altitude range with 30-31 km and 38-39 km, where trace gas is emitted. Four latitude regions span 30°. They are southern mid-latitudes at 60-30° S, northern tropics at 0-30° N, northern mid-latitudes at 30-60° N and north polar latitudes at 60-90° N. Clearly, south polar and southern tropics are missing. The two regions were not included because of two reasons. First, aircraft barely fly at southern polar regions, since most direct routes between city-pairs do not cross there. Therefore, they are not as important as an emission location. Second, since northern tropics are included, southern tropics are left out since they show very similar dynamic and chem-
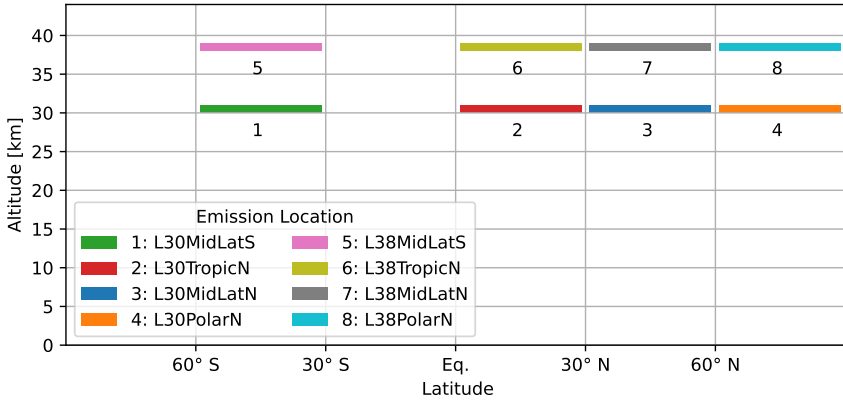
Figure 3.8: Altitude and latitude of the eight idealized emission scenarios.

ical conditions in the stratosphere. Southern mid-latitudes are included to quantify the impact on atmospheric composition and climate on the Southern Hemisphere.

Magnitude H_2O is emitted to the largest part and to a lesser extent nitrogen oxides and hydrogen. Table 3.5 shows the emission magnitude in teragram. The values originate from emissions above the tropopause for the LACPAT aircraft in Table 3.4, which were used as box emissions for the idealized emission scenarios. The idea of this selection is to estimate sensitivities of atmosphere and climate to realistic magnitudes of annual hypersonic aircraft emissions.

Table 3.5: Annual summed exhaust based on the HIKARI emission inventory as a reference for a hypersonic aircraft.

Emission	Magnitude	Unit
H_2O	21.24	Tg
NO_x	0.031	$TgNO_2$
H_2	0.236	Tg

3.4.3. THE APPLICATION OF A SPEED-UP TECHNIQUE

T HE number of simulated model years for one of the aircraft scenarios is 15 years. Ten years of simulation spin-up were required to achieve annual equilibrium of perturbations and five years for the purpose of a multi-annual mean (black dotted line for reference, Fig. 3.10). However, for the idealized aircraft emissions the scenarios number 24 and the computational cost would become exceedingly large. Therefore, the model simulations include a speed-up technique, which reduces the number of simulated years to two-thirds. The speed-up method can be described as follows. Equilibrium on the multi-annual mean is achieved faster and hence the simulated years are reduced to two-thirds. The emissions of the first year are increased with a factor *s* to reach approximately

equilibrium after this one year. The factor s can be calculated with equation 3.4, where τ is the perturbation lifetime of H_2O. The complete derivation of the factor s is part of the appendix (p. 170).

$$s \approx \tau + 0.5 \qquad (3.4)$$

H_2O perturbation lifetime values at stratospheric altitudes from Grewe and Stenke [21] and Pletzer et al. [33] were used as initial values and inter- and extrapolated to altitudes of 30 km and 38 km, respectively. The slopes of linear and quadratic extrapolation (35-42 km) were either very steep or too curved and the average of both values showed the best results.
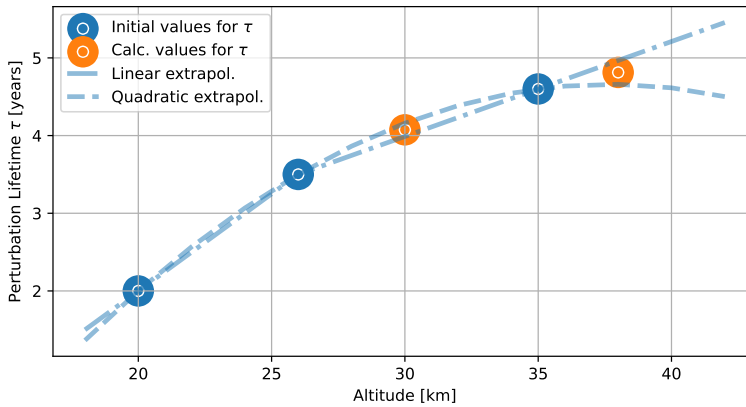
Figure 3.9: H_2O perturbation lifetime depending on altitude. Blue circles represent initial data that were used for inter- and extrapolation of orange data circles. Dashed and dashed-dotted blue lines shows the behavior of quadratic and linear inter- and extrapolation, respectively. Orange data circles are based on the average of linear and quadratic inter- and extrapolation.

The process during the actual model runs is as follows. After the first year of simulation, where the emitted trace gases are increased by the factor s, the initial values of trace gases are emitted for the following years in the simulation. The first year, on the one hand, ensures that atmospheric composition changes reach multi-annual equilibrium faster. On the other hand, by limiting the enhancement to the first year, the final mass perturbation is not disturbed, since the atmospheric lifetime of perturbations is shorter than the spin-up phase. Of the emitted trace gases H_2O has the longest perturbation lifetime and therefore serves as the medium to verify multi-annual mean equilibrium.

The year 2007 shows a sharp increase of H_2O mass perturbation due to the applied speed-up factor s (gray shaded area, Fig. 3.10). From 2008-2012, some scenarios overshot equilibrium values with the end of the first year, e.g. 30 km, 60-90°N, and level off to equilibrium values. Other scenarios continued to build up, e.g. most scenarios at 38 km, before reaching equilibrium latest in 2013 (green shaded area, Fig. 3.10). These differences could originate from latitudinal differences in H_2O perturbation lifetime, which were not included in the inter- and extrapolation in Fig. 3.9. Another explanation, which

3
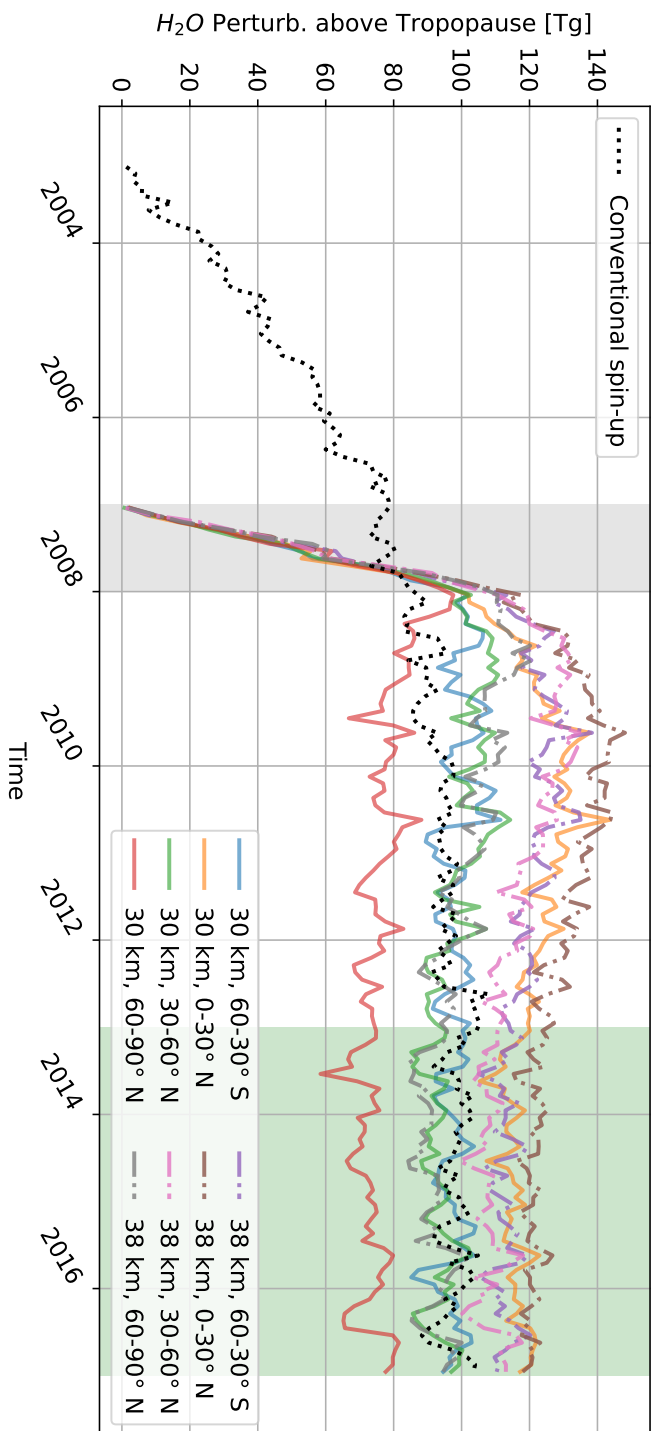
Figure 3.10: Timeline of monthly mean H_2O perturbation in teragram for scenarios, where H_2O is emitted. The first year (gray shaded area) of sped-up simulations shows the enhanced emission by the factor s, i.e. the speed-up. 2013-2016 (green shaded area) shows the years in multi-annual mean equilibrium. The white- and gray-shaded area (2007-2012) marks the spin-up phase. For comparison a conventional simulation timeline is shown, which takes 10 years to reach equilibrium (2003-2013).

is more likely, is that the increased perturbation from the first year has yet been transported to tropospheric altitudes, and the positive net of tropospheric loss and continuous emission of exhaust is continuing to add up for some years. The effect on results, i.e. error potential, should not be significant, since the time to equilibrate is sufficient for all scenarios and multi-annual mean equilibrium is reached latest in 2013. In summary, after six years all scenarios reached equilibrium on a multi-annual mean and for all 25 scenarios the years to be simulated were reduced from 375 to 250, i.e. by one-third.

3

4

WATER VAPOR IN THE MIDDLE ATMOSPHERE: A NEW INSIGHT

A decreasing (photo-)chemical water vapor lifetime with altitude suggests a decreasing water vapor perturbation lifetime with altitude. This chapter presents a new insight on water vapor chemistry in the middle atmosphere, which shows that this does not hold up and water vapor perturbations are actually enhanced by (photo-)chemistry for altitudes up to 40 km. Section 4.1 gives the background on (photo-)chemical conversion pathways, measurements of hydrogen compounds as well as their measurement and potential standard model limitations in currently existing literature. Section 4.2 compares both, measurements and model representation of water vapor and the underlying processes and limitations. The (photo-)chemical production and loss reactions within EMAC, that were included to apply an extensive diagnostic method, is the focus of section 4.3. Finally, the new insight is presented for combined and individual aircraft emissions in section 4.4 followed by a summary.

Parts of this chapter were published in *Atmospheric Chemistry and Physics*, Pletzer et al. [33] and Pletzer and Grewe [34].

4.1. Chemistry of Hydrogen Compounds in the Middle Atmosphere

I N the atmosphere water vapor is included in the reactions of hydrogen compounds, where the main species are atomic hydrogen (H), hydroxyl (OH) and hydroperoxyl (HO_2). In the upper stratosphere and mesosphere HO_x originates from water vapor via reaction with $O(^1D)$ and photolysis and the main loss reaction (R21) of HO_x reproduces water vapor.

$$HO_2 + OH \longrightarrow O_2 + H_2O \tag{R21}$$

While the larger concentration of NO_x and and other compounds like CH_4 or CO influence the hydrogen compound chemistry at (lower) stratospheric altitudes, the comparably low concentrations of these compounds and an increased photolysis in the mesosphere and lower thermosphere change the relation of the most active chemical reactions from Fig. 4.1(a) to 4.1(b). The main difference between (a) and (b) lies within the participating molecules, which include only compounds consisting of atomic oxygen and atomic hydrogen and exclude e.g. methane and the group of nitrogen oxides for the higher altitude regions. Additionally, the reactions controlling the HO_x partitioning do change.
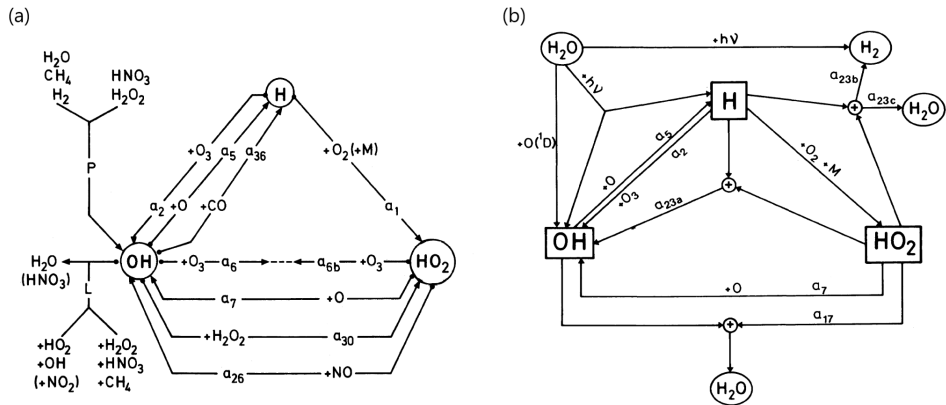
Figure 4.1: (a) Principal aeronomic reactions of hydrogen compounds in the stratosphere. (b) Principal aeronomic reactions of hydrogen compounds in the mesosphere and lower thermosphere. Images and captions reproduced from Brasseur and Solomon [167, Fig. 5.26 and 5.27] with permission of the rights holder, *Springer Nature* through RightsLink.

HO_x Partitioning   Figure 4.1 shows an overview of hydrogen compound partitioning. The partitioning is closely connected to the lifetime of hydrogen compounds shown in Fig. 2.13 and actually changes continuously with altitude. The reactions R22-R25 are largely responsible for the partitioning of HO_2 and OH. While reactions R22 and R23 dominate at altitudes above 38 km, since HO_x concentration increases with altitude, re-

actions R24 and R25 are more important at lower altitudes, simply due to larger concentrations of NO_x and O_3 [168].

$$HO_2 + O \longrightarrow OH + O_2 \tag{R22}$$

$$OH + O \longrightarrow O_2 + H \tag{R23}$$

$$HO_2 + NO \longrightarrow OH + NO_2 \tag{R24}$$

$$OH + O_3 \longrightarrow HO_2 + O_2 \tag{R25}$$

Mesosphere Measurements of HO_x   In the 1990s, OH and HO_2 measurements found larger densities of OH in the upper stratosphere and lower densities in the mesosphere [169] and larger densities of HO_2 in the mesosphere [170], than predicted by the standard (photo-)chemical HO_x model (Fig. 4.2). A more recent publication from 2006, comparing balloon and satellite measurements to (photo-)chemical models, could not confirm these differences and reported an agreement within the bounds of experimental precision [171].
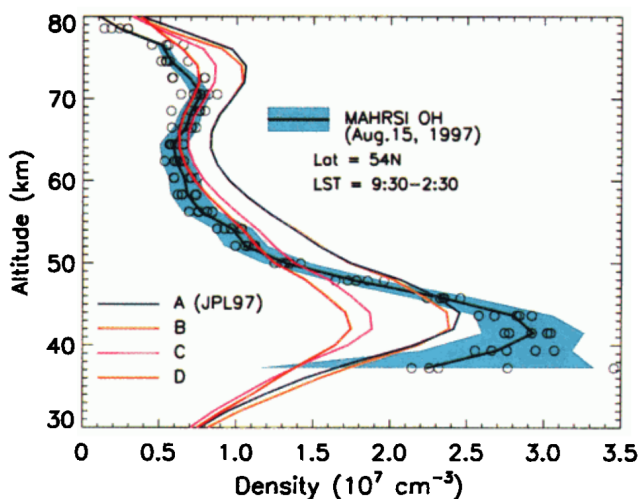
Figure 4.2: MAHRSI [Middle Atmosphere High Resolution Spectrograph Investigation] observations from August 15, 1997. The shaded area shows the 5-hour average of 34 limb scans for which the local time varied between 0930-1430, the solar zenith angle varied between 32-49° N, and latitudes ranged between 42-58° N. The circles represent five 1-hour averaged profiles. The (photo-)chemical models are (A) Standard chemical kinetics [...], (B) 50 % reduction for reaction (2), (C) 20 % reduction in rate coefficient for reaction (3) and a 30 % increase for reaction (5), and (D) 25 % reduction in the rate coefficients of (3) and (5). The figure shows that the shape of the observed profile is not explained by any of the models proposed for the mesosphere or the middle stratosphere. Images and captions reproduced from Conway et al. [169, Plate 2] with permission of the rights holder, *American Geophysical Union* through RightsLink.

To summarize briefly, concentrations of the individual HO_x components very much depend on the HO_x partitioning depending on altitude, which includes interaction with

important atmospheric compounds like ozone, methane or nitrogen oxides at specific altitudes. This is closely connected to the (photo-)chemical lifetime of reactants. It is important to note that deviations from the standard HO_x model could not be confirmed with multiple measurements.

4.2. Middle Atmospheric Water Vapor

Water vapor is part of the HO_x partitioning in the stratosphere, mesosphere and lower thermosphere (Fig. 4.1). Both, water vapor measurements and their representation in the EMAC model, are addressed in this section.

4.2.1. Water Vapor Measurements

Water vapor has been measured by multiple instruments and access is possible via different channels. First, SWOOSH (Stratospheric Water and OzOne Satellite Homogenized data set) offers stratospheric water vapor measurements from a number of instruments. Second, a more extensive data set from the SPARC Data Initiative [91] offers water vapor measurements from thirteen satellites over a long time period (1978-2010), which include the mesosphere. Additionally, the measurements are validated with much detail. Both, the SPARC and SWOOSH data set, include measurements from the Aura Microwave Limb Sounder, which show a very good performance compared to the average of all instruments [91].

Mesosphere Measurements of Water Vapor   Measurements with different instruments estimate the water vapor mixing ratios to be 6 ppmv up to 70 km, from where on it decreases sharply to approximately 4 ppmv at 75 km (Figure in [97, p. 311-313]). An explanation for a local maximum (7.5 ppmv) at 65-68 km in the tropics has not been found yet. It likely is not methane oxidation, since this process is nearly completed at 50 km.

To summarize briefly, water vapor measurements from high-level instruments are available, whereof SWOOSH data offers easy access to high-quality data and SPARC to even more extensive and validated data from multiple instruments.

4.2.2. Water Vapor Representation in EMAC

Water vapor concentrations above the tropopause depend mostly on how much water vapor passes the tropopause cold-point and on methane, formaldehyde and hydrogen oxidation. The feature of rising water vapor in the annual cycle from the tropopause to higher altitudes specific to the EMAC model was discussed before on p. 47. The following paragraph elaborates briefly on the topic of middle atmospheric water vapor from oxidation processes in the EMAC model, which further contribute to middle atmospheric water vapor concentrations.

Methane Oxidation in EMAC   Frank et al. [154] published an evaluation of the water vapor yield from methane oxidation in EMAC. They report that the yield γ_{H_2O} (Equation 4.1) differs from the value originally published by le Texier, Solomon, and Garcia [172] for specific altitudes. They calculate a yield γ_{H_2O} lower than two in the lower stratosphere and even larger than two in the upper stratosphere and lower mesosphere, originating

from the intermediate H_2. From 0.2 hPa upwards (approximately 60 km) the values decrease drastically due to the increased (photo-)chemical loss of H_2O and the increasing chemical lifetime of H_2.

$$\frac{d}{dt}[H_2O] = -\gamma_{H_2O} \cdot \frac{d}{dt}[CH_4] \tag{4.1}$$

4.3. REACTIONS INCLUDING WATER VAPOR IN EMAC

In the context of this thesis the submodel MECCA was applied to calculate gas and aqueous phase chemistry in EMAC. These include tropospheric and stratospheric chemical mechanism. In MESSy version 2.54 the chemical mechanism includes 45 reactions of water vapor production and five reactions of water vapor destruction. The first step was to identify the related reactions and then to add a counter to every single reaction and the combined reactions with additional diagnostic variables. As a second step, it was possible to track the chemical water vapor conversion processes during simulations. Note that to finish this process a recompilation of EMAC including the KPP kinetic preprocessor is required. Since the number of variables was quite large, only the significant contributions were selected (further information on p. 68) and the subset was continuously written to a channel file named *tr_H2O_bud*.

4.3.1. REACTIONS OF WATER VAPOR PRODUCTION

The reactions of water vapor production are to a large part related to HO_x chemistry, followed by NO_x and CH_4 chemistry. Additionally, non-methane hydrocarbon chemistry and halogen chemistry (Cl, Br) are listed; however, no iodine reactions and sulfur reactions were included in EMAC at the time of the simulations. The following four paragraphs list all active reactions during EMAC simulations grouped according to hydrogen oxide, atomic nitrogen, carbon and chlorine or bromine compounds. Note that the compounds of reactions can belong to more than one group and the distribution is therefore a rough classification. The initial analysis showed that R26-R29, R31, R32, R40, R41 and R56 are the most relevant in the context of hypersonic emissions (Fig. 4.5).

Reactions with HO_x Compounds

$$OH + H_2 \longrightarrow H_2O + H \tag{R26}$$

$$HO_2 + H \longrightarrow O(^3P) + H_2O \tag{R27}$$

$$HO_2 + OH \longrightarrow H_2O + O_2 \tag{R28}$$

$$H_2O_2 + OH \longrightarrow H_2O + HO_2 \tag{R29}$$
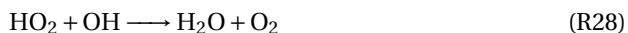
Reactions with Atomic Nitrogen Compounds

$$HONO + OH \longrightarrow NO_2 + H_2O \tag{R30}$$

$$HNO_3 + OH \longrightarrow H_2O + NO_3 \tag{R31}$$

$$HNO_4 + OH \longrightarrow NO_2 + H_2O \tag{R32}$$

$$NH_3 + OH \longrightarrow NH_2 + H_2O \tag{R33}$$

$$NH_2 + HO_2 \longrightarrow HNO + H_2O \tag{R34}$$

$$NH_2 + NO \longrightarrow N_2 + H_2O \tag{R35}$$

$$NH_2 + NO_2 \longrightarrow N_2O + H_2O \tag{R36}$$

$$HNO + OH \longrightarrow NO + H_2O \tag{R37}$$

$$NHOH + OH \longrightarrow HNO + H_2O \tag{R38}$$

$$NH_2OH + OH \longrightarrow NHOH + H_2O \tag{R39}$$
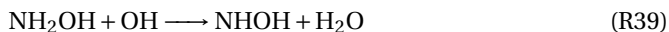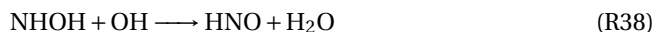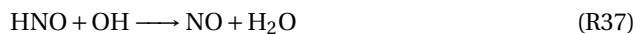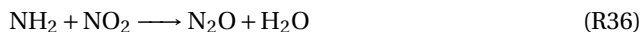
Reactions with Carbon Compounds

$$CH_4 + OH\{+O_2\} \longrightarrow CH_3O_2 + H_2O \tag{R40}$$

$$HCHO + OH \longrightarrow CO + H_2O + HO_2 \tag{R41}$$

$$CH_4 + h\nu \longrightarrow CO + 0.31\,H + 0.69\,H_2 + 1.155\,H_2O \tag{R42}$$

$$CH_3OOH + OH \longrightarrow 0.7\,CH_3O_2 + 0.3\,HCHO + 0.3\,OH + H_2O \tag{R43}$$

$$HCOOH + OH\{+O_2\} \longrightarrow CO_2 + HO_2 + H_2O \tag{R44}$$

$$C_2H_6 + OH \longrightarrow C_2H_5O_2 + H_2O \tag{R45}$$

$$CH_3CHO + OH \longrightarrow CH_3CO_3 + H_2O \tag{R46}$$

$$CH_3CO_2H + OH\{+O_2\} \longrightarrow CH_3O_2 + CO_2 + H_2O \tag{R47}$$

$$CH_3CO_3H + OH \longrightarrow CH_3CO_3 + H_2O \tag{R48}$$

$$PAN + OH \longrightarrow HCHO + CO + NO_2 + H_2O \tag{R49}$$

$$C_3H_8 + OH \longrightarrow 0.82\,IC_3H_7O_2 + 0.18\,C_2H_5O_2 + H_2O \tag{R50}$$

$$LHOC_3H_6OOH + OH \longrightarrow 0.5\,LHOC_3H_6O_2 + 0.5\,ACETOL + 0.5\,OH + H_2O \tag{R51}$$

$$CH_3COCH_3 + OH \longrightarrow CH_3COCH_2O_2 + H_2O \tag{R52}$$

$$NC_4H_{10} + OH \longrightarrow LC_4H_9O_2 + H_2O \tag{R53}$$

$$LC_4H_9OOH + OH \longrightarrow 0.15\,LC_4H_9O_2 + 0.85\,MEK + 0.85\,OH + 0.85\,H_2O \tag{R54}$$

$$LC_4H_9NO_3 + OH \longrightarrow MEK + NO_2 + H_2O \tag{R55}$$

Reactions with Clorine and Bromine Compounds

$$HCl + OH \longrightarrow Cl + H_2O \tag{R56}$$

$$HOCl + OH \longrightarrow ClO + H_2O \tag{R57}$$

$$CH_3Cl + OH \longrightarrow LCARBON + H_2O + Cl + \ldots \tag{R58}$$

$$CH_3CCl_3 + OH \longrightarrow 2\,LCARBON + H_2O + 3\,Cl + \ldots \tag{R59}$$

$$HBr + OH \longrightarrow Br + H_2O \tag{R60}$$

$$CH_3Br + OH \longrightarrow LCARBON + H_2O + Br + \ldots \tag{R61}$$

$$CHBr_3 + OH \longrightarrow LCARBON + H_2O + 3\,Br + \ldots \tag{R62}$$

$$CH_2Br_2 + OH \longrightarrow LCARBON + H_2O + 2\,Br + \ldots \tag{R63}$$

$$CHCl_2Br + OH \longrightarrow LCARBON + 2\,Cl + H_2O + Br\,\{+CH_3O_2\} \tag{R64}$$

$$HClBr_2 + OH \longrightarrow LCARBON + Cl + H_2O + 2\,Br \tag{R65}$$

$$H_2ClBr + OH \longrightarrow LCARBON + Cl + H_2O + Br \tag{R66}$$

$$HOCl + HCl \longrightarrow Cl_2 + H_2O \tag{R67}$$

$$HOBr + HBr \longrightarrow Br_2 + H_2O \tag{R68}$$

$$HOCl + HBr \longrightarrow BrCl + H_2O \tag{R69}$$

$$HOBr + HCl \longrightarrow BrCl + H_2O \tag{R70}$$

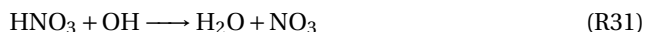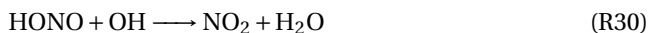LCARBON denotes a group of species with two or more carbon atoms (MECCA User Manual).

4.3.2. REACTIONS OF WATER VAPOR DESTRUCTION

Reactions of water vapor destruction are far fewer than of water vapor production. However, these include the two very important reactions R71 and R72 for the abundance of the hydroxyl radical. The other three are related to the production of nitric acid (HNO_3).

$$H_2O + O(^1D) \longrightarrow 2\,OH \tag{R71}$$

$$H_2O + h\nu\,(\lambda < 200\,nm) \longrightarrow H + OH \tag{R72}$$

$$N_2O_5 + H_2O \longrightarrow 2\,HNO_3 \tag{R73}$$

$$ClONO_2 + H_2O \longrightarrow HOCl + HNO_3 \tag{R74}$$

$$BrONO_2 + H_2O \longrightarrow HOBr + HNO_3 \tag{R75}$$
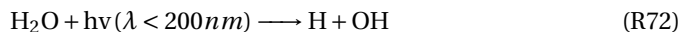
Future Extension of the Chemical Mechanism For completeness and future simulations with e.g. an extended model domain the following pieces of information are relevant. First, in further developed MESSy versions a reaction destroying water vapor and nine reactions producing water vapor were added, which include sulfur reactions. Sulfur reactions are especially interesting in the context of volcanic eruptions, which affect stratospheric water vapor concentrations. The two additional reactions are the following.

$$H_2SO_4 + h\nu \longrightarrow SO_3 + H_2O \tag{R76}$$

$$SO_3 + H_2O \longrightarrow H_2SO_4 \tag{R77}$$

Second, the photolysis reaction R78, destroying water vapor, becomes important in the thermosphere and is not included in MECCA, since the upper model limit is approximately 80 km. This might be of interest for a potential whole-atmosphere extension of EMAC.

$$H_2O + h\nu\,(\lambda < 147nm) \longrightarrow H_2 + O(^1D) \tag{R78}$$
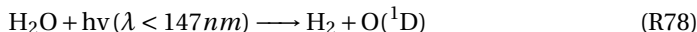
4.4. WATER VAPOR LOSS AND PRODUCTION FOLLOWING AIRCRAFT EMISSIONS

The following subsections present the change in production and loss reactions of water vapor. In this context the term *recombination* refers to the conversion of H and O compounds originating from water vapor depletion (R26-R70) back to water vapor (R71-R75). The prerequisite is the chemical conversion of water vapor emissions from aircraft to HO_x compounds. The results in the first subsection are based on the aircraft emission inventory HIKARI with combined emissions of the aircraft ZEHST and LAPCAT (p. 49). The second subsection is based on the idealized emission simulations with emission in different latitude and altitude regions (p. 51). The results are perturbations of the atmospheric background, i.e. the difference between emission scenario simulations and the reference simulation.

Water Vapor Loss Mass perturbation and perturbation lifetime are affected by the (photo-)chemical conversion of emitted water vapor. The key processes are photolysis and reaction with $O(^1D)$ (R71, R72). The average (photo-)chemical lifetime of water vapor of both processes is shown in Fig. 4.3 for the models LMDZ-INCA (a) and EMAC (b). Fig. A.4 in the appendix shows the (photo-)chemical and chemical lifetime separately. Photolysis clearly increases with altitude resulting in shortest lifetime at the upper end of the simulated altitude range and at the equator region, where incident sunlight is strongest on average. The reaction with $O(^1D)$ has a maximum at around 45-50 km, where the loss of O_3 due to photolysis and thus concentrations of excited atomic oxygen $O(^1D)$ is generally larger and the lifetime in turn is at a local minimum. The combination shows mainly the features of $H_2O + O(^1D)$, with contributions of photolysis at altitudes above 50 km. In comparison to literature (Fig. 2.13) the EMAC results (Fig. 4.3) agree well with a lifetime slightly below one year and LMDZ-INCA

results slightly above one year at 45-50 km. At 70 km literature expects a lifetime of around one month, which again agrees well with EMAC values and is only slightly lower than LMDZ-INCA values. Overall, the models show very similar lifetimes in altitude and latitude with small individual differences. Compared to Kinnison et al. [105, Fig. 3], the patterns are the same for WACCM results with very similar orders of magnitude.
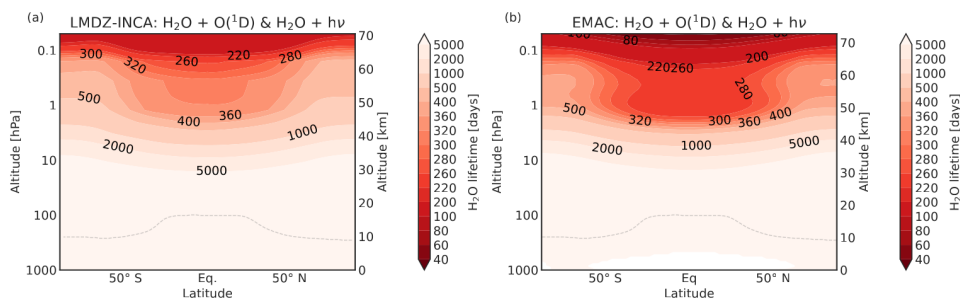
Figure 4.3: Zonal mean (photo-)chemical H_2O lifetime in days dependent on photolysis and reaction with $O(^1D)$ for LMDZ-INCA (a) and EMAC (b).

4.4.1. Aircraft Emission Scenarios

During operation aircraft emit water vapor, nitrogen oxides and hydrogen simultaneously. First, these emissions affect water vapor, nitrogen oxides and hydrogen concentrations directly. These changes are then passed on to the respective conversion cycles, like the HO_x-cycle (Fig. 4.1), until the initial emitted trace gases are distributed among many other trace gases via production and loss reactions. Hence, in model simulations with aircraft emissions the continuously emitted trace gases affect chemical loss and production of the atmosphere and the (photo-)chemical conversion rates (e.g. number of chemical transformations of a molecule per year) similarly show equilibrium perturbations.

Figure 4.4 shows these perturbations of production (red) and loss (blue) between EMAC simulations including aircraft emissions of water vapor, nitrogen oxides and hydrogen and the reference simulation. Water vapor equivalent to 30 % and 60 % of the annual emitted water vapor at stratospheric altitudes is chemically converted for the aircraft scenarios, ZEHST and LAPCAT, respectively (Table 3.4). Clearly the higher emission altitude of LAPCAT (35 km) comes with a larger water vapor loss, which agrees well with model results shown in Fig. 4.3. The main loss drivers are photolysis and the reaction with $O(^1D)$ and the latter dominates for both aircraft scenarios. The other reactants responsible for water vapor destruction, N_2O_5, $ClONO_2$ and $BrNO_3$, are not significantly contributing. The production, i.e. recombination, of water vapor is larger than the loss and overcompensates the loss by 0.76 Tg and 1.95 Tg in the case of ZEHST and LAPCAT, respectively (dark red bars). This equals an increase of the initial annual perturbation above 18 km by 5.5 % for the former and 9.3 % for the latter. The resulting change from emissions and (photo-)chemistry is balanced by transport to the troposphere.

In the used EMAC setup forty-five reactions are participating in the production of water vapor. Figure 4.5 shows the nine most important ones, that cover close to 100 %

4
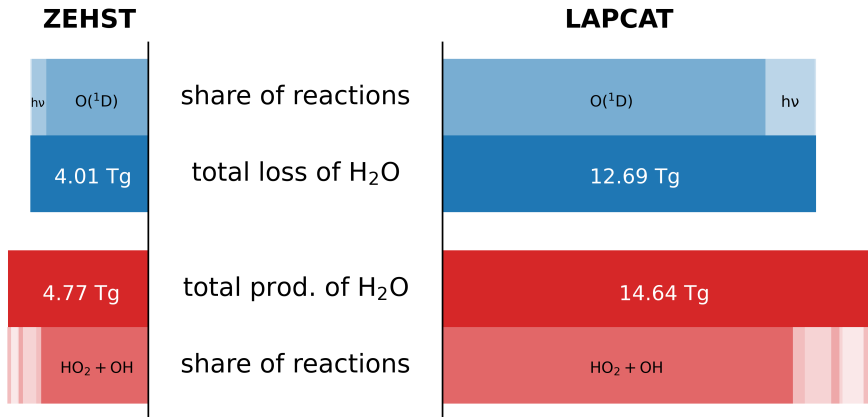
Figure 4.4: Annual chemical loss and production perturbation of H_2O at stratospheric altitudes (100-0.1 hPa) for the ZEHST (left) and the LAPCAT (right) scenarios due to emitted trace gases. This diagnosis includes a total of five H_2O destroying and 45 H_2O producing chemical reactions. The most relevant reactions of loss and production are shown as bright red and blue bars.

of water vapor recombination. Total values of recombination, 4.77 Tg/yr and 14.6 Tg/yr for ZEHST and LAPCAT are shown here with additional information (see Fig. 4.4). The reactions are grouped in four different categories, which are reactions with carbon (C), atomic nitrogen (N), chlorine (Cl) and atomic hydrogen-oxygen compounds (H,O). The main contributors by far is the HO_x-cycle (green) followed by methane oxidation for LAP-CAT (red) or contributions of nitric acids HNO_3 and HNO_4 for ZEHST (blue). The most important reaction for water vapor recombination is reaction R71, which on the one hand destroys hydroxyl and hydroperoxyl and on the other hand produces water vapor. The relative share of H-O compounds is larger for emission at the higher altitude scenario (LAPCAT), which agrees well with literature, since pathways via other compounds become less with altitude (Fig. 4.1). The results show that differences in the magnitude of pathways start to appear at stratospheric altitudes and the pathways might become negligible in the mesosphere and lower thermosphere.

4.4.2. Idealized Emission Scenarios

To be accurate, the term *recombination* is applicable only for water vapor emission scenarios. There, emitted water vapor is (photo-)chemically converted and only then a recombination is possible. For other emitted trace gases water vapor would simply be (photo-)chemically produced and technically not recombined. For the simulation setup with aircraft emissions, where trace gases, water vapor, nitrogen oxides and hydrogen, are emitted simultaneously, it remained an open question whether the recombination comes solely from water vapor or actually includes a production from hydrogen and nitrogen oxides. The idealized simulations, where each emission type is emitted on its own, will be able to address this question and this subsection presents the individual effect of water vapor, nitrogen oxides and hydrogen emissions on water vapor loss and water vapor production.
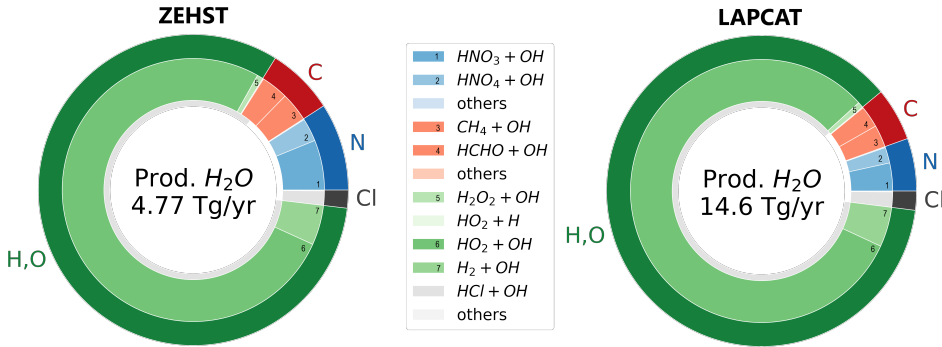
Figure 4.5: Chemical reactions responsible for H_2O recombination derived from EMAC simulation results. Left: ZEHST scenario. Right: LAPCAT scenario. The darker outer ring shows the molecular category the reactions belong to (carbon-, nitrogen-, chlorine- or hydrogen-based). The total sum of H_2O recombination is written in the center. The colored inner ring shows the proportion of different reactions within each category. Black numbers in the legend and the bright inner ring are meant as additional help to correctly distinguish colors.

Altitude Distribution   Figure 4.6 shows the vertical distribution of water vapor production (positive) and loss (negative) in the first row and the net of both terms in the second row. For nitrogen oxide emission scenarios the water vapor production and loss changes the most in the troposphere and small changes between 100-10 hPa (16-32 km), between 10-1 hPa (32-48 km) and at the top of the model domain 0.01 hPa (80 km). Overall, the production overcompensates the loss with some small deviations for specific scenarios. The low tropospheric water vapor perturbation lifetime should neutralize the net of production and loss for nitrogen oxide emission scenarios, which is largest below 100 hPa. For water vapor emission scenarios the loss and production is close to zero at tropospheric altitudes (mid, top), increases from 100 hPa upward, with a minimum between 1 and 0.1 hPa and increases sharply at the top of the model domain. Overall, the lines of recombination and loss look mirrored at first. However, the net values of recombination and loss show negative values at tropospheric altitudes. Positive values are between 100 hPa and 1 hPa, where the peak is at approximately 3 hPa for most scenarios. At the highest altitudes the net becomes negative quickly. In contrast to the symmetry seen for water vapor emission scenarios, hydrogen emission scenarios (right, top) show at first very similar patterns for the middle atmosphere, but include a shift of the production to larger values compared to the loss. The net values show very similar patterns compared to water vapor emission scenarios, with deviations at tropospheric altitudes, where production exceeds the loss in many cases. Tropospheric water vapor net-production should not contribute to water vapor perturbations, since the tropospheric water vapor perturbation lifetime is low compared to higher altitudes and background water vapor concentrations are very large compared to the stratosphere (Fig 7.9). Total annual changes of production and loss are therefore limited to stratosphere and mesosphere from 100 hPa upwards (Fig. 4.7 and 4.8).
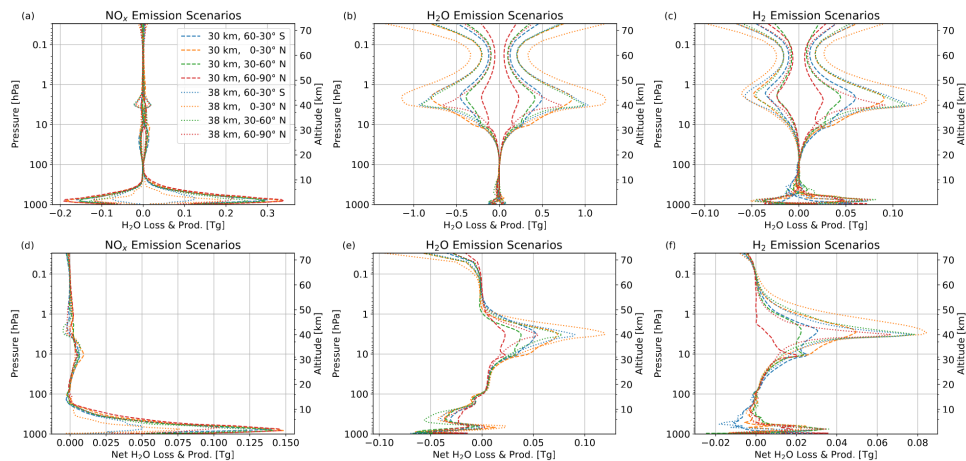
Figure 4.6: Altitude distribution of annual water vapor loss and recombination change. The upper row shows production (positive) and loss (negative) of water vapor. The lower row depicts the net of recombination and loss.

Total Annual Water Vapor Production and Loss   Figure 4.7 presents the vertically integrated production and loss in the first row and the net of both terms in the second row. Overall, all emission scenarios contribute to (photo-)chemical water vapor increase and it shows that the water vapor production and loss of water vapor and hydrogen emission scenarios is one and two order of magnitude larger, respectively, compared to nitrogen oxide emissions scenarios. Overall, values for production, loss and their net are larger the lower the latitude of emissions, which highlights the importance of high-energy radiation as a driver. For nitrogen oxide emission scenarios, only polar north emission shows a decrease of water vapor loss, which in combination with an increased production contributes to water vapor perturbation. The water vapor net-production for water vapor and hydrogen emission scenarios have the same order of magnitude, while nitrogen oxide emission scenarios net values are one order of magnitude smaller.

Main Reactions for Water Vapor Production   Figure 4.8 shows the ratio of the most important reactions for water vapor production and loss similar to Figure 4.5. The nine selected production reactions cover at least 95 % of the contributions of all 45 reactions. The contributions of individual reactions differ with emission scenarios. Nitrogen oxide emission scenarios show very variable patterns compared to water vapor and hydrogen emission scenarios, which are dominated by mostly two reactions. All nitrogen oxide emission scenarios have an increased production with reaction HNO_3 + OH (R31) in common. In contrast the production of water vapor from the reaction HO_2 + OH (R21) decreases due to NO_x emission. The latitude and altitude of nitrogen oxide emission comes with large variations of patterns and changes in the north polar region at 30 km altitude are exceptionally large. The water vapor recombination in water vapor emission scenarios looks very homogeneous with slight variations in the ratio of reactions. The largest contributor to water vapor production is always reaction HO_2 + OH (R21),
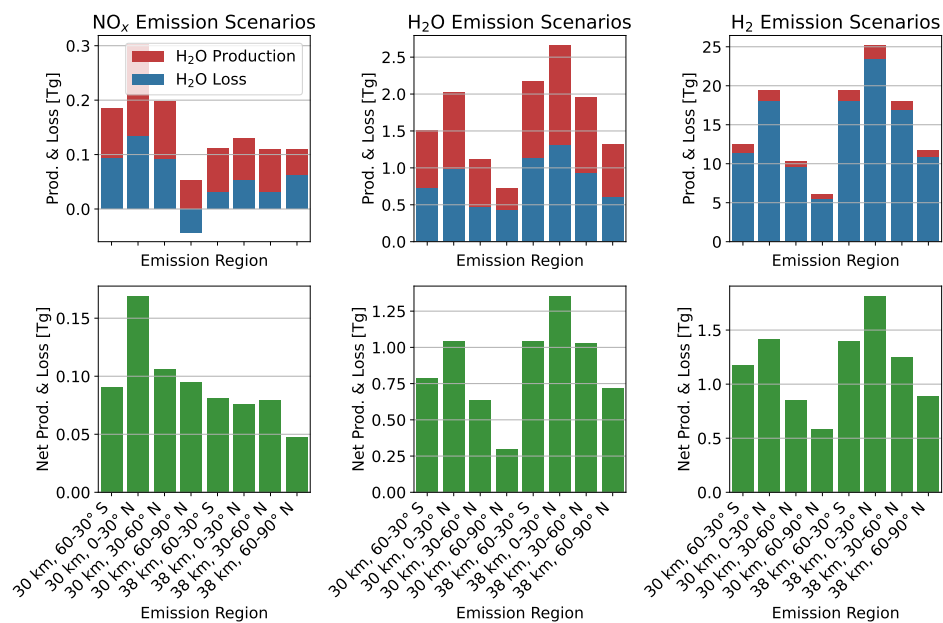
Figure 4.7: Total annual change of water vapor production and loss (upper row) and the net of production and loss (lower row) between emission scenarios and the reference. Values are integrated for 100-0.1 hPa.

which is clearly more dominant at the higher altitude water vapor emission. For hydrogen emission scenarios, the water vapor production shows a large contribution from reaction H_2 + OH (R26), where the emitted hydrogen is converted to water vapor. The largest contribution comes from reaction HO_2 + OH (R21), where water vapor perturbations are recombined. Interestingly, as the only one, the polar north emission scenario at 30 km shows a slight decrease of water vapor production from reaction CH_4 + OH (R40) and reaction HCHO + OH (R41).

Reactions for Water Vapor Loss   In nitrogen oxide emission scenarios, the two most important reactions for water vapor production are H_2O + O(^{1}D) [R71] and H_2O + N_2O_5 [R73]. In most cases the loss from the former decreases and from the latter increases. This excludes emission at 30 km in the tropics, where the former increases and excludes emission at 30 km from 60-90° N, where the change is inverted. The water vapor loss in water vapor and hydrogen emission scenarios has a very similar pattern, where the largest loss is from H_2O + O(^{1}D) [R71] and photolysis.

Effect of One Emitted Molecule   Previous figures compare the total effect of emissions and the magnitude of emissions differs by several orders of magnitude (Table 3.4). This representation makes it difficult to compare how the atmosphere reacts to one molecule of emitted trace gases. Therefore, Table 4.1 shows the net production of water vapor molecules per emitted molecule of either H_2O, NO_x or H_2 as an additional presenta-
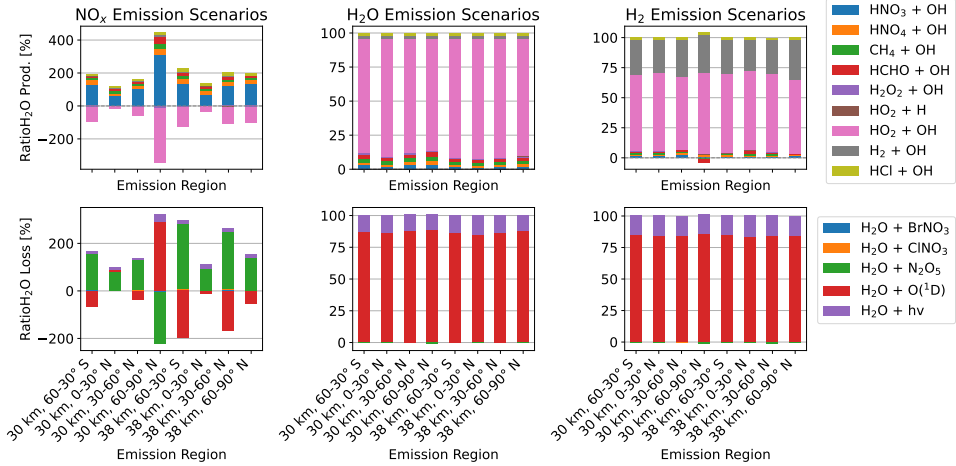
Figure 4.8: Ratio of the change of nine production reactions (upper row) and five loss reactions (lower row) between emission scenarios and the reference. Values are based on altitudes from 100-0.1 hPa.

tion. Columns 3-5 can easily be recalculated to column 6, by, first, using the molar mass of NO_2 (46.01 g/mol), H_2O (18.02 g/mol) and H_2 (2.02 g/mol), second, rescale to teragram and, third, sum up the individual values. Clearly, a substantial part of hydrogen molecules are converted to water vapor molecules within the HO_x cycle (56 % on average). The effect is larger for low latitude and high altitude emission and generally stronger in the Southern Hemisphere. The main contribution certainly comes from hydrogen oxidation $H_2 + OH$ [R26]. In contrast, each emitted water vapor molecule only creates a relative surplus in the lower single digits (4 % on average). Similar to emitted hydrogen molecules, the effect is larger for low latitude and high altitude emission. Differences between the Southern and the Northern Hemisphere are not as strong. In contrast, each emitted nitrogen oxide molecule causes 70-251 water vapor molecules to form (138 % on average). The effect decreases with altitude by up to a factor of two (0-30° north and 60-90° north). To summarize briefly, the water vapor net production caused by emitted nitrogen oxide molecules is largest per molecule, followed by emitted hydrogen molecule and emitted water vapor molecule.

4.4.3. COMPARISON OF COMBINED AND INDIVIDUAL EMISSIONS

How does net production from combined (Fig. 4.4 and 4.5) and individual (Fig. 4.7 and 4.8) hypersonic emissions compare? The comparison requires a linear estimate, since the emission altitude is different for both cases. Linear extrapolation and interpolation of summed net production of individual emissions to the cruise altitude of the aircraft designs with combined emissions (26 km and 35 km) shows values of 1.23 Tg and 2.07 Tg, respectively (Column 6, Table 4.1). The values for the calculations are based on mid-latitude emission scenarios in Table 4.1 (data row 3 & 7), since the emission region overlaps the most with hypersonic aircraft emission patterns (Fig. 3.6, Fig. 3.7). In comparison to net production for combined emission at 26 km (0.76 Tg) and at

Table 4.1: The table contains two kinds of values. First, the integrated net of (photo-)chemical water vapor production and loss for H_2O, NO_x and H_2 emission at each altitude and latitude. Second, the net of (photo-)chemical water vapor production and loss for an emitted molecule of either H_2O, NO_x or H_2. Values are based on altitudes from 100-0.1 hPa.

Altitude	Latitude	Molec. H_2O / molec. H_2	Molec. H_2O / molec. H_2O	Molec. H_2O / molec. NO_2	Net H_2O [Tg]
38	60-30° S	0,67	0,049	120	2,52
38	0-30° N	0,86	0,063	112	3,25
38	30-60° N	0,59	0,048	117	2,35
38	60-90° N	0,42	0,034	70	1,65
30	60-30° S	0,56	0,037	135	2,05
30	0-30° N	0,67	0,049	251	2,63
30	30-60° N	0,41	0,030	158	1,60
30	60-90° N	0,28	0,014	141	0,98

4

35 km (1.95 Tg), the summed values for individual emissions (1.23 Tg and 2.07 Tg) differ by 60 % and 6 %, respectively. Two explanations are possible. First, the linear extrapolation to 26 km altitude does not cover the (probably curvilinear) trend well. Second, atmospheric composition changes by three emitted trace gases at the same time, cause a difference in net production, which cannot be recreated completely accurate by estimates based on individual emission. To answer this open question an additional set of simulations at lower altitudes is probably required.

4.5. SUMMARY

In the brief review of historical HO_x and water vapor measurement it became clear that some open questions on middle atmospheric water vapor remain. However, these questions are often for regions close to the thermosphere and these regions are less important than the stratosphere for the accumulation of emitted trace gases from – and therefore the climate impact of – hypersonic aircraft. The main results show for the first time that (photo-)chemical depletion of water vapor is overcompensated by water vapor production for the combined emission of H_2O, NO_x and H_2 from aircraft. Clearly, the (photo-)chemical water vapor lifetime decrease with altitude as shown by Brasseur and Solomon [97, Fig. 5.23, p. 312] does not show an effect yet and the water vapor to hydrogen partitioning is in favour of water vapor in the stratosphere. Instead, in addition to HO_x recombination an increased methane, nitric acid and hydrogen chloride oxidation contributes to the production of water vapor and in combination creates a surplus, i.e. net production, of water vapor. This results in a longer H_2O perturbation lifetime at emission altitudes up to 40 km. This trend may change at even higher altitudes, where (photo-)chemical H_2O lifetime decreases and, more importantly, the (photo-)chemical lifetime of HO_x and H_2 increases substantially (Fig. 2.13). With the model setup, where three trace gases are emitted simultaneously, it was unclear to which trace gas this effect can be attributed to or how the trace gases contribute to the total effect. Hence, the individual chemical budget was analysed and it was shown that, for the here applied ratio of emitted trace gases, water vapor and hydrogen emissions contribute nearly equally to the net-production. Emissions of nitrogen oxides show the smallest net production,

that decrease with altitude of emission, which is conform with literature (Fig. 4.1). In comparison, hydrogen and water vapor emission scenarios show a net-production that is one to two order of magnitudes larger compared to nitrogen oxide emission and that increases with altitude of emission.

4

5

DYNAMICS AND TRANSPORT OF EMITTED TRACE GASES

Middle atmospheric (photo-)chemistry and general atmospheric sensitivities to hypersonic emissions were presented in previous chapters. For completeness, this chapter addresses the water vapor budget of the middle atmosphere in EMAC model simulations. This includes transport of middle atmospheric water vapor from and to the troposphere, water vapor originating from atmospheric chemistry and water vapor emission by hypersonic aircraft. Following the atmospheric air transport, the upward transport in tropical regions, the horizontal transport in subtropical regions, the downward transport in north polar regions and a potential re-circulation of water vapor perturbations are evaluated.

5.1. Introduction

Chapter 6 showed that water vapor perturbation is actually slightly increased – not depleted – through chemistry, which emphasizes that transport and not chemistry is the process limiting the annual perturbation and hence the climate impact from water vapor. In contrast, another emitted trace gas, nitrogen oxide, has reservoirs like HNO_3 or $ClONO_2$ it is converted to. In these reservoirs nitrogen oxides are rendered ineffective in relation to ozone and hence climate. Clearly, chemical conversion can largely affect partitioning of emitted trace gases and therefore controls the magnitude of climate active perturbations, while these are transported to the troposphere. However, for all emitted trace gases dynamics control the upper limit of the residence time in the middle atmosphere. The upper limit is approximately (excluding a potential re-circulation and chemical processes) the upper limit of the age of air, which is the time an air parcel needs to travel from the tropical upper troposphere–lower stratosphere back to the troposphere (6-8 years). Coarsely described, three domains of air transport exist, which are the tropical pipe, the surf-zone at mid-latitudes and the vortex at polar regions (Fig. 2.7 and 2.8). According to this simplified scheme, vertical upward transport elevates air at 10° S to 10° N, horizontal transport appears at the subtropics (10°-30° S and N), where vertical downward transport becomes increasingly important with latitude and dominates transport largely at high latitudes (75°-90° S and N) [173, Fig. 2]. This scheme describes a simple motion, where actually horizontal mixing can introduce re-circulation within the stratosphere, which is often referred to as a 'leaky' tropical pipe [174, 175]. Note that dynamics are strongly dependent on season and vertical air transport is fastest in polar winter. An example of a seasonal and second order process limited in space and time is the appearance of polar stratospheric clouds, where vertical downward transport of HNO_3 (and partly H_2O) is enhanced through sedimentation. The analysis in this chapter focuses on a potential re-circulation of emitted trace gases in the stratosphere that eventually enter the troposphere in the extra-tropic to polar regions and reenter the stratosphere in tropic or subtropic regions. Possible pathways for a tropical re-circulation are e.g. the main tropical updraught (Fig. 2.7) or the smaller-scale (quasi) isentropic exchange at lower latitudes between the middle and upper troposphere and the lower stratosphere (Fig. 2.8). Overall, air transport is very important for the climate impact of hypersonic aircraft and this chapter specifically addresses transport from and to the troposphere, a potential re-circulation and the water vapor transport budget within EMAC model results.

5.2. Transport from the Troposphere into the Stratosphere

Temperature in the tropical tropopause controls the humidity of uprising air. Water vapor is frozen and largely removed and the – comparably very dry – air rises further into the stratosphere. This feature was described as a 'tape recorder' by Mote et al. [176]. In these tape recorder images, tropospheric air rises in altitude with time. On the annual cycle between 10° S and 10° N this resembles a diagonal line in the dry stratospheric background. The tape recorder feature of EMAC results was compared to satellite measurements (p. 47). Figure 5.1 shows, first, the tape recorder feature simulated by the

EMAC model (first row) and, second, integrated water vapor perturbations for water vapor emission scenarios at 10° S to 10° N. Here, a focus is on water vapor emission scenarios at 38 km altitude (plots for 30 km altitude are shown in the appendix on p. 172). Note that for nitrogen oxide emission scenarios and hydrogen emission scenarios show similarities to the tape recorder features, with partly increases and decreases (not shown). These features are rather noise than significant perturbations. However, it is worthy to note that the year 2016 shows same tape recorder feature for not only water vapor emission scenarios, but all emission scenarios. Therefore, these perturbation features in 2016 do not originate from water vapor emissions, but from other model processes.

Figure 5.1: Timeline of integrated concentrations changes in the tropics (10° S-10° N) for water vapor emission scenarios at 38 km altitude and the reference simulation (first row). Theoretical position of tape recorder features were marked with green lines and potential similar features in the perturbation scenarios were marked with blue lines.

Tape Recorder Perturbation Analysis   For analysis, the tape recorder features (first row) or their theoretical position (other rows) were marked with green lines. Note that three signatures appear here. First, the green lines approximately start in the third quarter of each year (northern polar summer), second, they continue from the lower altitude at 100 hPa diagonally to higher altitudes and, third, concentrations reduce gradually. The latter signature should originate from the decreasing air density and does not appear in mixing ratio presentation of EMAC results or satellite data (Fig. 3.5). For rows showing results from emission scenarios most similar features were marked with blue lines. However, excluding the year 2016, there are very few features combining all three signatures. The largest concentration increases marked with blue lines do not rise from the lower altitude and mostly start to appear before or after the third quarter of a year, which hints more to horizontal exchanges with subtropical regions. Some tape recorder features appear at the same time as in the reference, originate from the lower altitude and decrease with altitude. These fulfill all signatures of the tape recorder feature. However, their concentration is small in comparison to other perturbations. That could mean that stratospheric air – transporting emitted water vapor from hypersonic aircraft – enters the troposphere, becomes drier via rain-out or freeze-out and eventually reenters the stratosphere in the tropics having lost most of the perturbations. Perturbations, where upward transport is visible at a similar time as the tape recorder feature, are approximately on the magnitude of 1 % of the background concentration and appear only very limited in time. Clearly, the magnitude should not suffice for a large scale re-circulation of perturbations from the troposphere into the stratosphere. The sometimes steeper or (less steep) vertical patterns marked in blue might potentially point towards other transport processes of troposphere to stratosphere transport. Other patterns that do not fulfill the three signatures, e.g. emission scenario for 0-30° N from 2014-07 to 2015 at 50 hPa-20 hPa or 30-60° N from 2015-06 to 2016 at 60 hPa-40 hPa, should originate from horizontal stratospheric transport from the subtropics and is approximately on the magnitude of 1.5-2.0 % compared to the background concentration.

5.3. HORIZONTAL TRANSPORT IN THE STRATOSPHERE

Figure 5.2 shows integrated water vapor perturbations of northern subtropics (10°-30° N). While the tape recorder feature is still visible in the background concentration (first row), vertical transport of perturbations does appear rarely in perturbation features. This is in contrast to the tropical perturbations, where uprising features are more clear. Hence, an increasing horizontal transport to other regions is clearer for the subtropic perturbations that show features of horizontal exchange to neighboring regions, like the tropics (10° S-10° N) or the mid-latitudes (30°-60° N), especially between 100-10 hPa. Largest concentrations accumulate from January to July, hence largest horizontal transport from the subtropics to other regions happens from August to December (Fig. 5.1). Vertical transport for emission at 4-3 hPa to higher (northern polar summer) or lower altitudes (northern polar winter) appears clearly (emission at 0-30° N), without a clear source (emission at 30°-60° N) or barely (emission at 60-90° N). For emission at the Southern Hemispheric mid-latitudes the source of perturbations is not visible and transport to lower or higher latitudes is inverted compared to emission at the Northern
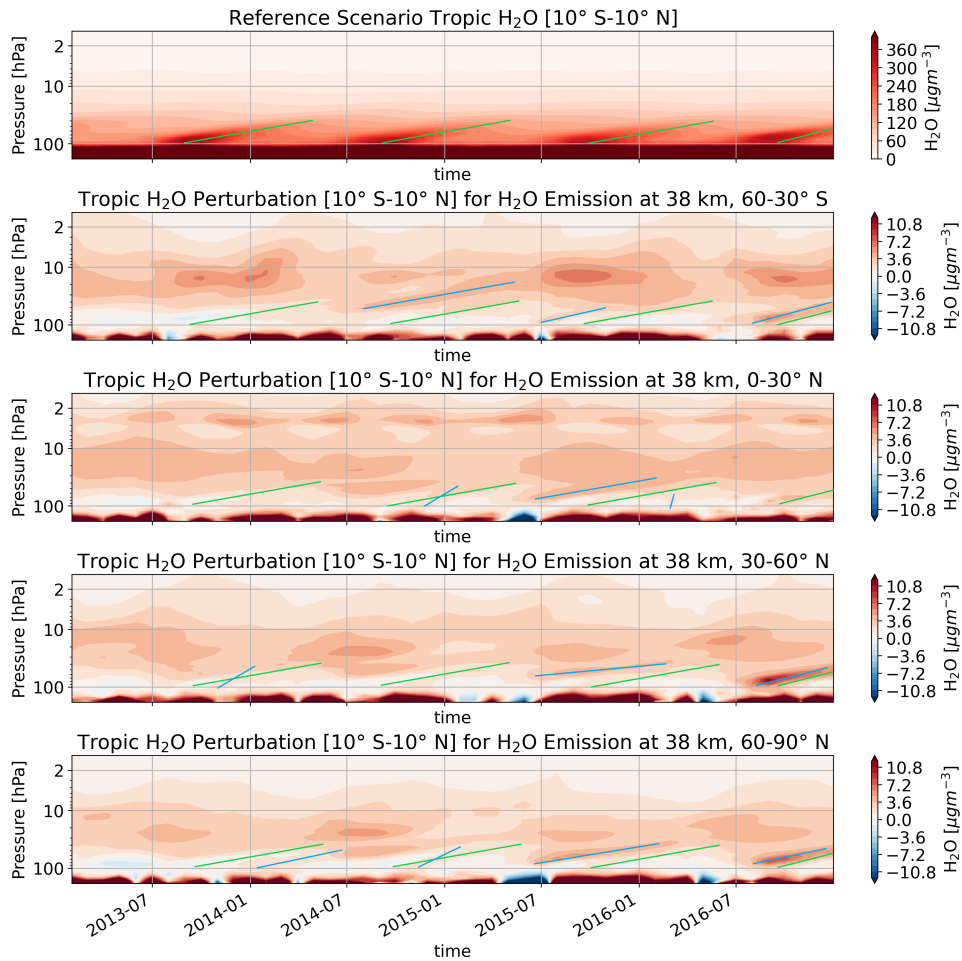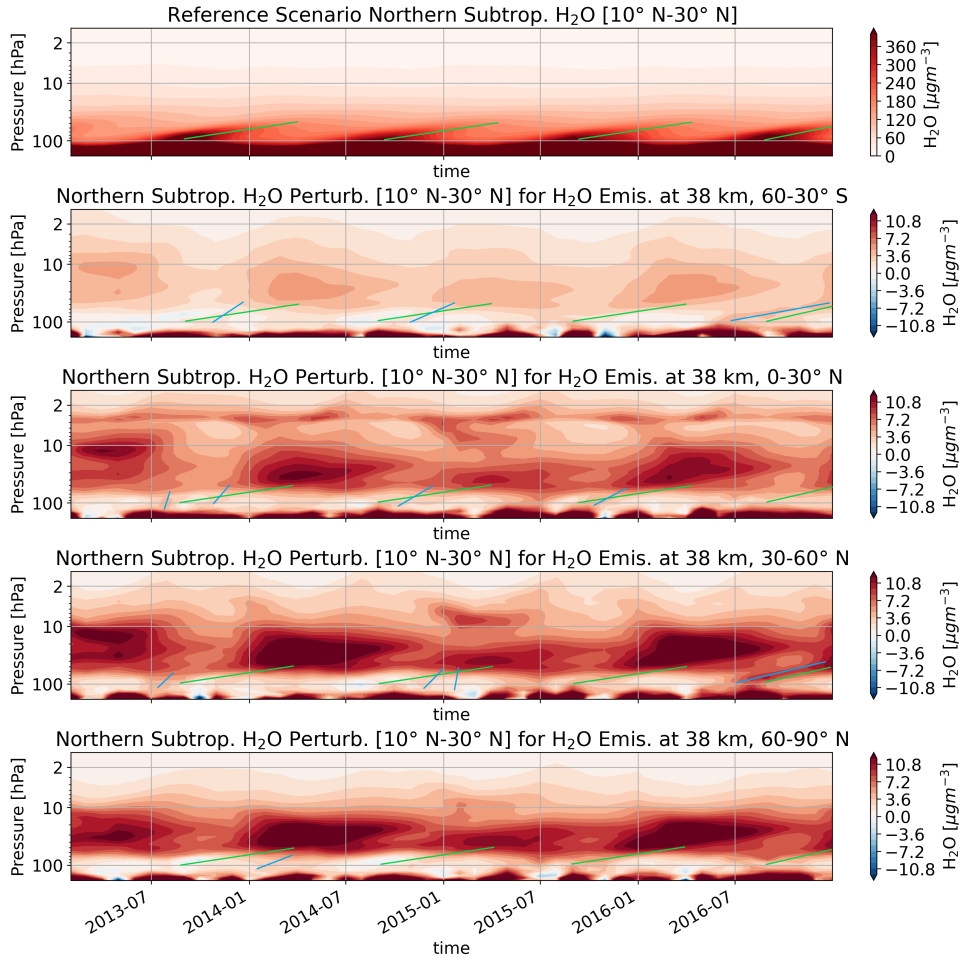
Figure 5.2: Timeline of integrated concentrations changes in the subtropics (10-30° N) for water vapor emission scenarios at 38 km altitude and the reference simulation (first row). Theoretical position of tape recorder features were marked with green lines and potential similar features in the perturbation scenarios were marked with blue lines.

Hemisphere (emission at 60°-30° S). Overall, horizontal transport dominates in the northern subtropics, which agrees well with net transport according to Fig. 2.7 (p. 13) and Fig 2.8 (p. 16) and Remsberg [173, Fig. 2].

5.4. Transport from the Stratosphere to the Troposphere

The Brewer-Dobson circulation describes parts of the atmospheric air flow, where air rises in the tropical upper-troposphere lower-stratosphere crosses the higher altitude

regions and sinks to the surface at polar regions. It therefore transports the emitted trace gases to regions where either rain-out or fall-out removes the perturbations or a residual gets re-circulated. The situation is quite different to the tape recorder feature, since dry and cold air sinks from higher altitudes to lower altitudes, where the environment is more humid. Hence, in contrast to the tape recorder feature, this feature is normally not visible in simulation results or measurements, simply because the background concentration of water vapor in the troposhere is too large.
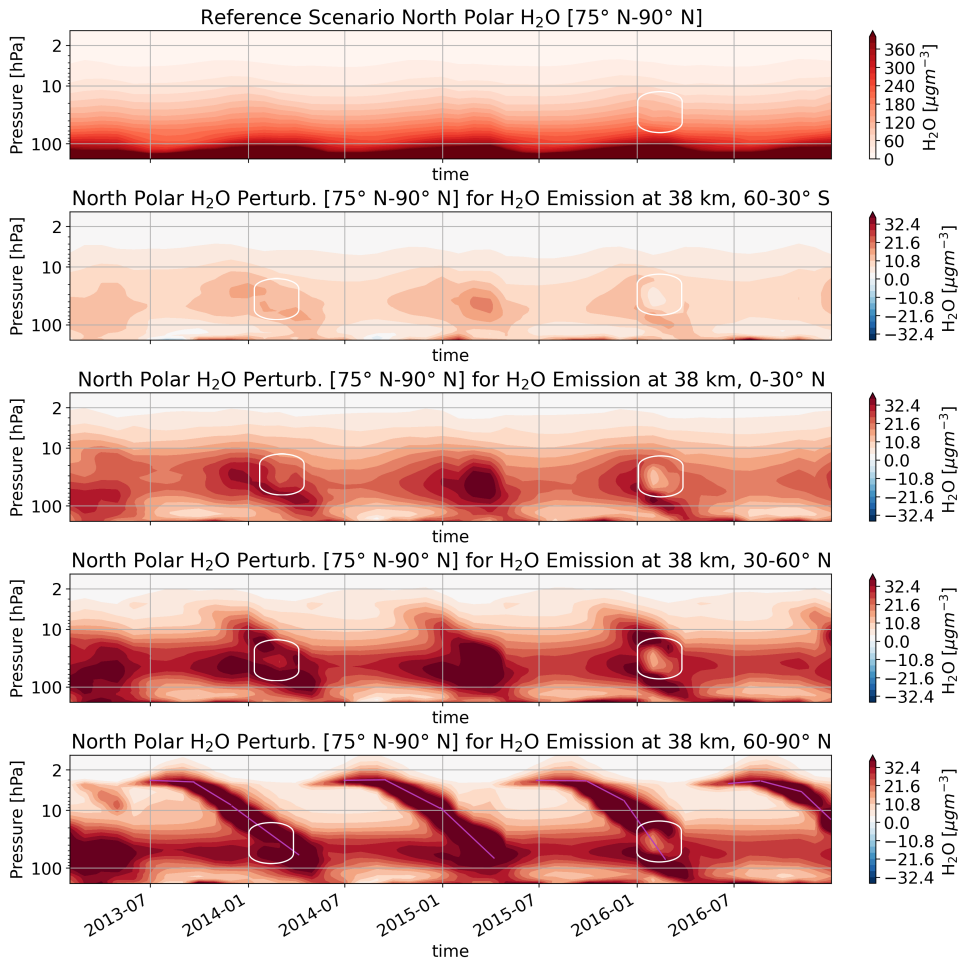
Figure 5.3: Timeline of north polar concentrations changes for water vapor emission scenarios at 38 km altitude and the reference simulation (first row). Sinking perturbations for north polar emission were marked with magenta coloured lines and appearance of dehydration via polar stratospheric clouds are outlined in white.

Figure 5.3 shows the reference simulation and integrated perturbations from 75°-90° N for water vapor emission at 38 km. The patterns of the perturbation scenarios are very similar and differ mostly in magnitude. The magnitude depends very much

on how far away the emission region is located from north polar latitudes. That means smallest patterns appear for emission at southern mid-latitudes and largest patterns (including the emission source) appear for north polar emission. Hence, for the latter diagonal trends were marked with purple lines, which appear regularly before the beginning of each year. The purple lines start horizontally in northern polar summer and become increasingly vertical until diagonal after. This very much represents the strong (weak) vertical transport in the Northern Hemisphere during winter (summer). Note that for the years 2014 and 2016 dehydration in northern polar winter (white outlines) is clearly visible in all scenarios and for 2016 it even appears weakly in the background concentration (first row). This is directly related to ice particles associated with polar stratospheric clouds (not shown) and appears significantly stronger in the Southern Hemisphere (Fig. A.10 and A.11). The ice dehydration affects water vapor perturbations strongly between 100-10 hPa and appears for 2 out of 4 years. NAT particles (1 HNO$_3$, 3 H$_2$O) appear slightly earlier (January) in 2015 in addition to 2014 and 2016 and the density perturbation is one order of magnitude smaller compared to ice particles (not shown). That denitrification appears sooner than dehydration was measured by satellite instruments [177]. Overall, the downward transport to tropospheric altitudes is clearly visible in a regular fashion for all scenarios. The most important process of vertical downward transport in the Northern Hemisphere is the seasonal appearance of the polar vortex, which is supported by sedimentation (mostly ice) between 100-10 hPa. Note that on the annual cycle transport does not remove all water vapor perturbations and perturbations to some part remain in the lower stratosphere at approximately 50 hPa, which is shown by horizontal patterns at around 80-60 hPa.

Table 5.1: Multi-annual mean water vapor production from three oxidation reactions, i.e. methane (CH$_4$), formaldehyde (CH$_2$O) and hydrogen (H$_2$) oxidation, at two different altitude regions in the EMAC reference simulation.

Reactions	H$_2$O [Tropop. (WMO)-30 km]	H$_2$O [30-80 km]
CH$_4$ + OH $\longrightarrow$ H$_2$O + ...	10.7 Tg a^{-1}	6.1 Tg a^{-1}
CH$_2$O + OH $\longrightarrow$ H$_2$O + ...	2.7 Tg a^{-1}	6.2 Tg a^{-1}
H$_2$ + OH $\longrightarrow$ H$_2$O + ...	3.5 Tg a^{-1}	5.0 Tg a^{-1}

5.5. TRANSPORT BUDGETS OF MIDDLE ATMOSPHERIC WATER VAPOR

Two main processes contribute to water vapor concentrations in the middle atmosphere. The first is dynamic in nature and consists of residual water vapor passing through the cold temperature region of the tropical upper–troposphere lower–stratosphere [178]. Dynamic process particularly affect the (tropical) lower stratosphere. The second and dominant one is chemical: oxidation of methane, formaldehyde and hydrogen ([154]). Note that the largest part of methane is oxidized at tropospheric altitudes and only a residual is oxidized in the middle atmosphere, which amounts to 3 % of the total methane oxidation (Table 5.1, paragraph on p. 42). Hypersonic emissions would contribute further to water vapor transport budgets that eventually reach tropospheric

heights at polar regions. EMAC results show that the largest part of middle atmospheric methane is oxidized at lower stratospheric altitudes (tropopause-30 km). In contrast, formaldehyde and hydrogen oxidation becomes larger at the higher altitude domain (30-80 km). In EMAC simulations, each year 34 teragram of water vapor are produced chemically in the middle atmosphere by these three reactions. This amounts to approximately one-tenth of the integrated water vapor mass in the middle atmosphere in EMAC (334 Tg).
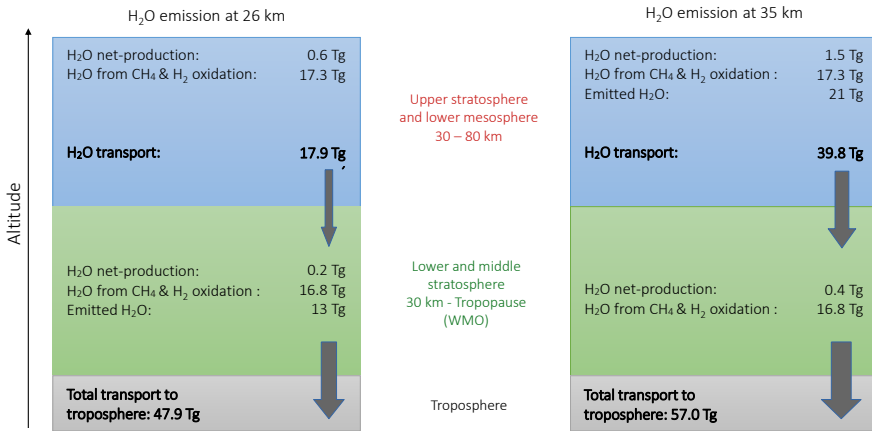
Figure 5.4: The transport budget of water vapor as an annual average in equilibrium. The budget includes water vapor from chemically converted origin – mostly from methane oxidation and hydrogen oxidation – as well as the annually emitted water vapor and the related chemically net-produced water vapor.

Figure 5.4 shows the budget of water vapor in two domains, i.e. lower and middle stratosphere and upper stratosphere to lower mesosphere and the resulting total transport to the troposphere. The budget includes the chemical production from methane, formaldehyde and hydrogen oxidation (Table 5.1), the annual emitted water vapor from hypersonic aircraft (Table 3.4) and the net-produced water vapor from (photo-)chemical water vapor destruction and production (chapter 4, Fig. 4.4). Annual emitted water vapor of hypersonic aircraft and water vapor from the oxidation of methane, formaldehyde and hydrogen are of the same order of magnitude. According to this scheme, the annual transport of water vapor from the middle atmosphere to the troposphere amounts to 48-57 teragram, depending on the emission scenario.

5.6. Summary

Hypersonic water vapor emissions become part of the hydrologic cycle in the Earth system. Emitted at altitudes from 25-40 km water vapor is (photo-)chemically converted with a net surplus and the collective perturbation is transported with the background middle atmospheric water vapor to tropospheric altitudes along the Brewer-Dobson circulation's minor and major pathways. Upon reaching the troposphere most of the water

vapor is removed from air in liquid (rain) or solid (ice) form. As air will eventually be re-circulated in the tropics, water vapor that remained in the air in gaseous form can potentially re-enter the middle atmosphere. Note that during a conventional simulation approximately ten simulated years are required until water vapor perturbations reach an annual quasi-equilibrium. In this chapter an analysis of perturbations in three main transport regions – the tropical pipe, subtropic-mid-latitudes and the polar vortex – was done including a check, whether this is a circular motion via re-circulation. In EMAC results, features that could be classified as re-circulation of water vapor perturbations do appear. However, their magnitude is small with 1-2% compared to background water vapor and their seasonal appearance is brief, does not always correlate with the tape recorder feature and might therefore involve smaller-scale exchange processes between troposphere and stratosphere. Seasonal upward motion via the tropical pipe is visible in all scenarios, especially for tropical emission at 30 km. In comparison, patterns of horizontal transport become stronger with decreasing pressure. This is shown particularly well for tropical emission at 38 km altitude, where emitted trace gases leave the tropical region to neighboring regions faster than for emission at 30 km and tropical perturbations at altitude of emission are hence much lower. Horizontal transport of perturbations becomes increasingly dominant with latitude, shown by the integrated northern subtropic perturbations. The increasing horizontal transport of perturbations with altitude in the tropics and the mainly horizontal transport of perturbations in the subtropics recreates very much the theory of the extratropical pump drawing air from tropical latitudes (p. 14) and strong horizontal transport in the subtropical region indirectly caused by planetary wave breaking at mid-latitudes. The features of polar downward transport of water vapor perturbations are clearly visible in regular intervals and a direct increase and decrease of transport speeds can be attributed to seasonal cycles and the appearance of the northern polar vortex. Locally (100-10 hPa) dehydration in the environment of polar stratospheric clouds does appear irregularly in polar perturbations results, which is very much controlled by temperature (p. 14). This effect might increase with decreasing stratospheric temperatures due to climate change [179] and in turn enhance vertical transport of water vapor via sedimentation. Besides the analysis of horizontal and vertical transport, the EMAC water vapor budget of the middle atmosphere was quantified for the three most important chemical reactions. The annual production of water vapor from oxidation of methane, formaldehyde and hydrogen is on the same order of magnitude as annual hypersonic emissions. As a reminder the annual emission very much depends on the total number of flights and the aircraft design. In this scheme, the annual transport budget of (photo-)chemically produced water vapor and emitted water vapor from aircraft is on the order of 50 teragram.

6

THE CLIMATE IMPACT OF DIFFERENT HYPERSONIC AIRCRAFT DESIGNS

This chapter presents results from two state-of-the-art chemistry-climate models and a climate response model. The focus is on atmospheric composition changes and respective climate impacts due to two potential hypersonic fleets flying at 26 km and 35 km, respectively, allowing to evaluate two of the currently most developed hypersonic aircraft designs. In addition, the altitude dependency of the climate impact is demonstrated using emission data of the new STRATOFLY aircraft based on sensitivities from chapter 7. The atmospheric composition changes of water vapor, hydrogen oxides, nitrogen oxides, ozone and methane caused by the combined emission of water vapor, nitrogen oxides and unburnt hydrogen are presented in section 6.1. Section 6.2 shows the calculated climate impact, i.e. stratosphere-adjusted radiative forcing, of the two hypersonic fleets. Section 6.3 is a discussion of results, which includes the STRATOFLY MR3 aircraft comparison of four different cruise altitudes of one specific flight path and sets it in context to the climate impact of the two hypersonic fleets. The chapter ends with a summary.

Parts of this chapter were published in *Atmospheric Chemistry and Physics*, Pletzer et al. [33].

6.1. ATMOSPHERIC COMPOSITION CHANGES

H$_2$O, O$_3$ and CH$_4$ are important greenhouse gases, whereas HO$_x$ and NO$_x$ components are important reservoirs controlling concentrations of the former.

6.1.1. WATER VAPOR PERTURBATION

Figure 6.1: Multi-annual mean (2010-2014) of H$_2$O perturbations (ppbv) for the ZEHST scenario (left) and the LAPCAT scenario (right) for both models LMDZ-INCA (upper) and EMAC (lower) after approximately thirteen years of continuous emission. Cruise altitudes are approximately at the respective perturbation maxima. The dotted region corresponds to the grid points where the mean perturbations are not significant at a 99.9 % level.

Middle atmospheric H$_2$O stems mostly from upward transport at tropical latitudes and oxidation of CH$_4$ and emissions of a potential fleet of hypersonic aircraft would change atmospheric composition and increase H$_2$O concentrations. The main factors for loss of middle atmospheric H$_2$O, which would also affect emitted trace gases, are reaction with O(^{1}D), photolysis and the transport into the troposphere at the subtropical tropopause breaks. Additionally, polar stratospheric clouds cause dehydration through sedimentation of particles. Note that those processes are considered in the model simulations (Further information on methods on p. 40). Figure 6.1 shows the increase of H$_2$O as volume mixing ratios in equilibrium as a 5-year average based on EMAC and LMDZ-INCA model results for H$_2$O, NO$_x$ and H$_2$ emissions of the ZEHST and LAPCAT aircraft. The H$_2$O perturbation is clearly visible in both models, especially at the Northern Hemisphere with the maximum located at around 50-60° N, which overlaps with the maximum trace gas emission location shown (Fig. 3.7). Overall, the perturbation patterns agree well between the models, especially for altitudes from 16 to 37 km (approx-

imately 100-4 hPa) and with differences at higher altitudes 37 to 80 km (approximately 4-0.01 hPa). The upper altitude range contains only a small amount of the mass perturbation, since the largest mass perturbation accumulates in the middle and lower stratosphere, where air density is larger (Fig. A.15). A t-test shows that all zonal-mean H_2O perturbations are statistically significant at a 99.9 % level and only parts in the tropical upper–troposphere lower–stratosphere (UTLS) (EMAC: ZEHST, LMDZ-INCA: ZEHST, LAPCAT) do not reach that value.

Table 6.1: Perturbation and perturbation lifetime of H_2O in teragram and years, respectively, for the ZEHST and the LAPCAT scenario and for each of the two models.

Model/Scenario	Perturbation ZEHST	Perturbation Lifetime ZEHST
LMDZ-INCA	38.3 Tg	2.79 yr
EMAC	47.8 Tg	3.50 yr
Model/Scenario	Perturbation LAPCAT	Perturbation Lifetime LAPCAT
LMDZ-INCA	89.5 Tg	4.21 yr
EMAC	98.5 Tg	4.61 yr

Absolute values of the mass perturbation and the resulting perturbation lifetime of H_2O are listed in Table 6.1. Values were calculated for perturbations above the tropopause (WMO, 1957). The total H_2O mass perturbation is approximately twice as large for the higher flying aircraft compared to the lower flying aircraft for each model, first, due to the longer transport to the troposphere and, second, due to the larger annual emission. The perturbation lifetime increases with cruise altitude from 2.8-3.5 years to 4.2-4.6 years at 26 and 35 km, respectively. Due to the difference in annually emitted H_2O of both aircraft, the perturbation lifetime scales differently compared to the mass perturbation.

The (photo-)chemical depletion of H_2O and shift to H_2 concentrations [88, e.g. Fig. 5.23, p. 312] is clearly not limiting the H_2O perturbation lifetime at these emission altitudes. Note that emitted H_2O molecules are depleted (photo-)chemically, but (photo-)chemical H_2O production overcompensates the loss (chapter 4). To summarize briefly, both models show an increase in H_2O perturbation lifetime and H_2O perturbation at the higher altitude, which is even further increased by (photo-)chemical H_2O net-production.

6.1.2. HO_x, NO_x AND OZONE PERTURBATIONS

Hydrogen oxide radicals (H, OH and HO_2) and nitrogen oxides radicals (NO + NO_2) destroy O_3 in catalytic cycles. Hence, a continuous emission of NO_x, H_2 and H_2O of hypersonic aircraft has a significant impact on O_3 chemistry, since they cause HO_x and NO_x perturbations. HO_x mixing ratio perturbations gradually increase with altitude and are largest at the top of the model domain at 80 km (Fig. A.12) for both emission scenarios, whereas the main mass perturbation accumulates between 10-1 hPa (Fig. A.13). Values for both, mixing ratio and concentration changes, are generally larger for the LAPCAT scenario. Figure 6.2 shows the perturbation of NO_x for each model and each aircraft fleet. In general, the perturbation patterns are similar, but EMAC results show a more detailed perturbation pattern. In LMDZ-INCA a general NO_x increase happens, whereas
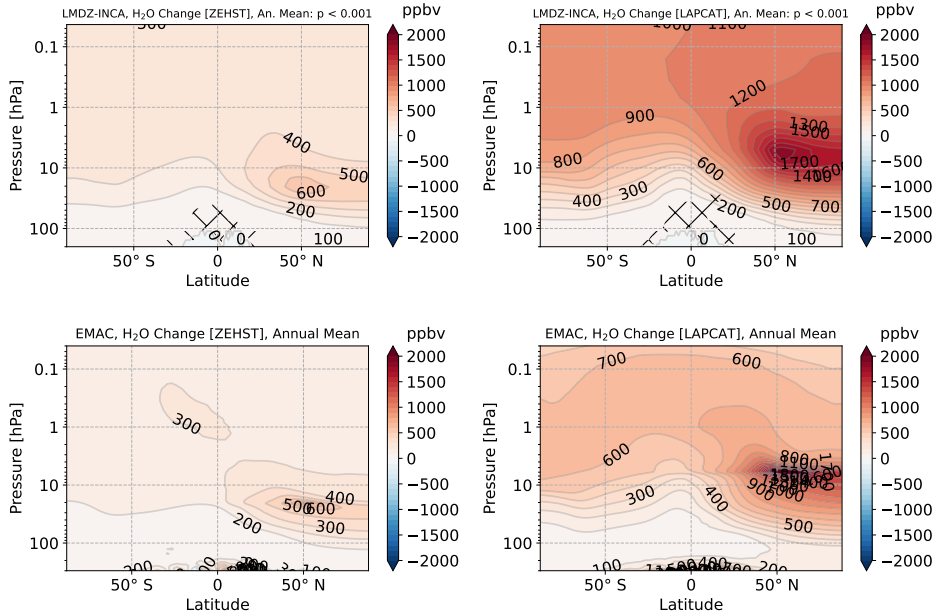
Figure 6.2: Multi-annual mean (2010-2014) of NO_x perturbation (pptv) for the ZEHST scenario (left) and the LAPCAT scenario (right) for both models LMDZ-INCA (top) and EMAC (bottom). Purple lines represent respective cruise altitudes. Hatched areas are characterized by a p-value higher than the threshold indicated in the title of each plot.

in EMAC, additionally, a decrease is visible at approximately 1 hPa upwards ranging from equatorial regions to midlatitude regions for LAPCAT. In comparison, LMDZ-INCA shows one cluster of NO_x perturbation originating from the emission location (purple bar), while EMAC shows 2-3 clusters. The clusters locations seem to overlap, but the larger emission of LAPCAT makes it difficult to distinguish the clusters, as it covers the clusters interspace. The clusters appear at two levels, i.e. at the respective cruise altitudes and at higher altitudes just below 1 hPa. Results for the lower flying aircraft are more often outside of the 5 % uncertainty margin in comparison to the higher flying aircraft. This may be related to the larger emission of the latter, resulting in a larger perturbation which differs from zero perturbation with higher confidence.

As mentioned before, NO_x are very reactive in catalytic cycles of O_3 chemistry. The perturbation of O_3 resulting mainly from H_2O and NO_2 emission is shown in Fig. 6.3. The correlation between the increase of NO_x and the decrease of O_3 is clearly visible in the patterns at mid-stratospheric altitudes and especially at the cruise altitudes. LMDZ-INCA shows a slight increase originating from the tropical UTLS and a decrease with multiple clusters everywhere else, apart from no perturbation at lower latitudes at the highest altitude. EMAC results show a higher vertical resolution pattern with clusters of O_3 increase and decrease, which may be due to the higher vertical resolution of EMAC (90 vertical grid levels) compared to LMDZ-INCA (39 vertical grid levels). The O_3 in-

Figure 6.3: Multi-annual mean (2010-2014) of O_3 perturbation (ppbv) for the ZEHST scenario (left) and the LAPCAT scenario (right) for both models LMDZ-INCA (top) and EMAC (bottom). Purple lines represent respective cruise altitudes. Hatched areas are characterized by a p-value higher than the threshold indicated in the title of each plot.

crease in areas below an O_3 decrease has already been reported by Solomon, Garcia, and Stordal [180], where high-energy radiation reaches lower altitudes due to the decrease of O_3 and in turn increases O_3 at altitudes below the increase. Solomon, Garcia, and Stordal [180] expect a larger effect for lower latitudes due to larger solar radiation there, which agrees with these results. Noteworthy is that the area of O_3 increase overlaps with the area where NO_x perturbations are close to zero. To conclude, the uncertainties due to the annual variability are lower in LMDZ-INCA compared to EMAC for both O_3 and NO_x. The total depletion of O_3 is listed in Table 6.2. In general, results are of the same order of magnitude. Both models show the same trend that the higher flying aircraft fleet has a larger impact on O_3 and for both aircraft the perturbation is larger in LMDZ-INCA results.

Table 6.2: Relative total O_3 mass change for each model and each aircraft fleet.

Scenario	EMAC	LMDZ-INCA
ZEHST	-0.068 %	-0.097 %
LAPCAT	-0.14 %	-0.17 %

Stable Nitrogen Oxide Reservoirs   The family of perturbed NO-compounds is collectively described as NO_y (NO_x + and their nitrogen reservoir species). While NO_x is very reactive in catalytic cycles of O_3 chemistry, NO_y additionally includes more stable molecules, like nitric acid (HNO_3 or HNO_4) that act as a sink and remove NO-compounds from catalytic O_3 cycles. NO_y perturbations are to a large part to combination of NO_x and nitric acid patterns (Fig. A.14) and the perturbation patterns of the latter are shown in Fig. 6.4. The patterns are very similar with an increase in the Northern Hemisphere and a decrease below an increase in the Southern Hemisphere. Overall, the increase dominates and is shifted to higher altitudes for emission at the higher altitude.
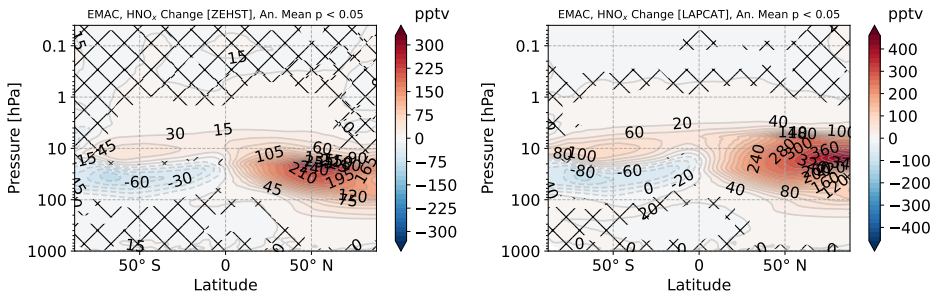
Figure 6.4: Multi-annual mean (2010-2014) of nitric acid (HNO_3 + HNO_4) perturbation (pptv) for the ZEHST scenario (left) and the LAPCAT scenario (right) for EMAC. Hatched areas are characterized by a p-value higher than the threshold indicated in the title of each plot.

6.1.3. Methane Perturbation

Besides H_2O and O_3, CH_4 is another important greenhouse gas and relevant for climate. CH_4 perturbations of EMAC results are shown in Fig. 6.5. Significant decreases appear in the Northern Hemisphere and the troposphere (same plot with mass units, not shown). Significant increases of CH_4 accumulate in the Southern Hemisphere between 100-10 hPa. These patterns oppose perturbation increase and decrease of nitric acid at these altitudes. Overall, the decrease dominates and the total CH_4 change is negative. Atmospheric perturbations at higher altitudes are to a large part statistically not significant. Note that CH_4 originating from the troposphere is nearly fully oxidized at 50 km [154].

A comparison of change in global CH_4 lifetimes is shown in Table 6.3. The CH_4 lifetime change is larger for the LAPCAT compared to the ZEHST scenario for both models and the relative CH_4 lifetime change is less for EMAC compared to LMDZ-INCA for both ZEHST and LAPCAT scenarios by a factor of three and two, respectively.

6.2. Climate Impact

The radiative forcing caused by atmospheric composition changes depends very much on location. For the greenhouse gases O_3, H_2O and CH_4 the sensitivity is largest around
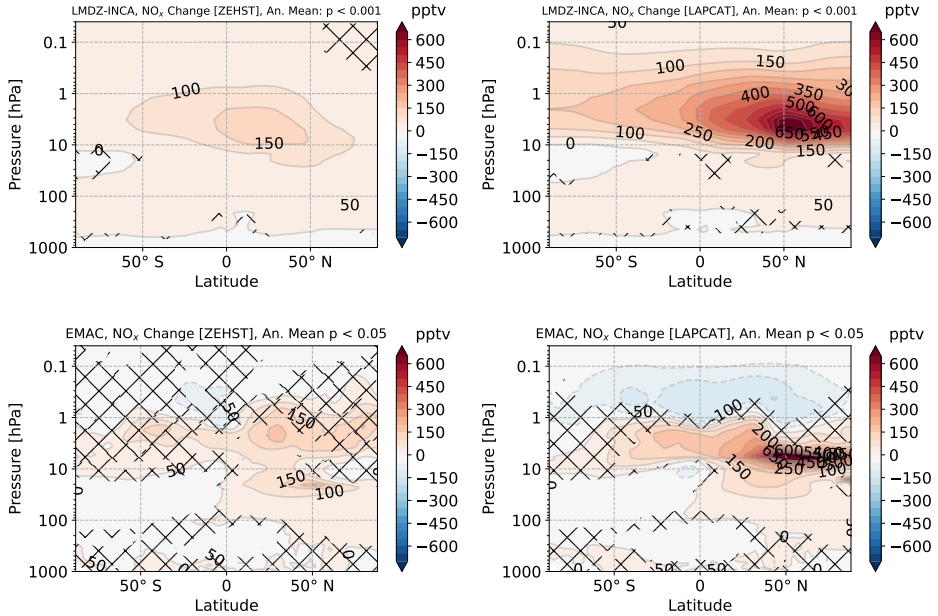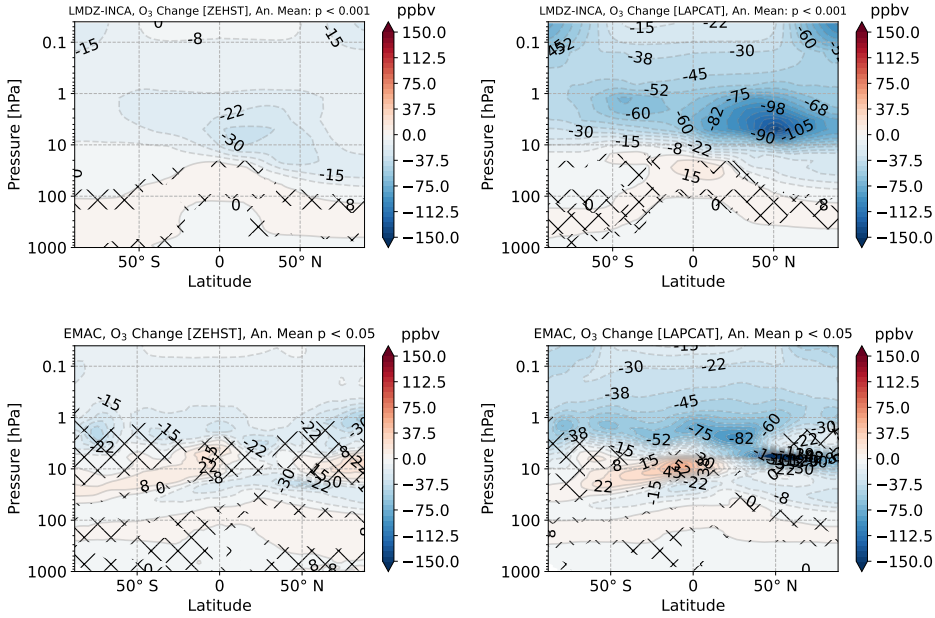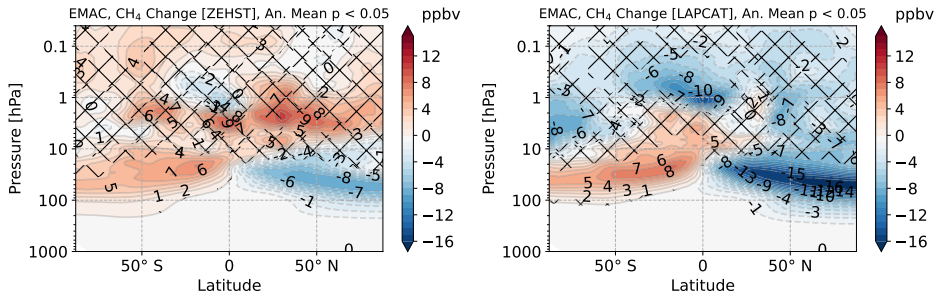
Figure 6.5: Multi-annual mean (2010-2014) of CH_4 perturbation (ppbv) for the ZEHST scenario (left) and the LAPCAT scenario (right) for EMAC. Hatched areas are characterized by a p-value higher than the threshold indicated in the title of each plot.

Table 6.3: Relative change in global CH_4 lifetime for LMDZ-INCA and EMAC and the ZEHST and LAPCAT scenarios.

Scenario	EMAC	LMDZ-INCA
ZEHST	-0.03 %	-0.09 %
LAPCAT	-0.09 %	-0.16 %

the tropopause and at lower latitudes [82, 84]. For hypersonic emissions the largest H_2O concentration change appears at lower stratospheric altitudes, where radiative sensitivity is large, and increases poleward (Fig. A.15). The differences in perturbation patterns between the ZEHST and LAPCAT scenario, except for magnitude, are small. Additionally, there are O_3 increases in the lower tropical stratosphere, where the radiative forcing sensitivity is large as well (Fig. 6.3). Hence, according to Lacis, Wuebbles, and Logan [82] and Riese et al. [84], a strong warming for both O_3 and H_2O changes is to be expected from that area.

6.2.1. INDIVIDUAL CONTRIBUTIONS TO RADIATIVE FORCING

The annual radiative impact was calculated with stratospheric adjusted radiative forcing at tropopause level using the equilibrium perturbation of H_2O, O_3 and CH_4. Atmospheric composition changes were used to calculate the radiative forcing with both models. The spin-up phase was three months and the averaged result is based on twelve monthly means. The results for both models and both aircraft fleets are listed in Table 6.4 with the LAPCAT scenario showing larger values mainly due to the larger H_2O perturbation. The normalized radiative forcing per teragram of H_2O perturbation is in good agreement with an average and standard deviation of 0.43 ± 0.02 mW$(m^2 \cdot Tg)^{-1}$ and 0.39 ± 0.02 mW$(m^2 \cdot Tg)^{-1}$ for EMAC and LMDZ-INCA, respectively. Another measure, the radiative forcing per teragram of annual H_2O emission, shows that the normalized radiative forcing correlates with altitude and the values are 25-41 % larger for LAPCAT in both model results.

The perturbations of H_2O, O_3 and CH_4 above the meteorological tropopause were used to calculate the stratospheric adjusted radiative forcing (approximately 100 hPa at

Table 6.4: Radiative forcing per year in mWm^{-2}, per teragram of H_2O perturbation and per teragram of annual H_2O emission (from Table 3.4), both in mW(m$^2 \cdot$ Tg)$^{-1}$, for each scenario and model calculated with atmospheric composition changes of H_2O, O_3 and CH_4.

Model	EMAC	EMAC	EMAC
Units	mWm^{-2}	mW(m^2 Tg)$^{-1}$	mW(m^2 Tg)$^{-1}$
ZEHST	20.95	0.44	1.52
LAPCAT	40.31	0.41	1.90
Model	LMDZ-INCA	LMDZ-INCA	LMDZ-INCA
Units	mWm^{-2}	mW(m^2 Tg)$^{-1}$	mW(m^2 Tg)$^{-1}$
ZEHST	15.42	0.40	1.12
LAPCAT	33.49	0.37	1.58

tropical and 300 hPa at polar latitudes). In comparison, the contribution to radiative forcing of H_2O is largest, followed by O_3 and a negative radiative forcing due to CH_4 reduction. More explicitly, O_3 changes contribute 8-22 % and H_2O changes contribute 78-92 % to the warming on average. The negative radiative forcing of CH_4 is due to the enhanced CH_4 oxidation and is larger for the LAPCAT scenario where hydroxyl radicals are clearly more active (Fig. 4.4). The detailed values with short- and longwave contributions are listed in Table 6.5.

Table 6.5: Short- and longwave contributions (respectively SW and LW) to radiative forcing (RF) in mWm^{-2}.

Aircraft	Model	Perturb.	SW RF	LW RF	RF
ZEHST	LMDZ-INCA	O_3	3.43	0.35	3.78
	EMAC	O_3	2.38	-0.73	1.65
	LMDZ-INCA	CH_4	-	-	-1.38
	EMAC	CH_4	-	-	-0.015
	LMDZ-INCA	H_2O	-2.27	15.29	13.02
	EMAC	H_2O	-1.59	20.90	19.32
LAPCAT	LMDZ-INCA	O_3	5.72	1.84	7.56
	EMAC	O_3	4.11	-0.78	3.34
	LMDZ-INCA	CH_4	-	-	-2.47
	EMAC	CH_4	-	-	-0.046
	LMDZ-INCA	H_2O	-4.25	32.65	28.40
	EMAC	H_2O	-2.27	39.90	37.01

LMDZ-INCA shows a smaller longwave radiative forcing (LW RF) and a larger negative shortwave radiative forcing (SW RF) for H_2O compared to EMAC. O_3 longwave radiative forcing has a negative sign for EMAC and positive for LMDZ-INCA. The differences in magnitude and sign of O_3 longwave radiative forcing may originate from the varying atmospheric composition changes in EMAC with areas of O_3 increase and decrease. This altitude dependency very much affects the contribution to radiative forcing [82, 83]. O_3 shortwave radiative forcing is generally larger by 40-44 % for LMDZ-INCA compared to EMAC. CH_4 net radiative forcing is 1-2 orders of magnitude smaller for EMAC compared to LMDZ-INCA. The reason for the different magnitude

in CH_4 net radiative forcing is not fully clear and should largely originate from the radiative forcing calculations, since CH_4 perturbations appear in both models and are on the same order of magnitude (Table 6.3). An update of the MESSy RAD submodel is in progress and a revision of CH_4 forcings up to a factor of five is within current estimates [181, preliminary results]. Overall, the contribution of CH_4 to radiative forcing is small in both models compared to H_2O and O_3 and should not affect the the total radiative forcing. The relative difference of EMAC and LMDZ-INCA results in the radiative forcing standard test was 55 %, presented in the chapter on Methods (p. 48). If applied to the values on LMDZ-INCA H_2O radiative forcing this results in 13.02 mWm^{-2} · 1.55 = 20.18 mWm^{-2} and 28.40 mWm^{-2} · 1.55 = 44.02 mWm^{-2}. Compared to EMAC results, which are 19.32 mWm^{-2} and 37.01 mWm^{-2} for ZEHST and LAPCAT, respectively, this agrees very well with ZEHST results and to a lesser extent with LAPCAT results.

6.2.2. IMPLICATIONS OF TROPOSPHERIC WATER VAPOR PERTURBATIONS

Perturbations at tropospheric altitudes were neglected mainly due to the large variability of H_2O, either with a reset to reference H_2O during the perturbation simulations (LMDZ-INCA) or due to exclusion in the radiative forcing calculations (EMAC). Hence, for EMAC the H_2O perturbations at tropospheric altitudes are not zero and therefore would in theory contribute to the radiative forcing calculations. However, the upper tropospheric H_2O perturbations have a very large variability in EMAC results, which is shown by the 5 % confidence intervals for the mean that are ±106 % and ±33 % for the ZEHST and LAPCAT scenarios, respectively. In comparison, for H_2O perturbations above the tropopause, variability is significantly smaller with ±3.1 % and ±1.8 % for the ZEHST and LAPCAT scenarios, respectively. Hence, H_2O perturbation in the upper troposphere could significantly contribute to radiative forcing, but the associated error due to the large variability is significantly larger. Nonetheless, the results from radiative forcing calculations with EMAC including the tropospheric perturbations is shown in Table 6.6 for comparison. The radiative forcing increases by approximately 51 to 63 % when the upper tropospheric perturbations are included. The difference originates from, first, a close to zero short wave cooling (compared to lower single digit shortwave cooling) and for the largest part a larger longwave warming. This is, of course, a large uncertainty factor that could increase the impact of hypersonic aircraft on climate by more than fifty percent.

Table 6.6: Short- and longwave contributions to radiative forcing in mWm^{-2} for EMAC, including upper tropospheric perturbation of H_2O, O_3 and CH_4, and the related error potential of approximately 51 to 63 % due to the integration of tropospheric perturbations.

Aircraft	Perturbation	SW RF	LW RF	RF
ZEHST	H_2O	0.07	31.43	31.50
LAPCAT	H_2O	-0.44	56.18	55.74

6.3. Discussion

6.3.1. Limitations of the Model Simulations

Strengthening of the Brewer-Dobson Circulation

The model simulations are based on atmospheric composition projections for the years 2050-2064 combined with present day meteorology (2000-2014). Hence, projections of the dynamic component are not included in the simulations. The main reason is that reanalysis data from the future are simply not available for nudging. Using another method was not an option, since the method relies on nudging to have the same meteorology in both models for a high signal-to-noise ratio. However, the changes of dynamic processes like the Brewer-Dobson circulation due to climate change are very likely significant and are therefore addressed accordingly [65, 182]. Generally, the transport associated to the Brewer-Dobson circulation is the dominant factor of H_2O perturbation lifetime and therefore of the climate impact of hypersonic aircraft. An increase in strength of the stratospheric and mesospheric circulation would most likely reduce the climate impact of hypersonic aircraft. Butchart et al. [182] estimate the troposphere-stratosphere mean mass exchange rate to increase with 2 % per decade (with considerable differences between the models). That would result in an approximately 8-10 % stronger circulation from 2050-2064 and in turn – if the effect can really be directly translated to perturbation lifetime – the climate impact of hypersonic aircraft would be reduced by approximately the same percentage.

Aerosol and Water Vapor from Volcanic Origin

The model simulations do not include volcanic eruptions. However, volcanic eruptions could occur during the decades of operation of new aircraft. Volcanic emissions, like H_2O or sulphate aerosols, affect the atmospheric composition in the stratosphere, especially through heterogeneous chemistry, and these changes are strongly dependent on latitude and season. The changes of lower stratospheric H_2O changes due to volcanic eruptions is on the order of two years and affect O_3 concentrations [183]. Sulfate aerosols are known to increase temperatures in the tropics and could in turn enhance the Brewer-Dobson circulation, eventually slightly reducing the perturbation lifetime of e.g. H_2O and in turn climate impact of hypersonic transport. Overall, the topic is very complex in itself and how hypersonic emissions and volcanic emissions influence each other remains to be answered with robust and topic specific simulations.

6.3.2. Atmospheric Composition Changes

Here, the focus is on the comparison to the publication by Kinnison et al. [105]. They estimate the O_3, H_2O, NO_x and HO_x perturbations by a fleet of hypersonic aircraft in independent scenarios where aircraft, powered with conventional fuel, fly at 30 km and 40 km, using the coupled chemistry-climate model WACCM (Whole Atmosphere Community Climate Model). Similar to LMDZ-INCA and EMAC model setups, WACCM simulates atmospheric chemistry and dynamics. For more details on the model setup, please refer to their publication. Similar to the LMDZ-INCA and EMAC setup they look at atmospheric conditions for the year 2050, however, the averaged annual results are based on one year, while LMDZ-INCA and EMAC results represent the mean over five years. In turn, a larger deviation from the long-term mean could be expected for their results. The

total annual emission in their setup amounts to 58.3 Tg of H_2O and 0.94 Tg of NO_2, which is approximately three to four times larger for the former, and 30 to 47 times larger for the latter, compared to the annual values of the two aircraft designs ZEHST and LAPCAT (Table 3.4). Similarly, they use globally distributed emissions along flight paths, where the largest emissions appear between the United States and Europe (similar to the setup in this thesis) and the United States and South-East Asia (in contrast to the setup in this thesis). They did report sensitivities, i.e. perturbations in $Tg yr^{-1}$, for O_3 only and not H_2O.

In agreement with results presented here, the H_2O perturbation for the higher fly-ing aircraft fleet is significantly larger and the perturbation patterns agree very well with the maximum perturbation being at midlatitudes at the Northern Hemisphere and at the cruise altitude. In their case the total emission per trace gas is the same for both altitudes, which is not the case in the LMDZ-INCA and EMAC model setup, since the emissions in HIKARI are based on two different aircraft designs. Total values of mass perturbation were not published for H_2O and thus cannot be compared with the results presented here. The agreement of latitudinal and altitude features of Fig. 4.3 with Kin-nison et al. [105, Fig. 3] is very good in general. There are differences in magnitude from 50 km upward, increasing with altitude where photolysis is dominant. If this originates from WACCM covering more of the atmosphere compared to LMDZ-INCA and EMAC model, and thus being more accurate at 50 km upwards, is an open question. How-ever, the stratosphere is well represented in the models LMDZ-INCA and EMAC, which is most important for the topic of this study, and the equilibrium mass perturbation at mesospheric altitudes is insignificant in comparison to stratospheric altitudes.
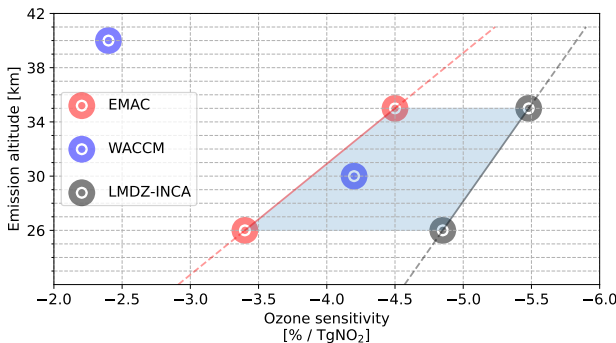
Figure 6.6: O_3 sensitivity from three different models WACCM, EMAC and LMDZ-INCA dependent on altitude. Results from this work were calculated using values from Table 3.4 and Table 6.2. Results for WACCM were published by Kinnison et al. [105, Table 2]. The shaded area highlights the good agreement of LMDZ-INCA and EMAC results with WACCM results for the region from approximately 26-35 km altitude.

Ozone Sensitivity   The calculated relative O_3 mass sensitivity with -4.2 % / Tg NO_2 and -2.4 % / Tg NO_2 for 30 km and 40 km altitude from Kinnison et al. [105, Table 2] is of the same order of magnitude compared to LMDZ-INCA results with -3.4 % / Tg NO_2 to -4.5 % / Tg NO_2 and EMAC results with -4.9 % / Tg NO_2 to -5.5 % / Tg NO_2 at 26 km and

35 km altitude, respectively. Figure 6.6 shows both results from this study and their study. LMDZ-INCA and EMAC results have a positive correlation between O_3 sensitivity and altitude. This might point to a maximum of absolute O_3 sensitivity at around 35 km altitude, since the absolute value for WACCM at 40 km altitude is already much smaller and the models seem to agree very well for the region between 26 and 35 km. The assumed tropical maximum of O_3 mixing ratio of 31 km overlaps with this region and is very close to the maximum value. However, the altitude of emission often does differ from perturbation maxima of NO_x and O_3. Be aware that only two data points per model are presented and to come to conclusions regarding the largest value of O_3 sensitivity might be inaccurate. Additionally, there are some differences between the setups, e.g. Kinnison et al. [105] estimate O_3 sensitivity based on NO_x perturbations only and with a larger amount, while LMDZ-INCA and EMAC results include the combined effects by NO_x, H_2O and H_2 emission. Furthermore, the HIKARI data include a vertical distribution of emission, in which take off and landing are present, and the fleet comprises not only hypersonic but subsonic aircraft as well, while they inject the emission in a single layer. The effect of tropospheric H_2O emission on stratospheric H_2O is negligible due to the tropical tropopause coldpoint, but NO_x emitted in the tropical troposphere may be transported to stratospheric altitudes and increase the uncertainty of the comparison.

6
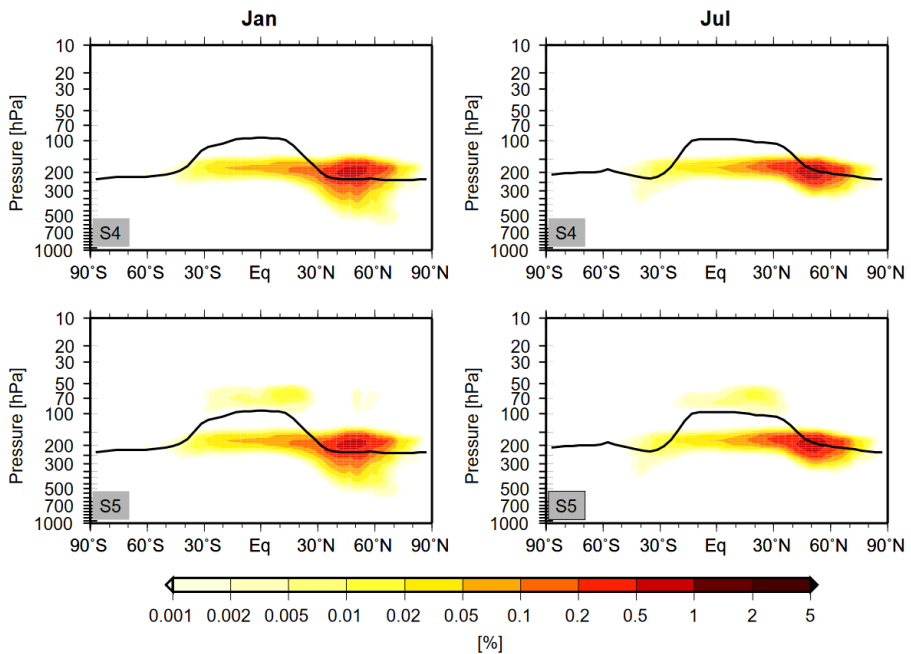
Figure 6.7: Zonally averaged contrail cover [%] for the subsonic fleet S4 and the mixed fleet S5 [S5 combines subsonic and supersonic aircraft] as simulated by ECHAM4 for January (left) and July (right), respectively. The bold line indicates a zonal mean tropopause as simulated by ECHAM4 for each respective month. The Figure and caption originate from Stenke, Grewe, and Pechtl [184, Fig. 4] and further information on the respective scenarios S4 and S5 can be found there.

Contrail Formation   Another type of atmospheric composition change that affects climate is the formation of contrails. A study from Stenke, Grewe, and Pechtl [184] estimates the change in contrail formation and the change of contrail radiative forcing for subsonic and supersonic aircraft, by replacing parts of the subsonic fleet with supersonic aircraft. They show the change in contrail radiative forcing and change in total contrail cover is very small because they report a shift of contrail cover from mid latitudes (200 hPa) to low latitudes at supersonic cruise altitude (Fig. 6.7). For hypersonic aircraft this relation might be changed. Hypersonic aircraft are flying above the tropical tropopause, where temperatures are warmer, and hence do not form contrails in the tropics. Therefore, the replacement of subsonic with hypersonic aircraft would probably lead to a reduction of contrail radiative forcing.

6.3.3. COMPARISON TO EMISSIONS AT LOWER ALTITUDES

An altitude dependent comparison of O_3 and H_2O radiative forcing normalized to fuel use was published by Zhang et al. [185, Fig. 6.8]. To compare their results on stratospheric adjusted radiative forcing to results in this thesis an extrapolation to higher altitudes is applied. As a first step of calculations their emission index ($EI(H_2O) = 1.237\,g(H_2O)/kg\,fuel$) and fuel use (47.18 Tg) were used to transform radiative forcing per teragram fuel burn as shown in Fig. 6.8 to radiative forcing per emitted H_2O in teragram. As a second step, the linear relation of radiative forcing per emitted H_2O per year to an increase in altitude of 2 km was calculated resulting in $0.1\,\mathrm{mWm^{-2}Tg^{-1}}$ yr/2 km. The final step, the linear extrapolation of the largest radiative forcing values to ZEHST and LAPCAT cruise altitudes brought the results $0.93\,\mathrm{mWm^{-2}Tg^{-1}}$ and $1.56\,\mathrm{mWm^{-2}Tg^{-1}}$ for ZEHST and LAPCAT, respectively. Compared to EMAC results (1.1-$1.5\,\mathrm{mWm^{-2}Tg^{-1}}$ and 1.6-$1.9\,\mathrm{mWm^{-2}Tg^{-1}}$ for ZEHST and LAPCAT, respectively), presented in Table 6.4, the calculated values from Zhang et al are generally lower than the EMAC results and very close to LMDZ-INCA results. Clearly, a linear relation extends well to higher altitudes (even for more than 10 km), showing the same trend and order of magnitude.

6.3.4. COMPARISON TO THE CLIMATE IMPACT OF OTHER AIRCRAFT DESIGNS

Sub-, super- and hypersonic aircraft are compared in Fig. 6.9. It shows an enhancement factor, i.e. the ratio of the climate impact of a specific aircraft compared to a conventional subsonic aircraft and hence without unit, depending on altitude. The numbers shown there were calculated using the climate response model AirClim [186, 187]. The subsonic estimate is based on contrail formation, CO_2, H_2O and NO_x (short-lived O_3, primary mode O_3, CH_4) effects. The comparison is based on results from multiple studies [188–190]. While subsonic is the reference case with a value of 1, supersonic aircraft show a climate impact that is increasing with altitude. The hypersonic aircraft ZEHST follows that trend with an enhancement factor of approximately 20 (near-surface temperature change or radiative forcing normalized to revenue passenger kilometers). However, the enhancement factor of the second hypersonic aircraft LAPCAT (PREPHA) is less than 10 due to its higher passenger capacity. Hence, a larger aircraft size, i.e. larger passenger number, is clearly a promising design option to reduce the climate impact per
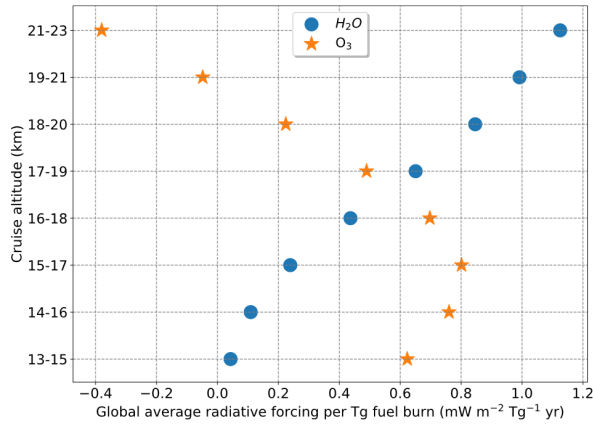
Figure 6.8: Annual and global average change in the stratospheric-adjusted radiative forcing per Tg of fuel burn $(mWm^{-2}Tg^{-1}yr)$ as a function of cruise altitudes for the changes in H_2O and O_3. The total cruise fuel burn is $47.18\ Tgyr^{-1}$ in this study. The Figure and caption originate from Zhang et al. [185, Fig. 11].

passenger and can compensate the climate impact due to higher cruise altitudes. The error estimate (blue shaded area) includes the tropospheric region with its very large variability (see p. 96). Blue squares represent an aircraft of type STRATOFLY MR3, developed in the STRATOFLY project, for four different altitudes and based on a single trajectory where the emitted trace gases are kept constant [130, 131]. There, the increasing climate impact with altitude is clearly visible. Calculations are based on atmospheric sensitivities from chapter 7 and the method is described in detail in chapter 8.

6.3.5. CLIMATE IMPACT OF HYPERSONIC AIRCRAFT

Estimates on the climate impact of hypersonic aircraft barely exist. A recent estimate was published by Ingenito [138]. The author approximates the climate impact by a fleet of hypersonic aircraft (type LAPCAT II MR2.4, 2015) based on H_2O perturbation only. In the study a fleet of 200 hypersonic aircraft fly from Brussels to Sydney 365 days a year and emit 376 Tg of H_2O, which results in a H_2O perturbation that increases surface temperature by 100 mK. The estimate is based on a correlation of an increase in global atmospheric H_2O and near-surface temperature from a third publication and the whole calculation can be described as a 1D box model. For comparison to Fig. 6.9, the change in surface temperature is normalized with passenger kilometers (pax-km). Therefore, a distance of 16,367 km between Brussels and Sydney and a passenger capacity of 300 (LAPCAT II) are assumed to obtain a normalized near-surface temperature change of $396\ 10^{-12}\ mK\ (pax\text{-}km)^{-1}$. This equals an enhancement factor of 61 and hence their estimate of the climate impact of hypersonic aircraft is 61 as much as subsonic aircraft. Compared to the enhancement factors in Fig. 6.9, this value is outside of the uncertainty range presented in Fig. 6.9. The upper limit of the uncertainty range is equal to radiative forcing calculations with composition changes including upper tropospheric H_2O. These were neglected in the main calculations due to the large variability and the focus

on stratospheric perturbation of trace gases.
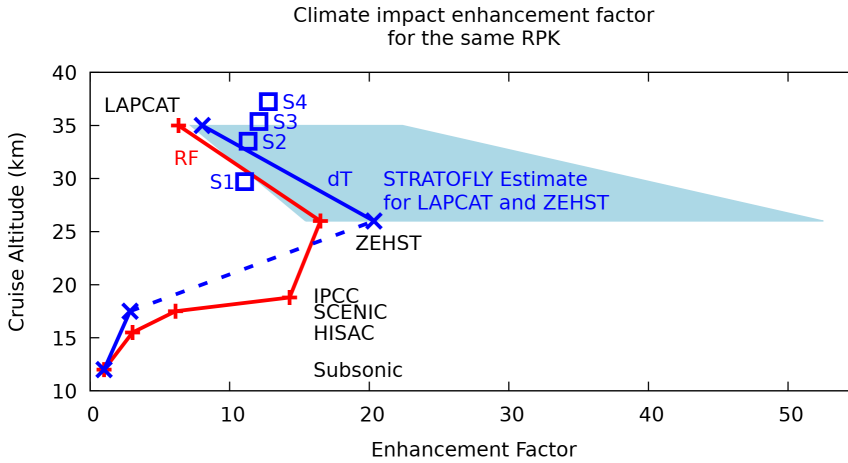
Figure 6.9: Radiative forcing (red) 50 years after entry into service (EIS) of a fleet of the respective aircraft and the near-surface temperature change (blue) based on the HIKARI project results. RPK (unit pax-km) refers to the revenue passenger kilometers, i.e. total kilometers travelled by all passengers on an aircraft or on a fleet of aircraft. The shaded area shows an uncertainty range from this work. This figure is from Grewe [190] and includes the values of four STRATOFLY MR3 versions for different altitudes (S1 to S4) based on data published by Viola et al. [131, Table 2].

6.4. SUMMARY

This chapter presents the radiative forcing and the climate impact of two different hypersonic aircraft designs, both fueled with liquid hydrogen. The difference in cruise altitude (26 km and 35 km) results in significant differences in atmospheric perturbations, perturbation lifetime and in turn climate impact. Clearly, H_2O is the largest contributor for the latter. An efficient (photo-)chemical destruction of H_2O is active at higher altitudes, as expected based on theory [88, Fig. 5.23, p. 312]. But a smaller H_2O perturbation at the higher emission altitude was not visible in LMDZ-INCA and EMAC results. In contrast, the higher altitude of emission comes with a larger perturbation of water vapor. The underlying (photo-)chemical mechanism was already explained in detail in chapter 4. For O_3, an overall depletion of the O_3 layer takes place, with a decrease at middle-to-upper stratospheric altitudes and an increase at lower stratospheric altitudes. Aircraft emissions cause an overall methane depletion and reduction of methane lifetime, which is larger for the higher flying aircraft. While results are very similar for H_2O and O_3 radiative forcing between the EMAC and LMDZ-INCA model, there are larger differences for CH_4, with a comparably small effect on the total radiative forcing. Overall, H_2O, O_3 and CH_4 perturbations result in a total positive radiative forcing, i.e. warming, for both aircraft, with a larger effect for the higher flying aircraft. The increase of total radiative forcing with altitude was further shown for the STRATOFLY MR3 aircraft as an example. For the ZEHST and LAPCAT aircraft H_2O radiative forcing is significantly

larger than O_3 radiative forcing, which has a more complex altitude dependency. This is clearly shown by the increase of H_2O perturbation lifetime and normalized radiative forcing with altitude. Due to larger fuel consumption with higher speed at high cruise altitudes on the one hand, and the atmospheric conditions at these cruise altitudes ((photo-)chemical net-production and perturbation lifetime of H_2O) on the other hand, hypersonic aircraft have a considerable larger climate impact than subsonic and supersonic aircraft. To conclude briefly, the impact on climate of aircraft emitting H_2O and flying above the tropopause increases very much with altitude.

6

7

SENSITIVITIES OF ATMOSPHERIC COMPOSITION AND CLIMATE TO ALTITUDE AND LATITUDE OF HYPERSONIC AIRCRAFT EMISSIONS

In the previous chapter the impacts of two specific aircraft designs were evaluated. This chapter presents general atmospheric and radiative sensitivities to emissions at specific latitude and altitude regions. These sensitivities serve, first, to assess the importance of atmospheric processes like the Brewer-Dobson circulation or polar stratospheric clouds, and, second, allow to estimate the climate impact of other hypersonic aircraft designs at much lower cost and time than before for all latitude regions and altitudes between 30-38 km. This is important because the evaluation of aircraft designs might easily change for technologically different aircraft designs, which for example emit trace gases in another ratio or cruise at different altitude and latitude regions. To obtain the relevant results, sensitivities of atmospheric composition and climate to emissions, equivalent to a fleet of hypersonic aircraft, were calculated. Section 7.1 discusses direct and indirect effects of emitted trace gases water vapor, nitrogen oxides and hydrogen on atmospheric water vapor, nitrogen oxides, ozone and methane and in addition the importance of polar stratospheric cloud chemistry for water vapor and nitrogen oxide concentrations. Section 7.2 addresses the stratospheric-adjusted radiative forcing resulting from atmospheric composition changes and section 7.3 accounts for the complex relation of atmospheric and radiative sensitivities. The chapter ends with a general discussion and a summary. Note that the main results of atmospheric and radiative sensitivities are condensed in two look-up tables.

7.1. Atmospheric Composition Changes

THIS section contains, first, as an overview of simulation results, i.e. the impact on the two most important climate active gases in the context of hypersonic aircraft exhaust, O_3 and H_2O, and, second, direct and indirect effects on atmospheric composition by the emission of H_2O, NO_x and H_2. Third, CH_4 lifetimes and H_2O perturbation lifetimes are addressed. Note that all presented data for each of the 24 simulations in this section is based on a multi-annual mean for the years 2013-2016.
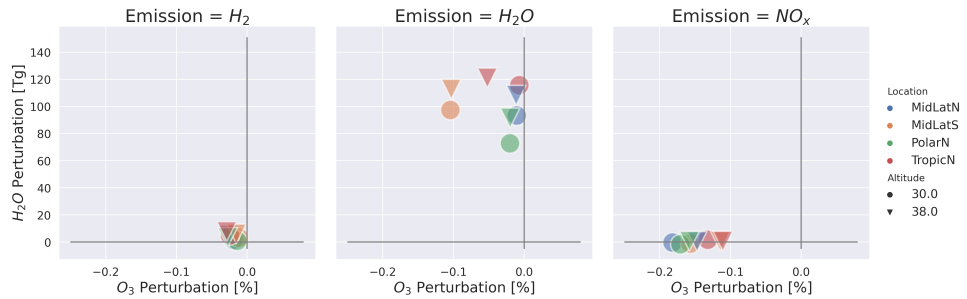
Figure 7.1: Overview of H_2O and O_3 changes for all 24 simulations grouped by initial emission of H_2, H_2O and NO_x (left, middle, right). Colors refer to the latitude region of emission (southern mid-latitudes, northern tropical latitudes, northern mid-latitudes, north polar latitudes) and markers to altitudes of emission. Please refer to Table 7.2 for statistical significance.

Fig. 7.1 shows the H_2O mass perturbation and relative O_3 changes above the meteorological tropopause (WMO) grouped by emitted species. Hydrogen (H_2) emission has a comparably small effect on both, H_2O and O_3. Relative O_3 depletion ranges from 0.01 % to 0.03 % for H_2 emission scenarios. The effect is larger for the higher altitude scenarios. H_2O changes are not larger than 8 Tg, with maximum values for the northern tropic emission scenario at 38 km. H_2O emission has a large effect on H_2O mass perturbation in all scenarios with a range of 73-121 Tg. Values for higher altitude and lower latitude scenarios are particularly large. Relative O_3 change is rather small, except in the southern mid-latitudes where O_3 depletion is approximately 0.1% for both altitudes. NO_x emission has the lowest effect on H_2O mass perturbation. The range of H_2O changes is -1.6 to 1.7 Tg and all higher altitude emission scenarios show an increase with medium values. In contrast, the lower altitude emission scenarios show larger values, but differ in H_2O increase and decrease. Relative O_3 depletion due to NO_x emission is larger than most other emission scenarios with a range of 0.11 to 0.18 %. Largest values appear at northern mid-latitudes and polar regions at 30 km.

The following subsections are further divided in 'Direct Effects' and 'Indirect Effects'. The former relates to the emission and its effect on the same molecular atmospheric compound, e.g. H_2O emission on H_2O trace gas concentrations. The latter includes indirect effects on other atmospheric compounds like CH_4 or O_3. The shaded box in each subfigure represents the altitude of emission. Hatched areas represent regions, where perturbations do not differ from zero with a probability larger than a certain value (Table. 3.2).

Figure 7.2: Zonal mean of H_2O perturbation (volume mixing ratio, ppmv) for scenarios where H_2O is emitted. The first and second row refer to 38 km and 30 km altitudes of emission, respectively. Columns represent the latitude region of emission. The emission regions are shaded in gray. Lines indicate statistically insignificant results and the probability level is written in the title of each subplot.
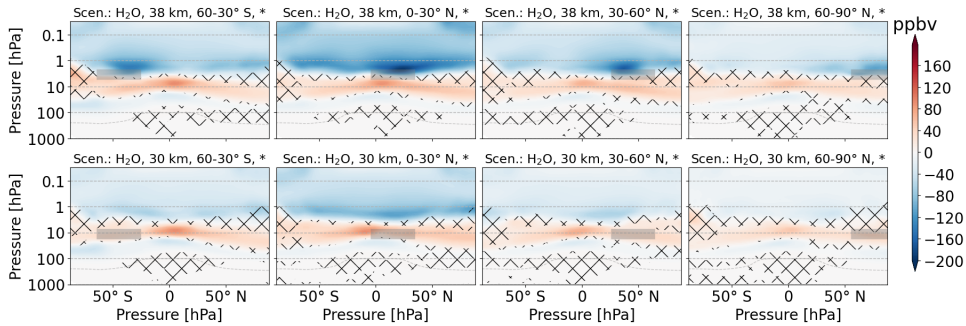
Figure 7.3: Zonal mean of O_3 perturbation (volume mixing ratio, ppbv) for scenarios where H_2O is emitted. The first and second row refer to 38 km and 30 km altitudes of emission, respectively. Columns represent the latitude region of emission. The emission regions are shaded in gray. Lines indicate statistically insignificant results and the probability level is written in the title of each subplot.

7.1.1. Water Vapor Emission

Direct Effects

Figure 7.2 shows the H_2O perturbation in parts per million volume for the H_2O emission scenarios. When comparing the altitudes 38 km and 30 km, which are the first and second line, respectively, the H_2O mixing ratios are generally higher for the former. H_2O emissions at low latitudes are distributed across both hemispheres. H_2O emissions at higher altitudes are to a significantly larger extent confined to one hemisphere. The threshold for failing the t-test is exceeded at and below the tropopause region.

Indirect Effects

Ozone In total, the H_2O emission causes O_3 depletion, especially for emission at southern latitudes (Fig. 7.1). In Fig. 7.3 the O_3 perturbation (volume mixing ratio) is divided into layers of O_3 decrease (above 3 hPa and below 10 hPa) and O_3 increase (3-10 hPa) in all subfigures. For emission at 38 km, the upper layer of O_3 decrease seems

to be strengthened. For emission at 30 km, the layer of O_3 increase overlaps with the emission region and seems to be weakened, especially for H_2O emission from 0-30° N. The threshold for failing the t-test has in general a large variation and appears at the interface of O_3 increase and O_3 decrease regions, the tropopause and polar regions. The largest values of O_3 increase is situated in the tropics for all scenarios. In contrast, the largest values of O_3 decrease move with the emission location.

Hydrogen The H_2O emission has a significant effect on H_2 (Fig. A.19) at the top of the modelled atmosphere (around 80 km). In general, the H_2 perturbation patterns are very similar with a broad layer at high latitudes and smaller width at mid to low latitudes. The magnitude, however, is larger for emission scenarios with low latitudes and the higher emission altitude (38 km).
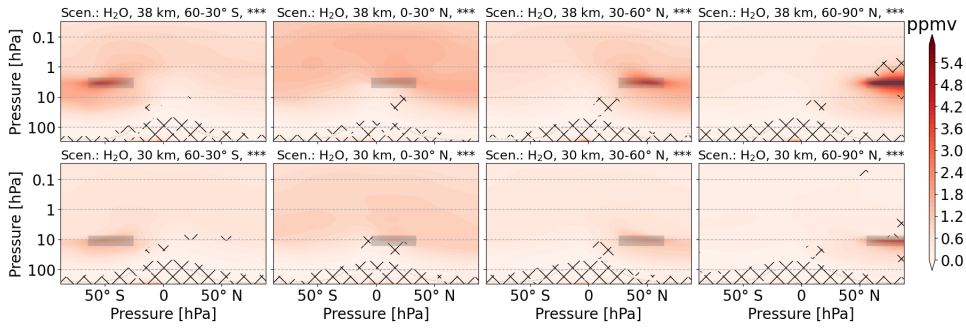

Figure 7.4: Zonal mean of CH_4 perturbation (volume mixing ratio, ppbv) for scenarios where H_2O is emitted. The first and second row refer to 38 km and 30 km altitudes of emission, respectively. Columns represent the latitude region of emission. The emission regions are shaded in gray. Lines indicate statistically insignificant results and the probability level is written in the title of each subplot.

Methane The impact of H_2O emission on CH_4 shows complex patterns, with areas of increase and decrease, and the multi-annual variability is clearly large, since the t-test restricts confidence in many areas (Fig. 7.4). It is common knowledge that OH oxidizes CH_4 and adds to H_2O concentrations in the stratosphere. Additionally, it was shown that emission of H_2O eventually increase CH_4 oxidation [33]. Overall, H_2O emissions reduce CH_4 concentrations the most compared to emissions of NO_x and H_2 (that changes when normalized to the number of emitted molecules). The features for emission at southern mid-latitudes are very similar with a decrease from 100-10 hPa and an additional decrease around the emission location of the higher altitude scenario. H_2O emission at northern tropics causes a wide-spread CH_4 depletion with a larger impact for the higher altitude emission. A CH_4 increase is visible in the tropics at 10 hPa for 30 km emission. For 38 km, the area with CH_4 increase, where p≤0.05, is barely visible. Northern mid-latitude emission of H_2O shows features similar to southern mid-latitude emission, but the decrease is at slightly higher altitudes. Areas of increase and decrease seem to have switched location. This statement should be taken with caution, since not all areas, included in the comparison, fulfil the t-test criteria, i.e. the error probability that means

are not different is larger than 5 %. North polar emission scenarios are very similar to the north mid-latitude emission scenarios. However, volume mixing ratios are generally smaller.

7.1.2. Nitrogen Oxide Emission and Ozone Perturbation

Direct Effects

The emitted NO_x is, compared to H_2O, more confined to the emission region. First, the NO_x perturbation maxima is clearly located at the altitude and latitude of emission; other maxima are not visible. Second, the multi-annual mean of emission scenarios and the reference scenario are different for most areas in direct proximity to the emission location (hatched area). NO_x changes are more distributed for low latitude emission scenarios. The vertical distribution shows downward transport for high latitudes and upward transport for low latitudes, depending on latitude of emission. A correlation plot of significant NO_x and O_3 changes (Fig. A.24) shows a near linear correlation for altitudes from the surface to 4 hPa with a tendency to saturation for larger NO_x perturbations in the lower altitude emission scenarios. For altitudes from 4 hPa to 0.01 hPa the correlation is curvilinear and the NO_x emission scenarios show a larger range of values, compared to the lower altitude range. Here, the sensitivity is very large to the altitude and latitude of emission.
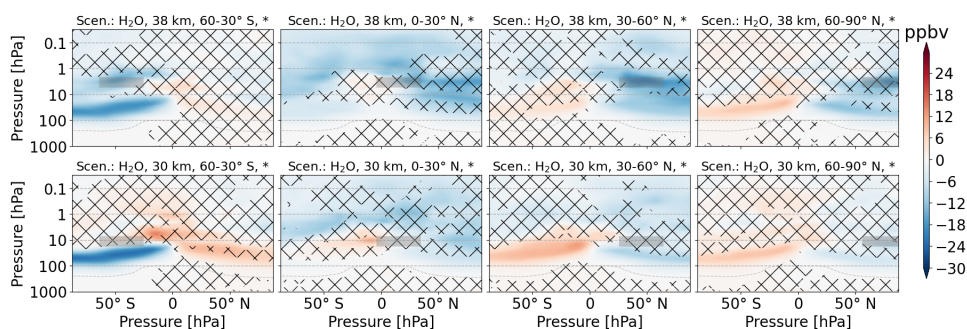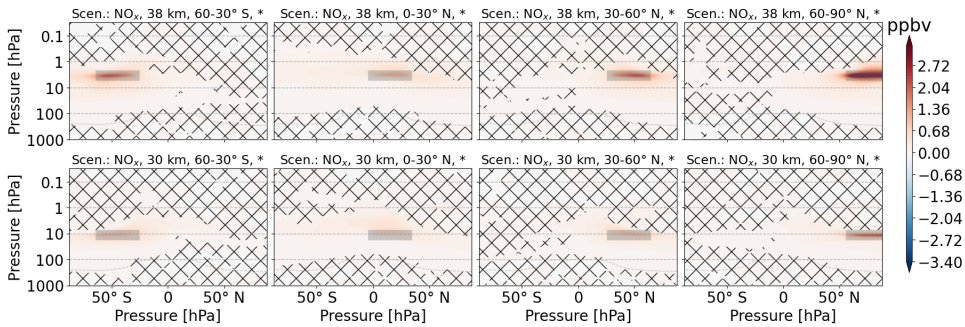

Figure 7.5: Zonal mean of NO_x perturbation (volume mixing ratio, ppbv) for scenarios where NO_x is emitted. The first and second row refer to 38 km and 30 km altitudes of emission, respectively. Columns represent the latitude region of emission. The emission regions are shaded in gray. Lines indicate statistically insignificant results and the probability level is written in the title of each subplot.

Since the correlation of O_3 and NO_x perturbation is well known, the O_3 perturbation is included as a 'direct' effect. When comparing Fig. 7.5 and Fig. 7.6 the similarity is clearly visible. Areas of NO_x increase overlap with areas of O_3 decrease. Additionally, there see areas of O_3 increase below areas of O_3 decrease at southern mid-latitude and northern tropic emission scenarios. For northern mid-latitude scenarios, these are barely visible in the tropics and for north polar emission scenarios they are not visible.

Indirect Effects

Overall, indirect effects of NO_x emission on H_2O, H_2 and CH_4 are basically insignificant for most areas. For some scenarios, significant areas appear for tropospheric and
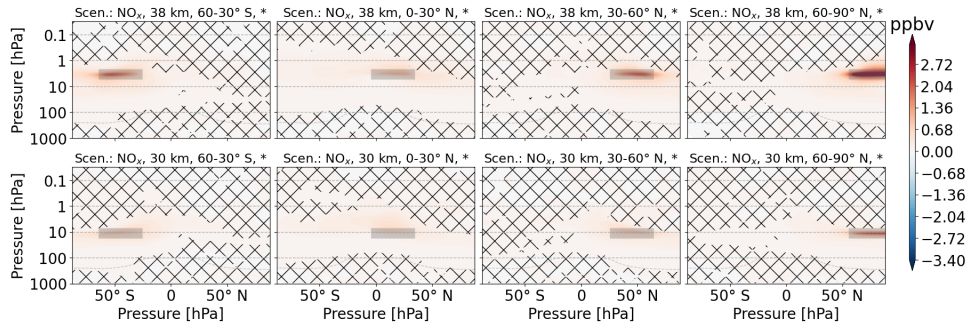
Figure 7.6: Zonal mean of O_3 perturbation (volume mixing ratio, ppbv) for scenarios where NO_x is emitted. The first and second row refer to 38 km and 30 km altitudes of emission, respectively. Columns represent the latitude region of emission. The emission regions are shaded in gray. Lines indicate statistically insignificant results and the probability level is written in the title of each subplot.

lower stratospheric altitudes, largely depending on which Hemisphere NO_x was emitted (Fig. A.25, Fig. A.26, Fig. A.27).

7.1.3. HYDROGEN EMISSION

DIRECT EFFECTS

The increase in atmospheric concentrations of H_2 by H_2 emission peaks at the emission location (Fig. 7.7). The perturbation pattern looks very similar to H_2O perturbation from H_2O emission and is therefore most probably dominated by transport, i.e. the Brewer-Dobson circulation, instead of (photo-)chemistry.
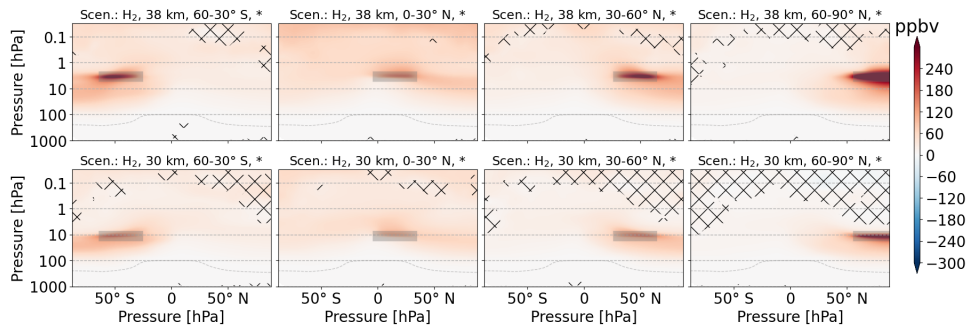
Figure 7.7: Zonal mean of H_2 perturbation (volume mixing ratio, ppbv) for scenarios where H_2 is emitted. The first and second row refer to 38 km and 30 km altitudes of emission, respectively. Columns represent the latitude region of emission. The emission regions are shaded in gray. Lines indicate statistically insignificant results and the probability level is written in the title of each subplot.

INDIRECT EFFECTS

The EMAC results show that H_2 emissions at 38 km generally and for the tropics at 30 km statistically significant reduce the O_3 abundance in the upper stratosphere (0.1-1 hPa).

It is known that above 40 km the HO_x cycle starts to dominate the O_3 depletion instead of the NO_x cycle [14, 192].

Maximum values of H_2O perturbation are approximately 5 % of the H_2O perturbation of the direct H_2O emission scenarios. Apart from the magnitude, the features are very similar, which again suggests that transport dominates these perturbations (Fig. A.29). Largest perturbations appear for the higher altitude scenarios and the low latitude scenarios. A correlation plot shows that statistically significant H_2O changes due to H_2 emission show different orders of magnitude depending on Hemisphere with larger gradients appearing rather in the Southern Hemisphere. Clearly, high latitude and low altitude emission scenarios show smaller H_2O changes and again suggests a dominant role of transport for the perturbation lifetime. CH_4 perturbation patterns are mostly not statistically significant (Fig. A.30).

7.1.4. LIFETIMES AND RELATIVE CHANGES

METHANE AND METHANE LIFETIME

Table 7.1: Multi-annual mean of CH_4, HO_2 and OH relative change averaged over latitude and altitude emission scenarios. Values are divided by troposphere (WMO) and middle atmosphere (troposphere-80 km). The last three columns shows the relative change per teramol of emitted trace gas.

Emission	Sphere	ΔCH4 [%]	ΔHO2 [%]	ΔOH [%]	ΔCH4/Tmol [%]	ΔHO2/Tmol [%]	ΔOH/Tmol [%]
H_2O	Troposphere	-0,0014	-1,12	-0,15	-0,001	-0,9	-0,1
H_2O	Middle Atmosphere	-0,0851	4,31	5,31	-0,072	3,7	4,5
NOx	Troposphere	-0,0015	0,05	0,07	-2,218	71,0	107,2
NOx	Middle Atmosphere	-0,0057	-0,44	0,09	-8,456	-655,1	126,6
H_2	Troposphere	-0,0002	0,02	-0,02	-0,002	0,1	-0,2
H_2	Middle Atmosphere	-0,0140	0,39	0,47	-0,120	3,3	4,0

It was shown already in the previous chapter that hypersonic emission do affect methane (CH_4) concentrations significantly. Here, the zonal mean perturbation patterns of emission scenarios are very much alike with a decrease in the Hemisphere of emission and an increase of CH_4 in the other Hemisphere (not shown). Overall, all three types of emission cause CH_4 depletion with varying magnitude. CH_4 lifetime in the atmosphere strongly depends on oxidation via hydroxyl (OH) and emitted trace gases perturb these and related trace gas concentrations like hydroperoxyl (HO_2). Note that HO_2 and OH are connected to water vapor, hydrogen and nitrogen oxide via multiple reactions (Fig. 2.9). One example is the oxidation of nitrogen monoxide to nitrogen dioxide transforming a HO_2 to OH.

$$NO + HO_2 \longrightarrow NO_2 + OH \qquad (R79)$$

Table 7.1 shows the relative change in CH_4, HO_2 and OH for the troposphere and the middle atmosphere. Clearly, CH_4 perturbations are largest in the middle atmosphere for all emission scenarios. At first it seems like water vapor emission scenarios have the largest impact. That, however, depends mostly on aircraft design and nitrogen oxides are the most potent if normalized to one teramol of emitted trace gas, followed by hydrogen

and water vapor. The latter two emissions share same order of magnitude with each other.

The following equation was used to calculate both, the tropospheric and whole domain CH_4 lifetime τ_{CH4}.

$$\tau_{CH_4}(t) = \frac{\sum\limits_{b \in B} M_{CH_4}^b(t)}{\sum\limits_{b \in B} k_{CH_4}^b(t) \cdot [OH]^b(t) \cdot M_{CH_4}^b(t)} \tag{7.1}$$

$M_{CH_4}^b$ is the CH_4 mass, $[OH]^b$ the concentration and $k_{CH_4}^b$ the reaction rate of $CH_4 + OH$ in grid box b. B is the set of all grid boxes.

Tropospheric and whole-model-domain CH_4 lifetime of all emission scenarios presented in this chapter is 8.39 and 9.54 years on average, respectively. Tropospheric CH_4 lifetimes show a range of values for other unrelated EMAC model setups [108, Fig. 18]. The average value over all setups is 8.0±0.6 for the years 2000-2004, which, according to the authors, is on the lower end of a set of values from other publications.
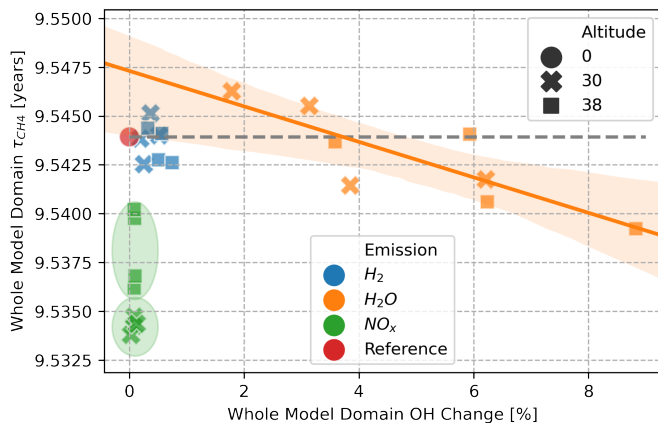
Figure 7.8: Methane lifetime (whole-model-domain) is shown in (a) and the water vapor mass perturbation (b) in relation to the relative hydroxyl radical mass change (whole-model-domain) for all emission scenarios (legend). Whole-model-domain methane lifetime is reduced or extended below or above the dashed gray line, respectively. The regression lines including the shaded areas depict the mean and standard deviation of scenarios.

Fig. 7.8 shows the CH_4 lifetime (a) and H_2O mass perturbation (b) in relation to the relative hydroxyl radical mass change. CH_4 lifetime changes of H_2 emission scenarios are quite close to the reference scenario and a clear trend is not visible. H_2O emission scenarios show a clear correlation between OH increase and CH_4 lifetime decrease, with an increase or only small change at higher northern latitude and lower altitude scenarios and a decrease of CH_4 lifetime for southern and tropical latitude scenarios (Table 7.2). An average over all emission scenarios per emission type shows an increase of relative hydroxyl and hydroperoxyl mass mostly in the middle atmosphere (Fig. A.2). This explains the decreasing global CH_4 lifetime for H_2O with a more efficient CH_4 oxidation

due to an increase in OH (Fig. 7.8, b).

NO_x emission scenarios, which show small OH perturbations close to zero, also show the largest reduction in τ_{CH4} with two altitude clusters (green shaded ellipses). As an addition, Fig. A.16 in the appendix shows the tropospheric CH_4 lifetime, which shows very similar trends for NO_x emission scenarios compared to the whole-model-domain CH_4 lifetime. According to literature two pathways of tropospheric chemistry connect NO_x and OH concentrations. On the one hand, HO_2 to OH recycling is speed-up by NO and eventually increases OH. On the other hand, NO_2 oxidation reduces OH concentrations and increases nitric acid (HNO_3) concentrations [193, p. 245]. Note that tropospheric OH concentrations are only slightly increased for NO_x emission scenarios (Fig. A.2). The above-mentioned processes might not allow large perturbations of OH to build up, even though the effect on CH_4 lifetime are the largest in all scenarios.

In the troposphere, H_2O emission and NO_x emission scenarios show an inverse trend with a tropospheric CH_4 lifetime increase (Fig. A.16,) combined with tropospheric hydroxyl decrease (Fig. A.2) for the former and tropospheric CH_4 lifetime decrease combined with tropospheric hydroxyl increase for the latter. In summary, the important processes for global CH_4 lifetime take place in the troposphere for NO_x scenarios and in the middle atmosphere for H_2O emission scenarios.
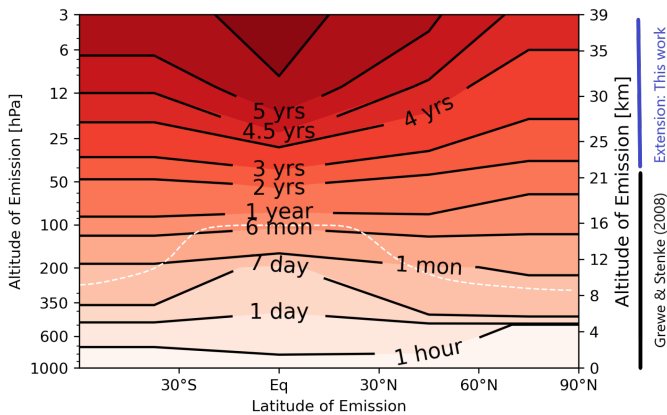
Figure 7.9: Reproduced from Grewe and Stenke [21], Fig. 6 (a), with permission from the authors, who provided the data. The figure shows the water vapor perturbation lifetime for the original pressure levels (1000 - 52 hPa) and the extended pressure levels (52 - 3 hPa) depending on latitude. The vertical regions are marked next to the right y-axis with black and blue lines, respectively.

WATER VAPOR PERTURBATION LIFETIME

Fig. 7.9 shows an increase in H_2O perturbation lifetime with altitude. Values at tropospheric altitudes range from approximately 1 hour to half a year. Generally, the H_2O perturbation lifetime is longest at tropical regions and high altitudes and gets less at higher latitudes and lower altitudes. The lifetime range at stratospheric altitudes is large from one month to five and a half years, which includes the extension that is based on

this work. Results from the sensitivity simulations were used to extend the altitude dependency of H_2O perturbation lifetime in existing literature to higher altitudes, which was previously limited to approximately 20 km (50 hPa) [21]. With the extension values now range up to approximately 40 km (3 hPa). The transport of low latitude high altitude H_2O emissions to the high latitudes of the troposphere along the shallow and deep branches of the Brewer-Dobson circulation takes the longest time. Hence, transport of H_2O perturbations dominates the perturbation lifetime for both, the previous and the extended altitudes. Pletzer et al. [33] showed that (photo-)chemistry does not reduce total H_2O perturbations at 26 and 35 km cruise altitude. Perturbation lifetime continues to increase with altitude for all latitudes and (photo-)chemistry does not deplete H_2O perturbations for emissions up to 38 km.

OVERVIEW ON ATMOSPHERIC COMPOSITION
For a quick-look overview of sensitivities Table 7.2 shows the effect of one gigamol or teramol of H_2O, NO_x and H_2 emission on H_2O (above the tropopause), whole-model-domain O_3 and whole-model-domain CH_4 lifetime τ_{CH4}. Background colors blue, yellow and green, indicate that the values differ from zero with a probability of 95 %, 99.9 % and 99.99 % (Table 3.2). The impact of NO_x, H_2O and H_2 emission on O_3 is statistically significant with 99.99 % confidence for all 24 sensitivities. For sensitivities of H_2O and CH_4 lifetime, 13 and 8 out of 24 means are different to the reference with at least 95 % confidence, respectively. The changes of H_2O, O_3 and τ_{CH4} are adressed in the following three paragraphs.

Water Vapor Perturbation in the Middle Atmosphere   The term stratospheric H_2O is quite common. Since the EMAC model includes parts of the mesosphere, here the term mid-atmospheric H_2O is used. For H_2O emission, the sensitivity of mid-atmospheric H_2O increases clearly with altitude and is higher for lower latitude emission scenarios, which is also shown in Fig. 7.9. The impact of H_2 emission on mid-atmospheric H_2O is very similar and increases with altitude and is larger for lower latitudes. The order of magnitude of changes per molecule of emitted species shows that a molecule of H_2 is roughly 50 % as effective in enhancing the mid-atmospheric H_2O concentration as a molecule of emitted H_2O (Table. A.1).

Whole-Model-Domain Ozone Perturbation   Generally, all three types of emissions cause O_3 depletion. However, the effect of NO_x emission on whole-model-domain O_3 is two and three orders of magnitude larger compared to H_2 and H_2O emission, respectively. Hence, a NO_x molecule is roughly 3 to 4 orders of magnitude more efficient in reducing the stratospheric O_3 burden than H_2 or H_2O. Interestingly, while in absolute values the H_2 emissions are of minor importance to the O_3 depletion, the average effectiveness in destroying O_3 is roughly 5-6 times larger for H_2 than for H_2O (Table. A.1).

Whole-Model-Domain Methane Lifetime Change   The number of significant results of CH_4 lifetime changes is low compared to atmospheric sensitivities of H_2O or O_3. CH_4 lifetime changes of NO_x emission scenarios are lower at the higher altitude and show

Table 7.2: Sensitivities of atmospheric composition changes, water vapor in teramol (ΔH_2O), relative ozone change in teramol (ΔO_3) and relative change of whole-model-domain methane lifetime ($\Delta \tau_{CH4}$), to emission of H_2O, NO_X and H_2 depending on altitude and latitude of emission.

Sensitivity of Atmospheric Composition Changes to Emission of NO_X, H_2O and H_2

Emission	Altitude	ΔH_2O (above tropopause, WMO)				Unit	ΔO_3 (Whole Model Domain)				Unit	$\Delta \tau_{CH4}$ (Whole Model Domain)				Unit
1 Gmol NOx	30 km	-0,09	0,14	-0,03	-0,13	Tmol	-0,17	-0,14	-0,20	-0,18	Tmol	-0,14	-0,15	-0,15	-0,16	%
	38 km	0,07	0,06	0,04	0,05	Tmol	-0,12	-0,12	-0,16	-0,17	Tmol	-0,06	-0,06	-0,12	-0,11	%
1 Tmol H_2O	30 km	4,58	5,44	4,39	3,42	Tmol	-6,43	-0,42	-0,64	-1,23	$x\,10^{-2}$ Tmol	-22,2	-19,2	14,3	21,0	$x\,10^{-3}$ %
	38 km	5,31	5,70	5,10	4,31	Tmol	-6,36	-3,21	-0,69	-1,22	$x\,10^{-2}$ Tmol	-29,6	-41,9	1,2	-2,1	$x\,10^{-3}$ %
1 Tmol H_2	30 km	1,56	2,35	0,81	0,44	Tmol	-7,4	-15,1	-12,2	-8,7	$x\,10^{-2}$ Tmol	10,9	0,9	-12,6	-0,8	$x\,10^{-2}$ %
	38 km	2,86	3,69	2,45	1,62	Tmol	-9,5	-17,9	-16,6	-17,1	$x\,10^{-2}$ Tmol	1,5	-12,0	-10,7	4,1	$x\,10^{-2}$ %
	Latitude	60-30° S	0-30° N	30-60° N	60-90° N		60-30° S	0-30° N	30-60° N	60-90° N		60-30° S	0-30° N	30-60° N	60-90° N	

*   **   ***

7

ranges between -0.06 to -0.16 % per Gmol of NO_x emission. Per molecule CH_4 lifetime changes of H_2O emission scenarios are four to five orders of magnitude smaller than compared to NO_x emission scenarios. Note that CH_4 lifetimes in H_2O and NO_x emission scenarios clearly show a linear trend and clusters depending on altitude, respectively. In contrast, H_2 emission scenarios do not show a clear trend (Fig. 7.8).

Figure 7.10: Zonal mean of HNO_3 perturbation (volume mixing ratio, ppbv) for scenarios where H_2O is emitted. The first and second row refer to 38 km and 30 km altitudes of emission, respectively. Columns represent the latitude region of emission. The emission regions are shaded in gray. Lines indicate statistically insignificant results and the probability level is written in the title of each subplot.
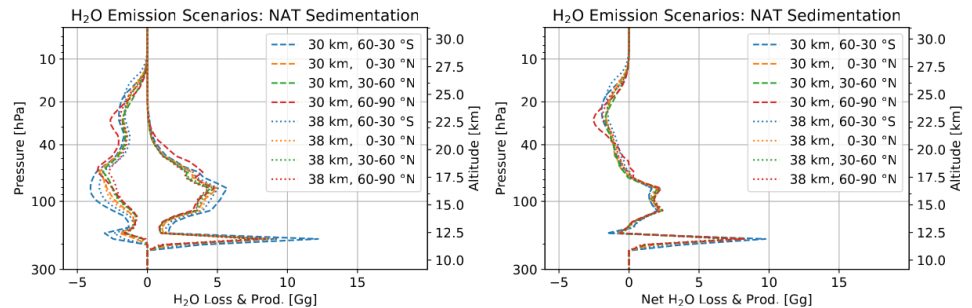
Figure 7.11: Water vapor emission scenarios: Annual values of integrated water vapor production (end of transport; positive values) and loss (start of transport; negative values) related to nitric acid trihydrate sedimentation. The net of production and loss is shown in the right figure.

7.1.5. Polar Stratospheric Clouds

Polar stratospheric clouds affect NO_y, especially HNO_3, and H_2O concentrations. Zonal mean perturbations of HNO_3 are largest at polar regions and become less with lower latitudes (Fig. 7.10 and 7.12). For nitrogen oxide emission scenarios the perturbations show an overall increase, while water vapor and hydrogen emission scenarios show both, regions of depleted and increased HNO_3. Note that for the latter two emissions the total annual depletion is dominant (not shown). The increase is mostly at or above 10 hPa, where the conditions for polar stratospheric clouds are not given and sedimentation does not contribute to the vertical transport (Fig. 7.11 and 7.13). Clearly, increased vertical transport of nitric acid trihydrate (NAT) particles reduces concentrations at higher

altitudes and increases concentrations at lower altitudes. Fig. 7.11 and 7.13 show the altitudes where nitric acid trihydrate is formed, which is followed by an increased vertical transport to altitudes where nitric acid trihydrate eventually disassembles again to HNO_3 and H_2O. Note that water vapor and nitric acid are not completely removed from the stratosphere via NAT sedimentation. The process only enhances the vertical transport of HNO_3 and H_2O. Here, NAT sedimentation related transport happens exclusively between 11-27 km altitude. Net values show that it starts mostly between 17-27 km altitude and ends between 11-17 km, where 11 km is similar to a barrier (Fig. 7.11 and 7.13). The net values show that absolute values of production and loss are nearly the same and at most 2.5 % of NAT particles are disassembled yet.

In water vapor emission scenarios (Fig. 7.11) production and loss of NAT particles is very much distributed and the production peak at 11 km is approximately only twice as large as the other peaks. In contrast, in nitrogen oxide emission scenarios (Fig. 7.13) the production peak at 11 km is many times larger compared to the values at higher altitudes. Hence, the vertical transport for nitrogen oxide emission scenarios is most likely associated with longer transport times and a longer transport distance for a single NAT-form-and-disassembly step. Whereas for water vapor emission scenarios the transport times should be comparably short and a single NAT particle has to form multiple times to reach the final loss destination at 11 km.
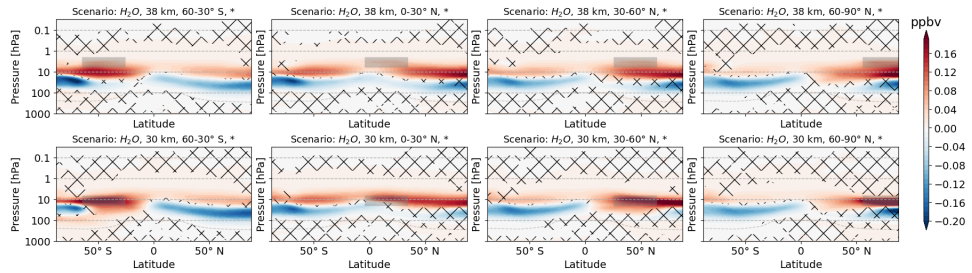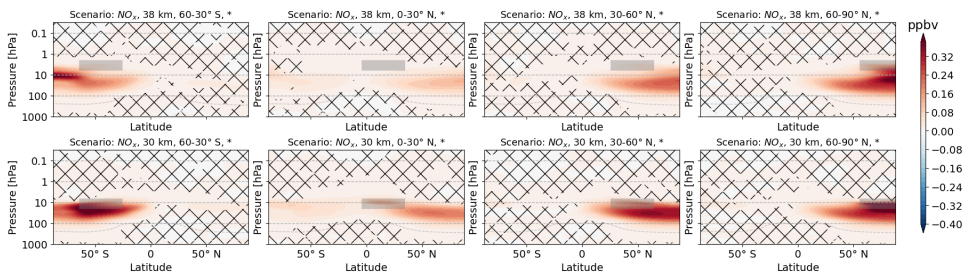

Figure 7.12: Zonal mean of HNO_3 perturbation (volume mixing ratio, ppbv) for scenarios where NO_x is emitted. The first and second row refer to 38 km and 30 km altitudes of emission, respectively. Columns represent the latitude region of emission. The emission regions are shaded in gray. Lines indicate statistically insignificant results and the probability level is written in the title of each subplot.

On average, the sedimentation of water in the form of nitric acid trihydrate is 0.04±0.02 % and 0.06±0.01 % compared to the water vapor perturbation in the middle atmosphere for hydrogen emission and water vapor emission scenarios, respectively. For comparison, the sedimentation of NO_y in the form of nitric acid trihydrate is 25±7 % compared to the NO_y perturbation in the middle atmosphere for nitrogen oxide emission scenarios. Clearly, nitric acid trihydrate sedimentation largely affects NO_y perturbations, while it is of minor importance for water vapor perturbations of this magnitude. How ice sedimentation affects water vapor perturbations is shown in chapter 5. Note that water vapor perturbations in hydrogen and water vapor emission scenarios strongly enhance NO_y sedimentation and contribute to NO_y depletion in the middle atmosphere and most likely cause the overall NO_y depletion. The effect is very strong in water vapor emission scenarios (-120±32 %) and weaker in hydrogen emission
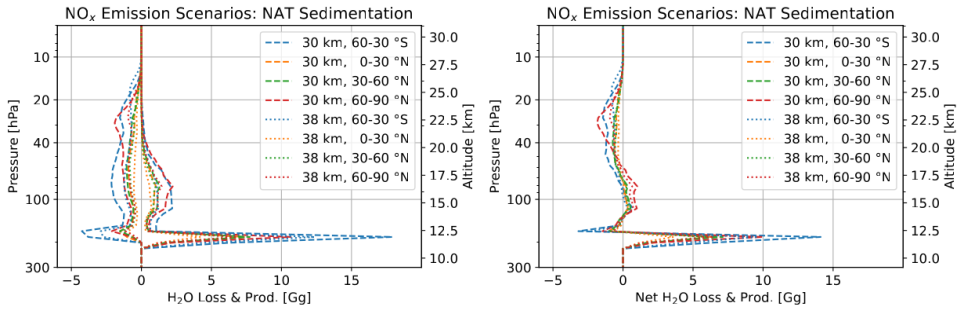
Figure 7.13: Nitrogen oxide emission scenarios: Annual values of integrated water vapor production (end of transport; positive values) and loss (start of transport; negative values) related to nitric acid trihydrate sedimentation. The net of production and loss is shown in the right figure.

scenarios (-14±22 %). Values are sometimes larger than a hundred percent and should be interpreted carefully, due to the possibility of multiple sedimentation steps of single molecules.

7.2. Radiative Forcing

The atmospheric changes of radiatively active gases, H_2O, O_3 and CH_4, were used to calculate the stratospheric-adjusted radiative forcing (total net RF) at the tropopause (about 180 hPa). Fig. 7.16 shows the total shortwave (SW), total longwave (LW) and total net RF grouped by emission and aligned by latitude and marked by altitudes of emission. Here, 'total' refers to the combined effect of RF due to H_2O, O_3 and CH_4 changes. In the following subsections, the individual, H_2O, O_3, CH_4 altitude and latitude dependencies of RF and the relation of RF to atmospheric composition changes are addressed. Comparing the magnitude, the H_2O emission scenarios show the largest total net RF, followed by NO_x and H_2 emission scenarios. H_2O emission scenarios all have a negative total SW RF (blue), which is smallest at southern mid-latitudes. The total LW RF (green) is largest for tropical, and smallest for the north polar emission scenarios. The high altitude emission scenarios show a larger total LW RF for all latitudes. NO_x emission scenarios show a positive total SW RF, which is larger for the lower altitude scenarios. In comparison, the total LW RF is negative and smaller, with no distinctive altitude dependency. H_2 emission scenarios have a positive total SW RF, apart from the lower altitude emission scenarios at southern mid-latitudes and the tropics. The total LW RF clearly depends on altitude with larger values for the high altitude emission scenarios, the Southern Hemisphere and the northern tropics.

7.2.1. Water Vapor Radiative Forcing

Water vapor emission scenarios have the largest radiative forcing of the emission scenarios, followed by H_2 and NO_x emission scenarios. Fig. 7.15 shows the H_2O SW RF, H_2O LW RF and H_2O net RF due to H_2O changes. For H_2O emission scenarios the H_2O SW RF has the largest negative values for emission in the tropics and the lowest negative values for emission at north polar latitudes. The H_2O LW RF shows the inverse trend with

Figure 7.14: The total shortwave, longwave and net radiative forcing in blue, green and black, respectively, for water vapor (a), nitrogen oxide (b) and hydrogen (c) emission scenarios due to atmospheric composition changes of water vapor, ozone and methane. For different altitude emission scenarios, refer to markers. Latitude regions of emission are aligned on the x-axis.

largest positive values for emission in the tropics and lowest positive values for emission at north polar latitudes. Overall, H_2O LW RF dominates the H_2O net RF. For NO_x emission scenarios the H_2O SW RF is mostly positive, whereas the H_2O LW RF is negative. The H_2O net RF is negative apart from the emission at 30 km in the tropics. For H_2 emission scenarios the H_2O SW RF is negative for emission at southern mid-latitudes and the tropics and positive for emission at most northern mid-latitudes and at the northernmost latitudes. The H_2O LW RF shows the inverse trend with warming at southern mid-latitude and tropic emission and cooling only for emission at the lower altitudes for northern mid- and high-latitudes. The LW RF dominates the net RF by an order of magnitude.

Figure 7.15: The shortwave, longwave and net radiative forcing in blue, green and black, respectively, for water vapor (a), nitrogen oxide (b) and hydrogen (c) emission scenarios due to water vapor changes. For different altitude emission scenarios, refer to markers. Latitude regions of emission are aligned on the x-axis.

7.2.2. OZONE RADIATIVE FORCING

Figure 7.16 is based on O_3 changes, excluding H_2O and CH_4 changes. For H_2O emission scenarios the O_3 SW RF is positive with maximum values of 1.75 mWm^{-2} for southern latitude emission and continuously becomes close to zero the further north H_2O is emitted. The O_3 LW RF shows an inverted trend with large negative values for emission at southern latitudes and values between 0 and -1 mWm^{-2} for other emission locations. The altitude dependency of O_3 SW RF is largest for emission at tropical regions and, in contrast,

O_3 LW RF shows larger altitude differences only at higher latitude emission scenarios. Overall, there is a clear altitude distinction of net O_3 RF due to H_2O emission and values are negative and positive. For H_2 emission scenarios the O_3 SW RF shows only a small latitude dependency around 0.4 mWm^{-2} for the higher altitude emission scenarios. In contrast, the higher altitude emission causes negative values up to -0.2 mWm^{-2} for emission at southern latitudes to the tropics and has positive values for north polar emission. The O_3 LW RF is negative and differences of high and low altitude emission are largest for emission at the tropics. Since O_3 LW and SW RF tend to cancel each other, the net O_3 RF has generally lower values than the individual contributions and a stronger cooling caused by O_3 perturbation due to H_2 emission for the lower altitude at all latitude emission scenarios, except north mid-latitude and north polar emission.
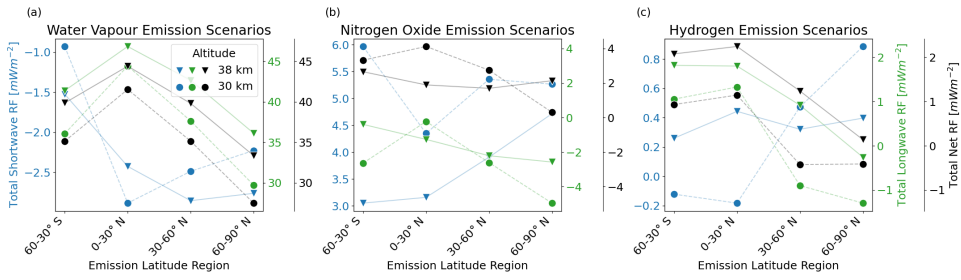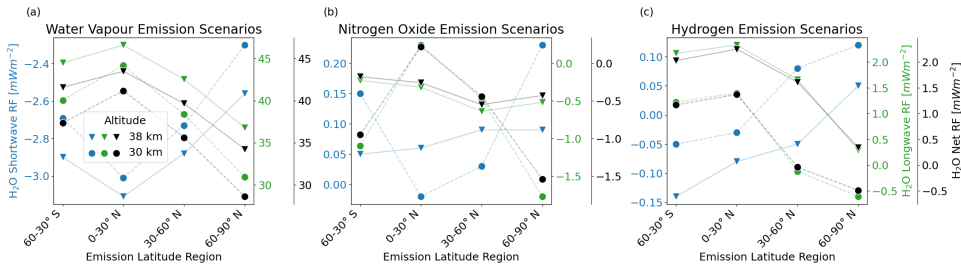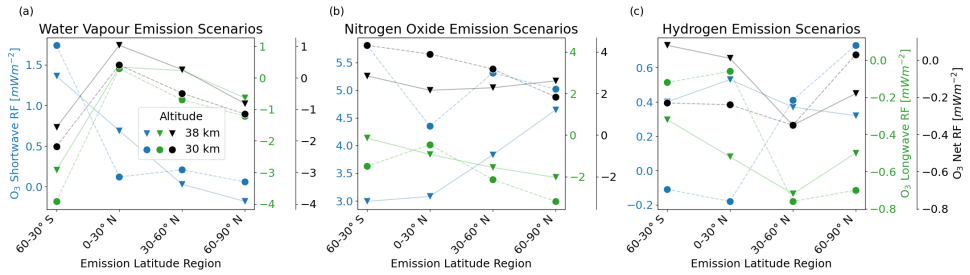

Figure 7.16: The shortwave, longwave and net radiative forcing in blue, green and black, respectively, for water vapor (a), nitrogen oxide (b) and hydrogen (c) emission scenarios due to ozone changes. For different altitude emission scenarios, refer to markers. Latitude regions of emission are aligned on the x-axis.

7.2.3. Methane Radiative Forcing

Methane composition changes contribute significantly less to RF than atmospheric composition changes of H_2O and O_3. The range of CH_4 net RF is -0.17 to 0.05 mWm^{-2} and LW RF is larger than SW RF in many scenarios (Fig. A.32, appendix). For H_2O emission scenarios the CH_4 net RF cools more for the higher altitude scenarios. For lower altitude scenarios radiation flux changes are smaller, apart for northern mid-latitude emission with an effect close to zero and north polar emission with a comparably small heating. The NO_x emission scenarios show a warming for the lower altitudes scenarios, apart for emission at southern latitudes, for which a comparably larger cooling effect occurs. For higher altitude emission scenarios the CH_4 net RF is close to zero for southern mid-latitude and tropic emission and cools for northern mid-latitude and north polar emission of NO_x. H_2 emission scenarios shows both warming and cooling with LW and SW due to the CH_4 perturbation. A continuous cooling appears for the higher altitude emission scenarios. The lower altitude emission scenarios show alternating values of warming and cooling depending on latitude.

7.2.4. CORRELATION OF RADIATIVE FORCING AND PERTURBATION MAG-
NITUDE

H_2O NET RADIATIVE FORCING

The average sensitivity of H_2O net RF to one teragram of H_2O increase is 0.37 ± 0.01 mW m^{-2} (TgH$_2$O)$^{-1}$for H_2O emission scenarios, 0.10 ± 0.79 mW m^{-2} (TgH$_2$O)$^{-1}$ for NO$_x$ emission scenarios and 0.14 ± 0.28 mW m^{-2} (TgH$_2$O)$^{-1}$ for H_2 emission scenarios. The standard deviation, i.e. latitude and altitude variation, is large for the latter two and only H_2O emission scenarios always result in a radiative warming with a low standard deviation. Fig. 7.17 shows the relation of H_2O net RF and H_2O perturbation above the tropopause for all emission scenarios. The relation increases linearly for low values of H_2O perturbation, with slight underestimate of NO$_x$ and H_2 emission scenarios. The results confirm the linear relation between stratospheric H_2O perturbations and RF from earlier findings and for lower emission altitudes (dashed gray line, [27, Fig. 8]). However, for higher perturbations deviations in RF appear and the relation $\frac{\Delta RF}{\Delta H_2O}$ continuous to decrease. A two dimensional polynomial fit captures the data points well with very small deviations.

Figure 7.17: Overview of H_2O net radiative forcing for all 24 simulations. Colors refer to the initial emission (H_2, H_2O and NO$_x$) and markers to altitudes of emission. The green cross for 35 km altitude refers to combined emissions from the LAPCAT MR2 aircraft shown before in chapter 6. The gray line refers to a correlation of RF and H_2O perturbation from another publication [27, Fig. 8]. The dotted black line is a two-dimensional polynomial fit with ax^2 + bx + c, where a = -0.88, b = 473.73 and c = -746.76 Wm^{-2}Tg^{-1}.

O_3 NET RADIATIVE FORCING

The average sensitivity of O_3 net RF to one percent of O_3 decrease is -9.9 ± 38.2 mW m^{-2} (%O$_3$)$^{-1}$ for H_2O emission scenarios, 20.2 ± 6.1 mW m^{-2} (%O$_3$)$^{-1}$ for NO$_x$ emission scenarios and -7.4 ± 8.7 mW m^{-2} (%O$_3$)$^{-1}$ for H_2 emission scenarios. The interannual variability is particularly large for H_2O emission scenarios. For the NO$_x$ emission scenarios, O_3 decrease always causes warming. Fig. 7.18 shows the relation of O_3 net RF to relative O_3 change for all emission scenarios. The NO$_x$ emission scenarios are clustered and the related O_3 depletion causes warming. For the lower altitude scenarios, different levels of O_3 decrease do not cause a large difference in warming. In contrast, for

Figure 7.18: Overview of O_3 net radiative forcing for all 24 simulations. Colors refer to the initial emission (H_2, H_2O and NO_x) and markers to altitudes of emission.

higher altitude scenarios the latitude of emission has a larger impact on both O_3 deple-
tion and O_3 net RF variability. H_2O and H_2 emission scenarios are clustered around close
to zero RF, apart from three single H_2O emission scenario values, where the pair is emis-
sion at southern mid-latitudes and the single value at northern tropics. The comparably
large O_3 depletion for H_2O emission at southern mid-latitudes originates from enhanced
denitrification by increased H_2O concentrations within polar stratospheric clouds (not
shown), which is known to be stronger in southern polar regions compared to northern
polar regions [177].

CH$_4$ Net Radiative Forcing
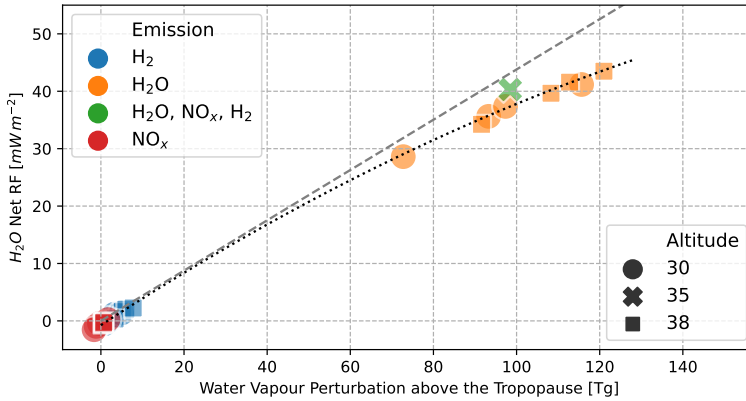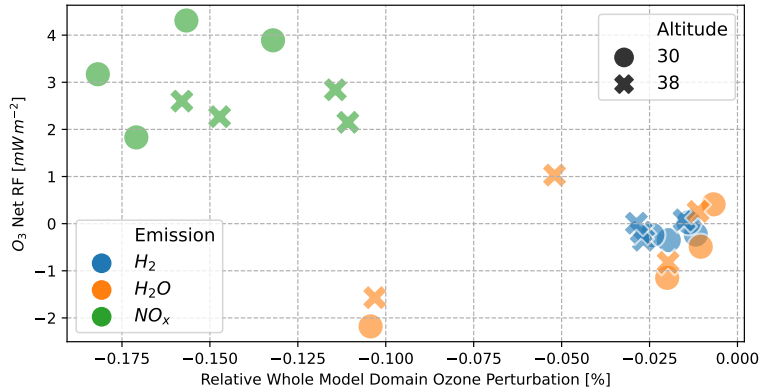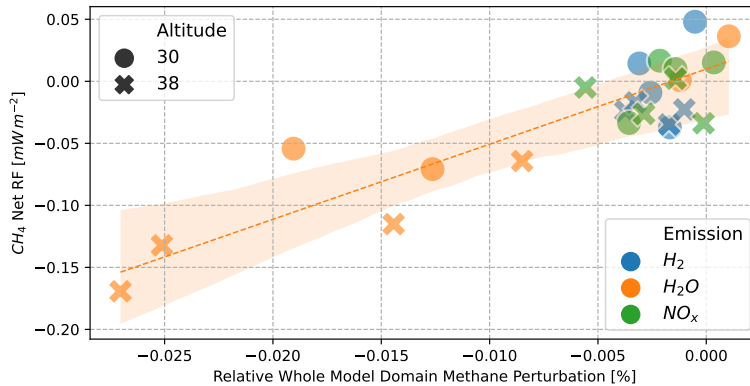

Figure 7.19: Overview of CH_4 net radiative forcing for all 24 simulations. Colors refer to the initial emission (H_2, H_2O and NO_x) and markers to altitudes of emission. The regression line including the shaded areas depict the mean and standard deviation of the eight H_2O emission scenarios.

The average sensitivity of CH_4 net RF to one percent of global CH_4 decrease is -

8.7 ± 10.2 mW^{-2}/% CH$_4$ for H$_2$O emission scenarios, -39.5 ± 88.1 mW m^{-2}/% CH$_4$ for NO$_x$ emission scenarios and 2.1 ± 35 mW m^{-2}/% CH$_4$ for H$_2$ emission scenarios. Clearly, the spread is large. All of NO$_x$ and H$_2$ emission scenarios are clustered around zero RF, with both radiative warming and cooling (Fig. 7.19). H$_2$O emission scenarios show warming, no change and cooling for the lower altitude emission. For higher altitude emission the larger CH$_4$ reduction comes with a cooling effect. Both altitudes combined scale approximately linear, however, the line crosses from cooling to warming slightly below the inversion of CH$_4$ decrease to CH$_4$ increase.

SUMMARY ON RADIATION

Table 7.3 shows an overview of radiative sensitivities normalised to perturbation per emitted mol. The error potential is labeled according to the t-test that was calculated for atmospheric composition changes and the related probabilities are listed in Table 3.2. The H$_2$O net RF of NO$_x$ emission scenarios is statistically not significant according to the t-test. Note that the normalisation to perturbation per emitted mol has a different magnitude for NO$_x$ emission scenarios (gigamol). In contrast to NO$_x$ emission scenarios, the H$_2$O net RF for H$_2$O emission scenarios are all statistically significant. Note that H$_2$O emission scenarios would contribute by far the most to net radiative forcing without the normalisation, followed by NO$_x$ and H$_2$ emission scenarios, which is mainly due to the large ratio of H$_2$O to NO$_x$ and H$_2$ in the exhaust. The normalized O$_3$ net RF is significant for all three types of emission. NO$_x$ emission scenarios show by far the largest O$_3$ net RF values, followed by H$_2$ and H$_2$O emission scenarios (if the order of magnitude is kept in mind). Normalized CH$_4$ net RF is significant for most NO$_x$ emission scenarios, however, the magnitude is small compared to the normalized O$_3$ net RF for NO$_x$ emission.

7.3. ATMOSPHERIC COMPOSITION CHANGES AND RADIATIVE FORCING

This section addresses the relation of emission, atmospheric composition changes and radiative forcing. A variety of publications exist where idealized atmospheric composition changes are used for sensitivity studies of the radiative effect [82–84, 133]. The here used approach adds a level of complexity, since not only the RF of idealized atmospheric composition changes is calculated, but rather of modeled atmospheric composition changes due to idealized emission scenarios. Hence, it is important to discuss the process of emission, followed by atmospheric composition changes and the radiative forcing.

7.3.1. WATER VAPOR ATMOSPHERIC AND RADIATIVE SENSITIVITIES

In the discussion of H$_2$O changes and their radiative forcing, NO$_x$ emission scenarios are excluded, since they show no statistically significant results (see Table 7.2 and Table 7.3). Middle atmospheric H$_2$O perturbation for H$_2$O and H$_2$ emission scenarios depends very much on altitude of emission and increases with altitude of emission. The H$_2$O perturbation lifetime follows more or less the Brewer-Dobson circulation, where H$_2$O emitted into the uprising tropical air has a larger lifetime than H$_2$O into the sinking polar air. In contrast to the increase with altitude, H$_2$O net RF develops a curvilinear trend

Table 7.3: Sensitivities of three net radiative forcings (H_2O, O_3, CH_4) to emission of H_2O, NO_x and H_2 depending on altitude and latitude of emission.

Sensitivity of Radiative Forcing caused by Atmospheric Composittion Changes to Emission of NO_x, H_2O and H_2

Emission	Altitude	Δ H_2O net RF					Δ O_3 net RF					Δ CH_4 net RF				
		60-30°S	0-30°N	30-60°N	60-90°N	Unit	60-30°S	0-30°N	30-60°N	60-90°N	Unit	60-30°S	0-30°N	30-60°N	60-90°N	Unit
1 Gmol NOx	30 km	-0,54	1,20	0,05	-1,02	mWm^{-2}	5,84	5,98	4,21	3,22	mWm^{-2}	0,009	0,028	0,023	0,021	mWm^{-2}
	38 km	0,84	0,45	0,57	0,43	mWm^{-2}	4,73	2,22	3,08	3,42	mWm^{-2}	0,018	0,028	-0,020	-0,022	mWm^{-2}
1 Tmol H_2O	30 km	30,66	34,19	29,74	24,07	mWm^{-2}	-3,60	-1,49	-2,14	-2,15	mWm^{-2}	0,016	0,005	0,028	0,010	mWm^{-2}
	38 km	34,09	35,59	32,78	28,67	mWm^{-2}	-3,38	-1,28	-1,66	-2,30	mWm^{-2}	0,012	-0,005	-0,003	-0,018	mWm^{-2}
1 Tmol H_2	30 km	10,45	15,67	6,01	3,27	mWm^{-2}	-6,14	-4,96	-4,31	-3,53	mWm^{-2}	0,324	0,230	-0,146	0,300	mWm^{-2}
	38 km	18,42	24,16	16,85	11,10	mWm^{-2}	-7,71	-5,22	-5,49	-4,96	mWm^{-2}	-0,005	-0,064	0,003	0,229	mWm^{-2}
	Latitude	60-30°S	0-30°N	30-60°N	60-90°N		60-30°S	0-30°N	30-60°N	60-90°N		60-30°S	0-30°N	30-60°N	60-90°N	

*** ** *

and begins to decrease with mass perturbation (Fig. 7.17). The effect is small compared to the total perturbation. Two possible explanations are, first, a saturation of reflected H_2O longwave radiation, and, second, altitude differences in peak H_2O mass accumulation with smaller radiative sensitivities for higher altitudes [84]. In a prior publication [33], H_2O net RF was tested according to Myhre et al. [161] and based on these results a dependency of H_2O net RF to stratospheric H_2O background is less likely. Fig. A.17 in the appendix shows vertical profiles of globally integrated H_2O concentration changes, which supports the second explanation. To explain, excluding Southern Hemisphere scenarios, the peak accumulation is at higher altitudes for scenarios where the trend of H_2O net RF deviates more from the linear trend in Fig. 7.17. Hence, an altitude and or latitude shift of the main mass accumulation to higher values should cause the lower H_2O net RF. Two publications reported a nearly linear dependency of stratospheric adjusted RF to emission magnitude for a range of 9.5-11.5 km [27, 194]. Apparently, there the radiative sensitivity to different magnitudes does not show curvilinear tendencies. In contrast, the radiative sensitivity shows a curvilinear trend around the tropopause [195, Fig. 2b]. To summarize briefly, two trends of atmospheric composition changes and radiative forcing oppose each other. First, the increase in H_2O perturbation with altitude and, second, the decreasing radiative sensitivity depending on altitude and latitude. The first dominates the H_2O net RF and the second is a second order variation of the H_2O net RF.

7.3.2. Ozone Atmospheric and Radiative Sensitivities

All scenarios show a total O_3 depletion, however, also increases in O_3 at various altitudes (Fig. 7.6, Fig. 7.3, Fig. A.28). Hence, regions of O_3 depletion are partly equilibrated by regions of O_3 increase in terms of total depletion. Clearly, the perturbation sensitivity to emission is complex. The radiative sensitivity further increases the complexity. Close to the tropopause and the tropics the radiative effect per unit mass change is large [84, Fig. 1]. In addition, several authors reported O_3 climate sensitivities, where an increase in O_3 either cools or warms near-surface air depending on domain [82, Fig. 1][196, Fig. 7]. This inversion point is slightly below 30 km, above which an increase in O_3 causes cooling of near-surface air. Even though the emission altitudes in this publication are 30 and 38 km and hence above the inversion point, the regions of O_3 increase or decrease are very much distributed at different altitude and latitude regions, where each region has its specific radiative sensitivity. Therefore, the regions with O_3 changes combined with the active radiative sensitivity there form a complex net total of warming and cooling. Since the O_3 net RF is positive for all NO_x emission scenarios, one could expect to see either one or both of O_3 depletion and hence warming at high altitudes above the inversion point and O_3 increase and hence warming at lower altitudes.

For presentation of stratospheric trace gas changes volume mixing rations are often preferred, e.g. because they are unaffected by transport processes. However, radiation impacts are mainly affected by density changes and this might change the point of view. For example, perturbations close to the tropopause might appear low as mixing ratios, but are larger in numbers due to higher air densities compared to higher altitude mixing ratio changes. Fig. A.18 in the appendix gives a direct comparison of profiles of density and volume mixing ratio changes. Many NO_x emission scenarios (Fig. A.18, mid) show

an increase in O_3 density from 9 km (300 hPa) upwards, which switches to a decrease between around 16 and 25 km (100 and 25 hPa) depending on the specific emission scenario. To summarize, while the total density increase is smaller than the total density decrease, the region of increase comes with a significantly larger radiative sensitivity, which explains the radiative warming associated with reported total O_3 depletion in the scenarios. For H_2O and H_2 emission scenarios regions of O_3 depletion and O_3 increase in combination with radiative sensitivities cause cooling in contrast to NO_x emission scenarios. Here, the distribution of perturbations in combination with radiative sensitivities results in the opposite result to O_3 changes by NO_x emissions.

In summary, both the radiative sensitivity and the location of perturbation patterns along latitude and altitude are crucial for the interpretation of the results. The radiative sensitivity is generally largest at the tropics and close to the upper-troposphere lower-stratosphere, while the perturbation patterns are complex and differ depending on emitted trace gas.

7.4. DISCUSSION

The previous sections concentrated on the main sensitivities of hypersonic emissions. Processes that are generally important that with respect to the effect of hypersonic emissions are only of secondary importance, are discussed here. This comprises the discussion of polar stratospheric clouds and heterogeneous chemistry and the net production of H_2O from hypersonic aircraft emissions. Additionally, a comparison to results from literature about atmospheric impacts of supersonic aircraft and synergy effects of simultaneous emissions are included.

7.4.1. POLAR STRATOSPHERIC CLOUDS

Throughout this chapter the focus was on homogeneous, i.e. gas phase, atmospheric composition, since most of the emissions affect atmospheric regions outside (spatial and temporal) polar night and spring processes. The model setup includes heterogeneous chemistry, i.e. particle effects like nucleation or condensation, which play a major role in polar stratospheric clouds, as well as chlorine and bromine activation of those particles. There are two reasons why this is important for hypersonic aircraft emission. First, sedimentation of nitric acid trihydrate (NAT) and ice particles transport of both, HNO_3 and H_2O, from high to lower altitudes [197, 198], which effectively increases denitrification and dehydration and in turn reduces perturbation lifetimes. Clearly, the effect only contributes to the vertical transport, which is dominated by the residual circulation in the middle atmosphere. Second, the chemistry within polar stratospheric clouds, where nonreactive chlorine becomes reactive, heavily depletes O_3 concentrations and is prolonged by denitrification [199, p. 248]. In EMAC model results, HNO_3 mixing ratios are increased between 100-10 hPa for NO_x emission scenarios. For H_2O and H_2 emission scenarios the mixing ratios are increased at around 10 hPa, depleted between 100-10 hPa and increased at and below 100 hPa (not shown). The effect is significant in most regions for the former and to a lesser extent for the latter. Sedimentation change of HNO_3 (excluding H_2 emission scenarios) and ice appears at 10-100 hPa, with a peak between 10-20 hPa and is increased particularly in the lower polar stratosphere at ap-

proximately 200 hPa, but peaks not appear below the tropopause. According to Iwasaka, Yasunobu and Hayashi, Masahiko [198] only NAT particles grown in the upper polar stratospheric clouds can reach the troposphere and ice particles are the ones that evaporate in the lower stratosphere. In the EMAC model the vertical falling distance is defined by the sedimentation velocity, which depends on the mean radius and a sedimentation factor [145]. Hence, the emitted trace gases, which become part of polar stratospheric cloud chemistry and sedimentation, should not increase particle size significantly, since they do not reach the troposphere. In summary, polar stratospheric clouds affect atmospheric composition by an enhanced vertical transport, which in turn affects nitrogen oxide concentrations to a larger extent compared to H_2O concentrations. The effect is more important for emission at high latitudes.

7.4.2. COMPARISON TO CURRENT LITERATURE ON SUPERSONIC AIRCRAFT

The sensitivities to emissions of supersonic aircraft have recently been reviewed by Matthes et al. [14]. They describe the effect of NO_x on O_3 and state that an inversion point of emission exists at 17 km below which emission of NO_x increases total O_3 [136]. Hypersonic aircraft cruising at 30 or 38 m show no clear picture and depletion of O_3 decreases or increases depending on latitude of emission with altitude. The importance of H_2O emissions of supersonic aircraft and their effect on O_3 are highlighted by results from this thesis. The total O_3 depletion due to H_2O emission is sometimes only a factor different to NO_x emission depending on scenario and the decreasing O_3 depletion with altitude for NO_x emission scenarios is compensated if combined with H_2O emission scenarios. Note that this depends very much on the ratio of emitted NO_x and H_2O and may easily change for a different ratio of exhaust. Matthes et al. [14] further report that supersonic aircraft affect the CH_4 lifetime through O_3 changes and increased OH availability and an increased UV radiation in the troposphere. According to them the effect is comparably less important than the others. However, as shown in Pletzer et al. [33], according to the trend calculated by both their models, CH_4 radiation changes might be more important for hypersonic aircraft compared to supersonic aircraft, where cooling by CH_4 changes compensates approximately one third of warming by O_3 changes (LMDZ-INCA model). In this study total CH_4 depletion for H_2O emission scenarios clearly increases with altitude and hence might the cooling associated with it, but open questions on the order of magnitude of radiative forcing by CH_4 changes remain.

7.4.3. SYNERGY EFFECTS OF SIMULTANEOUS EMISSIONS

In the model setup only one trace gas is emitted at a time. For comparison, Kinnison et al. [105] calculated individual (H_2O, NO_x) and combined emissions. This approach was not selected for the here used model setup for two reasons. First, due to the impression that their single emission perturbations add up to the simultaneous emission perturbation [105, Fig. 6-8] – and, second, to avoid a substantial increase in computation time. The results of this publication (e.g. Fig. 7.17) are very similar in magnitude compared to the combined emission calculated in chapter 6 (e.g. Fig. 7.17). Hence, effects due to simultaneous emission should at most be second order effects with small impact in

comparison to the total effect.

7.4.4. Comparison to Land Hydrogen Emissions

Ocko and Hamburg [90] combined multiple studies and made a comparison of (indirect) radiative efficiencies or as described in this dissertation 'radiative sensitivities' to H_2 emission with other land emissions. Here, 'indirect' refers to tropospheric CH_4 and O_3 changes and stratospheric H_2O changes due to land H_2 emissions. Recalculated, their range of sensitivities to land H_2 emission amounts to 0.74 and 1.02 mW(m$^2 \cdot$ TmolH$_2$)$^{-1}$, which include the stratospheric effects. Clearly, the radiative sensitivities to hypersonic aircraft H_2 emissions are up to one order of magnitude larger than the radiative sensitivity to land H_2 emission (Table 7.3). The large-scale removal of land H_2 emissions by soils (70-80 % [90] might explain the difference in radiative sensitivities to some extent.

7.4.5. Ozone Sensitivity

Results from chapter 6 and this chapter give insights on the ozone sensitivity at the altitude range from 26-40 km. Figure 7.20 is an extended version of Fig. 6.6, excludes LMDZ-INCA results and includes EMAC results of atmospheric sensitivities. A cubic fit of data points for each nitrogen oxide emission scenario including sensitivities at 26, 35 km (EMAC) and 40 km (WACCM [105]) shows that ozone sensitivity increases from 26-30 km and continues to increase up to 35 km (dashed line, tropic and southern mid-latitude emission) or decreases from a local maxima at 30 km to a local minima at 35 km (dotted line, north mid-latitude and polar emission). The dashed lines decrease from the maxima at 35 km up to 40 km, whereas the dotted lines reach another local maxima at 38 km altitude and from there decrease sharply. According to this fit, two regimes of ozone sensitivity exist. One ranging from the northern tropics to high southern latitudes and the other from northern mid-latitudes to the north pole.
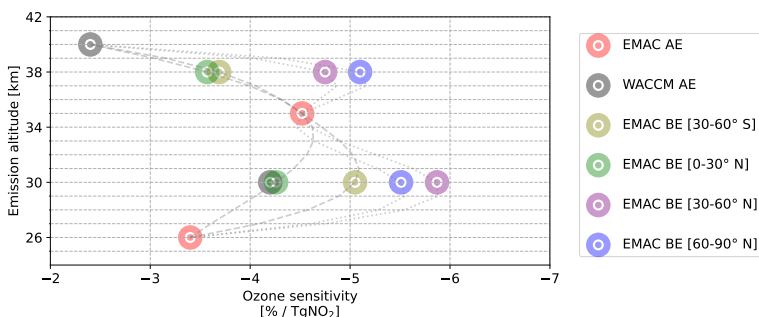
Figure 7.20: Ozone sensitivities of the WACCM and EMAC model to emission of nitrogen oxides. WACCM results are for altitude of aircraft emission (AE) of 30 and 40 km. EMAC results are from scenarios at 30 and 38 km altitude of box emission (BE) and 26 and 35 km altitude of AE. Gray lines represent a cubic interpolation between EMAC (BE and AE) results and the WACCM result for emission at 40 km. The gray dotted lines include a local minimum and gray dashed lines show a local maximum at 35 km.

7.4.6. DENITRIFICATION WITHIN POLAR STRATOSPHERIC CLOUDS

Denitrification within polar stratospheric clouds depends strongly on latitude of emission. For water vapor emission scenarios severe ozone loss due to widespread denitrification appears exceptionally strong in the Antarctic in EMAC results (Table 7.2). Clearly, an increase of water vapor at polar stratospheric altitudes in the Southern Hemisphere has a larger effect via polar stratospheric clouds chemistry than emission of nitrogen oxides. Note that a potential increase of ozone loss up to 30 % in the Arctic in combination with enhanced denitrification due to lower temperatures and longer polar stratospheric cloud lifetimes were reported for near-future scenarios in 2030 [177]. This effect might increase calculated sensitivities accordingly.

7.5. SUMMARY

In this study sensitivities with respect to location and emission type of hypersonic emissions were analysed, and showed, first, how emissions of hypersonic aircraft (H_2O, NO_x, H_2) affect atmospheric composition and, second, how this change in atmospheric composition affects climate, i.e. stratospheric-adjusted radiative forcing. The novelty here is the systematic emission at two different altitude regions (30 km, 38 km) and four different latitude regions (60-30° S, 0-30° N, 30-60° N, 60-90° N) and the individual impact of NO_x, H_2O and H_2 emissions. Atmospheric perturbations were calculated with the full-scale atmospheric chemistry and general circulation model EMAC and the resulting perturbations were used for a radiation model setup to calculate the stratospheric-adjusted radiative forcing. The method to calculate changes in atmospheric composition and associated stratospheric-adjusted radiative forcings for different emission regions allows a comparison of their specific sensitivities. The main results are condensed in two quick-look tables of atmospheric and radiative sensitivities (Table 7.2, Table 7.3) and other results are mostly for explanation and analysis. The main message is that sensitivities can differ manifold depending on latitude and altitude of emission and a change in latitude of emission can change sensitivities more than a change in altitude of emission. The most important large-scale process controlling the lifetime of perturbations certainly is the Brewer-Dobson circulation. Local processes within polar stratospheric clouds can contribute strongly depending on emission location. From the calculated sensitivities H_2O emission and the related H_2O perturbation in addition to NO_x emission which causes O_3 perturbation have the largest warming potential. Both share the regional pattern (except NO_x emission at 38 km) that emission at low latitudes is associated with the largest latitudinal sensitivities. However, their altitude sensitivities are (mostly) inverse, i.e. warming from H_2O perturbation increases with altitude, while warming from O_3 changes decreases with altitude at 30-38 km. The calculated sensitivities allow inexpensive and fast estimates of the stratospheric-adjusted radiative forcing of new hypersonic aircraft designs depending on latitude, altitude and ratio of emissions without the need to apply a complex atmospheric chemistry general circulation model.

7

8

CLIMATE IMPACT OPTIMISATION OF AN AIRCRAFT-DESIGN

The climate-optimisation potential of aircraft designs, in particular route networks, is important for the climate-evaluation of hypersonic aircraft. Mostly to quantify the reduction potential of the climate impact of hypersonic aircraft designs and with this to extend the climate-evaluation of hypersonic aircraft to real-life operation, i.e. route network planning. This chapter presents functions in python software, based on sensitivities from the previous chapter, to evaluate climate impact depending on altitude and latitude of emission. The software was developed as a peer-reviewed repository and is maintained on GitHub. As an intro, section 8.2 presents general parameters for the optimisation of new aircraft designs and section 8.3 shows and explains the software code and the individual functions. Section 8.4 is about the comparison and evaluation of two different trajectories and different output metrics and the climate-optimisation potential of one trajectory is analysed in section 8.5. The chapter ends with a brief description of the software's limitations and a summary.

Parts of this chapter will contribute to a forthcoming publication in *Aerospace*, Bodmer et al. [200].

8.1. Multidisciplinary Development of Hypersonic Aircraft Designs

Since 2008, a series of European projects have funded the development of high-speed civil transport [131]. One of the most recent is the Horizon2020 innovation project STRATOFLY. During the project phase Twelve European research centers contributed to the multi-disciplinary study addressing 'thermal and structural integrity, low-emissions combined propulsion cycles, subsystems design and integration, including smart energy management, environmental aspects impacting climate change, noise emissions and social acceptance, and economic viability accounting for safety and human factors' [131]. The project results include the first climate estimate of hydrogen-powered hypersonic aircraft calculated with atmospheric chemistry general circulation models, which were presented in chapter 6. A focus during the development of a new hypersonic aircraft, called STRATOFLY MR3, was the reduction of aircraft emissions [130]. The emission inventory was optimised based on numerical simulations and experimental tests of engine combustion and provides emission indexes along vertical flight profiles. The emission inventory allows the calculation of 4D emission flight data along a trajectory and serves as the basis for the scheme in Fig. 8.1. For reference a set of these trajectories varying in cruise altitude were used for climate impact calculations presented in Fig. 6.9 (Blue squares), where the increase with cruise altitude is shown for the case that other parameters like magnitude and horizontal distribution of emissions are kept fixed.

8.2. Trade-Offs during Aircraft Development

For successful commercial operation many parameters of hypersonic aircraft have to be optimised. The parameters include for example noise, climate impact, passenger comfort, health, market and technological requirements. On route network level these parameters include flight profile modelling, trajectory optimisation in terms of noise and emissions and eventually climate optimisation. However, these parameters are not independent. One example is that market requirements affect the choice of city-pairs and in turn flight paths and these very much define the climate impact. Another example is the noise of hypersonic engines. It is a legal requirement to reduce noise pollution on land by starting the hypersonic engine over the sea. The multi-disciplinary development of frontier technology very much relies on exchange of parameters and optimising the parameters across the multiple disciplines at some point becomes a trade-off. In particular, the climate impact of aircraft is closely connected to the exhaust, i.e. the emitted trace gases and the lateral and vertical flight pattern. An assessment of flight patterns can contribute to minimize the climate impact of route networks and the potential of climate optimised routing for conventional aircraft [19, 27–30] and climate optimised design [31, 32] was already shown before multiple times.

The magnitude of aircraft emissions depends on many parameters, for example air density, air resistance and technical solutions of aircraft designs and vary with speed and cruise altitude. Hence, they can be optimised by design, which is one of the steps for a climate-optimised hypersonic route network as shown in Fig. 8.1. The following sections present a software to estimate the stratospheric-adjusted radiative forcing of single trajectories, which can be included in addition to emission optimisation
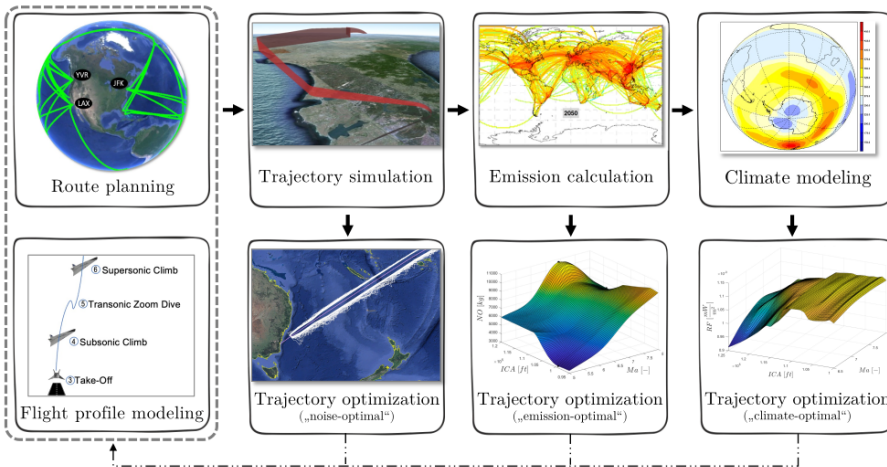
Figure 8.1: Scheme of a climate-optimised hypersonic route network based on flight profile modelling, route planning, trajectory simulation, emission calculation and climate modelling. Courtesy of Daniel Bodmer [201].

in the climate-optimised route network (Fig. 8.1). The software calculations are based on atmospheric and radiative sensitivities from chapter 7 (Table 7.3) and returns the stratospheric-adjusted radiative forcing for a 4D data set of water vapor, hydrogen and nitrogen oxide emissions.

8.3. PYTHON SOFTWARE RF_OF_TRAJECTORY()

The software consists of one class, i.e. rf_of_trajectory(). The class contains multiple python functions to calculate the stratospheric-adjusted radiative forcing. Individual functions of the software code are shown and briefly described in Table 8.1. Calling the class creates an instance, which is based on the specified trajectory-file and data are distributed internally via *self*. An additional function stored in an individual file writes the calculated values to an excel-file.

8.3.1. SOFTWARE CODE

The software is maintained on GitHub and the most recent version is v1.1. Each version is provided with a digital object identifier (DOI) and stored at zenodo.org for reference. The software code is written according to the PEP8 style, which for example proposes specific wording styles for variables, functions and classes. The modules flake8, black and pylint were used to improve the integrity and quality of the software code, which includes e.g. identification of unused variables, style recommendations and hidden bugs. From version 1.1 onward, the software is distributed as a python package. The directory contains the code files and an input file containing global tropopause levels. The software code itself (main executable and package) can be found in the appendix starting on page 189. The execution of the software code requires the modules *xarray,*

numpy, *pandas*, *scipy*, *xlsxwriter* and *netcdf4* to be imported within python. It is recommended to install via pip. The output is stored in an excel-file, which lists the calculated values for each input trajectory. The software can be executed with 'python3 main.py <path_to_trajectory_files>'.

8.3.2. Class Functions

The functions load trajectory data, mask vertical levels of emission data, calculate the stratospheric-adjusted radiative forcing to latitude and altitude of trajectory emission and estimate the water vapor, ozone and total stratospheric-adjusted radiative forcing. The object-oriented programming style improves overall clarity and comprehensibility. Most functions do directly apply changes to the *pandas* DataFrame stored in the class instance (*self*). The complete list of functions is as follows.

Table 8.1: Table of thirteen functions of the python class rf_of_trajectory().

Class function	Description
load_trajectory_as_dataframe(self)	Loads data, applies time normalization and recalculates altitude from feet to kilometer
horizontal_interp(self, ...)	Interpolates atmospheric sensitivities to latitude of emission
vertical_interp(self, ...)	Interpolate and extrapolates atmospheric sensitivities to altitude of emission
remove_emission_normalization(self, ...)	Adjusts weighted emissions to total emissions
drop_vertical_levels(self, ...)	Removes values, where altitude of emission is below the tropopause. Manual input of vertical threshold in hPa is optional
o3_rf_from_h2o_emis(self)	Calculates ozone radiative forcing from water vapor emissions
h2o_rf_from_h2o_emis(self)	Calculates water vapor radiative forcing from water vapor emissions
o3_rf_from_h2_emis(self)	Calculates ozone radiative forcing from hydrogen emissions
o3_rf_from_no_emis(self)	Calculates ozone radiative forcing from nitrogen oxide emissions
total_rf(self)	Sums columns of individual forcings and returns a net value
total_o3_rf(self)	Sums columns of individual ozone forcings and returns a net value
total_h2o_rf(self)	Sums columns of individual water vapor forcings and returns a net value
total_emis(self)	Sums columns of individual emissions and returns a list of total emissions

8

8.4. COMPARISON OF TWO TRAJECTORIES

8.4.1. OVERVIEW OF TRAJECTORIES

The stratospheric-adjusted radiative forcing of two trajectories – Brussels to Sidney and London to New York – were calculated with the software and are being compared in this subsection. Generally, aircraft trajectories are bound to city-pairs and each trajectory has its own properties. These properties are for example the flight path, the vertical flight profile, the cruise altitude and emitted trace gases along the flight path.
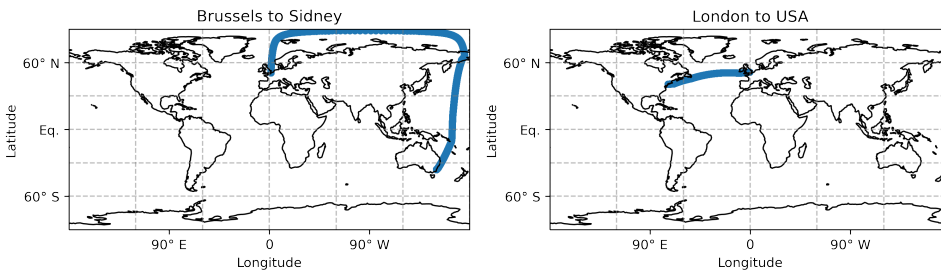
Figure 8.2: World map of trajectories between two city-pairs Brussels-Sidney (left) and London-New York (right).

Figure 8.2 shows the global flight path for both trajectories. The flight path from London to New York is a direct path across the Atlantic. In comparison, the flight from Brussels to Sidney initially tends towards the north-pole and then continuous to southern mid-latitudes crossing the the pacific Ocean. Figure 8.3 shows the vertical flight profile along the trajectory for two trajectories. Clearly, the distance of the two trajectories differs one order of magnitude. The cruise phase is comparably long for Brussels to Sidney with increasing cruise altitude. The cruise phase for the London to New York flight is shorter with constant cruise altitude.
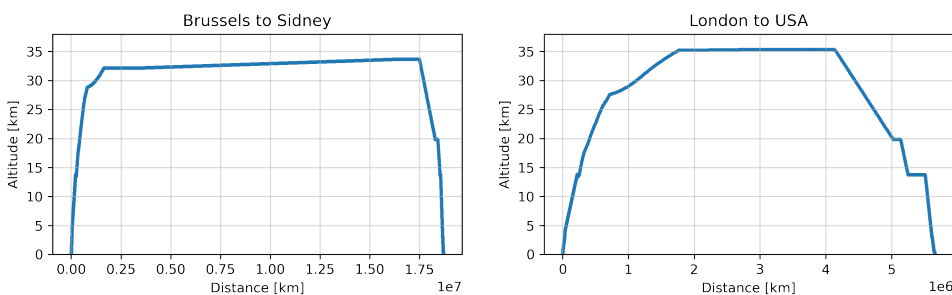

Figure 8.3: Altitude versus distance of trajectories between two city-pairs Brussels-Sidney (left) and London-New York (right).

Emitted Trace Gases   Table 8.2 shows the integrated H_2O, H_2 and NO_x emissions along the two flight paths. Clearly, the water vapor and nitrogen oxide emissions are larger

for the longer flight distance between Brussels and Sidney. Hydrogen emissions are very similar in magnitude and slightly higher for the flight from London to New York. The water vapor emission above the tropopause of one trajectory is approximately five orders of magnitude smaller than a hypersonic route network shown in Table 3.4. The ratio of emitted hydrogen to water vapor particle numbers is approximately a factor three smaller for the STRATOFLY MR3 aircraft compared to ZEHST and LACPAT PREPHA-type aircraft. Clearly, the newer STRATOFLY MR3 aircraft design comes with a more efficient hydrogen combustion. The ratio of emitted nitrogen to water vapor particle numbers is approximately one order of magnitude larger for the STRATOFLY MR3 aircraft. Here, the combustion efficiency is significantly less compared to the other aircraft designs. Clearly, the impact on ozone from nitrogen oxide emissions should increase accordingly.

Table 8.2: Integrated H_2O, H_2 and NO_x emissions of trajectories between two different city-pairs.

Emission	Domain	Brussels-Sidney	London-USA
H_2O	All altitudes	1378 t	817 t
H_2	All altitudes	6.5 t	6.9 t
NO_2	All altitudes	13.40 t	2.97 t
H_2O	above tropopause	1095 t	556 t
H_2	above tropopause	3.5 t	4.1 t
NO_2	above tropopause	13.26 t	2.87 t

8.4.2. ESTIMATE OF TRAJECTORY RADIATIVE FORCING

Total radiative forcing of hypersonic aircraft, as calculated in this thesis, includes contributions from water vapor, ozone and methane perturbations. As shown in chapter 7, the atmospheric perturbation calculations with the atmospheric chemistry general circulation models and the related radiative forcing are not always statistically significant. This includes in particular methane changes for all three emissions, water vapor changes due to hydrogen and nitrogen oxide emission.

Figure 8.4 shows each contribution to the total radiative forcing, excluding radiative forcing due to methane changes and water vapor changes due to nitrogen oxide emission. The contributions of water vapor radiative forcing due to water vapor emission and ozone radiative forcing due to all emissions shows values in accordance to chapter 7. Water vapor radiative forcing from hydrogen emission is two orders of magnitude smaller than from water vapor emission.

Table 8.3: Total radiative forcing for trajectories between two different city-pairs, which includes water vapor radiative forcing due to water vapor changes and ozone radiative forcing due to emission of water vapor, hydrogen and nitrogen oxide. Furthermore, radiative forcing normalized with the shortest distance between cities above ground (RF / km) and the flight distance (RF / flight-km).

City-Pair	RF	RF / km	RF / flight-km
Brussels-Sidney	2.3 $\mu W\,m^{-2}$	0.14 $nW\,m^{-2}$ / km	0.12 $nW\,m^{-2}$ / flight-km
London-USA	0.9 $\mu W\,m^{-2}$	0.16 $nW\,m^{-2}$ / km	0.16 $nW\,m^{-2}$ / flight-km

The total radiative forcing (Table 8.3) is larger for the flight from Brussels to Sidney.
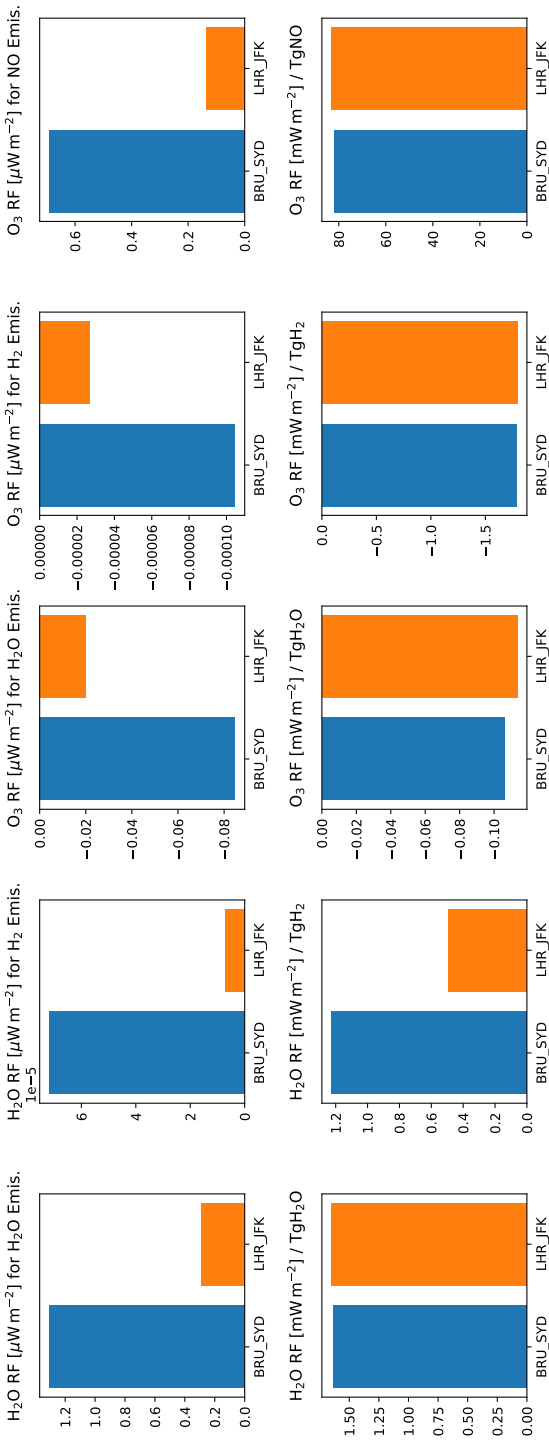
Figure 8.4: Stratospheric-adjusted radiative forcing due to atmospheric water vapor and ozone perturbations and the sensitivity ratio per Tg of emitted trace gas. 'BRU_SID' represents the trajectory Brussels-Sidney, while 'LHR_JFK' represents the trajectory London-New York.

8

However, considering that the distance is one order of magnitude apart (Fig 3.7), the total radiative forcing per flight kilometer is lower for the flight from Brussels to Sidney (0.12 nW m^{-2} / flight-km) than for the flight between the London and New York (0.16 nW m^{-2} / flight km). The same applies if the direct (geodesic) line connecting the city-pairs is used for normalization. There, the values are the same for London to New York and slightly larger for Brussels to Sidney for the direct line (0.14 nW m^{-2} / km) compared to the flight distance (0.12 nW m^{-2} / flight-km).

8.5. CRUISE ALTITUDE OPTIMISATION LOOP
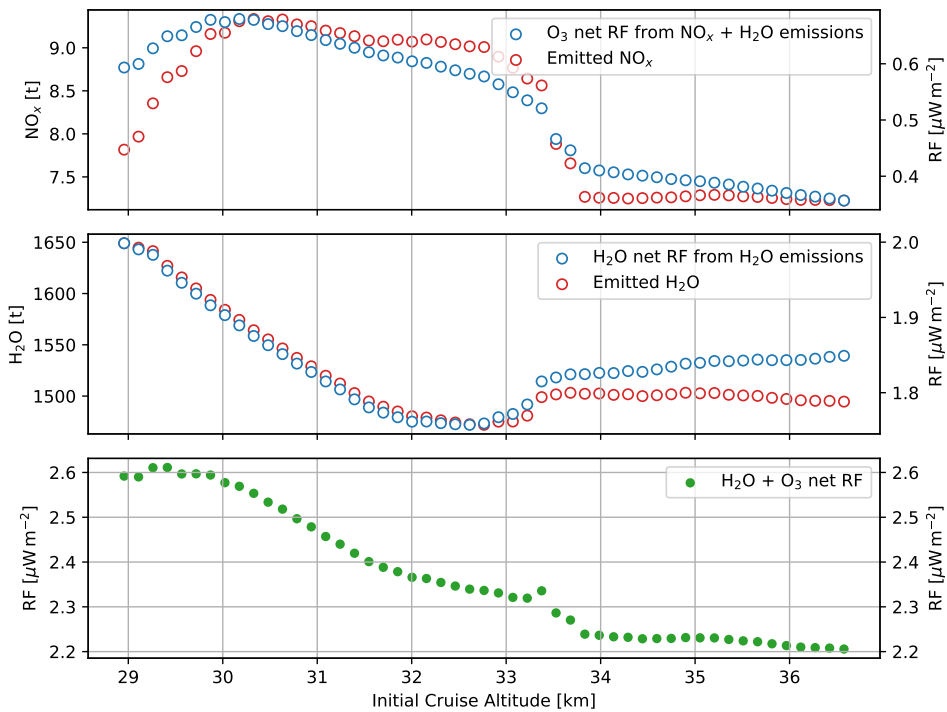
Figure 8.5: Optimised emissions for a trajectory from Brussels to Sidney of the STRATOFLY MR3 aircraft and the calculated stratospheric-adjusted radiative forcing using the software rf_of_trajectory(). (a) shows the ozone net radiative forcing for nitrogen oxide and water vapor emissions and the magnitude of nitrogen oxide emissions, (b) shows water vapor net radiative forcing and the magnitude of water vapor emissions and (c) depicts the total net radiative forcing of ozone and water vapor changes caused by nitrogen oxide and water vapor emissions.

The optimisation procedure over trajectories, emissions and climate as shown in Fig. 8.1 can be applied to calculate the climate-optimal cruise altitude for trajectories or complete route networks. Effectively, these calculations allow to calculate a 'global' minimum over a set of trade-off parameters instead of the local minimum in terms of climate. To achieve this, the python software rf_of_trajectory() is included in a loop, where the cruise altitude is varied from 29 km to 37 km with a step size of approximately

150 m and emission values depending on altitude and trajectory are fed to the software. Note that former calculations of the climate impact of the STRATOFLY MR3 aircraft were done with fixed emissions for each cruise altitude (p. 95). Here, at each cruise altitude step the software returns the stratospheric-adjusted radiative forcing for the calculated emissions. For this specific example, the magnitude of both H_2O and NO_x emissions varies approximately by 12 and 25 % with altitude (Fig. 8.5 a,b). Based on this input the optimisation potential of cruise altitude variation goes up to 17.6 %. Note that the radiative forcing calculation uses both, radiative sensitivities from Table 7.3 and cruise altitude dependent emissions, which ultimately results in an optimum on the upper end of the cruise altitude range based on these two parameters. Fig. 8.6 shows the relative optimisation potential for individual radiative forcings and the combined forcing based on the emitted trace gases for initial cruise altitudes. The climate and emission optimal cruise altitude for H_2O perturbations would be slightly below 33 km, for O_3 perturbations it would be at the upper end of cruise altitudes, i.e. approximately 36.5 km. The latter cruise altitude has also the largest relative optimisation potential for combined radiative forcings. These results will be part of a forthcoming publication with Daniel Bodmer [200].
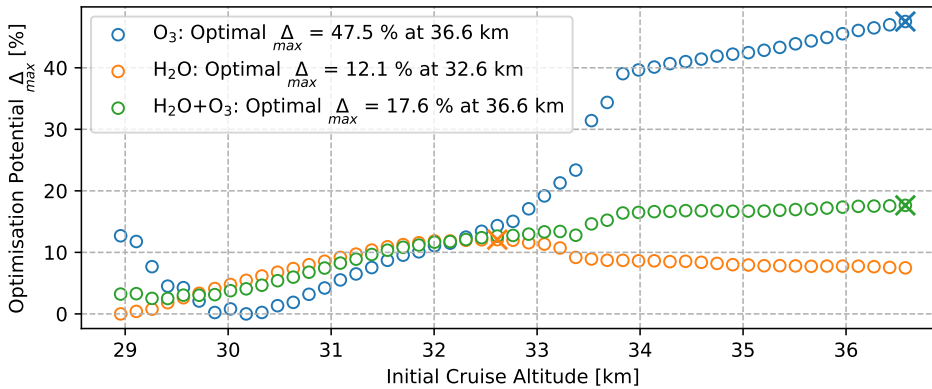
Figure 8.6: Relative optimisation potential Δ_{max} based on ozone and water vapor net radiative forcing calculations for the individual net radiative forcings and the total net radiative forcing.

8.6. LIMITATIONS OF THE TRAJECTORY RADIATIVE FORCING ESTIMATE

The software calculations are based on results of an atmospheric chemistry general circulation model and can be deemed very robust. Nevertheless, there are some limitations and the most important ones are listed in the following paragraphs. They should be considered as potential extensions for future versions and as points to bear in mind when using the software.

Climate Metric Limitation   A multitude of climate metrics exist and their comparability is not clear to everyone [202]. The metric used in this thesis is the annual average stratospheric-adjusted radiative forcing. Hypersonic aircraft results show significant radiative forcing from water vapor and ozone changes and for other models methane contributes as well [33]. The perturbation lifetime of ozone, which is on the first order on the scale of months, and the lifetime of water vapor, which is on the order of years, are comparably closer than for example contrail lifetime and carbon dioxide lifetime. For the latter two it would be crucial to include the accumulated impact on climate over centuries after aircraft operation. The effect of accumulative radiative forcing, which is major for carbon dioxide emissions, is certainly smaller in comparison for hypersonic aircraft with hydrogen propulsion and hence the stratospheric-adjusted radiative forcing is a good metric to estimate the climate impact of a fleet of hypersonic aircraft.

Normalization Metric Limitation   Table 8.3 shows that the application of normalization metrics, which makes the climate impact of trajectories more comparable, can cause difficulties in which metric to use. The correct choice is not obvious. For example it makes a difference if the shortest distance between airports or the flight distance is used. The latter differs very much from the shortest distance for hypersonic aircraft, since they are restricted to flying over the ocean to reduce noise close to human residences.

Seasonal Limitation   The seasonal variability of atmospheric composition changes and radiative forcing was estimated in the sensitivity study of chapter 7 with multi-annual mean values and hence are included in the trajectory estimate as an average. The seasonal effect is most probably significant, since dynamics (perturbation transport) and chemistry is largely influenced by the seasons and the inclusion of seasonal sensitivities could increase or decrease perturbations and in turn radiative forcing depending on season and latitude of emission. A time resolved treatment of trajectories is not included, neither in the input data nor in the software. However, monthly sensitivities could be included in the future based on the available data.

Altitude Limitation   Water vapor radiative forcing due to hydrogen emission shows negative values (Fig. 8.4), which disagrees with the findings from chapter 7. Clearly, the altitudes of the main hydrogen emission of the two trajectories (below cruise altitude) and the linear extrapolation to these altitudes could causes wrong results. It is recommended to limit the radiative forcing calculations of hydrogen (due to low altitude of emission) and ozone (non-linear perturbation and radiative forcing) within the software to cruise altitude with the function *drop_vertical_levels(self, ...)*. In contrast water vapor radiative sensitivities behave more linearly and EMAC results recreate the linear trend of radiative forcing at lower altitudes (see p. 6.3.3)[185].

Latitude Limitation   In the sensitivity studies two regions were not included in the latitude emission variation (Fig 3.8). They are emission at southern tropics and southern polar regions. Hence, for southern polar regions (90° S-60° S) sensitivities for southern mid-latitude emission scenarios are used. Since aircraft emissions rarely appear far

south, the impact of this approximation should be low. For southern tropical emission the values of northern tropical emission scenarios are used.

Input Data Limitation   Currently the software code is optimised for specific .mat files from TUHH. A generalized approach was not included, since, first, the number of applications will be limited compared to python modules like pandas or xarray and, second, the introduction of another file specific import function is easily achievable due to the standardized internal pandas DataFrame layout.

8.7. SUMMARY

The software is a helpful tool to include climate estimates in hypersonic route network planning. It facilitates – with low computing cost and low time investment – to estimate the climate impact of hypersonic aircraft and to reduce the climate impact of whole hypersonic route networks. Here, the altitude optimisation potential of hypersonic climate impact is estimated to be at most 18 % based on the estimate of one particular trajectory. Note that the STRATOFLY MR3 aircraft emit one order of magnitude more NO_x compared to ZEHST or LAPCAT. Clearly, the evaluation depends very much on the specific aircraft design and the aircraft combustion efficiency. The software code is based on widely used modules that have been continuously maintained for more than a decade and should persist for a long time. The internal calculations are based on one line *DataFrame* operations that can easily be read and comprehended. Future developments could include the export of plots (e.g. flight paths and bar plots), the selection of different normalization metrics (e.g. 'mW m^{-2} / km' and 'mW m^{-2} / (pax-km)') and a time resolved estimate. An implementation in an optimisation loop requires the correct normalization metric to find the most efficient route network with the least amount of trade-offs. Further, sensitivities from lower altitudes should be combined with sensitivities from this thesis to form a complete set and to reduce the error estimate for the lower altitudes. Before the extension, it is strongly advised to limit the stratospheric-adjusted radiative forcing calculations to cruise altitudes of aircraft designs. This should serve as a robust approximation, since most of the trace gases are emitted at cruise altitude. A potential merge candidate, which could incorporate this software, is AirClim [21, 31]. AirClim is continuously developed and a new version called Open AirClim [203] will be published. The merged software would be able to estimate the climate impact of aircraft at all technologically viable cruise altitudes to date and during all flight phases.

8

9

CONCLUSION

9.1. OVERVIEW

H YPERSONIC aircraft are a very interesting concept with an obvious advantage compared to conventional aircraft, i.e. travel time. While there are many areas of open research like propulsion, noise or customer well-being, this thesis focused on the climate impact of hydrogen fuelled hypersonic aircraft. The main message here certainly is that hydrogen powered hypersonic aircraft have a climate impact multiple times that of conventional aircraft. The advantage compared to aircraft with kerosene propulsion is the short perturbation lifetimes (years) compared to carbon dioxide perturbations (100-100000 years). Meaning, after an aircraft is taken out of service, the impact on climate will remain for shorter time and therefore is easier to assess and evaluate.

The methods included the application of two state-of-the-art numerical models (EMAC, LMDZ-INCA) with an atmospheric chemistry general circulation model setup and a radiation model setup. The spin-up for the former was ten years – to account for equilibrium of perturbations – and five years for the equilibrium results. The five years were used to assess statistical significance. For the radiation model setup three months spin-up – to account for stratospheric temperature adjustment – and twelve months for the equilibrium results were used. An additional speed-up technique to reduce the spin-up time was successfully applied for the EMAC sensitivity simulations.

Overall, the dominating climate impact of hypersonic aircraft comes from water vapor emissions increasing middle atmospheric water vapor and nitrogen oxide emissions causing ozone perturbations, both of which cause warming. Methane changes might contribute to the climate impact by lessening the warming to some extent, however, the LMDZ-INCA and EMAC model did not show consistent results in terms of magnitude. Three conclusions can be drawn from this.

First, a new set of simulations with the recently updated EMAC radiation scheme might bring new insights to the discrepancy in methane radiative forcing. This might be worth wile, since methane clearly has the potential to lessen the overall warming according to the LMDZ-INCA model.
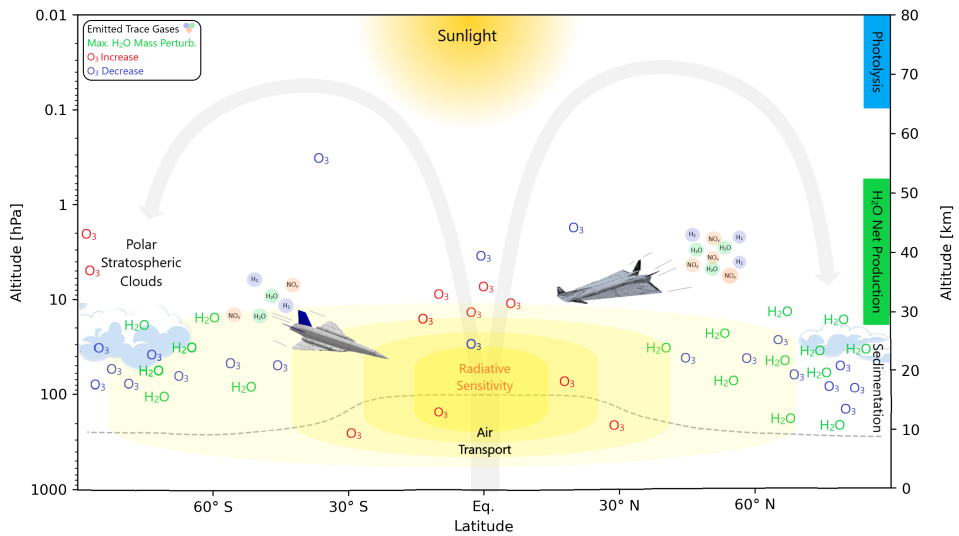
137

Figure 9.1: Overview of all relevant emissions and atmospheric processes with coarse orders of magnitude (not to scale) in the context of hypersonic aircraft.

Second, the reduction of nitrogen oxide emissions should be focused on as a development goal for hypersonic aircraft. The current and long-lasting situation with a recovering ozone layer approximately until the end of this century calls for technological advancements in combustion efficiency. The main point, from a climate point of view, is that with a reduced ozone depletion during hypersonic aircraft operation the climate warming will decrease as well.

Third, while room for improvement exists for combustion efficiency in terms of nitrogen oxides, the situation is different for water vapor emissions. Here, each of the potential fuel types (liquid natural gas, kerosene, liquid hydrogen) eventually causes water vapor emissions with a lower limit of optimization. Therefore, regardless of the type of fuel water vapor emissions will remain one of the main factors of the climate impact of hypersonic aircraft. As the water vapor perturbation lifetime increases with altitude of emission, this is a major challenge for the development of future high-flying aircraft. Note that according to a recent Fraunhofer Society report the use of hydrogen has no alternative for speeds above Mach 8 due to the required energy density of the fuel [129]. Therefore, opportunities to reduce the climate impact from water vapor lie in climate-optimized route networks, where the routes with the lowest water vapor perturbation time and hence lowest climate warming are selected. However, this certainly poses another challenge. On the one hand, hypersonic aircraft are well suited for long-distance travel and flying between city-pairs often covers many latitude regions. On the other hand, optimizing a route network to a reduced climate warming might increase the cost of aircraft operation due to an increased fuel burn.

The software developed during this thesis will be very helpful to assess new hypersonic aircraft designs. Since the climate impact of ozone perturbations and water vapor

perturbations has mostly opposing trends, which additionally can change with latitude of emission, an evaluation is not apparent and might bring surprising results. Hence, trajectory specific calculations based on sensitivities are very much required. Clearly, the altitude of emission and the travel latitudes are very important parameters that can be evaluated using the software. The former is probably easier to exploit with technological solutions, whereas the latter most probably requires economical trade-offs. Note that the identification of climate-optimal cruise altitudes based on optimised trajectories and emissions within a loop brings together multi-disciplinary research results and the resulting error propagation should be closely evaluated. Here, I want to stress that the software delivers robust results, but calculations will only be as good as the actual input data. The software itself can be further extended, e.g. by an option to include seasonal estimates, i.e. time of aircraft operation. Whether operation of aircraft during certain months of the year might be a significant mitigation opportunity remains an open question.

To conclude, in my opinion, to travel around the world within a few hours is a dream and in that regard hypersonic aircraft are a very interesting project for the future and coming generations. However, as I see it, the aircraft industry is currently trying to reach their climate target and hypersonic aircraft will not alleviate pressure, but rather might add difficulties to reach climate goals. Figure 9.2 by Grewe et al. [3] shows very nicely the temperature change contribution from the aircraft industry for scenarios with current technologies, business-as-usual and idealized scenarios. Clearly, reaching the ideal scenarios is a major challenge for it's future development. Hence, I think the question is not really if hypersonic aircraft will be built, but whether it will be in the next decades or rather in a century or later, when, hopefully reducing climate warming is not as urgent as today.
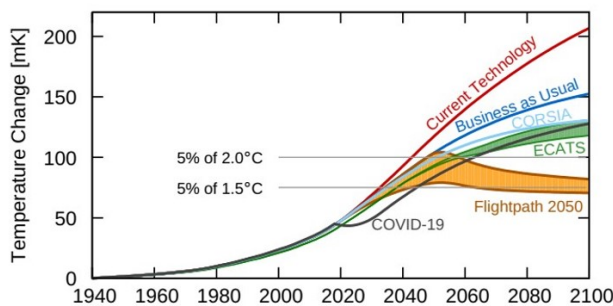
Figure 9.2: The horizontal lines indicate 5 % of a 2 °C and 1.5 °C climate target. The scenarios describe a future use of current technology, i.e. without technology improvements (CurTec, red), a business-as-usual future technological improvement (BAU, blue), the offsetting scheme of the international civil aviation organisation (CORSIA, light blue), and 2 Flightpath 2050 scenarios which differ in the speed of technology improvements (FP2050 and FP2050-cont, brown and orange, respectively).

Regarding an emerging hydrogen economy, the operation of hydrogen-powered hypersonic aircraft would unfortunately not contribute to the goal to reduce global warming. Even though hydrogen powered hypersonic aircraft only emit water vapor, nitrogen

oxides and unburnt hydrogen and probably avoid forming contrails at cruise altitudes.

9.2. ANSWERS TO SCIENTIFIC QUESTIONS

In the introduction of this thesis seven open scientific questions were listed (p. 3). Which questions were answered and to what extent is addressed in the text following – for a quick reference – the list of questions.

1. By how much do emissions of hydrogen powered hypersonic aircraft affect atmospheric composition?

2. Which and to what extent do dynamical and chemical processes control the perturbation lifetime of atmospheric composition changes?

3. How does cruise altitude control the atmospheric composition changes?

4. How large is the radiative forcing caused by these atmospheric composition changes?

5. How does the change in radiative forcing affect climate?

6. How does the climate impact of hypersonic aircraft compare to subsonic and supersonic aircraft?

7. What is the climate optimal cruise altitude of one of the currently most advanced hypersonic aircraft?

1. The question by how much hypersonic emissions affect atmospheric composition was answered in detail within the sensitivity study in chapter 7 and presented in two look-up tables. The atmospheric composition of H_2O, O_3 and CH_4 is most sensitive to emission of nitrogen oxides followed by hydrogen and water vapor. For altitude of emission between 30-38 km total ozone depletion reaches at most 0.21 % and water vapor in the middle atmosphere increases at most by 3.1 %. Note that these results are based on emissions, which magnitudes are inverse to these sensitivities, i.e. they consist mostly of water vapor, followed by hydrogen and nitrogen oxides. Hence, the largest impact comes from water vapor and nitrogen oxide emissions, while hydrogen emission can be deemed less important in comparison. The magnitude of atmospheric perturbations changes very much with latitude and altitude of emission. These changes for the most part differ by a factor and not by an order of magnitude. An exception is emission of water vapor at southern latitudes, which shows ozone perturbations one order of magnitude larger than most other water vapor emission scenarios. This effect is largely driven by polar stratospheric clouds, which are a very local and seasonal phenomenon.

2. The most important process controlling the perturbation lifetime is the residual circulation in the middle atmosphere, also called Brewer-Dobson circulation. Note that the speed of the Brewer-Dobson circulation is expected to increase due to climate change, which should decrease the perturbation lifetime of emitted trace gases accordingly. The importance of the residual circulation is further highlighted by a new scientific finding presented in this thesis. It was shown that an enhanced oxidation capacity

caused by hypersonic emissions ($H_2O \leq H_2 > NO_x$) (photo-)chemically increases water vapor perturbations and in turn increases perturbation lifetime. Results show that this trend increases with altitude at 25-40 km. How this trend continues to develop at even higher altitudes remains to be answered. This (photo-)chemical addition to water vapor perturbations is removed via the residual circulation the same way as the emitted trace gases and is a second order effect. The important message here is that a (photo-)chemical net depletion of water vapor does not reduce the climate impact of hypersonic aircraft. Another process combining chemistry and dynamics are polar stratospheric clouds, which were shown to be important for denitrification and comparably unimportant for dehydration of emitted nitrogen oxides and water vapor perturbations, respectively. Re-circulation of moist air via the troposphere might affect perturbation lifetime to a small extent and no large scale phenomena were visible in seasonal data. More important for perturbation lifetime should be the re-circulation within the middle-atmosphere, where sinking polar air can be re-circulated via horizontal mixing.

3. A change in cruise altitude very much changes the magnitude of atmospheric composition changes. The effect varies depending on emitted trace gases. For nitrogen oxide emissions, the effect on water vapor and ozone perturbations (up to 37 %) and methane lifetime decreases with altitude from 30-40 km. Results from combined emissions suggests that the relation is probably not linear and might include one or two local maxima around 35 km. This remains to be answered in more detail and would require more sensitivity studies at more altitude levels. For water vapor and hydrogen emissions, the effect on water vapor perturbation increases with altitude (by up to 26 % for water vapor emission), while ozone depletion stays nearly the same for most latitudes of emission for the former and increases for the latter at all latitudes of emission.

4. The order of magnitude of stratosphere-adjusted radiative forcing caused by a potential fleet of hypersonic aircraft is several tens of mWm^{-2} and thus would significantly contribute to radiative forcing of global aviation. In comparison to a conventional aircraft the two analysed hypersonic aircraft ZEHST and LAPCAT increase stratosphere-adjusted radiative forcing by 6 and 16 times, respectively, if compared to the same revenue passenger kilometers. The by far largest warming of total radiative forcing comes from water vapor perturbations, followed by net warming from ozone perturbations (cooling for H_2O and H_2 emissions and warming for NO_x emission). For combined emissions methane radiative forcing does contribute to cooling. The associated order of magnitude needs to be validated with further simulations.

5. For the calculation of global mean-surface temperature change, the stratospheric-adjusted radiative forcing is a comparably good measure [5]. Climate sensitivity parameters and efficacies, which are helpful to improve the global mean-surface temperature representation by radiative forcing, were not identified in this thesis. The same applies for effective radiative forcing, which would require a significantly more complex calculation method. The identification of the specific parameters might be of interest in the future, since, firstly, water vapor, ozone and methane perturbations from hypersonic aircraft are spatially inhomogeneously distributed, which was addressed to some extent by using the stratosphere-adjusted radiative forcing, and, secondly, due to reports on efficacies of stratospheric water vapour background concentrations ranging between 38-100 % [151, 204, 205]. Note that water vapour background concentrations and wa-

ter vapour perturbations of high-altitude emissions do not show identical distributions. The largest accumulation of water vapour particles due to hypersonic emissions appears mostly in one Hemisphere and for current route networks it would be at higher northern latitudes; an area which is known to have a higher climate sensitivity [206]. Nevertheless, this topic should be addressed in the future.

6. The climate warming associated with hypersonic aircraft transport is a multitude (8-21 times) of the climate warming of conventional aircraft transport. The former estimate is based on water vapor, ozone and methane perturbations and the latter on contrail formation, carbon dioxide, water vapor and nitrogen oxide (short-lived ozone, primary mode ozone, methane) effects and normalized to revenue passenger kilometers. The contribution of water vapor continuously increases with altitude from the troposphere up to 40 km. The same applies for supersonic aircraft, where the climate impact from water vapor perturbations is lower compared to hypersonic aircraft, because of the lower cruise altitude. The contribution of ozone radiative forcing is more complicated. For supersonic cruise altitudes (13-23 km) it shows strong non-linear behavior, with positive and negative radiative forcing for emission below and above 17-19 km, respectively [136]. In this dissertation four cruise altitudes (26 km, 30 km, 35 km, 38 km) of combined or individual emissions were evaluated and it was shown that ozone radiative forcing causes warming at all four cruise altitudes and remains non-linear up to 38 km, with a high variability between altitudes of 30-38 km. Above 38 km altitude of emission the ozone radiative forcing could become closer to zero or might even become negative.

7. Generally, the climate warming of hypersonic aircraft increases with altitude and zero emission of nitrogen oxides would be a best case in terms of climate warming. In reality, depending on aircraft design the emission ratio of nitrogen oxides to water vapor can create a minimum in radiative forcing at specific altitudes. Results from this dissertation showed that the climate optimal cruise altitude of the STRATOFLY MR3 aircraft is at around 37 km and the warming effect can be reduced by approximately 18 %. Note that this result is based on a single trajectory and calculations correlate strongly with the flight path, i.e. the horizontal distribution of emissions and might change significantly for other trajectories or aircraft designs.

9

BIBLIOGRAPHY

[1] UN. 2015. URL: https://unfccc.int/process-and-meetings/the-paris-agreement/the-paris-agreement.

[2] E. Terrenoire, D. A. Hauglustaine, T. Gasser, and O. Penanhoat. 'The contribution of carbon dioxide emissions from the aviation sector to future climate change'. In: *Environmental Research Letters* 14.8 (July 31, 2019), p. 084019. ISSN: 1748-9326. DOI: 10.1088/1748-9326/ab3086. URL: https://iopscience.iop.org/article/10.1088/1748-9326/ab3086 (visited on 10/29/2021).

[3] V. Grewe, A. Gangoli Rao, T. Grönstedt, C. Xisto, F. Linke, J. Melkert, J. Middel, B. Ohlenforst, S. Blakey, S. Christie, S. Matthes, and K. Dahlmann. 'Evaluating the climate impact of aviation emission scenarios towards the Paris agreement including COVID-19 effects'. In: *Nature Communications* 12.1 (June 22, 2021), p. 3841. ISSN: 2041-1723. DOI: 10.1038/s41467-021-24091-y. URL: https://www.nature.com/articles/s41467-021-24091-y (visited on 10/29/2021).

[4] T. Planès, S. Delbecq, V. Pommier-Budinger, and E. Bénard. 'Simulation and evaluation of sustainable climate trajectories for aviation'. In: *Journal of Environmental Management* 295 (Oct. 2021), p. 113079. ISSN: 0301-4797. DOI: 10.1016/j.jenvman.2021.113079. URL: https://www.sciencedirect.com/science/article/pii/S0301479721011415 (visited on 01/28/2023).

[5] D. S. Lee, D. W. Fahey, A. Skowron, M. R. Allen, U. Burkhardt, Q. Chen, S. J. Doherty, S. Freeman, P. M. Forster, J. Fuglestvedt, A. Gettelman, R. R. De León, L. L. Lim, M. T. Lund, R. J. Millar, B. Owen, J. E. Penner, G. Pitari, M. J. Prather, R. Sausen, and L. J. Wilcox. 'The contribution of global aviation to anthropogenic climate forcing for 2000 to 2018'. In: *Atmospheric Environment* 244 (Jan. 1, 2021), p. 117834. ISSN: 1352-2310. DOI: 10.1016/j.atmosenv.2020.117834. URL: https://www.sciencedirect.com/science/article/pii/S1352231020305689 (visited on 03/04/2022).

[6] *AR4 Climate Change: Synthesis Report — IPCC.* 2007. URL: https://www.ipcc.ch/report/ar4/syr/ (visited on 03/04/2022).

[7] *AR5 Synthesis Report: Climate Change 2014 — IPCC.* 2014. URL: https://www.ipcc.ch/report/ar5/syr/ (visited on 03/04/2022).

[8] D. W. Fahey, S. L. Baughcum, J. S. Fuglestvedt, M. Gupta, D. S. Lee, and R. Sausen. 'WHITE PAPER ON CLIMATE CHANGE AVIATION IMPACTS ON CLIMATE STATE OF THE SCIENCE'. In: *ICAO Environmental Report* (2016), p. 9.

[9]   V. Masson-Delmotte, P. Zhai, A. Pirani, S. L. Connors, C. Péan, S. Berger, N. Caud, Y. Chen, L. Goldfarb, M. I. Gomis, M. Huang, K. Leitzell, E. Lonnoy, J. B. R. Matthews, T. K. Maycock, T. Waterfield, Ö. Yelekçi, R. Yu, and B. Zhou, eds. *Climate Change 2021: The Physical Science Basis. Contribution of Working Group I to the Sixth Assessment Report of the Intergovernmental Panel on Climate Change*. Cambridge, United Kingdom and New York, NY, USA: Cambridge University Press, 2021. DOI: `10.1017/9781009157896`.

[10] Fuel Cells and Hydrogen: Joint Undertaking. *Hydrogen-powered Aviation*. [Online; accessed 4-May-2022]. 2020. URL: `https://www.fch.europa.eu/public ations/hydrogen-powered-aviation`.

[11] P. J. Crutzen. 'The influence of nitrogen oxides on the atmospheric ozone content'. en. In: *Quarterly Journal of the Royal Meteorological Society* 96.408 (1970), pp. 320–325. ISSN: 1477-870X. DOI: `10.1002/qj.49709640815`. URL: `http://o nlinelibrary.wiley.com/doi/abs/10.1002/qj.49709640815` (visited on 07/14/2022).

[12] P. J. Crutzen. 'SST's: A Threat to the Earth's Ozone Shield'. In: *Ambio* 1.2 (1972). Publisher: [Springer, Royal Swedish Academy of Sciences], pp. 41–51. ISSN: 0044-7447. URL: `http://www.jstor.org/stable/4311946` (visited on 07/14/2022).

[13] H. Johnston. 'Reduction of Stratospheric Ozone by Nitrogen Oxide Catalysts from Supersonic Transport Exhaust'. In: *Science* 173.3996 (Aug. 1971). Publisher: American Association for the Advancement of Science, pp. 517–522. DOI: `10.1126/science.173.3996.517`. URL: `http://www.science.org/doi/abs /10.1126/science.173.3996.517` (visited on 07/14/2022).

[14] S. Matthes, D. S. Lee, R. R. De Leon, L. Lim, B. Owen, A. Skowron, R. N. Thor, and E. Terrenoire. 'Review: The Effects of Supersonic Aviation on Ozone and Climate'. In: *Aerospace* 9.1 (Jan. 2022). Number: 1 Publisher: Multidisciplinary Digital Publishing Institute, p. 41. ISSN: 2226-4310. DOI: `10.3390/aerospace9010041`. URL: `https://www.mdpi.com/2226-4310/9/1/41` (visited on 03/04/2022).

[15] V. Grewe, A. Stenke, M. Plohr, and V. D. Korovkin. 'Climate functions for the use in multi-disciplinary optimisation in the pre-design of supersonic business jet'. en. In: *The Aeronautical Journal* 114.1154 (Apr. 2010). Publisher: Cambridge University Press, pp. 259–269. ISSN: 0001-9240, 2059-6464. DOI: `10.1017/S0001924 000003705`. URL: `http://www.cambridge.org/core/journals/aeronautic al-journal/article/climate-functions-for-the-use-in-multidisci plinary-optimisation-in-the-predesign-of-supersonic-business-j et/1B7C4FEFA1B0D1CD1492BF0CC240137B` (visited on 05/16/2022).

[16] V. Grewe, A. Stenke, M. Ponater, R. Sausen, G. Pitari, D. Iachetti, H. Rogers, O. Dessens, J. Pyle, I. S. A. Isaksen, L. Gulstad, O. A. Søvde, C. Marizy, and E. Pascuillo. 'Climate impact of supersonic air traffic: an approach to optimize a potential future supersonic fleet – results from the EU-project SCENIC'. English. In: *Atmospheric Chemistry and Physics* 7.19 (Oct. 2007). Publisher: Copernicus GmbH, pp. 5129–5145. ISSN: 1680-7316. DOI: `10.5194/acp-7-5129-2007`.

URL: https://acp.copernicus.org/articles/7/5129/2007/ (visited on 04/03/2023).

[17] IPCC. 'Special Report on Aviation and the Global Atmosphere. Prepared in collaboration with the Scientific Assessment Panel to the Montreal Protocol on Substances that Deplete the Ozone Layer'. In: *Intergovernmental Panel on Climate Change*. Ed. by J. E. Penner, D. H. Lister, D. J. Griggs, D. J. Dokken, and M. McFarland. The Edinburgh Building Shaftesbury Road, Cambridge CB2 2RU England: Through Cambridge University Press, 1999, pp. 1–373.

[18] J. M. Haywood, R. P. Allan, J. Bornemann, P. M. Forster, P. N. Francis, S. Milton, G. Rädel, A. Rap, K. P. Shine, and R. Thorpe. 'A case study of the radiative forcing of persistent contrails evolving into contrail-induced cirrus'. en. In: *Journal of Geophysical Research: Atmospheres* 114.D24 (2009). ISSN: 2156-2202. DOI: 10.1029/2009JD012650. URL: http://onlinelibrary.wiley.com/doi/abs/10.1029/2009JD012650 (visited on 08/03/2022).

[19] S. Matthes, U. Schumann, V. Grewe, C. Frömming, K. Dahlmann, A. Koch, and H. Mannstein. 'Climate Optimized Air Transport'. en. In: *Atmospheric Physics - Background – Methods – Trends*. Ed. by U. Schumann. Research Topics in Aerospace. Berlin, Heidelberg: Springer, 2012, pp. 727–746. ISBN: 978-3-642-30183-4. DOI: 10.1007/978-3-642-30183-4_44. URL: https://doi.org/10.1007/978-3-642-30183-4_44 (visited on 07/07/2022).

[20] Margarita R. Vázquez Navarro. 'Life cycle of contrails from a time series of geostationary satellite images'. en. PhD thesis. Munich: Ludwig-Maximilians-Universität, 2009. URL: https://elib.dlr.de/61990/1/vazquez_navarro_margarita_r.pdf.

[21] V. Grewe and A. Stenke. 'AirClim an efficient tool for climate evaluation of aircraft technology'. In: *Atmospheric Chemistry and Physics* 8.16 (Aug. 11, 2008), pp. 4621–4639. ISSN: 1680-7324. DOI: 10.5194/acp-8-4621-2008. URL: https://acp.copernicus.org/articles/8/4621/2008/ (visited on 10/29/2021).

[22] D. S. Stevenson, R. M. Doherty, M. G. Sanderson, W. J. Collins, C. E. Johnson, and R. G. Derwent. 'Radiative forcing from aircraft NOx emissions: Mechanisms and seasonal dependence'. en. In: *Journal of Geophysical Research: Atmospheres* 109.D17 (2004). ISSN: 2156-2202. DOI: 10.1029/2004JD004759. URL: http://onlinelibrary.wiley.com/doi/abs/10.1029/2004JD004759 (visited on 08/03/2022).

[23] C. Kemfert and W.-P. Schill. 'An Analysis of Methane Mitigation as a Response to Climate Change'. en. In: (2009), p. 39. URL: https://www.researchgate.net/profile/Richard-Tol/publication/221678750_An_Analysis_of_Mitigation_as_a_Response_to_Climate_Change/links/542677280cf26120b7b021a8/An-Analysis-of-Mitigation-as-a-Response-to-Climate-Change.pdf.

9

[24]   D. Archer and V. Brovkin. 'The millennial atmospheric lifetime of anthropogenic
        CO2'. en. In: *Climatic Change* 90.3 (Oct. 2008), pp. 283–297. ISSN: 1573-1480. DOI:
        10.1007/s10584-008-9413-1. URL: https://doi.org/10.1007/s10584-00
        8-9413-1 (visited on 07/06/2022).

[25]   D. Archer, M. Eby, V. Brovkin, A. Ridgwell, L. Cao, U. Mikolajewicz, K. Caldeira, K.
        Matsumoto, G. Munhoven, A. Montenegro, and K. Tokos. 'Atmospheric Lifetime
        of Fossil Fuel Carbon Dioxide'. In: *Annual Review of Earth and Planetary Sciences*
        37.1 (May 1, 2009), pp. 117–134. ISSN: 0084-6597, 1545-4495. DOI: 10.1146/annu
        rev.earth.031208.100206. URL: https://www.annualreviews.org/doi/1
        0.1146/annurev.earth.031208.100206 (visited on 10/29/2021).

[26]   F. C. a. H. 2. J. Undertaking. *Hydrogen-powered aviation*. en. Tech. rep. European
        Union, May 2020, p. 96. URL: https://op.europa.eu/en/publication-deta
        il/-/publication/55fe3eb1-cc8a-11ea-adf7-01aa75ed71a1/language
        -en.

[27]   V. Grewe, C. Frömming, S. Matthes, S. Brinkop, M. Ponater, S. Dietmüller, P.
        Jöckel, H. Garny, E. Tsati, K. Dahlmann, O. A. Søvde, J. Fuglestvedt, T. K. Berntsen,
        K. P. Shine, E. A. Irvine, T. Champougny, and P. Hullah. 'Aircraft routing with min-
        imal climate impact: the REACT4C climate cost function modelling approach
        (V1.0)'. In: *Geoscientific Model Development* 7.1 (Jan. 28, 2014). Publisher: Coper-
        nicus GmbH, pp. 175–201. ISSN: 1991-959X. DOI: 10.5194/gmd-7-175-2014.
        URL: https://gmd.copernicus.org/articles/7/175/2014/ (visited on
        03/04/2022).

[28]   S. Matthes, L. Lim, U. Burkhardt, K. Dahlmann, S. Dietmüller, V. Grewe, A. S.
        Haslerud, J. Hendricks, B. Owen, G. Pitari, M. Righi, and A. Skowron. 'Mitiga-
        tion of Non-CO2 Aviation's Climate Impact by Changing Cruise Altitudes'. In:
        Aerospace 8.2 (Jan. 31, 2021), p. 36. ISSN: 2226-4310. DOI: 10.3390/aerospac
        e8020036. URL: https://www.mdpi.com/2226-4310/8/2/36 (visited on
        10/29/2021).

[29]   B. Sridhar, H. K. Ng, and N. Y. Chen. 'Aircraft Trajectory Optimization and Con-
        trails Avoidance in the Presence of Winds'. en. In: *Journal of Guidance, Control,
        and Dynamics* 34.5 (Sept. 2011), pp. 1577–1584. ISSN: 0731-5090, 1533-3884. DOI:
        10.2514/1.53378. URL: https://arc.aiaa.org/doi/10.2514/1.53378
        (visited on 07/07/2022).

[30]   V. Grewe, T. Champougny, S. Matthes, C. Frömming, S. Brinkop, O. A. Søvde, E. A.
        Irvine, and L. Halscheidt. 'Reduction of the air traffic's contribution to climate
        change: A REACT4C case study'. In: *Atmospheric Environment* 94 (Sept. 1, 2014),
        pp. 616–625. ISSN: 1352-2310. DOI: 10.1016/j.atmosenv.2014.05.059. URL:
        https://www.sciencedirect.com/science/article/pii/S135223101400
        4063 (visited on 03/04/2022).

[31]   K. Dahlmann, A. Koch, F. Linke, B. Lührs, V. Grewe, T. Otten, D. Seider, V. Gollnick,
        and U. Schumann. 'Climate-Compatible Air Transport System—Climate Impact
        Mitigation Potential for Actual and Future Aircraft'. In: *Aerospace* 3.4 (Dec. 2016).
        Number: 4 Publisher: Multidisciplinary Digital Publishing Institute, p. 38. ISSN:

2226-4310. DOI: `10.3390/aerospace3040038`. URL: `https://www.mdpi.com/2226-4310/3/4/38` (visited on 03/04/2022).

[32] V. Grewe, L. Bock, U. Burkhardt, K. Dahlmann, K. Gierens, L. Hüttenhofer, S. Unterstrasser, A. G. Rao, A. Bhat, F. Yin, T. G. Reichel, O. Paschereit, and Y. Levy. 'Assessing the climate impact of the AHEAD multi-fuel blended wing body'. In: *Meteorologische Zeitschrift* 26.6 (Dec. 8, 2017), pp. 711–725. ISSN: 0941-2948. DOI: `10.1127/metz/2016/0758`. URL: `http://www.schweizerbart.de/papers/metz/detail/26/87038/Assessing_the_climate_impact_of_the_AHEAD_multi_fu?af=crossref` (visited on 10/29/2021).

[33] J. Pletzer, D. Hauglustaine, Y. Cohen, P. Jöckel, and V. Grewe. 'The climate impact of hydrogen-powered hypersonic transport'. English. In: *Atmospheric Chemistry and Physics* 22.21 (Nov. 2022). Publisher: Copernicus GmbH, pp. 14323–14354. ISSN: 1680-7316. DOI: `10.5194/acp-22-14323-2022`. URL: `https://acp.copernicus.org/articles/22/14323/2022/` (visited on 01/22/2023).

[34] J. F. Pletzer and V. Grewe. 'Sensitivities of Atmospheric Composition and Climate to Hypersonic Aircraft as a Function of Altitude and Latitude of Emissions'. In: *Atmospheric Chemistry and Physics* (2023). in preparation.

[35] V. I. Vernadsky. *The Biosphere*. New York, NY: Springer New York, 1998. ISBN: 978-1-4612-1750-3. DOI: `10.1007/978-1-4612-1750-3_1`. URL: `https://doi.org/10.1007/978-1-4612-1750-3_1`.

[36] T. Lenton. *Earth System Science: A Very Short Introduction*. Publication Title: Earth System Science: A Very Short Introduction. Oxford University Press, 2016. ISBN: 978-0-19-178833-8. URL: `https://www.veryshortintroductions.com/view/10.1093/actrade/9780198718871.001.0001/actrade-9780198718871` (visited on 03/15/2022).

[37] B. Dailey and R. Kent. *Environmental Science and Management*. Revised by Vaughan Redfern and Frauke Urban. 2015.

[38] A. Kuhn and T. Heckelei. 'Anthroposphere'. In: *Impacts of Global Change on the Hydrological Cycle in West and Northwest Africa*. Ed. by P. Speth, M. Christoph, and B. Diekkrüger. Berlin, Heidelberg: Springer, 2010, pp. 282–341. ISBN: 978-3-642-12957-5. DOI: `10.1007/978-3-642-12957-5_8`. URL: `https://doi.org/10.1007/978-3-642-12957-5_8` (visited on 03/16/2022).

[39] A. Gettelman and R. B. Rood. 'Components of the Climate System'. In: *Demystifying Climate Models: A Users Guide to Earth System Models*. Berlin, Heidelberg: Springer Berlin Heidelberg, 2016, pp. 13–22. ISBN: 978-3-662-48959-8. DOI: `10.1007/978-3-662-48959-8_2`. URL: `https://doi.org/10.1007/978-3-662-48959-8_2`.

[40] W. Steffen, K. Richardson, J. Rockström, H. J. Schellnhuber, O. P. Dube, S. Dutreuil, T. M. Lenton, and J. Lubchenco. 'The emergence and evolution of Earth System Science'. In: *Nature Reviews Earth & Environment* 1.1 (Jan. 13, 2020), pp. 54–63. ISSN: 2662-138X. DOI: `10.1038/s43017-019-0005-6`. URL: `http://www.nature.com/articles/s43017-019-0005-6` (visited on 03/15/2022).

9

[41]   K. E. Trenberth, J. T. Fasullo, and J. Kiehl. 'Earth's Global Energy Budget'. In: *Bulletin of the American Meteorological Society* 90.3 (Mar. 1, 2009). Publisher: American Meteorological Society Section: Bulletin of the American Meteorological Society, pp. 311–324. ISSN: 0003-0007, 1520-0477. DOI: 10.1175/2008BAMS2634.1. URL: http://journals.ametsoc.org/view/journals/bams/90/3/2008bams2634_1.xml (visited on 03/17/2022).

[42]   G. A. Schmidt, R. A. Ruedy, R. L. Miller, and A. A. Lacis. 'Attribution of the present-day total greenhouse effect'. In: *Journal of Geophysical Research: Atmospheres* 115 (D20 2010). ISSN: 2156-2202. DOI: 10.1029/2010JD014287. URL: http://onlinelibrary.wiley.com/doi/abs/10.1029/2010JD014287 (visited on 03/17/2022).

[43]   R. P. Allan. 'The Role of Water Vapour in Earth's Energy Flows'. In: *Surveys in Geophysics* 33.3 (July 1, 2012). ISSN: 1573-0956. DOI: 10.1007/s10712-011-9157-8. URL: https://doi.org/10.1007/s10712-011-9157-8 (visited on 03/17/2022).

[44]   L. Gimeno, J. Eiras-Barca, A. M. Durán-Quesada, F. Dominguez, R. van der Ent, H. Sodemann, R. Sánchez-Murillo, R. Nieto, and J. W. Kirchner. 'The residence time of water vapour in the atmosphere'. en. In: *Nature Reviews Earth & Environment* 2.8 (Aug. 2021). Number: 8 Publisher: Nature Publishing Group, pp. 558–569. ISSN: 2662-138X. DOI: 10.1038/s43017-021-00181-9. URL: http://www.nature.com/articles/s43017-021-00181-9 (visited on 04/06/2022).

[45]   A. Läderach and H. Sodemann. 'A revised picture of the atmospheric moisture residence time'. en. In: *Geophysical Research Letters* 43.2 (2016), pp. 924–933. ISSN: 1944-8007. DOI: 10.1002/2015GL067449. URL: http://onlinelibrary.wiley.com/doi/abs/10.1002/2015GL067449 (visited on 04/06/2022).

[46]   J. Kim and S.-W. Son. 'Tropical Cold-Point Tropopause - Climatology, Seasonal Cycle, and Intraseasonal Variability Derived from COSMIC GPS Radio Occultation Measurements'. EN. In: *Journal of Climate* 25.15 (Aug. 2012). Publisher: American Meteorological Society Section: Journal of Climate, pp. 5343–5360. ISSN: 0894-8755, 1520-0442. DOI: 10.1175/JCLI-D-11-00554.1. URL: http://journals.ametsoc.org/view/journals/clim/25/15/jcli-d-11-00554.1.xml (visited on 04/06/2022).

[47]   L. L. Pan, S. B. Honomichl, T. V. Bui, T. Thornberry, A. Rollins, E. Hintsa, and E. J. Jensen. 'Lapse Rate or Cold Point- The Tropical Tropopause Identified by In Situ Trace Gas Measurements'. en. In: *Geophysical Research Letters* 45.19 (2018), pp. 10, 756–10, 763. ISSN: 1944-8007. DOI: 10.1029/2018GL079573. URL: http://onlinelibrary.wiley.com/doi/abs/10.1029/2018GL079573 (visited on 04/06/2022).

[48]   W.-L. Wang, Y. Wang, and R.-S. WU. 'A New View on the Ferrel Cell'. In: *Chinese Journal of Geophysics* 48.3 (2005), pp. 539–545. ISSN: 2326-0440. DOI: 10.1002/cjg2.686. URL: http://onlinelibrary.wiley.com/doi/abs/10.1002/cjg2.686 (visited on 04/07/2022).

[49]   O. Pauluis, A. Czaja, and R. Korty. 'The Global Atmospheric Circulation on Moist
       Isentropes'. In: *Science* 321.5892 (Aug. 2008). Publisher: American Association for
       the Advancement of Science, pp. 1075–1078. DOI: `10.1126/science.1159649`.
       URL: `http://www.science.org/doi/full/10.1126/science.1159649`
       (visited on 04/07/2022).

[50]   G. R. North, J. Pyle, and F. Zhang. '23.7 Zonal Mean Climatology'. In: *Encyclopedia
       of Atmospheric Sciences, 6 Volume Set (2nd Edition)*. Elsevier, 2015. ISBN: 978-0-
       12-382225-3. URL: `https://app.knovel.com/hotlink/khtml/id:kt011A8`
       `P77/encyclopedia-atmospheric/zonal-mean-climatology`.

[51]   G. R. North, J. Pyle, and F. Zhang. '23.6 Transport Circulation'. In: *Encyclopedia of
       Atmospheric Sciences, 6 Volume Set (2nd Edition)*. Elsevier, 2015. ISBN: 978-0-12-
       382225-3. URL: `https://app.knovel.com/hotlink/khtml/id:kt011A8OT2`
       `/encyclopedia-atmospheric/transport-circulation`.

[52]   A. W. Brewer. 'Evidence for a world circulation provided by the measurements
       of helium and water vapour distribution in the stratosphere'. en. In: *Quarterly
       Journal of the Royal Meteorological Society* 75.326 (1949), pp. 351–363. ISSN: 1477-
       870X. DOI: `10.1002/qj.49707532603`. URL: `https://onlinelibrary.wiley`
       `.com/doi/abs/10.1002/qj.49707532603` (visited on 04/12/2023).

[53]   D. Waugh and T. Hall. 'Age of Stratospheric Air - Theory, Observations, and Mod-
       els'. en. In: *Reviews of Geophysics* 40.4 (2002), pp. 1–1–1–26. ISSN: 1944-9208. DOI:
       `10.1029/2000RG000101`. URL: `http://onlinelibrary.wiley.com/doi/abs`
       `/10.1029/2000RG000101` (visited on 04/08/2022).

[54]   B. M. Monge-Sanz, M. P. Chipperfield, A. J. Simmons, and S. M. Uppala. 'Mean
       age of air and transport in a CTM - Comparison of different ECMWF analyses'.
       en. In: *Geophysical Research Letters* 34.4 (2007). ISSN: 1944-8007. DOI: `10.1029/2`
       `006GL028515`. URL: `http://onlinelibrary.wiley.com/doi/abs/10.1029`
       `/2006GL028515` (visited on 04/08/2022).

[55]   R. A. Plumb and J. Eluszkiewicz. 'The Brewer–Dobson Circulation - Dynamics of
       the Tropical Upwelling'. EN. In: *Journal of the Atmospheric Sciences* 56.6 (Mar.
       1999). Publisher: American Meteorological Society Section: Journal of the Atmo-
       spheric Sciences, pp. 868–890. ISSN: 0022-4928, 1520-0469. DOI: `10.1175/1520-`
       `0469(1999)056<0868:TBDCDO>2.0.CO;2`. URL: `http://journals.ametsoc`
       `.org/view/journals/atsc/56/6/1520-0469_1999_056_0868_tbdcdo_2.0`
       `.co_2.xml` (visited on 04/09/2022).

[56]   N. Y. Cohen, E. P. Gerber, and O. Bühler. 'What Drives the Brewer–Dobson Cir-
       culation?' en. In: *Journal of the Atmospheric Sciences* 71.10 (Oct. 2014), pp. 3837–
       3855. ISSN: 0022-4928, 1520-0469. DOI: `10.1175/JAS-D-14-0021.1`. URL: `http`
       `s://journals.ametsoc.org/doi/10.1175/JAS-D-14-0021.1` (visited on
       04/09/2022).

[57]   G. R. North, J. Pyle, and F. Zhang. '17.1.1 Introduction'. In: *Encyclopedia of At-
       mospheric Sciences, 6 Volume Set (2nd Edition)*. Elsevier, 2015. ISBN: 978-0-12-
       382225-3. URL: `https://app.knovel.com/hotlink/khtml/id:kt011A8C6`
       `E/encyclopedia-atmospheric/gravity-wa-introduction`.

9

[58] J. G. Charney and P. G. Drazin. 'Propagation of planetary-scale disturbances from the lower into the upper atmosphere'. en. In: *Journal of Geophysical Research (1896-1977)* 66.1 (1961), pp. 83–109. ISSN: 2156-2202. DOI: 10.1029/JZ066i001p00083. URL: https://onlinelibrary.wiley.com/doi/abs/10.1029/JZ066i001p00083 (visited on 04/12/2023).

[59] G. R. North, J. Pyle, and F. Zhang. '23.3 Quasi-Biennial Oscillation'. In: *Encyclopedia of Atmospheric Sciences, 6 Volume Set (2nd Edition)*. Elsevier, 2015. ISBN: 978-0-12-382225-3. URL: https://app.knovel.com/hotlink/khtml/id:kt011A8O07/encyclopedia-atmospheric/encycloped-quasi-biennial.

[60] G. R. North, J. Pyle, and F. Zhang. '23.4 Semiannual Oscillation'. In: *Encyclopedia of Atmospheric Sciences, 6 Volume Set (2nd Edition)*. Elsevier, 2015. ISBN: 978-0-12-382225-3. URL: https://app.knovel.com/hotlink/khtml/id:kt011A8O62/encyclopedia-atmospheric/semiannual-oscillation.

[61] G. R. North, J. Pyle, and F. Zhang. '23.2 Polar Vortex'. In: *Encyclopedia of Atmospheric Sciences, 6 Volume Set (2nd Edition)*. Elsevier, 2015. ISBN: 978-0-12-382225-3. URL: https://app.knovel.com/hotlink/khtml/id:kt011A8NT1/encyclopedia-atmospheric/polar-vortex.

[62] I. Tritscher, M. C. Pitts, L. R. Poole, S. P. Alexander, F. Cairo, M. P. Chipperfield, J.-U. Grooß, M. Höpfner, A. Lambert, B. Luo, S. Molleker, A. Orr, R. Salawitch, M. Snels, R. Spang, W. Woiwode, and T. Peter. 'Polar Stratospheric Clouds: Satellite Observations, Processes, and Role in Ozone Depletion'. en. In: *Reviews of Geophysics* 59.2 (2021). _eprint: https://agupubs.onlinelibrary.wiley.com/doi/pdf/10.1029/2020RG000702. ISSN: 1944-9208. DOI: 10.1029/2020RG000702. URL: https://onlinelibrary.wiley.com/doi/abs/10.1029/2020RG000702 (visited on 05/12/2023).

[63] G. R. North, J. Pyle, and F. Zhang. '23.5 Stratospheric Sudden Warmings'. In: *Encyclopedia of Atmospheric Sciences, 6 Volume Set (2nd Edition)*. Elsevier, 2015. ISBN: 978-0-12-382225-3. URL: https://app.knovel.com/hotlink/khtml/id:kt011A8OBG/encyclopedia-atmospheric/stratospheric-sudden.

[64] M. P. Baldwin, L. J. Gray, T. J. Dunkerton, K. Hamilton, P. H. Haynes, W. J. Randel, J. R. Holton, M. J. Alexander, I. Hirota, T. Horinouchi, D. B. A. Jones, J. S. Kinnersley, C. Marquardt, K. Sato, and M. Takahashi. 'The quasi-biennial oscillation'. In: *Reviews of Geophysics* 39.2 (2001), pp. 179–229. ISSN: 1944-9208. DOI: 10.1029/1999RG000073. URL: http://onlinelibrary.wiley.com/doi/abs/10.1029/1999RG000073 (visited on 04/08/2022).

[65] T. G. Shepherd and C. McLandress. 'A Robust Mechanism for Strengthening of the Brewer–Dobson Circulation in Response to Climate Change - Critical-Layer Control of Subtropical Wave Breaking'. EN. In: *Journal of the Atmospheric Sciences* 68.4 (Apr. 2011). Publisher: American Meteorological Society Section: Journal of the Atmospheric Sciences, pp. 784–797. ISSN: 0022-4928, 1520-0469. DOI: 10.1175/2010JAS3608.1. URL: http://journals.ametsoc.org/view/journals/atsc/68/4/2010jas3608.1.xml (visited on 04/09/2022).

9

[66] J. Austin and F. Li. 'On the relationship between the strength of the Brewer-Dobson circulation and the age of stratospheric air'. en. In: *Geophysical Research Letters* 33.17 (2006). ISSN: 1944-8007. DOI: 10 . 1029 / 2006GL026867. URL: http://onlinelibrary.wiley.com/doi/abs/10.1029/2006GL026867 (visited on 04/09/2022).

[67] R. R. Garcia and W. J. Randel. 'Acceleration of the Brewer–Dobson Circulation due to Increases in Greenhouse Gases'. EN. In: *Journal of the Atmospheric Sciences* 65.8 (Aug. 2008). Publisher: American Meteorological Society Section: Journal of the Atmospheric Sciences, pp. 2731–2739. ISSN: 0022-4928, 1520-0469. DOI: 10.1175/2008JAS2712.1. URL: http://journals.ametsoc.org/view/journals/atsc/65/8/2008jas2712.1.xml (visited on 04/09/2022).

[68] K. Semeniuk and T. G. Shepherd. 'Mechanisms for Tropical Upwelling in the Stratosphere'. EN. In: *Journal of the Atmospheric Sciences* 58.21 (Nov. 2001). Publisher: American Meteorological Society Section: Journal of the Atmospheric Sciences, pp. 3097–3115. ISSN: 0022-4928, 1520-0469. DOI: 10.1175/1520-0469 (2001)058<3097:MFTUIT>2.0.CO;2. URL: http://journals.ametsoc.org /view/journals/atsc/58/21/1520-0469_2001_058_3097_mftuit_2.0.co _2.xml (visited on 04/11/2022).

[69] G. Chen and L. Sun. 'Mechanisms of the Tropical Upwelling Branch of the Brewer Dobson Circulation - The Role of Extratropical Waves'. EN. In: *Journal of the Atmospheric Sciences* 68.12 (Dec. 2011). Publisher: American Meteorological Society Section: Journal of the Atmospheric Sciences, pp. 2878–2892. ISSN: 0022-4928, 1520-0469. DOI: 10.1175/JAS-D-11-044.1. URL: http://journals.amets oc.org/view/journals/atsc/68/12/jas-d-11-044.1.xml (visited on 04/11/2022).

[70] M. Sprenger, M. Croci Maspoli, and H. Wernli. 'Tropopause folds and cross-tropopause exchange: A global investigation based upon ECMWF analyses for the time period March 2000 to February 2001'. en. In: *Journal of Geophysical Research: Atmospheres* 108.D12 (2003). ISSN: 2156-2202. DOI: 10.1029/2002JD0 02587. URL: http://onlinelibrary.wiley.com/doi/abs/10.1029/2002 JD002587 (visited on 04/11/2022).

[71] R. Nieto, M. Sprenger, H. Wernli, R. M. Trigo, and L. Gimeno. 'Identification and Climatology of Cut-off Lows near the Tropopause'. en. In: *Annals of the New York Academy of Sciences* 1146.1 (Dec. 2008), pp. 256–290. ISSN: 00778923, 17496632. DOI: 10.1196/annals.1446.016. URL: http://doi.wiley.com/10.1196/an nals.1446.016 (visited on 04/11/2022).

[72] A. R. Ivanova. 'Stratosphere-troposphere exchange and its specific features at extratropical latitudes'. en. In: *Russian Meteorology and Hydrology* 41.3 (Mar. 2016), pp. 170–185. ISSN: 1934-8096. DOI: 10.3103/S106837391603002X. URL: https: //doi.org/10.3103/S106837391603002X (visited on 04/11/2022).

9

[73] A. Gettelman, P. Hoor, L. L. Pan, W. J. Randel, M. I. Hegglin, and T. Birner. 'The Extratropical Upper Troposphere and Lower Stratosphere'. en. In: *Reviews of Geophysics* 49.3 (2011). ISSN: 1944-9208. DOI: 10.1029/2011RG000355. URL: http://onlinelibrary.wiley.com/doi/abs/10.1029/2011RG000355 (visited on 04/06/2022).

[74] H. Yang, G. Chen, Q. Tang, and P. Hess. 'Quantifying isentropic stratosphere-troposphere exchange of ozone'. en. In: *Journal of Geophysical Research: Atmospheres* 121.7 (2016), pp. 3372–3387. ISSN: 2169-8996. DOI: 10.1002/2015JD024180. URL: https://onlinelibrary.wiley.com/doi/abs/10.1002/2015JD024180 (visited on 05/05/2023).

[75] A. Dethof, A. O'Neill, J. M. Slingo, and P. Berrisford. 'Quantification of isentropic water-vapour transport into the lower stratosphere'. en. In: *Quarterly Journal of the Royal Meteorological Society* 126.566 (2000), pp. 1771–1788. ISSN: 1477-870X. DOI: 10.1002/qj.49712656611. URL: https://onlinelibrary.wiley.com/doi/abs/10.1002/qj.49712656611 (visited on 05/09/2023).

[76] G. R. North, J. Pyle, and F. Zhang. '42. Tropospheric Chemistry and Composition'. In: *Encyclopedia of Atmospheric Sciences, 6 Volume Set (2nd Edition)*. Elsevier, 2015. ISBN: 978-0-12-382225-3. URL: https://app.knovel.com/hotlink/khtml/id:kt011A9QY1/encyclopedia-atmospheric/encycloped-tropospheric.

[77] G. Brasseur, J. Orlando, G. Tyndall, and N. C. f. A. Research (U.S.) *Atmospheric Chemistry and Global Change*. Topics in environmental chemistry. Oxford University Press, 1999. ISBN: 978-0-19-510521-6. URL: https://books.google.de/books?id=eLAi0eWzDssC.

[78] G. R. North, J. Pyle, and F. Zhang. '8.1 Chemical Kinetics'. In: *Encyclopedia of Atmospheric Sciences, 6 Volume Set (2nd Edition)*. Elsevier, 2015. ISBN: 978-0-12-382225-3. URL: https://app.knovel.com/hotlink/khtml/id:kt011A7K42/encyclopedia-atmospheric/chemical-kinetics.

[79] D. H. Ehhalt. 'Photooxidation of trace gases in the troposphere Plenary Lecture'. en. In: *Physical Chemistry Chemical Physics* 1.24 (Jan. 1999). Publisher: The Royal Society of Chemistry, pp. 5401–5408. ISSN: 1463-9084. DOI: 10.1039/A905097C. URL: http://pubs.rsc.org/en/content/articlelanding/1999/cp/a905097c (visited on 05/20/2022).

[80] M. J. Prather, C. D. Holmes, and J. Hsu. 'Reactive greenhouse gas scenarios | Systematic exploration of uncertainties and the role of atmospheric chemistry'. en. In: *Geophysical Research Letters* 39.9 (2012). ISSN: 1944-8007. DOI: 10.1029/2012GL051440. URL: https://onlinelibrary.wiley.com/doi/abs/10.1029/2012GL051440 (visited on 04/13/2023).

[81] D. S. Stevenson, A. Zhao, V. Naik, F. M. O'Connor, S. Tilmes, G. Zeng, L. T. Murray, W. J. Collins, P. T. Griffiths, S. Shim, L. W. Horowitz, L. T. Sentman, and L. Emmons. 'Trends in global tropospheric hydroxyl radical and methane lifetime since 1850 from AerChemMIP'. English. In: *Atmospheric Chemistry and Physics* 20.21 (Nov. 2020). Publisher: Copernicus GmbH, pp. 12905–12920. ISSN: 1680-7316. DOI: 10

.5194/acp-20-12905-2020. URL: https://acp.copernicus.org/articles
/20/12905/2020/ (visited on 04/13/2023).

[82]   A. A. Lacis, D. J. Wuebbles, and J. A. Logan. 'Radiative forcing of climate by
       changes in the vertical distribution of ozone'. In: *Journal of Geophysical Re-
       search: Atmospheres* 95 (1990), pp. 9971–9981. DOI: https://doi.org/10.1029
       /JD095iD07p09971. URL: https://agupubs.onlinelibrary.wiley.com/do
       i/abs/10.1029/JD095iD07p09971.

[83]   J. Hansen, M. Sato, and R. Ruedy. 'Radiative forcing and climate response'. In:
       Journal of Geophysical Research: Atmospheres 102 (D6 Mar. 27, 1997), pp. 6831–
       6864. ISSN: 01480227. DOI: 10.1029/96JD03436. URL: http://doi.wiley.com
       /10.1029/96JD03436 (visited on 10/29/2021).

[84]   M. Riese, F. Ploeger, A. Rap, B. Vogel, P. Konopka, M. Dameris, and P. Forster.
       'Impact of uncertainties in atmospheric mixing on simulated UTLS composition
       and related radiative effects'. en. In: *Journal of Geophysical Research: Atmospheres*
       117.D16 (2012). ISSN: 2156-2202. DOI: 10.1029/2012JD017751. URL: http://o
       nlinelibrary.wiley.com/doi/abs/10.1029/2012JD017751 (visited on
       07/06/2022).

[85]   R. Wayne. 'CHEMISTRY OF THE ATMOSPHERE | Chemical Kinetics'. en. In: *En-
       cyclopedia of Atmospheric Sciences*. Elsevier, 2015, pp. 324–332. ISBN: 978-0-12-
       382225-3. DOI: 10.1016/B978-0-12-382225-3.00099-2. URL: https://lin
       kinghub.elsevier.com/retrieve/pii/B9780123822253000992 (visited on
       04/08/2022).

[86]   D. J. Wuebbles and K. Hayhoe. 'Atmospheric methane and global change'. en. In:
       Earth-Science Reviews 57.3 (May 2002), pp. 177–210. ISSN: 0012-8252. DOI: 10.10
       16/S0012-8252(01)00062-9. URL: https://www.sciencedirect.com/scie
       nce/article/pii/S0012825201000629 (visited on 04/28/2023).

[87]   D. H. Ehhalt. 'The atmospheric cycle of methane'. In: *Tellus* 26.1-2 (Jan. 1974).
       Publisher: Taylor & Francis, pp. 58–70. ISSN: 0040-2826. DOI: 10.3402/tellusa
       .v26i1-2.9737. URL: https://doi.org/10.3402/tellusa.v26i1-2.9737
       (visited on 04/28/2023).

[88]   G. Brasseur and S. Solomon. *Aeronomy of the middle atmosphere: chemistry
       and physics of the stratosphere and mesosphere*. en. 3rd rev. and enlarged ed.
       Atmospheric and oceanographic sciences library v. 32. OCLC: ocm62343740.
       Dordrecht ; [Great Britain]: Springer, 2005. ISBN: 978-1-4020-3284-4.

[89]   V. Grewe. 'Impact of Lightning on Air Chemistry and Climate'. en. In: *Lightning |
       Principles, Instruments and Applications | Review of Modern Lightning Research*.
       Ed. by H. D. Betz, U. Schumann, and P. Laroche. Dordrecht: Springer Netherlands,
       2009, pp. 537–549. ISBN: 978-1-4020-9079-0. DOI: 10.1007/978-1-4020-9079-
       0_25. URL: https://doi.org/10.1007/978-1-4020-9079-0_25 (visited on
       04/13/2023).

[90]   I. B. Ocko and S. P. Hamburg. 'Climate consequences of hydrogen emissions'. English. In: *Atmospheric Chemistry and Physics* 22.14 (July 2022). Publisher: Copernicus GmbH, pp. 9349–9368. ISSN: 1680-7316. DOI: 10.5194/acp-22-9349-2022. URL: https://acp.copernicus.org/articles/22/9349/2022/ (visited on 03/29/2023).

[91]   M. I. Hegglin, S. Tegtmeier, J. Anderson, L. Froidevaux, R. Fuller, B. Funke, A. Jones, G. Lingenfelser, J. Lumpe, D. Pendlebury, E. Remsberg, A. Rozanov, M. Toohey, J. Urban, T. von Clarmann, K. A. Walker, R. Wang, and K. Weigel. 'SPARC Data Initiative - Comparison of water vapor climatologies from international satellite limb sounders - SPARC DATA INITIATIVE WATER VAPOR COMPARISONS'. In: *Journal of Geophysical Research: Atmospheres* 118.20 (Oct. 27, 2013), pp. 11, 824–11, 846. ISSN: 2169897X. DOI: 10.1002/jgrd.50752. URL: http://doi.wiley.com/10.1002/jgrd.50752 (visited on 10/29/2021).

[92]   S. Tegtmeier, M. I. Hegglin, J. Anderson, A. Bourassa, S. Brohede, D. Degenstein, L. Froidevaux, R. Fuller, B. Funke, J. Gille, A. Jones, Y. Kasai, K. Krüger, E. Kyrölä, G. Lingenfelser, J. Lumpe, B. Nardi, J. Neu, D. Pendlebury, E. Remsberg, A. Rozanov, L. Smith, M. Toohey, J. Urban, T. von Clarmann, K. A. Walker, and R. H. J. Wang. 'SPARC Data Initiative - A comparison of ozone climatologies from international satellite limb sounders: OZONE CLIMATOLOGIES FROM LIMB SOUNDERS'. In: *Journal of Geophysical Research: Atmospheres* 118.21 (Nov. 16, 2013), pp. 12, 229–12, 247. ISSN: 2169897X. DOI: 10.1002/2013JD019877. URL: http://doi.wiley.com/10.1002/2013JD019877 (visited on 10/29/2021).

[93]   S. M. Davis, K. H. Rosenlof, B. Hassler, D. F. Hurst, W. G. Read, H. Vömel, H. Selkirk, M. Fujiwara, and R. Damadeo. 'The Stratospheric Water and Ozone Satellite Homogenized (SWOOSH) database: a long-term database for climate studies'. In: (2016), p. 30.

[94]   G. R. North, J. Pyle, and F. Zhang. '36. Stratospheric Chemistry Topics'. In: *Encyclopedia of Atmospheric Sciences, 6 Volume Set (2nd Edition)*. Elsevier, 2015. ISBN: 978-0-12-382225-3. URL: https://app.knovel.com/hotlink/khtml/id:kt011A9EE5/encyclopedia-atmospheric/stratospheric-chemistry.

[95]   Y. Kondo. 'STRATOSPHERIC CHEMISTRY TOPICS | Reactive Nitrogen (NOx and NOy)'. en. In: *Encyclopedia of Atmospheric Sciences (Second Edition)*. Ed. by G. R. North, J. Pyle, and F. Zhang. Oxford: Academic Press, Jan. 2015, pp. 242–249. ISBN: 978-0-12-382225-3. DOI: 10.1016/B978-0-12-382225-3.00386-8. URL: https://www.sciencedirect.com/science/article/pii/B9780123822253003868 (visited on 04/13/2023).

[96]   Y. Zhu, O. B. Toon, D. Kinnison, V. L. Harvey, M. J. Mills, C. G. Bardeen, M. Pitts, N. Bègue, J.-B. Renard, G. Berthet, and F. Jégou. 'Stratospheric Aerosols, Polar Stratospheric Clouds, and Polar Ozone Depletion After the Mount Calbuco Eruption in 2015'. en. In: *Journal of Geophysical Research: Atmospheres* 123.21 (2018). _eprint: https://agupubs.onlinelibrary.wiley.com/doi/pdf/10.1029/2018JD028974, pp. 12, 308–12, 331. ISSN: 2169-8996. DOI: 10.1029/2018JD028974. URL: https://onlinelibrary.wiley.com/doi/abs/10.1029/2018JD028974 (visited on 06/06/2023).

9

[97]   'Composition and Chemistry'. en. In: *Aeronomy of the Middle Atmosphere -
        Chemistry and Physics of the Stratosphere and Mesosphere*. Ed. by G. P. Brasseur
        and S. Solomon. Atmospheric and Oceanographic Sciences Library. Dordrecht:
        Springer Netherlands, 2005, pp. 265–442. ISBN: 978-1-4020-3824-2. DOI: 10.100
        7/1-4020-3824-0_5. URL: https://doi.org/10.1007/1-4020-3824-0_5
        (visited on 05/19/2022).

[98]   J. Steelant, R. Varvill, C. Walton, S. Defoort, K. Hannemann, and M. Marini.
        'Achievements Obtained for Sustained Hypersonic Flight within the LAPCAT-II
        project'. In: *20th AIAA International Space Planes and Hypersonic Systems and
        Technologies Conference*. 20th AIAA International Space Planes and Hypersonic
        Systems and Technologies Conference. Glasgow, Scotland: American Institute of
        Aeronautics and Astronautics, July 6, 2015. ISBN: 978-1-62410-320-9. DOI: 10.25
        14/6.2015-3677. URL: http://arc.aiaa.org/doi/10.2514/6.2015-3677
        (visited on 10/29/2021).

[99]   S. Arrhenius. 'On the Influence of Carbonic Acid in the Air upon the Temperature
        of the Ground'. In: *The Future of Nature*. Ed. by L. Robin, S. Sörlin, and P. Warde.
        Yale University Press, Dec. 1896, pp. 303–315. ISBN: 978-0-300-18847-9. DOI: 10
        .12987/9780300188479-028. URL: https://www.degruyter.com/document
        /doi/10.12987/9780300188479-028/html (visited on 04/13/2023).

[100] P. Voosen. 'Europe builds 'digital twin' of Earth to hone climate forecasts'. In: *Sci-
        ence* 370.6512 (Oct. 2020). Publisher: American Association for the Advancement
        of Science, pp. 16–17. DOI: 10.1126/science.370.6512.16. URL: http://w
        ww.science.org/doi/full/10.1126/science.370.6512.16 (visited on
        05/03/2022).

[101] K. E. Taylor, R. J. Stouffer, and G. A. Meehl. 'An Overview of CMIP5 and the Exper-
        iment Design'. EN. In: *Bulletin of the American Meteorological Society* 93.4 (Apr.
        2012), pp. 485–498. DOI: 10.1175/BAMS-D-11-00094.1. URL: https://journ
        als.ametsoc.org/view/journals/bams/93/4/bams-d-11-00094.1.xml
        (visited on 04/13/2023).

[102] V. Eyring, S. Bony, G. A. Meehl, C. A. Senior, B. Stevens, R. J. Stouffer, and K. E. Tay-
        lor. 'Overview of the Coupled Model Intercomparison Project Phase 6 (CMIP6)
        experimental design and organization'. English. In: *Geoscientific Model Develop-
        ment* 9.5 (May 2016). Publisher: Copernicus GmbH, pp. 1937–1958. ISSN: 1991-
        959X. DOI: 10.5194/gmd-9-1937-2016. URL: https://gmd.copernicus.org
        /articles/9/1937/2016/gmd-9-1937-2016.html (visited on 04/13/2023).

[103] A. Gettelman and R. B. Rood. 'Simulating the Atmosphere'. In: *Demystifying Cli-
        mate Models: A Users Guide to Earth System Models*. Berlin, Heidelberg: Springer
        Berlin Heidelberg, 2016, pp. 61–85. ISBN: 978-3-662-48959-8. DOI: 10.1007/978
        -3-662-48959-8_5. URL: https://doi.org/10.1007/978-3-662-48959-8
        _5.

9

[104]   A. Gettelman and R. B. Rood. 'Bringing The System Together: Coupling and Com-
         plexity'. In: *Demystifying Climate Models: A Users Guide to Earth System Models*.
         Berlin, Heidelberg: Springer Berlin Heidelberg, 2016, pp. 139–158. ISBN: 978-3-
         662-48959-8. DOI: 10.1007/978-3-662-48959-8_8. URL: https://doi.org
         /10.1007/978-3-662-48959-8_8.

[105]   D. Kinnison, G. P. Brasseur, S. L. Baughcum, J. Zhang, and D. Wuebbles. 'The
         Impact on the Ozone Layer of a Potential Fleet of Civil Hypersonic Aircraft'. In:
         Earth's Future 8.10 (Oct. 2020). ISSN: 2328-4277, 2328-4277. DOI: 10.1029/2020
         EF001626. URL: https://onlinelibrary.wiley.com/doi/10.1029/2020
         EF001626 (visited on 10/29/2021).

[106]   E. Roeckner, R. Brokopf, M. Esch, M. Giorgetta, S. Hagemann, L. Kornblueh, E.
         Manzini, U. Schlese, and U. Schulzweida. 'Sensitivity of Simulated Climate to
         Horizontal and Vertical Resolution in the ECHAM5 Atmosphere Model'. In: *Jour-
         nal of Climate* 19.16 (Aug. 15, 2006), pp. 3771–3791. ISSN: 1520-0442, 0894-8755.
         DOI: 10.1175/JCLI3824.1. URL: http://journals.ametsoc.org/doi/10.1
         175/JCLI3824.1 (visited on 10/29/2021).

[107]   P. Jöckel, H. Tost, A. Pozzer, R. Sander, B. Steil, G. Stiller, M. Tanarhte, D. Tarabor-
         relli, J. van Aardenne, and J. Lelieveld. 'The atmospheric chemistry general circu-
         lation model ECHAM5/MESSy1: consistent simulation of ozone from the surface
         to the mesosphere'. In: *Atmos. Chem. Phys.* (Nov. 7, 2006), p. 38.

[108]   P. Jöckel, H. Tost, A. Pozzer, M. Kunze, O. Kirner, C. A. M. Brenninkmeijer, S.
         Brinkop, D. S. Cai, C. Dyroff, J. Eckstein, F. Frank, H. Garny, K.-D. Gottschaldt,
         P. Graf, V. Grewe, A. Kerkweg, B. Kern, S. Matthes, M. Mertens, S. Meul, M.
         Neumaier, M. Nützel, S. Oberländer-Hayn, R. Ruhnke, T. Runde, R. Sander, D.
         Scharffe, and A. Zahn. 'Earth System Chemistry integrated Modelling (ESCiMo)
         with the Modular Earth Submodel System (MESSy) version 2.51'. In: *Geoscientific
         Model Development* 9.3 (Mar. 31, 2016), pp. 1153–1200. ISSN: 1991-9603. DOI:
         10.5194/gmd-9-1153-2016. URL: https://gmd.copernicus.org/articles
         /9/1153/2016/.

[109]   P. Jöckel, A. Kerkweg, A. Pozzer, R. Sander, H. Tost, H. Riede, A. Baumgaertner, S.
         Gromov, and B. Kern. 'Development cycle 2 of the Modular Earth Submodel Sys-
         tem (MESSy2)'. In: *Geoscientific Model Development* 3.2 (Dec. 22, 2010), pp. 717–
         752. ISSN: 1991-9603. DOI: 10.5194/gmd-3-717-2010. URL: https://gmd.cop
         ernicus.org/articles/3/717/2010/.

[110]   F. Hourdin, C. Rio, J.-Y. Grandpeix, J.-B. Madeleine, F. Cheruy, N. Rochetin, A.
         Jam, I. Musat, A. Idelkadi, L. Fairhead, M.-A. Foujols, L. Mellul, A.-K. Traore, J.-L.
         Dufresne, O. Boucher, M.-P. Lefebvre, E. Millour, E. Vignon, J. Jouhaud, F. B. Di-
         allo, F. Lott, G. Gastineau, A. Caubel, Y. Meurdesoif, and J. Ghattas. 'LMDZ6A - The
         Atmospheric Component of the IPSL Climate Model With Improved and Better
         Tuned Physics'. In: *Journal of Advances in Modeling Earth Systems* 12.7 (2020).
         ISSN: 1942-2466. DOI: 10.1029/2019MS001892. URL: http://onlinelibrary
         .wiley.com/doi/abs/10.1029/2019MS001892 (visited on 05/31/2022).

9

[111] D. A. Hauglustaine, F. Hourdin, L. Jourdain, M.-A. Filiberti, S. Walters, J.-F. Lamarque, and E. A. Holland. 'Interactive chemistry in the Laboratoire de Météorologie Dynamique general circulation model: Description and background tropospheric chemistry evaluation'. en. In: *Journal of Geophysical Research: Atmospheres* 109.D4 (2004). ISSN: 2156-2202. DOI: 10.1029/2003JD003957. URL: http://onlinelibrary.wiley.com/doi/abs/10.1029/2003JD003957 (visited on 05/31/2022).

[112] G. Krinner, N. Viovy, N. de Noblet-Ducoudré, J. Ogée, J. Polcher, P. Friedlingstein, P. Ciais, S. Sitch, and I. C. Prentice. 'A dynamic global vegetation model for studies of the coupled atmosphere-biosphere system'. In: *Global Biogeochemical Cycles* 19.1 (2005). ISSN: 1944-9224. DOI: 10.1029/2003GB002199. URL: http://onlinelibrary.wiley.com/doi/abs/10.1029/2003GB002199 (visited on 05/31/2022).

[113] K. Hasselmann, R. Sausen, E. Maier-Reimer, and R. Voss. 'On the cold start problem in transient simulations with coupled atmosphere-ocean models'. In: *Climate Dynamics* 9.2 (Nov. 1993), pp. 53–61. ISSN: 0930-7575, 1432-0894. DOI: 10.1007/BF00210008. URL: http://link.springer.com/10.1007/BF00210008 (visited on 10/29/2021).

[114] H. Kargbo, J. S. Harris, and A. N. Phan. 'Drop-in fuel production from biomass: Critical review on techno-economic feasibility and sustainability'. en. In: *Renewable and Sustainable Energy Reviews* 135 (Jan. 2021), p. 110168. ISSN: 1364-0321. DOI: 10.1016/j.rser.2020.110168. URL: https://www.sciencedirect.com/science/article/pii/S1364032120304597 (visited on 04/13/2023).

[115] R. Schäppi, D. Rutz, F. Dähler, A. Muroyama, P. Haueter, J. Lilliestam, A. Patt, P. Furler, and A. Steinfeld. 'Drop-in fuels from sunlight and air'. en. In: *Nature* 601.7891 (Jan. 2022), pp. 63–68. ISSN: 1476-4687. DOI: 10.1038/s41586-021-04174-y. URL: https://www.nature.com/articles/s41586-021-04174-y (visited on 04/13/2023).

[116] M. F. Shahriar and A. Khanal. 'The current techno-economic, environmental, policy status and perspectives of sustainable aviation fuel (SAF)'. en. In: *Fuel* 325 (Oct. 2022), p. 124905. ISSN: 0016-2361. DOI: 10.1016/j.fuel.2022.124905. URL: https://www.sciencedirect.com/science/article/pii/S0016236122017471 (visited on 04/13/2023).

[117] G. R. North, J. Pyle, and F. Zhang. '5.1 Aircraft Emissions'. In: *Encyclopedia of Atmospheric Sciences, 6 Volume Set (2nd Edition)*. Elsevier, 2015. ISBN: 978-0-12-382225-3. URL: https://app.knovel.com/hotlink/khtml/id:kt011A7CN1/encyclopedia-atmospheric/aircraft-emissions.

[118] V. Grewe, M. Plohr, G. Cerino, M. D. Muzio, Y. Deremaux, M. Galerneau, P. d. S. Martin, T. Chaika, A. Hasselrot, U. Tengzelius, and V. D. Korovkin. 'Estimates of the climate impact of future small-scale supersonic transport aircraft – results from the HISAC EU-project'. en. In: *The Aeronautical Journal* 114.1153 (Mar. 2010), pp. 199–206. ISSN: 0001-9240, 2059-6464. DOI: 10.1017/S000192400000

9

364X. URL: https://www.cambridge.org/core/product/identifier/S000
192400000364X/type/journal_article (visited on 10/29/2021).

[119]   S. Randolph, G. Anderson, L. Baughcum, A. Brock, H. Brune, C. Cohen, E. Kinni-
        son, P. A. Newman, M. Rodriguez, and S. Stolarski. 'Assessment of the Effects of
        High-Speed Aircraft in the Stratosphere'. en. In: (1998), p. 232.

[120]   Wikipedia contributors. *Supersonic aircraft — Wikipedia, The Free Encyclopedia.*
        [Online; accessed 4-May-2022]. 2022. URL: https://en.wikipedia.org/w/in
        dex.php?title=Supersonic_aircraft&oldid=1077756224.

[121]   B. Khandelwal, A. Karakurt, P. R. Sekaran, V. Sethi, and R. Singh. 'Hydrogen pow-
        ered aircraft : The future of air transport'. en. In: *Progress in Aerospace Sciences* 60
        (July 2013), pp. 45–59. ISSN: 0376-0421. DOI: 10.1016/j.paerosci.2012.12.0
        02. URL: https://www.sciencedirect.com/science/article/pii/S03760
        42112000887 (visited on 07/24/2023).

[122]   R. J. Weber. 'Liquefied Natural Gas As A Fuel For Supersonic Aircraft'. en. In:
        (1967), p. 13. URL: https://ntrs.nasa.gov/api/citations/1967001398
        6/downloads/19670013986.pdf.

[123]   R. A. Roberts, S. R. Nuzum, and M. Wolff. 'Liquefied Natural Gas as the Next Avia-
        tion Fuel'. In: *13th International Energy Conversion Engineering Conference.* AIAA
        Propulsion and Energy Forum. American Institute of Aeronautics and Astronau-
        tics, July 2015. DOI: 10.2514/6.2015-4247. URL: http://arc.aiaa.org/doi
        /10.2514/6.2015-4247 (visited on 05/17/2022).

[124]   G. D. Brewer. *Hydrogen Aircraft Technology.* New York: Routledge, Oct. 2017. ISBN:
        978-0-203-75148-0. DOI: 10.1201/9780203751480. URL: https://doi-org.t
        udelft.idm.oclc.org/10.1201/9780203751480.

[125]   H. Nojoumi, I. Dincer, and G. F. Naterer. 'Greenhouse gas emissions assessment
        of hydrogen and kerosene-fueled aircraft propulsion'. en. In: *International Jour-
        nal of Hydrogen Energy* 34.3 (Feb. 2009), pp. 1363–1369. ISSN: 0360-3199. DOI: 10
        .1016/j.ijhydene.2008.11.017. URL: https://www.sciencedirect.com
        /science/article/pii/S0360319908015048 (visited on 08/09/2023).

[126]   EUROCONTROL. *Think Paper #21 - Long-haul flight decarbonisation: When can
        cutting-edge energies & technologies make a difference?* en. Aug. 2023. URL: http
        s://www.eurocontrol.int/publication/eurocontrol-think-paper-21
        -long-haul-flight-decarbonisation-when-can-cutting-edge (visited
        on 08/24/2023).

[127]   F. M. Troeltsch, M. Engelmann, A. E. Scholz, F. Peter, J. Kaiser, and M. Hornung.
        'Hydrogen Powered Long Haul Aircraft with Minimized Climate Impact'. en. In:
        AIAA AVIATION 2020 FORUM. VIRTUAL EVENT: American Institute of Aeronau-
        tics and Astronautics, June 2020. ISBN: 978-1-62410-598-2. DOI: 10.2514/6.202
        0-2660. URL: https://arc.aiaa.org/doi/10.2514/6.2020-2660 (visited
        on 08/24/2023).

9

[128] R. G. Derwent. 'Global warming potential (GWP) for hydrogen: Sensitivities, uncertainties and meta-analysis'. en. In: *International Journal of Hydrogen Energy* 48.22 (Mar. 2023), pp. 8328–8341. ISSN: 0360-3199. DOI: 10.1016/j.ijhydene.2022.11.219. URL: https://www.sciencedirect.com/science/article/pii/S0360319922055380 (visited on 03/31/2023).

[129] W. Nätzker. *Hyperschall-Antriebe*. Trendanalyse. Fraunhofer-Institut, Aug. 2017, p. 92. URL: https://www.int.fraunhofer.de/de/geschaeftsfelder/wehrtechnische-zukunftsanalyse/neue_technologien/Archiv.html (visited on 06/29/2023).

[130] N. Viola, R. Fusaro, O. Gori, M. Marini, P. Roncioni, G. Saccone, B. Saracoglu, A. C. Ispir, C. Fureby, T. Nilson, C. Iron, A. Vincent, J. Martinez Schramm, V. Grewe, J. Emmerig, D. Hauglustaine, F. Linke, and D. Bodmer. 'STRATOFLY MR3 – how to reduce the environmental impact of high-speed transportation'. In: *AIAA Scitech 2021 Forum*. AIAA Scitech 2021 Forum. VIRTUAL EVENT: American Institute of Aeronautics and Astronautics, Jan. 11, 2021. ISBN: 978-1-62410-609-5. DOI: 10.2514/6.2021-1877. URL: https://arc.aiaa.org/doi/10.2514/6.2021-1877 (visited on 03/25/2022).

[131] N. Viola, R. Fusaro, D. Ferretto, O. Gori, B. Saracoglu, A. C. Ispir, V. Grewe, J. F. Plezer, J. Martinez, M. Marini, L. Cutrone, S. Hernandez, K. Lammers, A. Vincent, D. Hauglustaine, F. Linke, D. Bodmer, T. Nilsson, and C. Fureby. 'H2020 STRATOFLY Project - From Europe To Australia in less than three hours'. en. In: *Congress of the International Council of the Aeronautical Sciences* (2021), p. 21.

[132] P. Forster, V. Ramaswamy, P. Artaxo, T. Berntsen, R. Betts, D. W. Fahey, J. Haywood, J. Lean, D. C. Lowe, G. Raga, M. Schulz, R. V. Dorland, G. Bodeker, D. Etheridge, P. Foukal, P. Fraser, M. Geller, F. Joos, C. D. Keeling, R. Keeling, S. Kinne, K. Lassey, D. Oram, K. O'Shaughnessy, N. Ramankutty, G. Reid, D. Rind, K. Rosenlof, R. Sausen, D. Schwarzkopf, S. K. Solanki, G. Stenchikov, N. Stuber, T. Takemura, C. Textor, R. Wang, R. Weiss, T. Whorf, T. Nakajima, V. Ramanathan, V. Ramaswamy, P. Artaxo, T. Berntsen, R. Betts, D. W. Fahey, J. Haywood, J. Lean, D. C. Lowe, G. Myhre, J. Nganga, R. Prinn, G. Raga, M. Schulz, and R. V. Dorland. 'Changes in Atmospheric Constituents and in Radiative Forcing'. en. In: AR4.Working Group 1 Chapter 2 (2014), p. 106.

[133] P. M. de F. Forster and K. P. Shine. 'Radiative forcing and temperature trends from stratospheric ozone changes'. In: *Journal of Geophysical Research: Atmospheres* 102 (D9 May 20, 1997), pp. 10841–10855. ISSN: 01480227. DOI: 10.1029/96JD03510. URL: http://doi.wiley.com/10.1029/96JD03510 (visited on 03/14/2022).

[134] C. J. Smith, R. J. Kramer, G. Myhre, K. Alterskjær, W. Collins, A. Sima, O. Boucher, J.-L. Dufresne, P. Nabat, M. Michou, S. Yukimoto, J. Cole, D. Paynter, H. Shiogama, F. M. O'Connor, E. Robertson, A. Wiltshire, T. Andrews, C. Hannay, R. Miller, L. Nazarenko, A. Kirkevåg, D. Olivié, S. Fiedler, A. Lewinschal, C. Mackallah, M. Dix, R. Pincus, and P. M. Forster. 'Effective radiative forcing and adjustments in CMIP6 models'. English. In: *Atmospheric Chemistry and Physics* 20.16 (Aug. 2020). Publisher: Copernicus GmbH, pp. 9591–9618. ISSN: 1680-7316. DOI: 10.5194/acp-2

9

0-9591-2020. URL: https://acp.copernicus.org/articles/20/9591/202
0/ (visited on 01/21/2024).

[135]   S. C. Sherwood, S. Bony, O. Boucher, C. Bretherton, P. M. Forster, J. M. Gregory,
        and B. Stevens. 'Adjustments in the Forcing-Feedback Framework for Under-
        standing Climate Change'. EN. In: *Bulletin of the American Meteorological Society*
        96.2 (Feb. 2015). Publisher: American Meteorological Society Section: Bulletin of
        the American Meteorological Society, pp. 217–228. ISSN: 0003-0007, 1520-0477.
        DOI: 10.1175/BAMS-D-13-00167.1. URL: https://journals.ametsoc
        .org/view/journals/bams/96/2/bams-d-13-00167.1.xml (visited on
        01/21/2024).

[136]   J. Zhang, D. Wuebbles, D. Kinnison, and S. L. Baughcum. 'Stratospheric Ozone
        and Climate Forcing Sensitivity to Cruise Altitudes for Fleets of Potential Super-
        sonic Transport Aircraft'. en. In: *Journal of Geophysical Research: Atmospheres*
        126.16 (2021). ISSN: 2169-8996. DOI: 10.1029/2021JD034971. URL: http://o
        nlinelibrary.wiley.com/doi/abs/10.1029/2021JD034971 (visited on
        05/04/2022).

[137]   T. Yuhara, Y. Makino, and K. Rinoie. 'Conceptual Design Study on Liquid
        Hydrogen-Fueled Supersonic Transport Considering Environmental Impacts'.
        In: *Journal of Aircraft* 53.4 (2016). Publisher: American Institute of Aeronautics
        and Astronautics, pp. 1168–1173. DOI: 10.2514/1.C033369. URL: https://doi
        .org/10.2514/1.C033369 (visited on 05/16/2022).

[138]   A. Ingenito. 'Impact of hydrogen fueled hypersonic airliners on the O_3 layer
        depletion'. In: *International Journal of Hydrogen Energy* 43.50 (Dec. 2018),
        pp. 22694–22704. ISSN: 03603199. DOI: 10.1016/j.ijhydene.2018.09.208.
        URL: https://linkinghub.elsevier.com/retrieve/pii/S0360319918331
        379 (visited on 10/29/2021).

[139]   W. M. Organization (WMO), (N. O. a. A. Administration, (U. N. E. Programme,
        (N. A. a. S. Administration, E. Commission, and W. M. O. (WMO). *GAW Report,
        278. Scientific Assessment of Ozone Depletion: 2022 (GAW 278).* Geneva: WMO,
        2022. ISBN: 978-9914-733-97-6. URL: https://library.wmo.int/doc_num.ph
        p?explnum_id=11529.

[140]   T. Christoudias, S. Gromov, M. Kohl, R. Sander, D. Stolzenburg, A. Pozzer, M.
        Barra, M. Kilian, and J. Pletzer. 'New Developments in MESSy2.55: H2OEMIS,
        NAN, BIOBURN, DOMINT, MECCA, JVAL, ENSEMBLE'. In: *Geoscientific Model
        Development* x.x (2024). in preparation, pp. xx–xx. DOI: 10.5194/.... URL: http
        s....

[141]   D. A. Hauglustaine, Y. Balkanski, and M. Schulz. 'A global model simulation of
        present and future nitrate aerosols and their direct radiative forcing of climate'.
        English. In: *Atmospheric Chemistry and Physics* 14.20 (Oct. 2014). Publisher:
        Copernicus GmbH, pp. 11031–11063. ISSN: 1680-7316. DOI: 10.5194/acp-14-1
        1031-2014. URL: https://acp.copernicus.org/articles/14/11031/2014
        / (visited on 07/10/2023).

[142] A. Pozzer, P. Jockel, R. Sander, J. Williams, L. Ganzeveld, and J. Lelieveld. 'Technical Note: The MESSy-submodel AIRSEA calculating the air-sea exchange of chemical species'. In: *Atmos. Chem. Phys.* (2006), p. 10.

[143] F. Winterstein and P. Jöckel. 'Methane chemistry in a nutshell – the new submodels CH4 (v1.0) and TRSYNC (v1.0) in MESSy (v2.54.0)'. In: *Geoscientific Model Development* 14.2 (Feb. 2, 2021). Publisher: Copernicus GmbH, pp. 661–674. ISSN: 1991-959X. DOI: 10.5194/gmd-14-661-2021. URL: https://gmd.copernicus.org/articles/14/661/2021/ (visited on 03/08/2022).

[144] H. Tost, P. Jockel, and J. Lelieveld. 'Lightning and convection parameterisations – uncertainties in global modelling'. In: *Atmos. Chem. Phys.* (2007), p. 16.

[145] O. Kirner, R. Ruhnke, J. Buchholz-Dietsch, P. Jöckel, C. Brühl, and B. Steil. 'Simulation of polar stratospheric clouds in the chemistry-climate-model EMAC via the submodel PSC'. English. In: *Geoscientific Model Development* 4.1 (Mar. 2011). Publisher: Copernicus GmbH, pp. 169–182. ISSN: 1991-959X. DOI: 10.5194/gmd-4-169-2011. URL: https://gmd.copernicus.org/articles/4/169/2011/ (visited on 07/05/2022).

[146] A. Kerkweg, J. Buchholz, L. Ganzeveld, A. Pozzer, H. Tost, and P. Jockel. 'Technical Note: An implementation of the dry removal processes DRY DEPosition and SEDImentation in the Modular Earth Submodel System (MESSy)'. In: *Atmos. Chem. Phys.* (2006), p. 16.

[147] H. Tost, P. Jockel, A. Kerkweg, R. Sander, and J. Lelieveld. 'Technical note: A new comprehensive SCAVenging submodel for global atmospheric chemistry modelling'. In: *Atmos. Chem. Phys.* (2006), p. 10.

[148] E. Roeckner, G. Bäuml, L. Bonaventura, R. Brokopf, M. Esch, M. Giorgetta, S. Hagemann, I. Kirchner, L. Kornblueh, E. Manzini, A. Rhodin, U. Schlese, U. Schulzweida, and A. Tompkins. 'The atmospheric general circulation model ECHAM 5. PART I - Model description'. eng. In: (Nov. 2003). Publisher: Max-Planck-Institut für Meteorologie. DOI: 10.17617/2.995269. URL: https://pure.mpg.de/pubman/faces/ViewItemOverviewPage.jsp?itemId=item_995269 (visited on 06/07/2022).

[149] C. D. Holmes, M. J. Prather, O. A. Søvde, and G. Myhre. 'Future methane, hydroxyl, and their uncertainties: key climate and emission parameters for future predictions'. English. In: *Atmospheric Chemistry and Physics* 13.1 (Jan. 2013). Publisher: Copernicus GmbH, pp. 285–302. ISSN: 1680-7316. DOI: 10.5194/acp-13-285-2013. URL: https://acp.copernicus.org/articles/13/285/2013/ (visited on 04/28/2023).

[150] K. H. Rosenlof, S. J. Oltmans, D. Kley, J. M. Russell III, E.-W. Chiou, W. P. Chu, D. G. Johnson, K. K. Kelly, H. A. Michelsen, G. E. Nedoluha, E. E. Remsberg, G. C. Toon, and M. P. McCormick. 'Stratospheric water vapor increases over the past half-century'. en. In: *Geophysical Research Letters* 28.7 (2001), pp. 1195–1198. ISSN: 1944-8007. DOI: 10.1029/2000GL012502. URL: https://onlinelibrary.wiley.com/doi/abs/10.1029/2000GL012502 (visited on 04/28/2023).

9

[151]   A. E. Dessler, M. R. Schoeberl, T. Wang, S. M. Davis, and K. H. Rosenlof. 'Strato-
        spheric water vapor feedback'. In: *Proceedings of the National Academy of Sci-
        ences* 110.45 (Nov. 2013). Publisher: Proceedings of the National Academy of Sci-
        ences, pp. 18087–18091. DOI: `10.1073/pnas.1310344110`. URL: `https://www`
        `.pnas.org/doi/abs/10.1073/pnas.1310344110` (visited on 02/07/2024).

[152]   D. Kinnison, G. Brasseur, and J. Pletzer. personal communication. May 25, 2023.

[153]   R. Eichinger, P. Jöckel, S. Brinkop, M. Werner, and S. Lossow. 'Simulation of the
        isotopic composition of stratospheric water vapour – Part 1: Description and
        evaluation of the EMAC model'. In: *Atmospheric Chemistry and Physics* 15.10
        (May 21, 2015), pp. 5537–5555. ISSN: 1680-7324. DOI: `10.5194/acp-15-5537`
        `-2015`. URL: `https://acp.copernicus.org/articles/15/5537/2015/`
        (visited on 10/29/2021).

[154]   F. Frank, P. Jöckel, S. Gromov, and M. Dameris. 'Investigating the yield of H2O and
        H2 from methane oxidation in the stratosphere'. In: *Atmospheric Chemistry and
        Physics* 18.13 (July 13, 2018), pp. 9955–9973. ISSN: 1680-7324. DOI: `10.5194/acp`
        `-18-9955-2018`. URL: `https://acp.copernicus.org/articles/18/9955/2`
        `018/` (visited on 10/29/2021).

[155]   S. Noël, K. Weigel, K. Bramstedt, A. Rozanov, M. Weber, H. Bovensmann, and
        J. P. Burrows. 'Water vapour and methane coupling in the stratosphere observed
        using SCIAMACHY solar occultation measurements'. In: *Atmospheric Chemistry
        and Physics* 18.7 (Apr. 3, 2018), pp. 4463–4476. ISSN: 1680-7324. DOI: `10.5194/a`
        `cp-18-4463-2018`. URL: `https://acp.copernicus.org/articles/18/4463`
        `/2018/` (visited on 10/29/2021).

[156]   R. Sander, A. Kerkweg, P. Jockel, and J. Lelieveld. 'Technical note: The new
        comprehensive atmospheric chemistry module MECCA'. In: *Atmos. Chem. Phys.*
        (2005), p. 6.

[157]   R. Sander, A. Baumgaertner, S. Gromov, H. Harder, P. Jöckel, A. Kerkweg, D. Ku-
        bistin, E. Regelin, H. Riede, A. Sandu, D. Taraborrelli, H. Tost, and Z.-Q. Xie. 'The
        atmospheric chemistry box model CAABA/MECCA-3.0'. In: *Geoscientific Model
        Development* 4.2 (May 6, 2011), pp. 373–380. ISSN: 1991-9603. DOI: `10.5194/gmd`
        `-4-373-2011`. URL: `https://gmd.copernicus.org/articles/4/373/2011/`
        (visited on 10/29/2021).

[158]   A. Kerkweg and P. Jöckel. *The infrastructure MESSy submodels GRID (v1.0) and
        IMPORT (v1.0)*. preprint. Atmospheric Sciences, Oct. 8, 2015. DOI: `10.5194/gmd`
        `d-8-8607-2015`. URL: `https://gmd.copernicus.org/preprints/8/8607/2`
        `015/` (visited on 10/29/2021).

[159]   S. Brinkop, M. Dameris, P. Jöckel, H. Garny, S. Lossow, and G. Stiller. 'The mil-
        lennium water vapour drop in chemistry–climate model simulations'. In: *Atmo-
        spheric Chemistry and Physics* 16.13 (July 6, 2016), pp. 8125–8140. ISSN: 1680-
        7324. DOI: `10.5194/acp-16-8125-2016`. URL: `https://acp.copernicus`
        `.org/articles/16/8125/2016/` (visited on 10/29/2021).

[160]   *TPChange - DFG TRR 301*. de-DE. URL: `https://tpchange.de/` (visited on
        04/14/2023).

9

[161] G. Myhre, M. Kvalevåg, G. Rädel, J. Cook, K. P. Shine, H. Clark, F. Karcher, K. Markowicz, A. Kardas, P. Wolkenberg, Y. Balkanski, M. Ponater, P. Forster, A. Rap, R. Leon, and Rodriguez. 'Intercomparison of radiative forcing calculations of stratospheric water vapour and contrails'. In: *Meteorologische Zeitschrift* 18.6 (Dec. 1, 2009), pp. 585–596. ISSN: 0941-2948. DOI: 10.1127/0941-2948/2009/0 411. URL: http://www.schweizerbart.de/papers/metz/detail/18/74377 /Intercomparison_of_radiative_forcing_calculations_?af=crossref (visited on 10/29/2021).

[162] E. Blanvillain and G. Gallic. 'HIKARI Paving the way towards High Speed Air Transport'. In: *20th AIAA International Space Planes and Hypersonic Systems and Technologies Conference*. 20th AIAA International Space Planes and Hypersonic Systems and Technologies Conference. Glasgow, Scotland: American Institute of Aeronautics and Astronautics, July 6, 2015. ISBN: 978-1-62410-320-9. DOI: 10.25 14/6.2015-3676. URL: http://arc.aiaa.org/doi/10.2514/6.2015-3676 (visited on 10/29/2021).

[163] S. Defoort, L. Serre, R. Grenon, J. Varnier, G. Carrier, and D. Scherrer. 'ZEHST - environmental challenges for hypersonic passenger transport'. In: *18th AIAA/3AF International Space Planes and Hypersonic Systems and Technologies Conference*. 18th AIAA/3AF International Space Planes and Hypersonic Systems and Technologies Conference. Tours, France: American Institute of Aeronautics and Astronautics, Sept. 24, 2012. ISBN: 978-1-60086-931-0. DOI: 10.2514/6.2012-58 73. URL: https://arc.aiaa.org/doi/10.2514/6.2012-5873 (visited on 10/29/2021).

[164] J. Steelant. 'LAPCAT - High-Speed Propulsion Technology'. In: (2014), p. 38.

[165] F. Falempin, D. Scherrer, G. Laruelle, P. Rostand, G. Fratacci, and J. Schultz. 'French Hypersonic Propulsion Program PREPHA - Results, lessons and perspectives'. en. In: *8th AIAA International Space Planes and Hypersonic Systems and Technologies Conference*. Norfolk,VA,U.S.A.: American Institute of Aeronautics and Astronautics, Apr. 1998. DOI: 10.2514/6.1998-1565. URL: https://arc.aiaa.org/doi/10.2514/6.1998-1565 (visited on 04/04/2022).

[166] D. Scherrer, O. Dessornes, M. Ferrier, A. Vincent-Randonnier, Y. Moule, and V. Sabel'nikov. 'Research on Supersonic Combustion and Scramjet Combustors at ONERA'. en. In: *AerospaceLab Journal* Issue 11 (2016). Artwork Size: 20 pages Medium: PDF Publisher: ONERA, 20 pages. DOI: 10.12762/2016.AL11-04. URL: https://aerospacelab.onera.fr/sites/www.aerospacelab-journa l.org/files/AL11-04.pdf (visited on 04/04/2022).

[167] G. Brasseur and S. Solomon. 'Composition and Chemistry'. en. In: *Aeronomy of the Middle Atmosphere - Chemistry and Physics of the Stratosphere and Mesosphere*. Ed. by G. Brasseur and S. Solomon. Atmospheric Sciences Library. Dordrecht: Springer Netherlands, 1984, pp. 201–319. ISBN: 978-94-009-6401-3. DOI: 10.1007/978-94-009-6401-3_5. URL: https://doi.org/10.1007/978-94 -009-6401-3_5 (visited on 06/10/2022).

9

[168] K. W. Jucks, D. G. Johnson, K. V. Chance, W. A. Traub, J. J. Margitan, G. B. Oster-man, R. J. Salawitch, and Y. Sasano. 'Observations of OH, HO2, H2O, and O3 in the upper stratosphere: Implications for HOx photochemistry'. en. In: *Geophysical Research Letters* 25.21 (1998), pp. 3935–3938. ISSN: 1944-8007. DOI: 10.1029/1998GL900009. URL: http://onlinelibrary.wiley.com/doi/abs/10.1029/1998GL900009 (visited on 06/13/2022).

[169] R. R. Conway, M. E. Summers, M. H. Stevens, J. G. Cardon, P. Preusse, and D. Offermann. 'Satellite observations of upper stratospheric and mesospheric OH - The HOxdilemma'. en. In: *Geophysical Research Letters* 27.17 (2000), pp. 2613–2616. ISSN: 1944-8007. DOI: 10.1029/2000GL011698. URL: http://onlinelibrary.wiley.com/doi/abs/10.1029/2000GL011698 (visited on 06/13/2022).

[170] B. J. Sandor and R. T. Clancy. 'Mesospheric HOx chemistry from diurnal microwave observations of HO2, O3, and H2O'. en. In: *Journal of Geophysical Research: Atmospheres* 103.D11 (1998), pp. 13337–13351. ISSN: 2156-2202. DOI: 10.1029/98JD00432. URL: http://onlinelibrary.wiley.com/doi/abs/10.1029/98JD00432 (visited on 06/13/2022).

[171] H. M. Pickett, B. J. Drouin, T. Canty, L. J. Kovalenko, R. J. Salawitch, N. J. Livesey, W. G. Read, J. W. Waters, K. W. Jucks, and W. A. Traub. 'Validation of Aura MLS HOx measurements with remote-sensing balloon instruments'. en. In: *Geophysical Research Letters* 33.1 (2006). ISSN: 1944-8007. DOI: 10.1029/2005GL024048. URL: https://onlinelibrary.wiley.com/doi/abs/10.1029/2005GL024048 (visited on 04/19/2023).

[172] H. le Texier, S. Solomon, and R. R. Garcia. 'The role of molecular hydrogen and methane oxidation in the water vapour budget of the stratosphere'. In: *Quarterly Journal of the Royal Meteorological Society* 114.480 (Jan. 1988), pp. 281–295. ISSN: 00359009, 1477870X. DOI: 10.1002/qj.49711448002. URL: https://onlinelibrary.wiley.com/doi/10.1002/qj.49711448002 (visited on 10/29/2021).

[173] E. E. Remsberg. 'Methane as a diagnostic tracer of changes in the Brewer–Dobson circulation of the stratosphere'. English. In: *Atmospheric Chemistry and Physics* 15.7 (Apr. 2015). Publisher: Copernicus GmbH, pp. 3739–3754. ISSN: 1680-7316. DOI: 10.5194/acp-15-3739-2015. URL: https://acp.copernicus.org/articles/15/3739/2015/ (visited on 05/05/2023).

[174] J. L. Neu and R. A. Plumb. 'Age of air in a "leaky pipe" model of stratospheric transport'. en. In: *Journal of Geophysical Research: Atmospheres* 104.D16 (1999), pp. 19243–19255. ISSN: 2156-2202. DOI: 10.1029/1999JD900251. URL: https://onlinelibrary.wiley.com/doi/abs/10.1029/1999JD900251 (visited on 05/09/2023).

[175] H. Garny, T. Birner, H. Bönisch, and F. Bunzel. 'The effects of mixing on age of air'. en. In: *Journal of Geophysical Research: Atmospheres* 119.12 (2014), pp. 7015–7034. ISSN: 2169-8996. DOI: 10.1002/2013JD021417. URL: https://onlinelibrary.wiley.com/doi/abs/10.1002/2013JD021417 (visited on 05/09/2023).

9

[176] P. W. Mote, K. H. Rosenlof, M. E. McIntyre, E. S. Carr, J. C. Gille, J. R. Holton, J. S. Kinnersley, H. C. Pumphrey, J. M. Russell III, and J. W. Waters. 'An atmospheric tape recorder: The imprint of tropical tropopause temperatures on stratospheric water vapor'. In: *Journal of Geophysical Research: Atmospheres* 101.D2 (1996), pp. 3989–4006. ISSN: 2156-2202. DOI: 10.1029/95JD03422. URL: http://onlin elibrary.wiley.com/doi/abs/10.1029/95JD03422 (visited on 06/14/2022).

[177] A. Tabazadeh, M. L. Santee, M. Y. Danilin, H. C. Pumphrey, P. A. Newman, P. J. Hamill, and J. L. Mergenthaler. 'Quantifying Denitrification and Its Effect on Ozone Recovery'. In: *Science* 288.5470 (May 2000). Publisher: American Association for the Advancement of Science, pp. 1407–1411. DOI: 10.1126/science.28 8.5470.1407. URL: https://www.science.org/doi/10.1126/science.288 .5470.1407 (visited on 05/12/2023).

[178] W. Randel and M. Park. 'Diagnosing Observed Stratospheric Water Vapor Relationships to the Cold Point Tropical Tropopause'. en. In: *Journal of Geophysical Research: Atmospheres* 124.13 (2019), pp. 7018–7033. ISSN: 2169-8996. DOI: 10.1 029/2019JD030648. URL: https://onlinelibrary.wiley.com/doi/abs/10 .1029/2019JD030648 (visited on 02/27/2023).

[179] D. T. Shindell. 'Climate and ozone response to increased stratospheric water vapor'. In: *Geophysical Research Letters* 28.8 (Apr. 15, 2001), pp. 1551–1554. ISSN: 00948276. DOI: 10.1029/1999GL011197. URL: http://doi.wiley.com/10.10 29/1999GL011197 (visited on 10/29/2021).

[180] S. Solomon, R. R. Garcia, and F. Stordal. 'Transport processes and ozone perturbations'. In: *Journal of Geophysical Research: Atmospheres* 90.D7 (1985), pp. 12981–12989. DOI: https://doi.org/10.1029/JD090iD07p12981. URL: https://ag upubs.onlinelibrary.wiley.com/doi/abs/10.1029/JD090iD07p12981.

[181] M. Nützel and J. Pletzer. personal communication. May 8, 2022.

[182] N. Butchart, A. A. Scaife, M. Bourqui, J. de Grandpré, S. H. E. Hare, J. Kettleborough, U. Langematz, E. Manzini, F. Sassi, K. Shibata, D. Shindell, and M. Sigmond. 'Simulations of anthropogenic change in the strength of the Brewer–Dobson circulation'. In: *Climate Dynamics* 27.7 (Dec. 2006), pp. 727–741. ISSN: 1432-0894. DOI: 10.1007/s00382-006-0162-4. URL: https://doi.org/10.1007/s0038 2-006-0162-4 (visited on 06/20/2022).

[183] A. Stenke and V. Grewe. 'Simulation of stratospheric water vapor trends: impact on stratospheric ozone chemistry'. In: *Atmospheric Chemistry and Physics* 5.5 (2005), pp. 1257–1272. DOI: 10.5194/acp-5-1257-2005. URL: https://ac p.copernicus.org/articles/5/1257/2005/.

[184] A. Stenke, V. Grewe, and S. Pechtl. 'Do supersonic aircraft avoid contrails?' English. In: *Atmospheric Chemistry and Physics* 8.4 (Feb. 2008). Publisher: Copernicus GmbH, pp. 955–967. ISSN: 1680-7316. DOI: 10.5194/acp-8-955-2008. URL: https://acp.copernicus.org/articles/8/955/2008/acp-8-955-2008 .html (visited on 07/14/2022).

9

[185] J. Zhang, D. Wuebbles, D. Kinnison, and S. L. Baughcum. 'Potential Impacts of Supersonic Aircraft Emissions on Ozone and Resulting Forcing on Climate: An Update on Historical Analysis'. In: *Journal of Geophysical Research: Atmospheres* (2021). DOI: `https://doi.org/10.1029/2020JD034130`. URL: `https://agup ubs.onlinelibrary.wiley.com/doi/abs/10.1029/2020JD034130`.

[186] V. Grewe and A. Stenke. 'AirClim: an efficient tool for climate evaluation of aircraft technology'. In: *Atmospheric Chemistry and Physics* 8.16 (2008), pp. 4621–4639. DOI: `10.5194/acp-8-4621-2008`. URL: `https://acp.copernicus.org/arti cles/8/4621/2008/`.

[187] K. Dahlmann, V. Grewe, C. Frömming, and U. Burkhardt. 'Can we reliably assess climate mitigation options for air traffic scenarios despite large uncertainties in atmospheric processes?' In: *Transportation Research Part D: Transport and Environment* 46 (July 1, 2016), pp. 40–55. ISSN: 1361-9209. DOI: `10.1016/j.trd.201 6.03.006`. URL: `https://www.sciencedirect.com/science/article/pii /S1361920916000353` (visited on 03/29/2022).

[188] V. Grewe, A. Stenke, M. Ponater, R. Sausen, G. Pitari, D. Iachetti, H. Rogers, O. Dessens, J. Pyle, I. S. A. Isaksen, L. Gulstad, O. A. Søvde, C. Marizy, and E. Pascuillo. 'Climate impact of supersonic air traffic: an approach to optimize a potential future supersonic fleet; results from the EU-project SCENIC'. In: *Atmospheric Chemistry and Physics* 7.19 (2007), pp. 5129–5145. DOI: `10.5194/acp-7-5129-2007`. URL: `https://acp.copernicus.org/articles/7/5129/2007/`.

[189] V. Grewe, M. Plohr, G. Cerino, M. D. Muzio, Y. Deremaux, M. Galerneau, P. de Staint Martin, T. Chaika, A. Hasselrot, U. Tengzelius, and V. D. Korovkin. 'Estimates of the climate impact of future small-scale supersonic transport aircraft – results from the HISAC EU-project'. In: *The Aeronautical Journal* 114.1153 (Mar. 2010), pp. 199–206. URL: `https://elib.dlr.de/82770/`.

[190] V. Grewe. 'Climate Impact of Hypersonic Aviation'. In: *State-of-the-Art Hypersonic Civilian Transportation - Design, Technologies and Environmental Impact* (2021). Ed. by B. H. Saracoglu. access via lsvki.ac.be or secretariatvki.ac.be.

[191] ESA. *LAPCAT II*. [Online; accessed 4-May-2022]. 2015. URL: `https://www.esa.i nt/Enabling_Support/Space_Engineering_Technology/LAPCAT_II`.

[192] J. Zhang, D. Wuebbles, D. Kinnison, and S. L. Baughcum. 'Potential Impacts of Supersonic Aircraft Emissions on Ozone and Resulting Forcing on Climate: An Update on Historical Analysis'. In: *Journal of Geophysical Research: Atmospheres* 126.6 (Mar. 27, 2021). ISSN: 2169-897X, 2169-8996. DOI: `10.1029/2020JD03413 0`. URL: `https://onlinelibrary.wiley.com/doi/10.1029/2020JD034130` (visited on 10/29/2021).

[193] D. H. Ehhalt, F. Rohrer, and A. Wahner. 'TROPOSPHERIC CHEMISTRY AND COMPOSITION | Oxidizing Capacity'. en. In: *Encyclopedia of Atmospheric Sciences (Second Edition)*. Ed. by G. R. North, J. Pyle, and F. Zhang. Oxford: Academic Press, Jan. 2015, pp. 243–250. ISBN: 978-0-12-382225-3. DOI: `10.1016/B978-0-1 2-382225-3.00437-0`. URL: `https://www.sciencedirect.com/science/ar ticle/pii/B9780123822253004370` (visited on 07/27/2022).

9

[194]   L. Wilcox, K. Shine, and B. Hoskins. 'Radiative forcing due to aviation water vapour emissions'. In: *Atmospheric Environment* 63 (Dec. 2012), pp. 1–13. ISSN: 13522310. DOI: `10.1016/j.atmosenv.2012.08.072`. URL: `https://linkinghub.elsevier.com/retrieve/pii/S135223101200859X` (visited on 10/29/2021).

[195]   J. van Manen and V. Grewe. 'Algorithmic climate change functions for the use in eco-efficient flight planning'. In: *Transportation Research Part D: Transport and Environment* 67 (Feb. 2019), pp. 388–405. ISSN: 13619209. DOI: `10.1016/j.trd.2018.12.016`. URL: `https://linkinghub.elsevier.com/retrieve/pii/S1361920917309781` (visited on 10/29/2021).

[196]   J. Hansen, M. Sato, and R. Ruedy. 'Radiative forcing and climate response'. In: *Journal of Geophysical Research: Atmospheres* 102 (D6 Mar. 27, 1997), pp. 6831–6864. ISSN: 01480227. DOI: `10.1029/96JD03436`. URL: `http://doi.wiley.com/10.1029/96JD03436` (visited on 03/14/2022).

[197]   P. J. Crutzen and F. Arnold. 'Nitric acid cloud formation in the cold Antarctic stratosphere: a major cause for the springtime 'ozone hole''. en. In: *Nature* 324.6098 (Dec. 1986). Number: 6098 Publisher: Nature Publishing Group, pp. 651–655. ISSN: 1476-4687. DOI: `10.1038/324651a0`. URL: `http://www.nature.com/articles/324651a0` (visited on 07/26/2022).

[198]   Iwasaka, Yasunobu and Hayashi, Masahiko. *Nitric Acid Transport From The Stratosphere to The Troposphere and Ice Sheet in Antarctica Through Polar Stratosphere*. English. Solar Terrestrial Environment Laboratory, Nagoya University. 1991. URL: `https://nipr.repo.nii.ac.jp/?action=pages_view_main&active_action=repository_view_main_item_detail&item_id=3638&item_no=1&page_id=13&block_id=104`.

[199]   J. Pyle. 'STRATOSPHERIC CHEMISTRY TOPICS | Overview'. en. In: *Encyclopedia of Atmospheric Sciences*. Elsevier, 2015, pp. 211–214. ISBN: 978-0-12-382225-3. DOI: `10.1016/B978-0-12-382225-3.00512-0`. URL: `https://linkinghub.elsevier.com/retrieve/pii/B9780123822253005120` (visited on 04/08/2022).

[200]   D. Bodmer, J. F. Pletzer, V. Grewe, and L. F. 'Climate-Optimised Hypersonic Flight on Mission-Level and Fleet-Level'. In: *Aerospace* (2024). in preparation.

[201]   Bodmer, Daniel and Gollnick, Volker. *Klimaoptimierter Hyperschall-Flugbetrieb auf Missions- und Flottenebene*. Manching, May 2023.

[202]   V. Grewe and K. Dahlmann. 'How ambiguous are climate metrics? And are we prepared to assess and compare the climate impact of new air traffic technologies?' en. In: *Atmospheric Environment* 106 (Apr. 2015), pp. 373–374. ISSN: 1352-2310. DOI: `10.1016/j.atmosenv.2015.02.039`. URL: `https://www.sciencedirect.com/science/article/pii/S1352231015001582` (visited on 07/21/2022).

[203]   V. Grewe and J. Pletzer. personal communication. July 25, 2022.

9

[204]   P. M. de F. Forster and K. P. Shine. 'Stratospheric water vapour changes as a pos-
        sible contributor to observed stratospheric cooling'. en. In: *Geophysical Research
        Letters* 26.21 (1999), pp. 3309–3312. ISSN: 1944-8007. DOI: 10.1029/1999GL0104
        87. URL: https://onlinelibrary.wiley.com/doi/abs/10.1029/1999GL01
        0487 (visited on 02/07/2024).

[205]   Y. Wang and Y. Huang. 'The Surface Warming Attributable to Stratospheric Water
        Vapor in CO2-Caused Global Warming'. en. In: *Journal of Geophysical Research:
        Atmospheres* 125.17 (2020). _eprint: https://agupubs.onlinelibrary.wiley.com/doi/pdf/10.102
        ISSN: 2169-8996. DOI: 10.1029/2020JD032752. URL: https://onlinelibrary
        .wiley.com/doi/abs/10.1029/2020JD032752 (visited on 02/07/2024).

[206]   F. Pithan and T. Mauritsen. 'Arctic amplification dominated by temperature feed-
        backs in contemporary climate models'. en. In: *Nature Geoscience* 7.3 (Mar. 2014).
        Number: 3 Publisher: Nature Publishing Group, pp. 181–184. ISSN: 1752-0908.
        DOI: 10.1038/ngeo2071. URL: https://www.nature.com/articles/ngeo
        2071 (visited on 02/07/2024).

A

ADDITIONAL EQUATIONS AND FIGURES

A.1. METHODS AND MODEL SETUP
A.1.1. MODEL EVALUATION WITH SWOOSH SATELLITE DATA
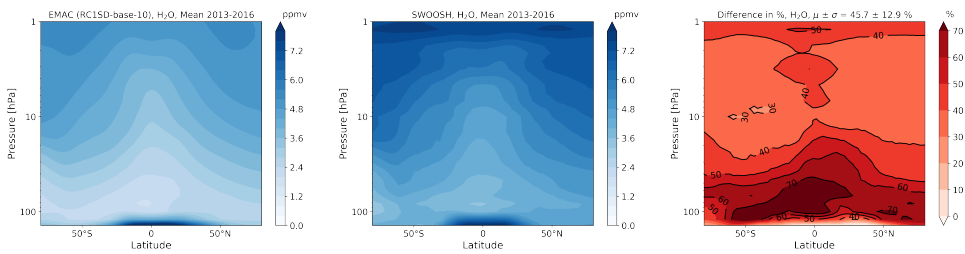
Figure A.1: Multi-annual mean (2013-2016) of H_2O volume mixing ratios for the EMAC setup RC1SD-base-10 (left), SWOOSH satellite data (middle) and the difference (observation-model) in percent (right).
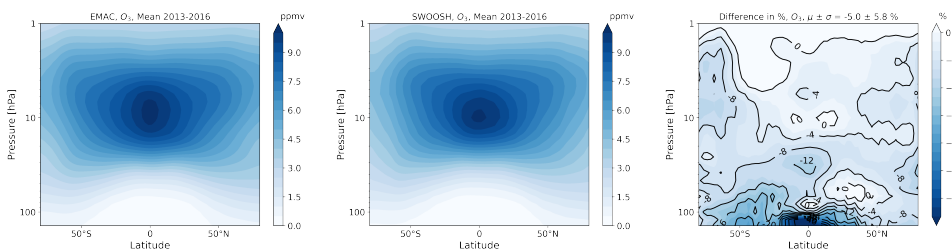
Figure A.2: Multi-annual mean (2013-2016) of O_3 volume mixing ratios for the EMAC setup RC1SD-base-10 (left), SWOOSH satellite data (middle) and the difference (observation-model) in percent (right).

A.1.2. AIRCRAFT EMISSION SCENARIOS
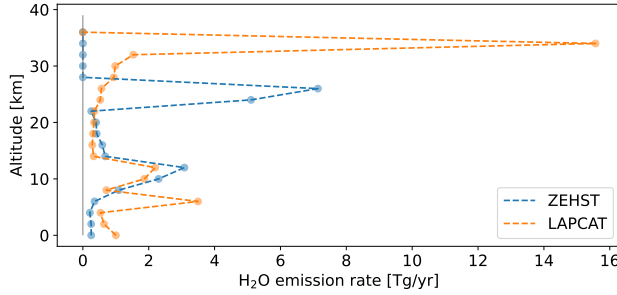
Figure A.3: Annual emission rate of water vapor versus altitude for the aircraft ZEHST and LAPCAT. Annual emission rate is collected in bins with bin size of 2 km.

A.1.3. DERIVATION OF SPIN-UP FACTOR S

The factor s is calculated using a one-dimensional differential equation containing the water vapor perturbation lifetime, boundary conditions of zero perturbation at t=0 and equilibrium perturbation at t=1 year and is therefore depending on altitude. In a quasi-steady state with a stratospheric water vapor mass perturbation X (kg), an annual emission E (kg/year) and a perturbation lifetime τ (years) the following equation is obtained

$$0 = \frac{\delta X}{\delta t} = E - \frac{1}{\tau} X \tag{A.1}$$

or, in other words,

$$X = \tau E \tag{A.2}$$

To obtain the value of s the differential equation is solved with the evolution of the stratospheric water vapor mass change to Y for an emission sX

$$\frac{\delta Y(t)}{\delta t} = sE - \frac{1}{\tau} Y \tag{A.3}$$

with the boundary conditions $Y(t = 0) = 0$ and $Y(t = 1) = \tau E$. The solution of the differential equation that fulfills the first boundary condition is then

$$Y(t) = s\tau E(1 - e^{-\frac{1}{\tau}t}) \tag{A.4}$$

In combination with the second boundary condition this gives us

$$s = \frac{1}{1 - e^{-\frac{1}{\tau}}} \tag{A.5}$$

Hence, if we estimate s with a Taylor approximation we obtain the perturbation lifetime of τ. However, if we enhance the emission by this factor, we additionally have to consider the loss during the first year with a factor of 0.5, which applies for τ between 2 to 5 years.

A.1.4. WATER VAPOR LIFETIME IN EMAC AND LMDZ-INCA MODEL
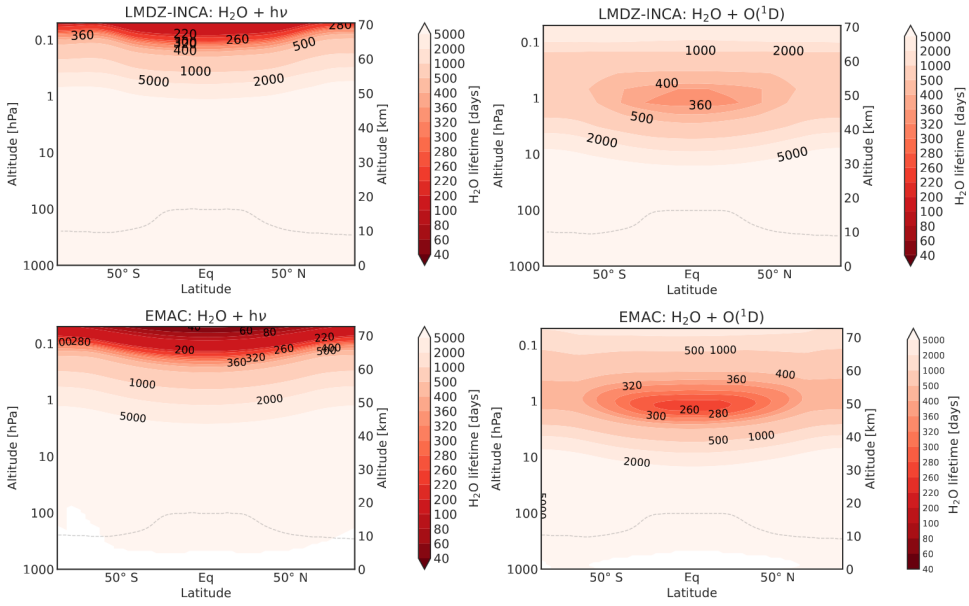
Figure A.4: Zonal mean H_2O lifetime in days for photolysis (left) and reaction with $O(^1D)$ (right) for LMDZ-INCA (upper) and EMAC (lower).

A

A.2. Vertical and Horizontal Transport of Emitted Trace Gases

Figure A.5: Timeline of integrated concentrations changes in northern subtropics (10-30° N) for water vapor emission scenarios at 38 km and the reference simulation (first row).
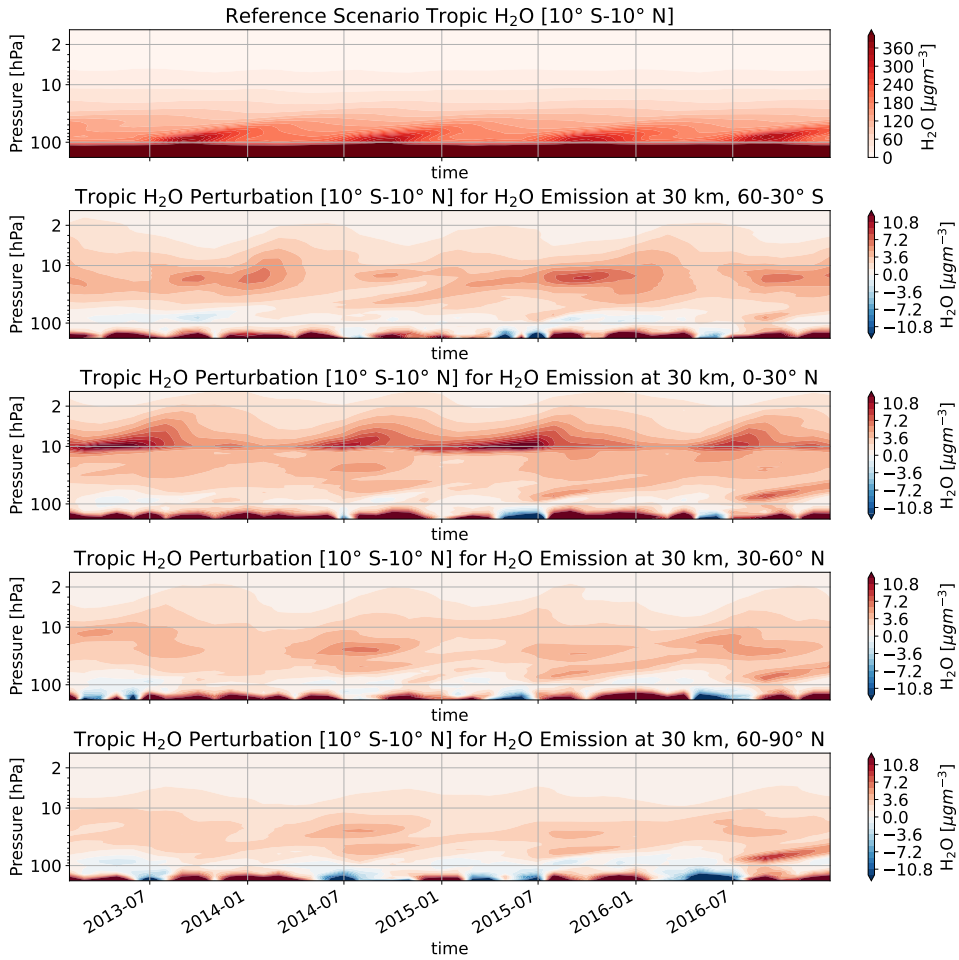
Figure A.6: Timeline of integrated concentrations changes in the tropics (10° S-10° N) for water vapor emission scenarios and the reference simulation (first row).
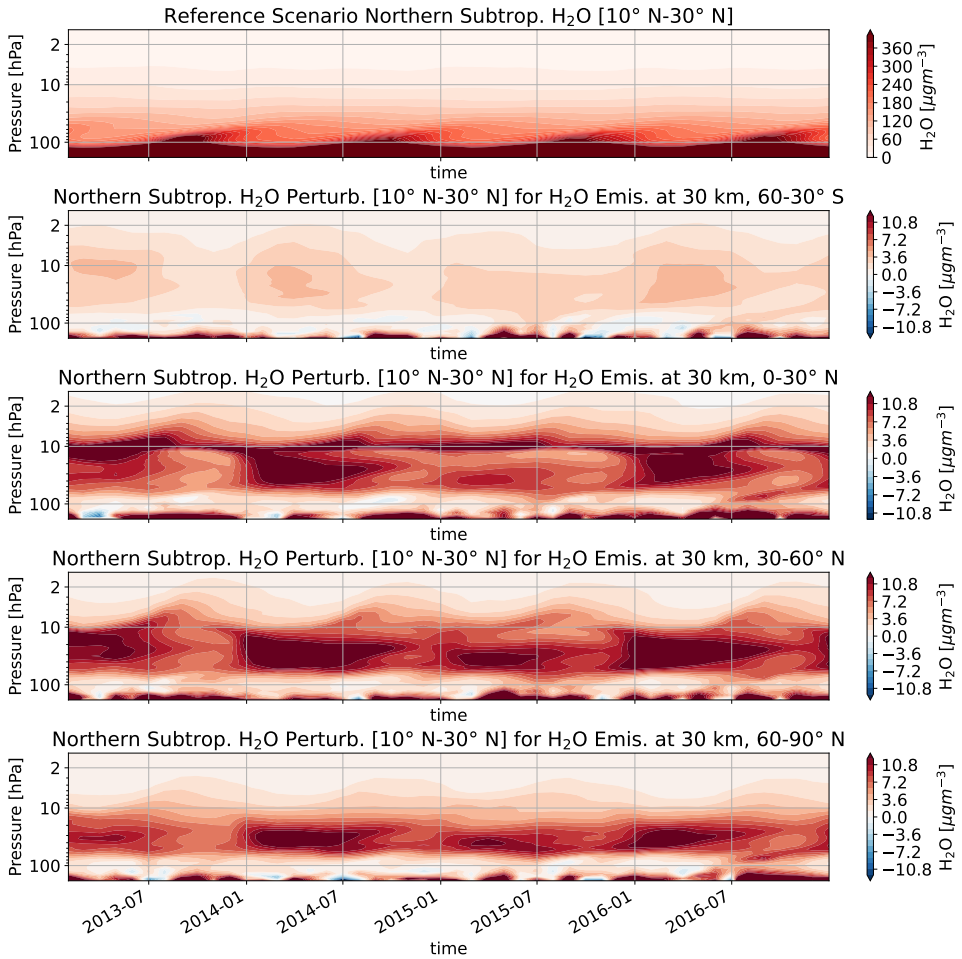
Figure A.7: Timeline of integrated concentrations changes in northern subtropics (10-30° N) for water vapor emission scenarios at 30 km and the reference simulation (first row).

Figure A.8: Timeline of integrated concentrations changes in northern subtropics (10-30° N) for water vapor emission scenarios at 30 km and the reference simulation (first row).
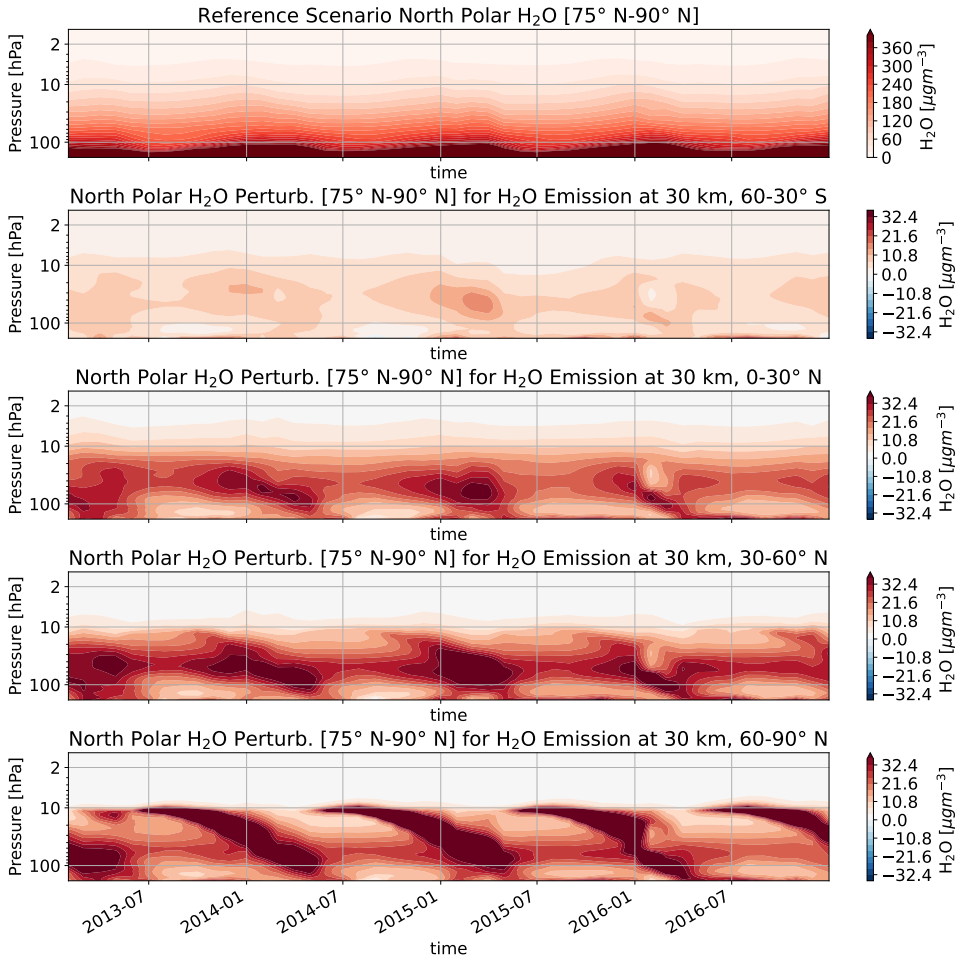
Figure A.9: Timeline of integrated concentrations changes in northern polar regions (75-90° N) for water vapor emission scenarios at 30 km and the reference simulation (first row).
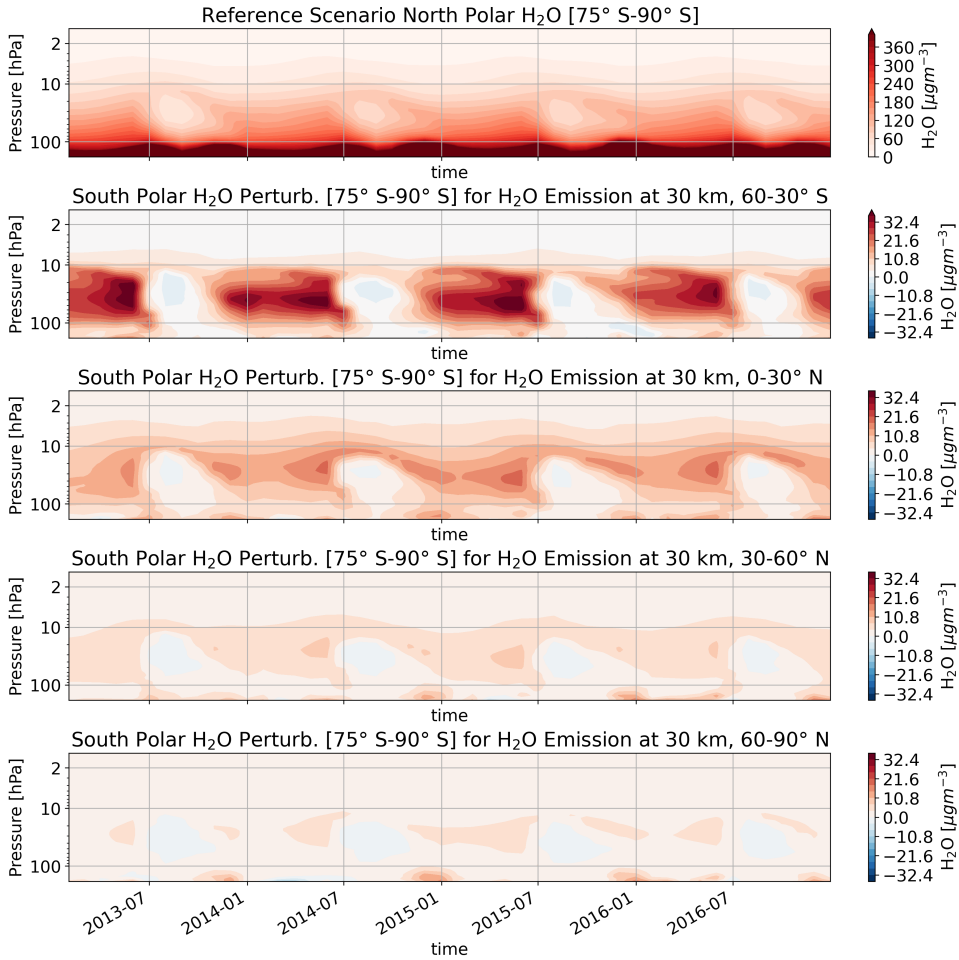
Figure A.10: Timeline of integrated concentrations changes in south polar regions (75-90° S) for water vapor emission scenarios at 30 km and the reference simulation (first row).

A
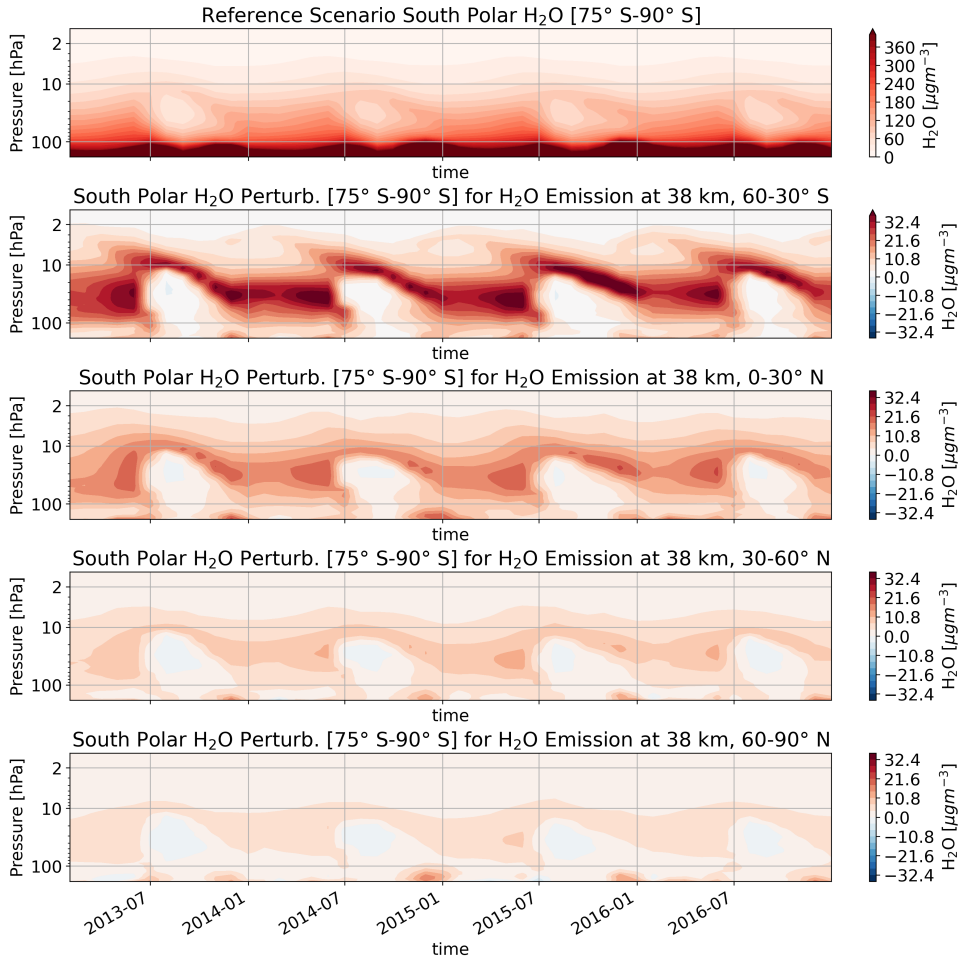
Figure A.11: Timeline of integrated concentrations changes in south polar regions (75-90° S) for water vapor emission scenarios at 38 km and the reference simulation (first row).

A.3. Atmospheric Composition Changes for Combined Emissions
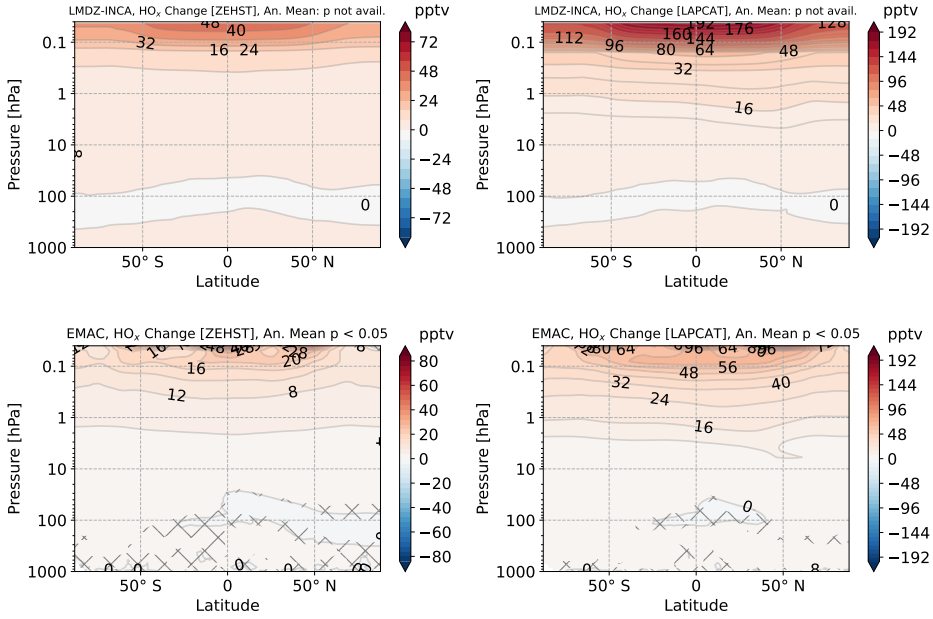
Figure A.12: Annual mean (2010-2014) of HO_x ($OH + HO_2 + H$) perturbation (pptv) for the ZEHST scenario (left) and the LAPCAT scenario (right) for EMAC (lower) and LMDZ-INCA (upper). hatched areas are characterized by a p-value higher than the threshold indicated in the title of each plot.
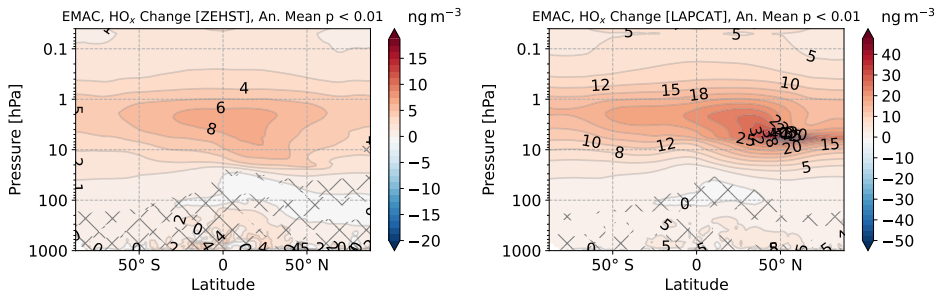
Figure A.13: Annual mean (2010-2014) of HO_x perturbation ($\mathrm{ng\,m^{-3}}$) for the ZEHST scenario (left) and the LAPCAT scenario (right) for EMAC. hatched areas are characterized by a p-value higher than the threshold indicated in the title of each plot.
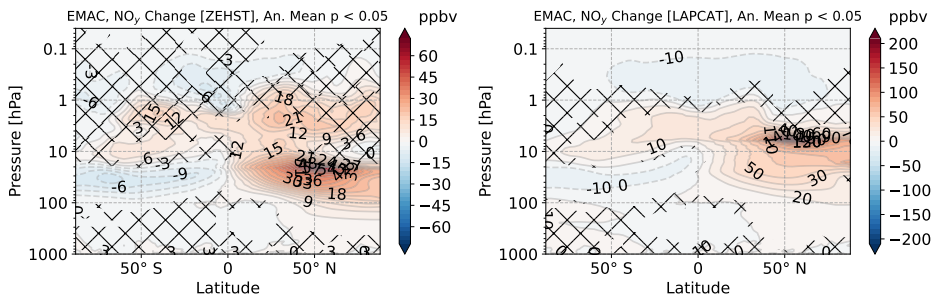
Figure A.14: Annual mean (2010-2014) of NO_y perturbation (ppbv) for the ZEHST scenario (left) and the LAPCAT scenario (right) for the EMAC model. Hatched areas are characterized by a p-value higher than the threshold indicated in the title of each plot.
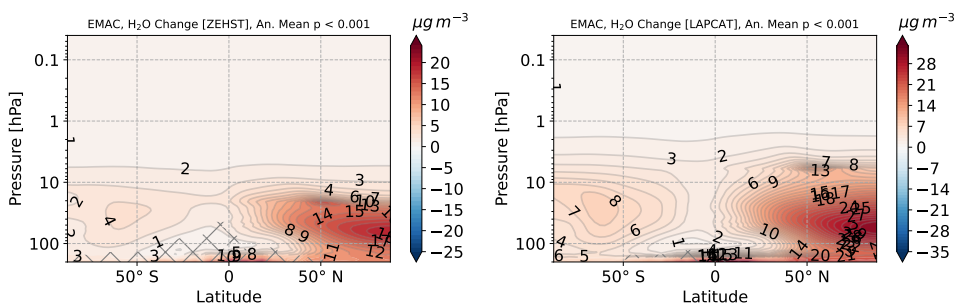
Figure A.15: Annual mean (2010-2014) of H_2O perturbation ($\mathrm{\mu g\,m^{-3}}$) for the ZEHST scenario (left) and the LAPCAT scenario (right) for both models LMDZ-INCA (top) and EMAC (bottom). Hatched areas are characterized by a p-value higher than the threshold indicated in the title of each plot.

A.4. ATMOSPHERIC COMPOSITION CHANGES FOR INDIVID-UAL EMISSIONS
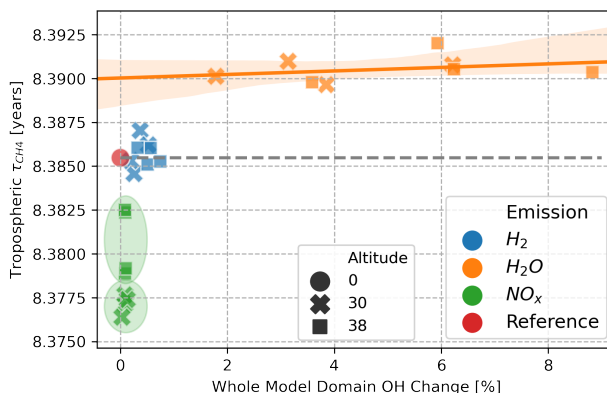
Figure A.16: Tropospheric methane lifetime in relation to hydroxyl change (whole-model-domain) for all emission scenarios (legend). Tropospheric methane lifetime is reduced or extended below or above the dashed gray line, respectively. The regression lines including the shaded areas depict the standard deviation of scenarios.

Table A.1: Markers for probability levels of significance test.

Emission	ΔH_2O	ΔH_2O / molecule	ΔO_3	ΔO_3 / molecule
H_2O	100 Tg	85 Tg $(Tmol/year)^{-1}$	-0.04 %	-0.03 % $(Tmol/year)^{-1}$
NO_x	0 Tg	0 Tg $(Tmol/year)^{-1}$	-0.15 %	-242 % $(Tmol/year)^{-1}$
H_2	5 Tg	42 Tg $(Tmol/year)^{-1}$	-0.02 %	-0.17 % $(Tmol/year)^{-1}$

Table A.2: Relative atmospheric composition change of CH_4, HO_2 and OH (average) for the troposphere and middle atmosphere

Emission	Sphere	ΔCH4 [%]	ΔHO2 [%]	ΔOH [%]	ΔCH4/Tmol [%]	ΔHO2/Tmol [%]	ΔOH/Tmol [%]
H_2O	Troposphere	-0,0014	-1,12	-0,15	-0,001	-0,9	-0,1
H_2O	Middle Atmosphere	-0,0851	4,31	5,31	-0,072	3,7	4,5
NOx	Troposphere	-0,0015	0,05	0,07	-2,218	71,0	107,2
NOx	Middle Atmosphere	-0,0057	-0,44	0,09	-8,456	-655,1	126,6
H_2	Troposphere	-0,0002	0,02	-0,02	-0,002	0,1	-0,2
H_2	Middle Atmosphere	-0,0140	0,39	0,47	-0,120	3,3	4,0

A

Figure A.17: Vertical distribution of global H_2O change as concentration (a, b, c) and volume mixing ratio (d, e, f). Subfigures (a, d), (b, e) and (c, f) depict H_2O change due to H_2O, NO_x and H_2 emission respectively,
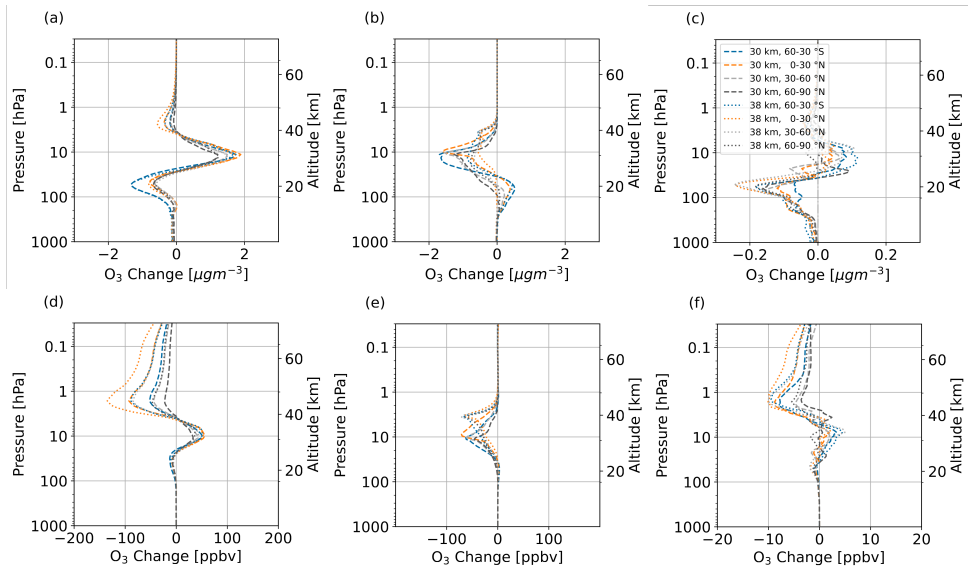
Figure A.18: Vertical distribution of global O_3 change as concentration (a, b, c) and volume mixing ratio (d, e, f). Subfigures (a, d), (b, e) and (c, f) depict O_3 change due to H_2O, NO_x and H_2 emission respectively,
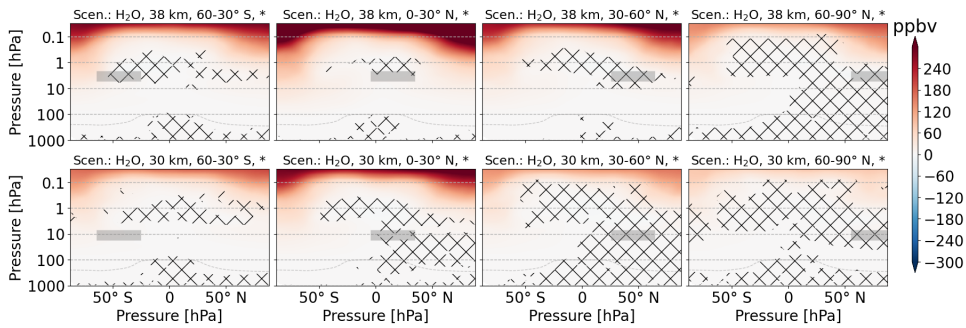
Figure A.19: Zonal mean of H_2 perturbation (volume mixing ratio, ppbv) for scenarios where H_2O is emitted. The first and second row refer to 38 km and 30 km altitudes of emission, respectively. Columns represent the latitude region of emission. The emission regions are shaded in gray. Lines indicate statistically insignificant results and the probability level is written in the title of each subplot.
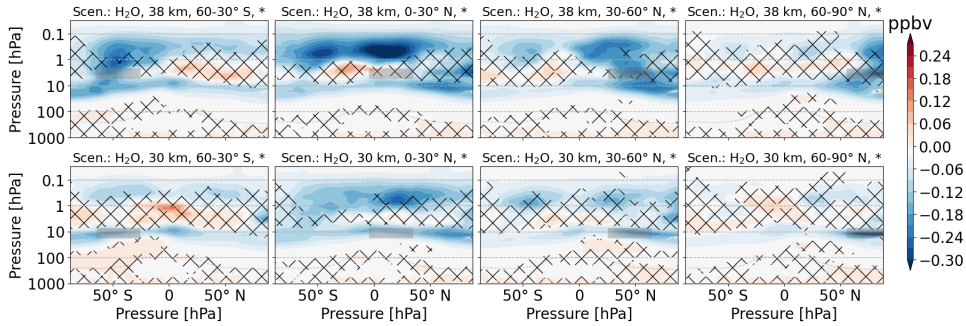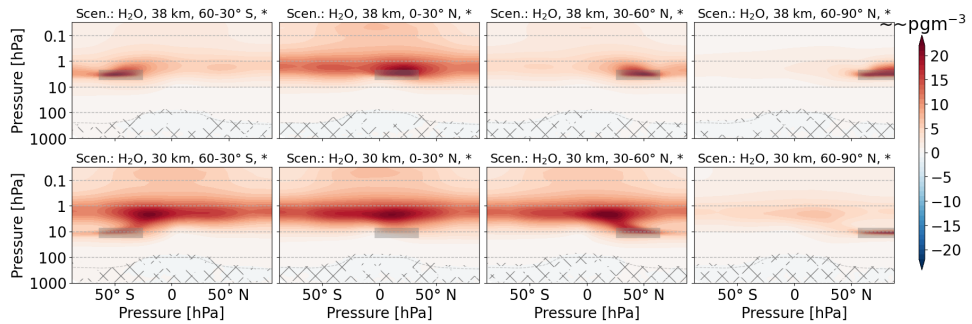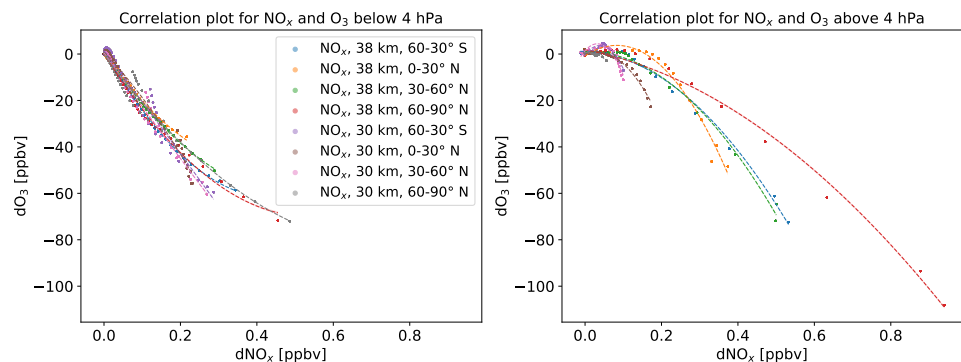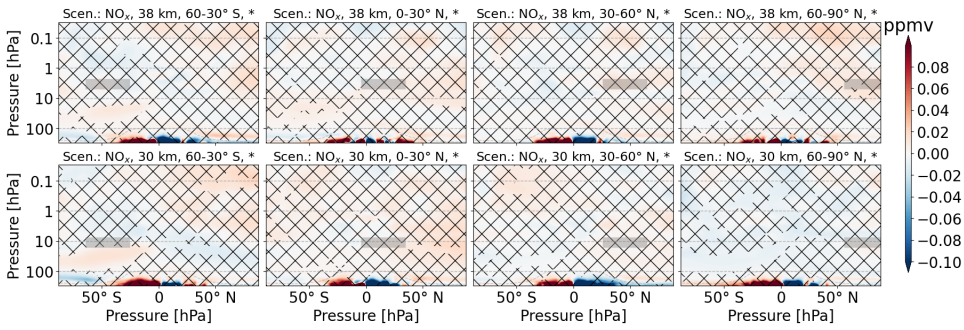

Figure A.20: Zonal mean of NO_x perturbation (volume mixing ratio, ppbv) for scenarios where H_2O is emitted. The first and second row refer to 38 km and 30 km altitudes of emission, respectively. Columns represent the latitude region of emission. The emission regions are shaded in gray. Lines indicate statistically insignificant results and the probability level is written in the title of each subplot.
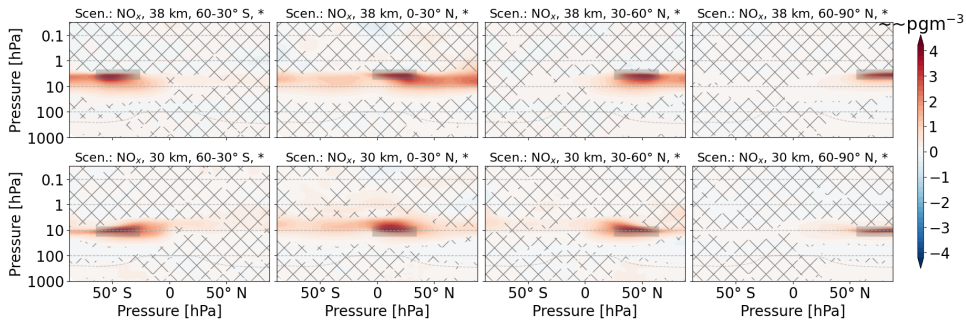
Figure A.21: Zonal mean of OH perturbation (concentration) for scenarios where NO_x is emitted. The first and second row refer to 38 km and 30 km altitudes of emission, respectively. Columns represent the latitude region of emission. The emission regions are shaded in gray. Lines indicate statistically insignificant results and the probability level is written in the title of each subplot.
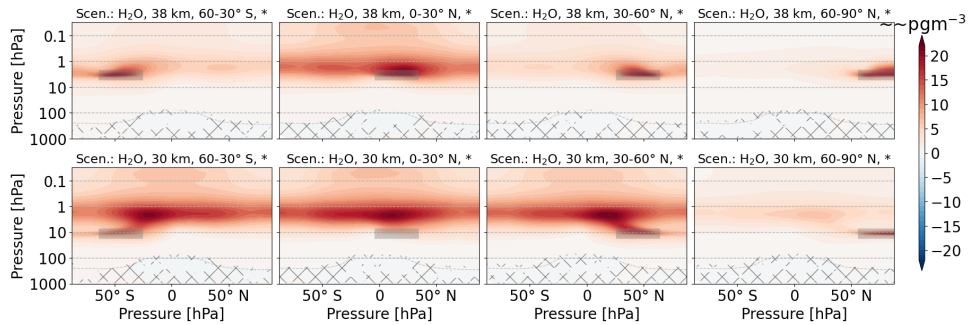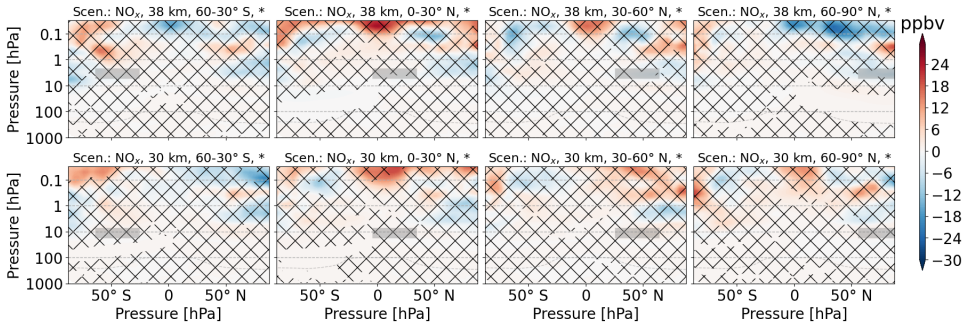
Figure A.22: Zonal mean of OH perturbation (concentration) for scenarios where H_2O is emitted. The first and second row refer to 38 km and 30 km altitudes of emission, respectively. Columns represent the latitude region of emission. The emission regions are shaded in gray. Lines indicate statistically insignificant results and the probability level is written in the title of each subplot.

Figure A.23: Zonal mean of OH perturbation (concentration) for scenarios where H_2 is emitted. The first and second row refer to 38 km and 30 km altitudes of emission, respectively. Columns represent the latitude region of emission. The emission regions are shaded in gray. Lines indicate statistically insignificant results and the probability level is written in the title of each subplot.


Figure A.24: Correlation of nitrogen oxide change and ozone change for two altitudes regions (surface-4 hPa and 4-0.01 hPa). The values are averaged over latitude and limited to statistically significant values with a 95 % confidence.

A

Figure A.25: Zonal mean of H_2O perturbation (volume mixing ratio, ppbv) for scenarios where NO_x is emitted. The first and second row refer to 38 km and 30 km altitudes of emission, respectively. Columns represent the latitude region of emission. The emission regions are shaded in gray. Lines indicate statistically insignificant results and the probability level is written in the title of each subplot.
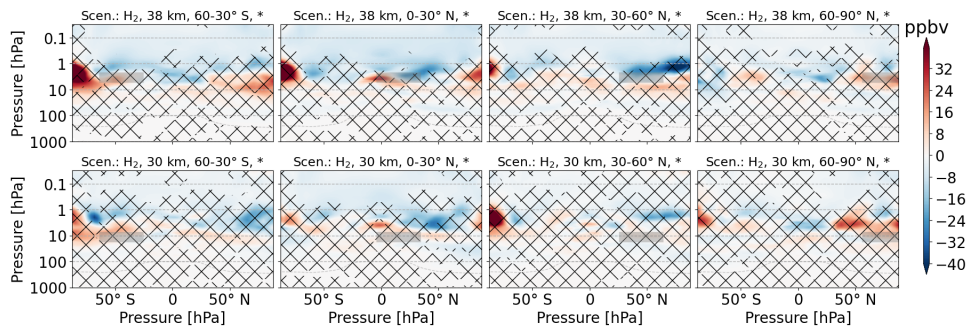

Figure A.26: Zonal mean of H_2 perturbation (volume mixing ratio, ppbv) for scenarios where NO_x is emitted. The first and second row refer to 38 km and 30 km altitudes of emission, respectively. Columns represent the latitude region of emission. The emission regions are shaded in gray. Lines indicate statistically insignificant results and the probability level is written in the title of each subplot.
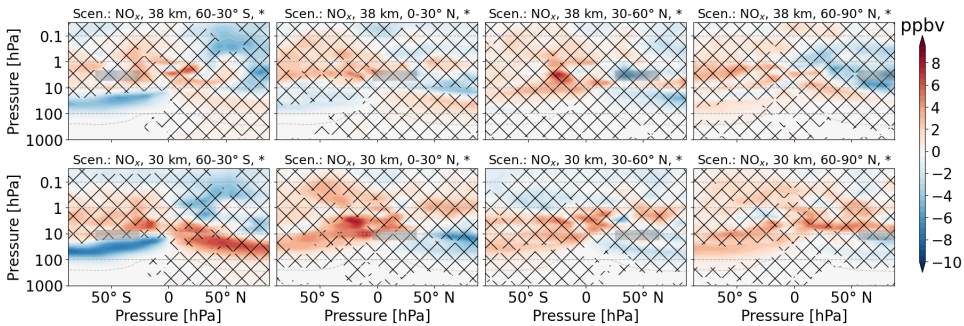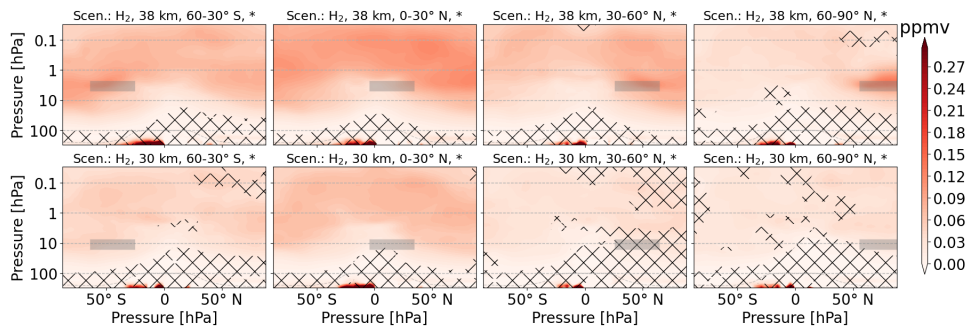

Figure A.27: Zonal mean of CH_4 perturbation (volume mixing ratio, ppbv) for scenarios where NO_x is emitted. The first and second row refer to 38 km and 30 km altitudes of emission, respectively. Columns represent the latitude region of emission. The emission regions are shaded in gray. Lines indicate statistically insignificant results and the probability level is written in the title of each subplot.
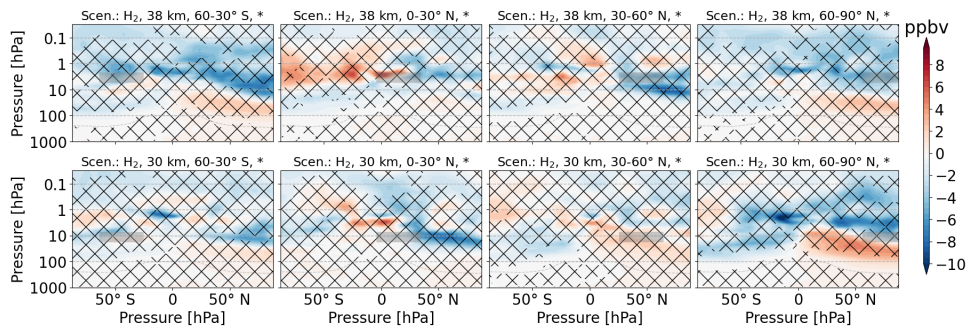
Figure A.28: Zonal mean of O_3 perturbation (volume mixing ratio, ppbv) for scenarios where H_2 is emitted. The first and second row refer to 38 km and 30 km altitudes of emission, respectively. Columns represent the latitude region of emission. The emission regions are shaded in gray. Lines indicate statistically insignificant results and the probability level is written in the title of each subplot.

Figure A.29: Zonal mean of H_2O perturbation (volume mixing ratio, ppmv) for scenarios where H_2 is emitted. The first and second row refer to 38 km and 30 km altitudes of emission, respectively. Columns represent the latitude region of emission. The emission regions are shaded in gray. Lines indicate statistically insignificant results and the probability level is written in the title of each subplot.

Figure A.30: Zonal mean of CH_4 perturbation (volume mixing ratio, ppbv) for scenarios where H_2 is emitted. The first and second row refer to 38 km and 30 km altitudes of emission, respectively. Columns represent the latitude region of emission. The emission regions are shaded in gray. Lines indicate statistically insignificant results and the probability level is written in the title of each subplot.
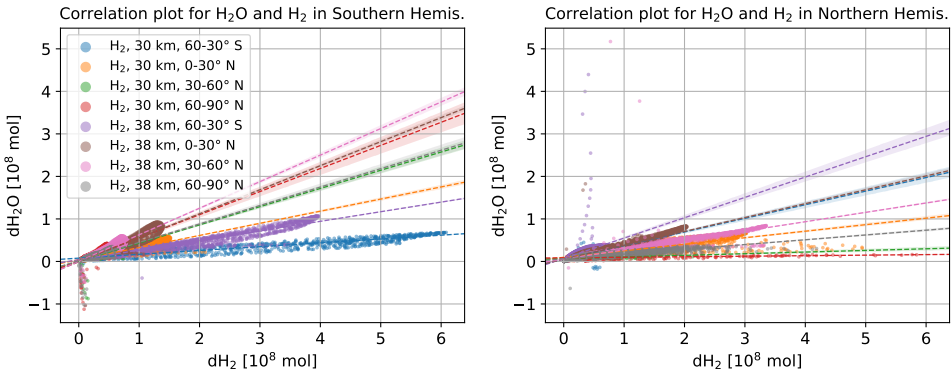
Figure A.31: Correlation of molar water vapor and hydrogen change for the Southern (left) and Northern (right) Hemisphere. The values are limited to statistically significant values with a 95 % confidence.
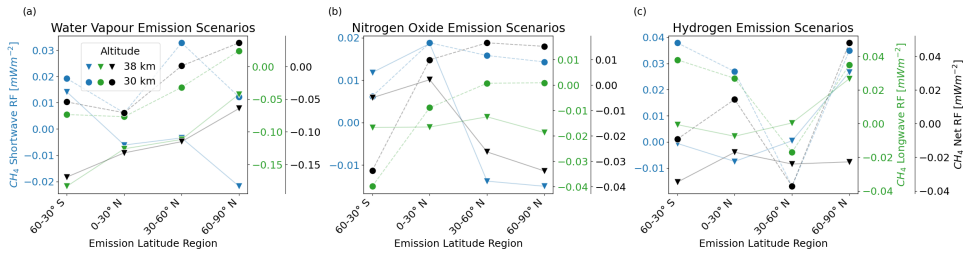

Figure A.32: The shortwave, longwave and net radiative forcing in blue, green and black, respectively, for water vapor (a), nitrogen oxide (b) and hydrogen (c) emission scenarios due to methane changes. For different altitude emission scenarios refer to markers. Latitude regions of emission are aligned on the x-axis.
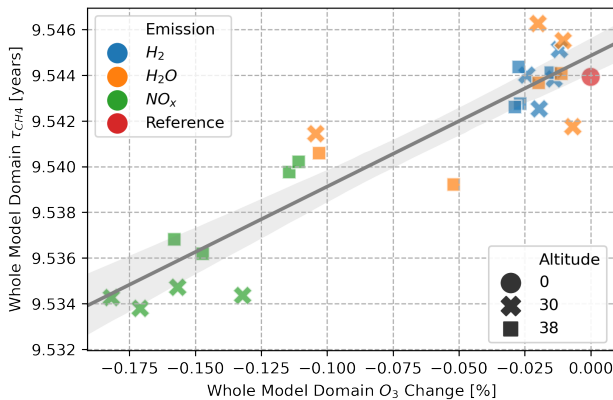

Figure A.33: Methane lifetime in relation to ozone change (both whole-model-domain) for all emission scenarios (legend). The gray regression line including the shaded area depict the 95 % confidence interval of all scenarios.

B

SOFTWARE CODE

```python
1  """Python file to read Trajectory .mat files from the folder 'data'
2     and return the radiative forcing as an excel file."""
3
4  import sys
5
6  from glob import glob
7
8  from package import to_excel as rte
9
10 from package import rf_of_trajectory as rot
11
12
13 def main():
14     """Main code. Loads files and extracts labels, calculates
15        radiative forcing, writes to excel file."""
16
17     try:
18         filepath = sys.argv[1]
19     except IndexError:
20         print(
21             "\n\tDon't forget to add the filepath \
22             like 'python3 main.py <path_to_trajectory_data>'\n"
23         )
24         sys.exit(1)
25
26     files = glob(filepath + "/*Traj*.mat")
27     labels = [a.rsplit("ory_",maxsplit=1)[-1].split("_2022",maxsplit=1)[0] for a in
      files]
28
29     # Create lists for each radiative forcing
30     tot_rf, h2o_rf, o3_rf = [], [], []
31
32     # Calculate radiative forcing for each trajectory
33     for file in files:
34         trajectory = rot.RadiativeForcingOfTrajectory(file.split()[-1])
35
```

189

B

```python
36          # Load data
37          trajectory.load_trajectory_as_dataframe()
38
39          # Mask values below tropopause
40          trajectory.drop_vertical_levels()
41
42          tot_rf.append(trajectory.total_rf())
43          h2o_rf.append(trajectory.total_h2o_rf())
44          o3_rf.append(trajectory.total_o3_rf())
45
46      # Write results to excel file
47      rte.to_excel(labels, tot_rf, h2o_rf, o3_rf)
48
49
50  if __name__ == "__main__":
51      main()
```

chap–6/py/main.py

```python
1  """First the imports are done and then the class code starts."""
2
3  from os import path
4
5  from pandas import DataFrame, to_numeric
6  from scipy.interpolate import interp1d
7  from scipy.io import loadmat
8  from xarray import open_dataset
9
10
11 class RadiativeForcingOfTrajectory:
12     """The class contains multiple functions to calculate the radiative forcing
13     of a .mat aircraft trajectory file. First developed by Johannes Pletzer (DLR)
14     for Daniel Bodmer (TUHH). The calculations are based on pandas data structure.
15     It is highly recommended to use the mask of tropospheric emission, since
16     calculations are interpolated for altitudes from 30–38 km and extrapolated
17     for all others, which potentially introduces a large error."""
18
19     def __init__(self, filepath):
20         self.filepath = filepath
21
22         self.resources_dir = path.join(path.dirname(__file__), "resources")
23
24         # outer edges and mid points of latitude regions
25         self.lat_mid_point = [-90, -75, -45, -15, 15, 45, 75, 90]
26
27         # sensitivities for outer edges and mid points of latitude regions
28         self.o3_rf_at_30_km_for_h2 = [-3.04, -3.04, -3.04, -2.46, -2.46, -2.13,
           -1.75, -1.75]
29
30         self.o3_rf_at_38_km_for_h2 = [-3.81, -3.81, -3.81, -2.59, -2.59, -2.72,
           -2.46, -2.46]
31
32         self.o3_rf_at_30_km_for_h2o = [-0.20, -0.20, -0.20, -0.08, -0.08, -0.12,
           -0.12, -0.12]
33
34         self.o3_rf_at_38_km_for_h2o = [-0.19, -0.19, -0.19, -0.07, -0.07, -0.09,
           -0.13, -0.13]
35
36         self.o3_rf_at_30_km_for_no = [127.0, 127.0, 127.0, 129.9, 129.9, 91.6, 69.9,
           69.9]
37
38         self.o3_rf_at_38_km_for_no = [102.9, 102.9, 102.9, 48.2, 48.2, 66.9, 74.3,
           74.3]
39
40         self.h2o_rf_at_30_km_for_h2o = [1.70, 1.70, 1.70, 1.90, 1.90, 1.65, 1.34,
           1.34]
41
42         self.h2o_rf_at_38_km_for_h2o = [1.89, 1.89, 1.89, 1.97, 1.97, 1.82, 1.59,
           1.59]
43
44         self.data = self.load_trajectory_as_dataframe()
45
46     def load_trajectory_as_dataframe(self):
47         """This function creates a DataFrame from a MatLab file and selects certain
           variables."""
```

```
48
49          mat = loadmat(self.filepath, squeeze_me=True)
50
51          new_data = list(
52              zip(
53                  mat["Trajectory"]["poslon"],
54                  mat["Trajectory"]["poslat"],
55                  mat["Trajectory"]["altft"],
56                  mat["Trajectory"]["pressure"],
57                  mat["Trajectory"]["H2O"],
58                  mat["Trajectory"]["H2"],
59                  mat["Trajectory"]["NO"],
60                  mat["Trajectory"]["ST"],
61              )
62          )
63
64          columns = [
65              "Longitude",
66              "Latitude",
67              "Altitude [ft]",
68              "Altitude [Pa]",
69              "H2O",
70              "H2",
71              "NO",
72              "dt",
73          ]
74
75          data_frame = DataFrame(new_data, columns=columns)
76
77          # transform altitude from ft to km
78          data_frame["Altitude [km]"] = data_frame["Altitude [ft]"] * 0.3048 / 1000
79
80          # normalize emission with duration at flight path
81          data_frame["H2O [kg]"] = data_frame["H2O"] * data_frame["dt"] / 1000
82          data_frame["NO [kg]"] = data_frame["NO"] * data_frame["dt"] / 1000
83          data_frame["H2 [kg]"] = data_frame["H2"] * data_frame["dt"] / 1000
84
85          # select final DataFrame
86          data_frame = data_frame[
87              [
88                  "Latitude",
89                  "Longitude",
90                  "Altitude [km]",
91                  "Altitude [Pa]",
92                  "H2O [kg]",
93                  "NO [kg]",
94                  "H2 [kg]",
95              ]
96          ]
97          data_frame = data_frame.apply(to_numeric, downcast="float", errors="coerce")
98
99          return data_frame
100
101      def horizontal_interp(self, val_30_km, val_38_km, var_30km, var_38km):
102          """This function interpolates input values to latitude of
103          DataFrame columns. Beware to use to the correct input."""
104
```

B

```python
105             # define interpolation functions (linear, cubic)
106
107             func_30_polar = interp1d(self.lat_mid_point, val_30_km, kind="linear")
108             func_30_tropic = interp1d(self.lat_mid_point, val_30_km, kind="cubic")
109
110             func_38_polar = interp1d(self.lat_mid_point, val_38_km, kind="linear")
111             func_38_tropic = interp1d(self.lat_mid_point, val_38_km, kind="cubic")
112
113             # linear interp. above 45 degree N, S; cubic below 45 degree N, S
114             self.data[var_30km] = self.data["Latitude"].apply(
115                 lambda x: func_30_tropic(x) if abs(x) <= 45 else func_30_polar(x)
116             )
117             self.data[var_38km] = self.data["Latitude"].apply(
118                 lambda x: func_38_tropic(x) if abs(x) <= 45 else func_38_polar(x)
119             )
120
121         def vertical_interp(self, var):
122             """This function linearly inter- and extrapolates variable
123             to altitude of DataFrame columns."""
124
125             # create columns with 30 and 38 km as x values for interpolation
126             self.data["30 km"] = 30
127             self.data["38 km"] = 38
128
129             # apply linear interpolation
130             self.data[var] = self.data.apply(
131                 lambda column: interp1d(
132                     [column["30 km"], column["38 km"]],
133                     [column[var + " [30 km]"], column[var + " [38 km]"]],
134                     fill_value="extrapolate",
135                 )(column["Altitude [km]"]),
136                 axis=1,
137             )
138
139             # clean DataFrame, remove variables
140             self.data.drop(
141                 ["30 km", "38 km", var + " [30 km]", var + " [38 km]"], axis=1, inplace=
        True
142             )
143
144         def remove_emission_normalization(self, emis, var):
145             """This function calculates total values of emission weighted variables."""
146
147             new_col = self.data[var + " / Tg"] / 1e9  # Tg to kg
148             new_col = new_col * self.data[emis]
149
150             return new_col
151
152         def drop_vertical_levels(self, alt=True):
153             """This function removes rows, where the altitude is below
154             the tropopause or another altitude. Input value has to be
155             in hectopascal. Default is below the tropopause."""
156
157             if alt is True:
158                 # load tropopause variable tp_WMO as pandas series
159                 tropause = open_dataset(
160                     self.resources_dir + "/STRATOFLY_1.0_SC0_X_tp-T42L90MA_X-X.nc"
```

B

```
161                  )
162                  tropause = tropause.mean("timem").tp_WMO.to_series()
163
164                  # get index from trajectory data
165                  idx = self.data[["Latitude", "Longitude"]].set_index(
166                      ["Latitude", "Longitude"]
167                  )
168                  idx.index.rename(["lat", "lon"], inplace=True)
169
170                  # reindex and interpolate tropopause data to trajectory index
171                  self.data["tp_WMO"] = (
172                      tropause.reindex(tropause.index.union(idx.index))
173                      .interpolate()
174                      .reindex_like(idx)
175                      .values
176                  )
177
178                  # drop data below tropopause, drop tropopause variable
179                  self.data.drop(
180                      self.data[self.data["Altitude [Pa]"] > self.data["tp_WMO"]].index,
181                      inplace=True,
182                  )
183          else:
184              # drop data below altitude
185              self.data.drop(
186                  self.data[self.data["Altitude [Pa]"] > alt * 100].index, inplace=True
187              )
188
189      def o3_rf_from_h2o_emis(self):
190          """This function calculates the ozone radiative
191          forcing due to water vapour emission."""
192
193          # use interp and weight functions
194          self.horizontal_interp(
195              self.o3_rf_at_30_km_for_h2o,
196              self.o3_rf_at_38_km_for_h2o,
197              "RF / Tg [30 km]",
198              "RF / Tg [38 km]",
199          )
200          self.vertical_interp("RF / Tg")
201
202          # calculate radiative forcing
203          self.data["O3 RF from H2O [mW m-2]"] = self.remove_emission_normalization(
204              "H2O [kg]", "RF"
205          )
206          self.data.drop(["RF / Tg"], axis=1, inplace=True)
207
208          # clean and set dtype
209          self.data.apply(to_numeric, downcast="float", errors="coerce")
210
211      def h2o_rf_from_h2o_emis(self):
212          """This function calculates the water vapour radiative
213          forcing due to water vapour emission."""
214
215          # use interp and weight functions
216          self.horizontal_interp(
217              self.h2o_rf_at_30_km_for_h2o,
```

```
218             self.h2o_rf_at_38_km_for_h2o,
219             "RF / Tg [30 km]",
220             "RF / Tg [38 km]",
221         )
222         self.vertical_interp("RF / Tg")
223
224         # radiative forcing
225         self.data["H2O RF from H2O [mW m−2]"] = self.remove_emission_normalization(
226             "H2O [kg]", "RF"
227         )
228         self.data.drop(["RF / Tg"], axis=1, inplace=True)
229
230         # clean and set dtype
231         self.data.apply(to_numeric, downcast="float", errors="coerce")
232
233     def o3_rf_from_h2_emis(self):
234         """This function calculates the ozone radiative forcing due to hydrogen
     emission."""
235
236         # use interp and weight functions
237         self.horizontal_interp(
238             self.o3_rf_at_30_km_for_h2,
239             self.o3_rf_at_38_km_for_h2,
240             "RF / Tg [30 km]",
241             "RF / Tg [38 km]",
242         )
243         self.vertical_interp("RF / Tg")
244
245         # calculate radiative forcing
246         self.data["O3 RF from H2 [mW m−2]"] = self.remove_emission_normalization(
247             "H2 [kg]", "RF"
248         )
249         self.data.drop(["RF / Tg"], axis=1, inplace=True)
250
251         # clean and set dtype
252         self.data.apply(to_numeric, downcast="float", errors="coerce")
253
254     def o3_rf_from_no_emis(self):
255         """This function calculates the ozone radiative
256         forcing due to nitrogen oxide emission."""
257
258         # use interp and weight functions
259         self.horizontal_interp(
260             self.o3_rf_at_30_km_for_no,
261             self.o3_rf_at_38_km_for_no,
262             "RF / Tg [30 km]",
263             "RF / Tg [38 km]",
264         )
265         self.vertical_interp("RF / Tg")
266
267         # calculate radiative forcing
268         self.data["O3 RF from NO [mW m−2]"] = self.remove_emission_normalization(
269             "NO [kg]", "RF"
270         )
271         self.data.drop(["RF / Tg"], axis=1, inplace=True)
272
273         # clean and set dtype
```

B

B

```python
274            self.data.apply(to_numeric, downcast="float", errors="coerce")
275
276        def total_rf(self):
277            """This function returns the net radiative forcing from ozone
278            (H2O, H2, NO emission) and water vapour (H2O emission)."""
279
280            # calculate radiative forcings for each point of trajectory
281            self.h2o_rf_from_h2o_emis()
282            self.o3_rf_from_h2o_emis()
283            self.o3_rf_from_h2_emis()
284            self.o3_rf_from_no_emis()
285
286            # Calculate net of all individual radiative forcings
287            net = (
288                self.data["H2O RF from H2O [mW m−2]"].sum()
289                + self.data["O3 RF from H2O [mW m−2]"].sum()
290                + self.data["O3 RF from H2 [mW m−2]"].sum()
291                + self.data["O3 RF from NO [mW m−2]"].sum()
292            )
293
294            return net
295
296        def total_o3_rf(self):
297            """This function returns the net radiative forcing
298            from ozone (H2O, H2, NO emission)."""
299
300            # calculate radiative forcings for each point of trajectory
301            self.o3_rf_from_h2o_emis()
302            self.o3_rf_from_h2_emis()
303            self.o3_rf_from_no_emis()
304
305            # Calculate net of all individual o3 radiative forcings
306            net = (
307                self.data["O3 RF from H2O [mW m−2]"].sum()
308                + self.data["O3 RF from H2 [mW m−2]"].sum()
309                + self.data["O3 RF from NO [mW m−2]"].sum()
310            )
311
312            return net
313
314        def total_h2o_rf(self):
315            """This function returns the net radiative forcing
316            from water vapour (H2O emission)."""
317
318            # calculate radiative forcings for each point of trajectory
319            self.h2o_rf_from_h2o_emis()
320
321            # Calculate net of all individual h2o radiative forcings
322            net = self.data["H2O RF from H2O [mW m−2]"].sum()
323
324            return net
325
326        def total_emis(self):
327            """This function returns a list of the mass emission
328            in tons (H2O, H2, NO) for the selected altitude."""
329
330            # Calculate mass emission
```

```
331          h2o_emis = round(self.data["H2O [kg]"].sum() / 1e3, 2)
332          h2_emis = round(self.data["H2 [kg]"].sum() / 1e3, 2)
333          no_emis = round(self.data["NO [kg]"].sum() / 1e3, 2)
334
335          return [h2o_emis, h2_emis, no_emis]
```

chap–6/py/rf_of_trajectory.py

B

```python
 1  """Function to export lists of radiative forcings to excel file."""
 2
 3  from pandas import DataFrame, ExcelWriter
 4
 5
 6  def to_excel(labels, tot_rf, h2o_rf, o3_rf):
 7      """Function to export the radiative forcings to an excel file"""
 8
 9      # Create DataFrame from lists
10      data_frame = DataFrame([labels, tot_rf, h2o_rf, o3_rf]).T
11      data_frame.columns = [
12          "Trajectory",
13          "RF [mW m-2]",
14          "H2O RF [mW m-2]",
15          "O3 RF [mW m-2]",
16      ]
17      data_frame.set_index("Trajectory", inplace=True)
18
19      # Write excel file
20      writer = ExcelWriter("rf_of_trajectories.xlsx")
21      data_frame.to_excel(
22          writer,
23          sheet_name="Radiative Forcing",
24          index=True,
25          na_rep="NaN",
26          engine="xlsxwriter",
27      )
28
29      # Adjust column width of excel file
30      for column in data_frame:
31          column_length = max(data_frame[column].astype(str).map(len).max(), len(column
32  ))
          col_idx = data_frame.columns.get_loc(column) + 1
33          try:
34              writer.sheets["Radiative Forcing"].set_column(
35                  col_idx, col_idx, column_length
36              )
37          except AttributeError:
38              pass
39
40      writer.save()
```

chap–6/py/to_excel.py

ACKNOWLEDGEMENTS

CURRICULUM VITÆ

Johannes Friedrich PLETZER

22-04-1990	Born in Ebersberg, Germany.

EDUCATION

1996–2010	Montessori-Schule Niederseeon (1996–2006) Karolinen–Gymnasium Rosenheim (2006–2007) Max–Mannheimer–Gymnasium Grafing (2007–2010)
2011–2018	Bachelor and Master of Science in Physics Ludwigs–Maximilians–Universität, Germany
2015	Erasmus+ Semester Universitetet i Tromsø, Norway
2019–2024	PhD candidate at Delft University of Technology *Thesis title:* The climate impact of hypersonic aircraft *Promotor:* Prof.dr. V. Grewe
2023	Visiting scientist at Institut Pierre-Simon Laplace Sorbonne Université, France

AWARDS

2022	Highlight paper in *Atmospheric Chemistry and Physics*
2023	Paper on shortlist for Paul Crutzen Publication Award 2022 by the *Atmospheric Chemistry and Physics* journal.

LIST OF PUBLICATIONS

JOURNAL PAPERS

6. Jurriaan van 't Hoff, ..., **J. Pletzer**, ..., *Inter-model comparison of the atmospheric composition impacts of emissions from a supersonic aircraft fleet*, Atmospheric Chemistry and Physics, 2024 (in preparation).

5. D. Bodmer, ..., **J. Pletzer**, ..., *Climate-optimised hypersonic flight on mission-level and fleet-level*, Aerospace, 2024 (in preparation).

4. A. Pozzer, ..., **J. Pletzer**, ..., *New developments in MESSy2.55: H2OEMIS, NAN, BIOBURN, DOMINT, MECCA, JVAL, ENSEMBLE*, Geoscientific Model Development, 2024 (in preparation).

3. K. Dahlmann, ..., **J. Pletzer**, ..., *An Eco2Fly update to the aviation climate impact assessment*, Atmospheric Chemistry and Physics, 2024 (in preparation).

2. **J. Pletzer** & V. Grewe, *Sensitivities of atmospheric composition and climate to altitude and latitude of hypersonic aircraft emissions*, `https://doi.org/10.5194/acp-24-1743-2024`, Atmospheric Chemistry and Physics, 2024.

1. **J. Pletzer**, D. Hauglustaine, Y. Cohen, P. Jöckel, and V. Grewe, *The climate impact of hydrogen powered hypersonic aircraft*, `https://doi.org/10.5194/acp-22-14323-2022`, Atmospheric Chemistry and Physics, 2022.

CONFERENCE PAPERS

3. ..., **J. Pletzer**, ..., *The effect of future supersonic aircraft emissions on air quality, climate and atmospheric composition*, Conference of the 34th Congress of the International Council of the Aeronautical Sciences, 2024 (in preparation).

2. N. Viola, ..., **J. Pletzer**, ..., *H2020 STRATOFLY project: From Europe to Australia in less than 3 hours*, `https://elib.dlr.de/185362/`, Conference of the 32nd Congress of the International Council of the Aeronautical Sciences, 2021.

1. N. Viola, ..., **J. Emmerig (now Pletzer)**, ..., *STRATOFLY MR3 – How to reduce the environmental impact of high-speed transportation*, `http://dx.doi.org/10.2514/6.2021-1877`, AIAA Scitech, 2021.

OTHER CONTRIBUTIONS

3. **J. Pletzer**, and V. Grewe *Wirkung von Emissionen in 30–38 km Höhe auf die Atmosphäre (Impact of emissions at 30-38 km altitude on the atmosphere)*, `https://www.dglr.de/vernetzen/fachbereiche/luftfahrt/l6-flugmechanikflugfuehrung/workshop-2023-l6-missionsfuehrung-bahnfuehrung-und-bahnplanung-fuer-innovative-luftfahrtanwendungen/`, DGLR-Workshop "Missionsführung, Bahnführung und Bahnplanung für innovative Luftfahrtanwendungen", May 24, 2023.

2. **J. Pletzer**, *johannespletzer/rf-of-hypersonic-trajectories: Software to estimate the radiative forcing of hypersonic emission inventories*, Zenodo, `https://doi.org/10.5281/zenodo.8422189`, October 9, 2023.

1. **J. Pletzer**, *Data underlying the PhD thesis: The climate impact of hypersonic aircraft*, `https://doi.org/10.4121/772f102d-6d41-428b-b3fb-65ea6ea1ee9e`, October 5, 2023.

B